

Recent Advances in Near-Field to Far-Field Transformation Techniques

Guest Editors: Claudio Gennarelli, Amedeo Capozzoli,
Lars J. Foged, Jeff Fordham, and Daniël Janse van Rensburg





Recent Advances in Near-Field to Far-Field Transformation Techniques

International Journal of Antennas and Propagation

Recent Advances in Near-Field to Far-Field Transformation Techniques

Guest Editors: Claudio Gennarelli, Amedeo Capozzoli,
Lars J. Foged, Jeff Fordham, and Daniël Janse van Rensburg



Copyright © 2012 Hindawi Publishing Corporation. All rights reserved.

This is a special issue published in “International Journal of Antennas and Propagation.” All articles are open access articles distributed under the Creative Commons Attribution License, which permits unrestricted use, distribution, and reproduction in any medium, provided the original work is properly cited.

Editorial Board

M. Ali, USA
Charles Bunting, USA
Dau-Chyrh Chang, Taiwan
Deb Chatterjee, USA
Z. Chen, Singapore
Christos Christodoulou, USA
Shyh-Jong Chung, Taiwan
Tayeb A. Denidni, Canada
Karu P. Esselle, Australia
Miguel Ferrando, Spain
Wei Hong, China
Hon Tat Hui, Singapore
Tamer S. Ibrahim, USA

Shyh-Kang Jeng, Taiwan
Mandeep Jit Singh, Malaysia
Ahmed A. Kishk, Canada
Ju-Hong Lee, Taiwan
Byungje Lee, Republic of Korea
L. Li, Singapore
Yilong Lu, Singapore
Andrea Massa, Italy
Derek McNamara, Canada
Ananda S. Mohan, Australia
Pavel Nikitin, USA
A. D. Panagopoulos, Greece
Matteo Pastorino, Italy

Sadasiva M. Rao, USA
Stefano Selleri, Italy
Krishnasamy T. Selvan, India
Zhongxiang Q. Shen, Singapore
Seong-Youp Suh, USA
Parveen Wahid, USA
Yuanxun Ethan Wang, USA
Quan Xue, Hong Kong
Tat Soon Yeo, Singapore
Wenhua Yu, USA
Lei Zhu, Singapore

Contents

Recent Advances in Near-Field to Far-Field Transformation Techniques, Claudio Gennarelli, Amedeo Capozzoli, Lars J. Foged, Jeff Fordham, and Daniël Janse van Rensburg
Volume 2012, Article ID 243203, 3 pages

Development of a Near-Field Bistatic Synthetic Aperture Radar for Complex Target Reconstruction, David G. Johnson and Graham M. Brooker
Volume 2012, Article ID 761816, 22 pages

Examination of Far-Field Mathematical Absorber Reflection Suppression through Computational Electromagnetic Simulation, S. F. Gregson, A. C. Newell, and G. E. Hindman
Volume 2012, Article ID 623268, 10 pages

An Innovative Direct NF-FF Transformation Technique with Helicoidal Scanning, Francesco D'Agostino, Flaminio Ferrara, Claudio Gennarelli, Rocco Guerriero, and Massimo Migliozzi
Volume 2012, Article ID 912948, 9 pages

Using Truncated Data Sets in Spherical-Scanning Antenna Measurements, Ronald C. Wittmann, Carl F. Stubenrauch, and Michael H. Francis
Volume 2012, Article ID 979846, 6 pages

A Probe-Compensated Helicoidal NF-FF Transformation for Aperture Antennas Using a Prolate Spheroidal Expansion, Amedeo Capozzoli, Claudio Curcio, Giuseppe D'Elia, Flaminio Ferrara, Claudio Gennarelli, Rocco Guerriero, and Angelo Liseno
Volume 2012, Article ID 753156, 13 pages

Near-Field Antenna Measurements Using Photonic Sensor of Mach-Zehnder Interferometer, Masanobu Hirose, Satoru Kurokawa, Michitaka Ameya, and Koji Komiyama
Volume 2012, Article ID 470541, 11 pages

A Microwave Holographic Procedure for Large Symmetric Reflector Antennas Using a Fresnel-Zone Field Data Processing, Giuseppe Mazzarella, Giorgio Montisci, and Giampaolo Serra
Volume 2012, Article ID 420398, 11 pages

Application of Nonredundant Sampling Representations of Electromagnetic Fields to NF-FF Transformation Techniques, Ovidio M. Bucci and Claudio Gennarelli
Volume 2012, Article ID 319856, 14 pages

Numerical Investigation of the System-Matrix Method for Higher-Order Probe Correction in Spherical Near-Field Antenna Measurements, Thorkild B. Hansen
Volume 2012, Article ID 493705, 8 pages

Reduction of Truncation Errors in Planar, Cylindrical, and Partial Spherical Near-Field Antenna Measurements, Francisco José Cano-Fácila, Sergey Pivnenko, and Manuel Sierra-Castañer
Volume 2012, Article ID 438727, 19 pages

Editorial

Recent Advances in Near-Field to Far-Field Transformation Techniques

**Claudio Gennarelli,¹ Amedeo Capozzoli,² Lars J. Foged,³
Jeff Fordham,⁴ and Daniël Janse van Rensburg⁵**

¹*Dipartimento di Ingegneria Elettronica ed Ingegneria Informatica, Università di Salerno, Via Ponte Don Melillo, 84084 Fisciano, Italy*

²*Dipartimento di Ingegneria Biomedica, Elettronica e delle Telecomunicazioni, Università di Napoli Federico II, Via Claudio 21, 80125 Naples, Italy*

³*SATIMO Italian Office, Via Castelli Romani 59, 00040 Pomezia, Italy*

⁴*MI Technologies, Suite 100, 1125 Satellite Boulevard, Suwanee, GA 30024-4629, USA*

⁵*Nearfield Systems Inc. 19730 Magellan Drive, Torrance, CA 90503, USA*

Correspondence should be addressed to Claudio Gennarelli, gennar@diie.unisa.it

Received 28 May 2012; Accepted 28 May 2012

Copyright © 2012 Claudio Gennarelli et al. This is an open access article distributed under the Creative Commons Attribution License, which permits unrestricted use, distribution, and reproduction in any medium, provided the original work is properly cited.

For electrically large antenna systems, far-field (FF) range size limitations, transportation, and mounting problems make it difficult or absolutely impractical to measure the radiation pattern using conventional FF ranges. On the other hand, the increase of high-performance antennas, as those employed in radar and satellite systems, requires more accurate and complete measurements of their radiating characteristics, generally requiring the use of controlled indoor anechoic chambers, to overcome drawbacks associated with outdoor FF measurements. As a consequence, the problem of determining the antenna FF pattern from near-field (NF) measurements has attracted considerable attention in the last fifty years [1–11].

Indeed, NF scanning techniques have become the best choice as long as complete pattern and polarization measurements are required. In addition they allow to determine the field at the surface of the antenna, even if generally, within the “visible” resolution, which can be exploited usefully to determine surface errors in reflector antennas as well as to identify faulty elements in arrays.

Generally speaking, NF antenna characterization can exploit complex field data or phaseless field data, the first choice being the most commonly used in practice.

In an NF system processing complex field data, a probe antenna is moved along a surface (the scanning surface) whose shape is typically planar, cylindrical, or spherical. It

collects complex voltage samples, which, together with their positions, allow the desired quantities to be computed. For instance, from the phase and amplitude data, and taking into account the probe effect, the FF pattern can be computed. Commonly, the measured NF data are transformed into FF patterns by using an expansion of the field radiated by the antenna under test (AUT) in terms of modes, that is, a complete set of solutions of the vector wave equation in the region exterior to the antenna. Plane, cylindrical, or spherical waves are generally used. The type of modal expansions used for representing the field is typically determined by the shape of scanning surface, which, accordingly, will be a plane, a cylinder, or a sphere, respectively. The orthogonality properties of the modes on such surfaces are then exploited to calculate the modal expansion coefficients, allowing the reconstruction of the AUT far field.

The use of different scanning geometries is justified from the fact that each approach has its own specific advantages, depending on both the AUT characteristics and the measurement requirements.

The aim of this special issue is to provide an international forum for the researchers working in the antenna measurement field to disseminate new ideas and describe recent advances on NF methods in characterization techniques, simulations, and applications.

This special issue collects ten papers from 29 authors, belonging to several countries and coming from universities, research institutions, and companies. These papers cover many of the hot topics related to NF-FF transformation techniques.

The topic “mitigation of the error due to the measurement area truncation” is addressed in the paper “*Reduction of truncation errors in planar, cylindrical, and partial spherical near-field antenna measurements*” by F. J. Cano-Fácila et al. and in the other “*Using truncated data sets in spherical scanning antenna measurements*” by R. C. Wittmann et al.

The paper “*Numerical investigation of the system-matrix method for higher-order probe correction in spherical near-field antenna measurements*” by T. B. Hansen and that “*Application of nonredundant sampling representations of electromagnetic fields to NF-FF transformation techniques*” by O. M. Bucci and C. Gennarelli fall within the topic “advances in NF-FF transformation techniques.”

The theme “NF probe design and characterization” is covered in the paper “*Near-field antenna measurements using photonic sensor of Mach-Zehnder interferometer*” by M. Hirose et al.

The paper “*A microwave holographic procedure for large symmetric reflector antennas using a Fresnel-zone field data processing*” by G. Mazzarella, G. Montisci, and G. Serra deals with the topic “microwave holography.”

Innovative NF measurement techniques is the theme of the paper “*A probe-compensated helicoidal NF-FF transformation for aperture antennas using a prolate spheroidal expansion*” by A. Capozzoli et al. as well as of “*An innovative direct NF-FF transformation technique with helicoidal scanning*” by F. D’Agostino et al.

The topic “electromagnetic algorithms and data processing” is dealt with in the paper “*Examination of far-field mathematical absorber reflection suppression through computational electromagnetic simulation*” by S. Gregson et al. and in the other “*Development of a near-field bistatic synthetic aperture radar for complex target reconstruction*” by D. G. Johnson and G. M. Brooker.

A brief description of each of the papers contained in this special issue is reported in the following for the reader’s convenience, being the presentation order just related to the publication date order.

In the paper by F. J. Cano-Fácila et al., they present an effective method to reduce the truncation error when measuring the field in the most common truncated scanning surfaces (plane, cylinder, and partial sphere). The method makes use of the classical Gerchberg-Papoulis algorithm, widely used in the literature to extrapolate band-limited signals.

The paper by T. B. Hansen concerns a detailed numerical investigation of the system-matrix method, recently proposed by the same author, for higher-order probe correction in the NF-FF transformation with spherical scanning.

The paper by O. M. Bucci and C. Gennarelli presents an overview of the application of the nonredundant sampling representations of electromagnetic (EM) fields to NF-FF transformations with conventional or spiral scanning,

outlining the remarkable reduction in the number of needed NF samples and measurement time so achievable.

A new holographic procedure for the diagnosis of large reflector antennas is proposed in the paper by G. Mazzarella et al. The procedure is based on the direct use of Fresnel-field data and employs a regularized singular value decomposition technique.

The paper by M. Hirose et al. deals with a photonic sensor of the Mach-Zehnder interferometer type allowing the electric field measurement in the very near-field range of the AUT. It is shown that such a sensor can be applied to planar, spherical, and cylindrical NF measurements without any probe compensation approximately below 10 GHz.

A probe-compensated NF-FF transformation with helicoidal scanning for aperture antennas is presented in the paper by A. Capozzoli et al. It exploits a proper aperture field expansion, based on the use of the prolate spheroidal wave functions, accounting for the *a priori* information on the AUT and allows a significant reduction of the field data.

In the paper by R. C. Wittmann et al., they propose a method to mitigate the errors arising in the spherical scanning measurements when the data are not collected over an entire sphere. The technique uses a least-square estimation method with an energy constraint.

A direct NF-FF transformation with helicoidal scanning, which allows the evaluation of the antenna far field from a minimum set of NF data without interpolating them, is developed in the paper by F. D’Agostino et al. It relies on the nonredundant sampling representation of EM fields and matches the advantage of the fast helicoidal scanning with those of the direct cylindrical NF-FF transformation.

The paper by S. F. Gregson et al. concerns a new approach for suppressing the effect of spurious scattering in the far field as an extension of techniques already presented for NF measurements. A numerical simulator able to evaluate the antenna field in the presence of scattering objects is employed to investigate the proposed technique.

In the paper by D. G. Johnson and G. M. Brooker, they illustrate the development of a near-field bistatic inverse synthetic aperture radar for the analysis of rock samples. Moreover, they discuss an imaging algorithm matched to spherical shapes by providing numerical and experimental inversions.

Acknowledgments

We wish to thank all authors, who have decided to present some relevant aspects of their research activities in such a special issue, and the reviewers, whose suggestions have contributed to improve the quality of the papers. Finally, a very special acknowledgement is due to the Editorial Board of the International Journal of Antennas and Propagation who has made possible the publication of this special issue.

Claudio Gennarelli
Amedeo Capozzoli

Lars J. Foged

Jeff Fordham

Daniël Janse van Rensburg

References

- [1] R. C. Johnson, H. A. Ecker, and J. S. Hollis, "Determination of far-field antenna patterns from near-field measurements," *Proceedings of the IEEE*, vol. 61, no. 12, pp. 1668–1694, 1973.
- [2] J. Appel-Hansen, J. D. Dyson, E. S. Gillespie, and T. G. Hickman, "Antenna measurements," in *The Handbook of Antenna Design*, A. W. Rudge, K. Milne, A. D. Olver, and P. Knight, Eds., chapter 8, Peter Peregrinus Ltd, London, UK, 1982.
- [3] A. D. Yaghjian, "An overview of near-field antenna measurements," *IEEE Transactions on Antennas and Propagation*, vol. AP-34, no. 1, pp. 30–45, 1986.
- [4] E. S. Gillespie, Ed., "Special Issue on near-field scanning techniques," *IEEE Transactions on Antennas and Propagation*, vol. AP-36, no. 6, pp. 727–901, 1988.
- [5] J. Hald, J. E. Hansen, F. Jensen, and F. H. Larsen, *Spherical Near-Field Antenna Measurements*, Peter Peregrinus Ltd, London, UK, 1988.
- [6] G. E. Evans, *Antenna Measurement Techniques*, Artech House, Boston, Mass, USA, 1990.
- [7] D. Slater, *Near-Field Antenna Measurements*, Artech House, Boston, Mass, USA, 1991.
- [8] C. Gennarelli, G. Riccio, F. D'Agostino, F. Ferrara, and R. Guerriero, *Near-Field—Far-Field Transformation Techniques*, vol. 1, CUES, Salerno, Italy, 2004.
- [9] C. Gennarelli, G. Riccio, F. D'Agostino, F. Ferrara, and R. Guerriero, *Near-Field—Far-Field Transformation Techniques*, vol. 2, CUES, Salerno, Italy, 2006.
- [10] S. F. Gregson, J. McCormick, and C. G. Parini, *Principles of Planar Near-Field Antenna Measurements*, The Institution of Engineering and Technology, London, UK, 2007.
- [11] M. H. Francis and R. W. Wittmann, "Near-field scanning measurements: theory and practice," in *Modern Antenna Handbook*, C. A. Balanis, Ed., chapter 19, John Wiley & Sons, Hoboken, NJ, USA, 2008.

Research Article

Development of a Near-Field Bistatic Synthetic Aperture Radar for Complex Target Reconstruction

David G. Johnson and Graham M. Brooker

ACFR, University of Sydney, Rose Street Building (J04), NSW 2006, Australia

Correspondence should be addressed to David G. Johnson, d.johnson@acfr.usyd.edu.au

Received 6 September 2011; Revised 13 February 2012; Accepted 14 March 2012

Academic Editor: Amedeo Capozzoli

Copyright © 2012 D. G. Johnson and G. M. Brooker. This is an open access article distributed under the Creative Commons Attribution License, which permits unrestricted use, distribution, and reproduction in any medium, provided the original work is properly cited.

This paper begins with a description of the design, construction, and characterization of a small electromagnetic anechoic chamber, developed specifically to house a bistatic ISAR system for the analysis of rock samples. Particular emphasis is given to the practicalities of construction, with the intention of assisting those in a similar position, wishing to build an anechoic chamber on a tight budget. The second part of the paper outlines efficient algorithms that may be applied to the tomographic and topographic reconstruction of complex targets within the viewing geometry of this ISAR system.

1. Introduction

This paper describes the development of a radar system designed for the 3D topographic reconstruction of unstructured surfaces. This was motivated by the need within the open-pit mining industry to determine the precise size distribution of rock fragments postblasting and precrushing. In these environments laser and camera systems are often unsuitable due to the presence of large amounts of dust. As a solution to this problem, a *linear-frequency-modulated continuous-wave* (LFM-CW) radar-based approach was envisioned that would be able to operate at short range, and provide sufficient range and angular resolution to compete with fair-weather optical systems. A coherent near-field multistatic methodology was chosen using *synthetic-aperture-radar* (SAR) techniques to minimise the number of moving parts, whilst providing the greatest number of measurement degrees of freedom and the best possible resolution [1]. A prototype bistatic system, operating in *inverse-SAR* (ISAR) mode within the well-behaved confines of an anechoic chamber, was therefore constructed to determine whether the required performance characteristics were achievable, prior to the development of a full-scale system on a platform, such as that shown in Figure 1. This paper describes solely the theory and measurements for this prototype system. The extension to the real world must be accompanied by further research. It should be noted that both the anechoic chamber

and prototype radar system were built for a combined cost of US \$35k. This compares to the quoted cost of a full professional installation of the chamber alone of in excess of US \$80k.

Multiple papers and books have been written on the subject of anechoic chamber design for standard RCS and antenna measurements, for example, [2, 3]. However, little information can be found on the construction and installation processes, particularly when working in the near-field. The paper, therefore, includes a number of innovative cost and labour saving techniques for near-field test-facility design, test, and measurement.

In the radiative near field, $0.6(D^3/\lambda)^{1/2} \leq R \leq 2D^2/\lambda$, as defined by the maximum extent of both the radar aperture and the targets themselves, D , relative to the wavelength, λ , plane-wave approximations become inaccurate. Spherical wave functions must then be applied to solve the system imaging problem, extending the ISAR methodology described previously to a *spherical-wave* form, known as SWISAR [4]. The computational burden of solving these complex functions in the Fourier domain can then be reduced by employing the *method of stationary phase* (MoSP). This algorithm approximates the dominant signal from each target as the region over which its phase is slow-moving or stationary, generally found around the point of closest (or furthest) approach to the radar. Whilst this is commonly described by

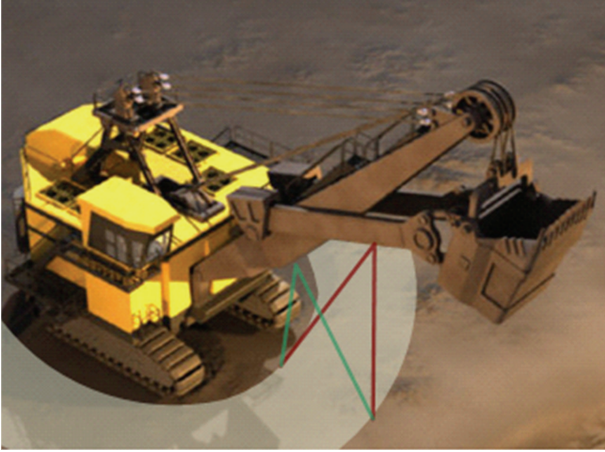


FIGURE 1: Artists impression of radar system on-board an electric-roped shovel, showing the approximate radar imaging region in grey for the given bistatic antenna configuration. Further receivers could then be added along the shovel arm to extend this to a full multistatic system.

a quadratic expansion of the phase, as in [5, 6], it can be, and for the full bistatic case, must be, more accurately described by considering higher-order polynomials.

ISAR Fourier imaging is a form of convolution back-projection [7] and is, therefore, well suited to coherently processing large angular sectors, as the full azimuth spectral bandwidth must be calculated in any case. This is particularly of use at short range where a target's translation leads to a larger rotational movement. One of the principal difficulties that then arise is the aspect dependence of dispersive target scattering. This can be dealt with either by assuming an anisotropic (i.e., non-point-like) scatterer model, or, as is described here, by applying a Fourier-domain-matched filter-bank tailored to the local curvature of the (*unknown*) target. In this sense, there is a strong correspondence between the current work and the use of microlocal-analysis techniques [8–12], based on geometric optics and the MoSP, which identifies the coherent scattering centres of *known* topography and provides an analytic solution to the subsequent imaging problem. *A priori* known topography is also utilised in a similar manner by [13], to identify and equate coherent regions in the Fourier domain, observed from spatially separated positions, in order to optimise a *coherent change detection* (CCD) process. The current work may also prove useful in terms of providing an experimental means of justifying these techniques and extending the same ideas to target detection and the mapping of unknown topography.

Section 2 of this paper describes the development and characterisation of the prototype SWISAR system and the near-field test chamber that was custom-built to hold it, whilst Section 3 describes measures taken to achieve a 1D range resolution of <20 mm. Sections 4 and 5 then describe algorithms to perform focussed multistatic 3D imaging of point and spherical targets, respectively, using banks of spatially-variant Fourier-domain-matched filters, extending the work of [14].

2. Development and Characterisation of the Near-Field Test Chamber

A small anechoic chamber ($2.9\text{ m} \times 2.5\text{ m} \times 2.3\text{ m}$) was built at the *Australian Centre for Field Robotics* (ACFR) as described in [15] and shown in Figure 2(a). The main features of this facility are as follows.

- (i) A polystyrene/steel sandwich wall construction [16], with seams sealed using AT526 35 micron copper foil shielding tape and SOFT-SHIELD 2000 gaskets; lined with 300 mm pyramidal foam *radar absorbing material* (RAM). Some simple construction tips and a RAM mitre-joint cutting template are provided in the Appendix.
- (ii) A pallet-mounted (and removable) 1.2 m diameter turntable. The turntable was constructed from 20 mm *medium density fibreboard* (MDF), with the drive mechanism consisting of a geared stepper motor and a timing-belt pulley made from a bicycle wheel. An important feature of the turntable design (owing to the high torque requirement and temperature variations within the lab) was the belt-tensioners. These allowed occasional adjustment of belt tension (using a rubber mallet) to reduce belt-skip. The trucks from two skateboards provide additional load-bearing support. When operated under correct tension, the turntable was capable of rotating 300 kg rock samples with an angular accuracy of $<0.01^\circ$.
- (iii) A 90° sector arc, of radius 2 m, on which two independently powered trolleys could transit, each carrying a 2–18 GHz antenna linked to the radar hardware described shortly, and a 5 mega-pixel remote-operated camera (with flash). The compact cameras (Olympus FE130) were particularly useful for the formation of bistatic photographs, employing the flash from the Tx-mounted camera to illuminate the scene viewed by the Rx-mounted camera, from which bistatic scattering centres at optical frequencies could be identified and related to similar topology radar measurements.
- (iv) Radar hardware installed directly above the chamber to minimise cable lengths (which pass through filtered connectors in the ceiling).
- (v) Double doors provide the ability to obtain far-field measurements at MMW using the full length of the ACFR field-research-laboratory ($\sim 40\text{ m}$). For an example of this functionality, see [17].

At each stage in construction, measurements of reflectivity from and transmission through the chamber walls were made at H- and V-polarisations to maximise the anechoic performance of the chamber. The transmission tests involved transmitting a swept 1–19 GHz, +10 dBm signal, from a Marconi 6313 synthesiser, via 1 m of Ultraflex FM402 flexible coax, to a Q-Par Angus Broadband Horn Antenna (WBH218S) placed outside the chamber 1 m from the wall.

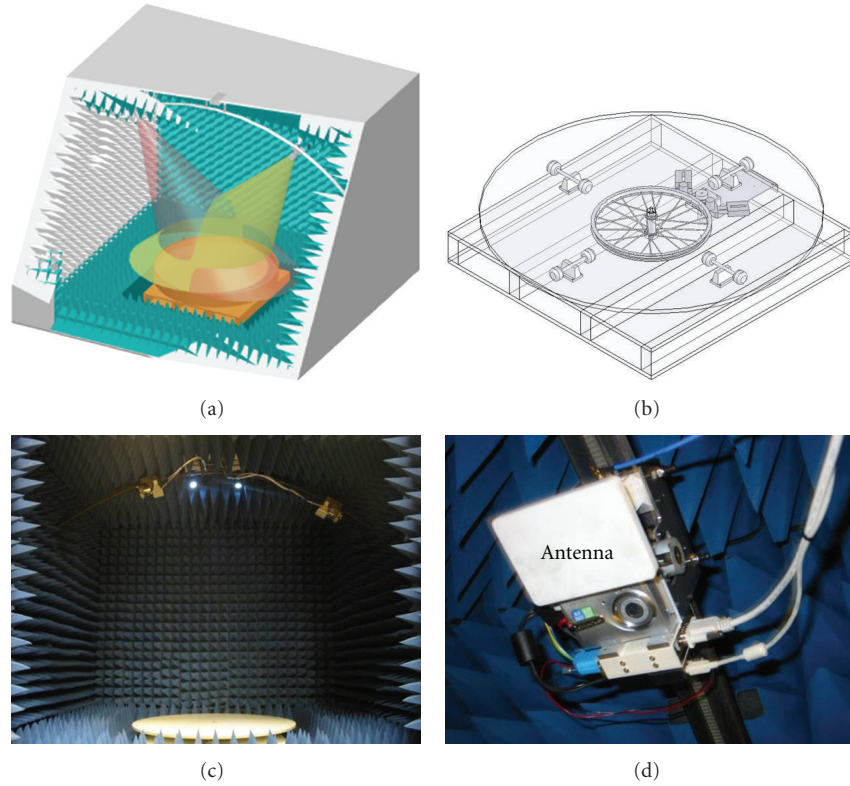


FIGURE 2: (a) Cutaway schematic of anechoic chamber showing transmit and receive beams. (b) Schematic of turntable. (c) View of anechoic chamber through open doors. (d) Close-up view of antenna trolley showing camera and antenna.

The signal was then received by an identical antenna 1 m inside the chamber and passed via 8 m of FM402 cable to an HP8563E Spectrum Analyser. Both the Sweep Generator and Spectrum Analyser were controlled synchronously by a remote PC, thus forming a basic scalar network analyser. Reflectivity measurements were made in the same manner, with the antennas placed side by side inside the chamber. As an example, Figure 3 displays the V-pol. side-wall transmission measurements (without compensation for antenna gain).

3. Nonlinearity Correction for cm Level Resolution

Figure 4 shows a schematic of the zero-IF (homodyne) LFM-CW radar and the power levels expected over the frequency of operation. The advantage of this configuration is the small number of components required, which minimises both cost and system losses. The recent development of multi-octave “ultra” broadband components for use in electromagnetic test chambers and electronic warfare devices has opened the door to radar system bandwidths in excess of 15 GHz. All radio-frequency (RF) components (including cables and connectors) are, therefore, rated from 2–18 GHz, giving a theoretical range-resolution of 9.4 mm. In reality, the amplitude and phase linearity of the components within this configuration is not perfect, leading to some degradation in resolution.

Although the range-resolution of LFM-CW radar is in theory only limited by its swept bandwidth, it is more

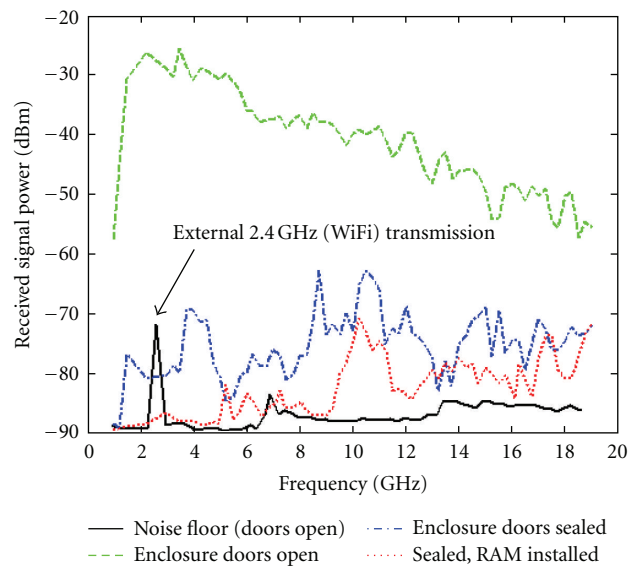


FIGURE 3: Anechoic chamber characterisation results. Measurements were made with the transmitter outside the chamber and the receiver inside, each aligned orthogonally to the chamber wall.

realistically limited by the linearity of the frequency chirp and the spectral purity of the instantaneous transmitted signal. Before the radar data can be passed to the SWISAR algorithm for conversion to a 3D image, it must therefore be

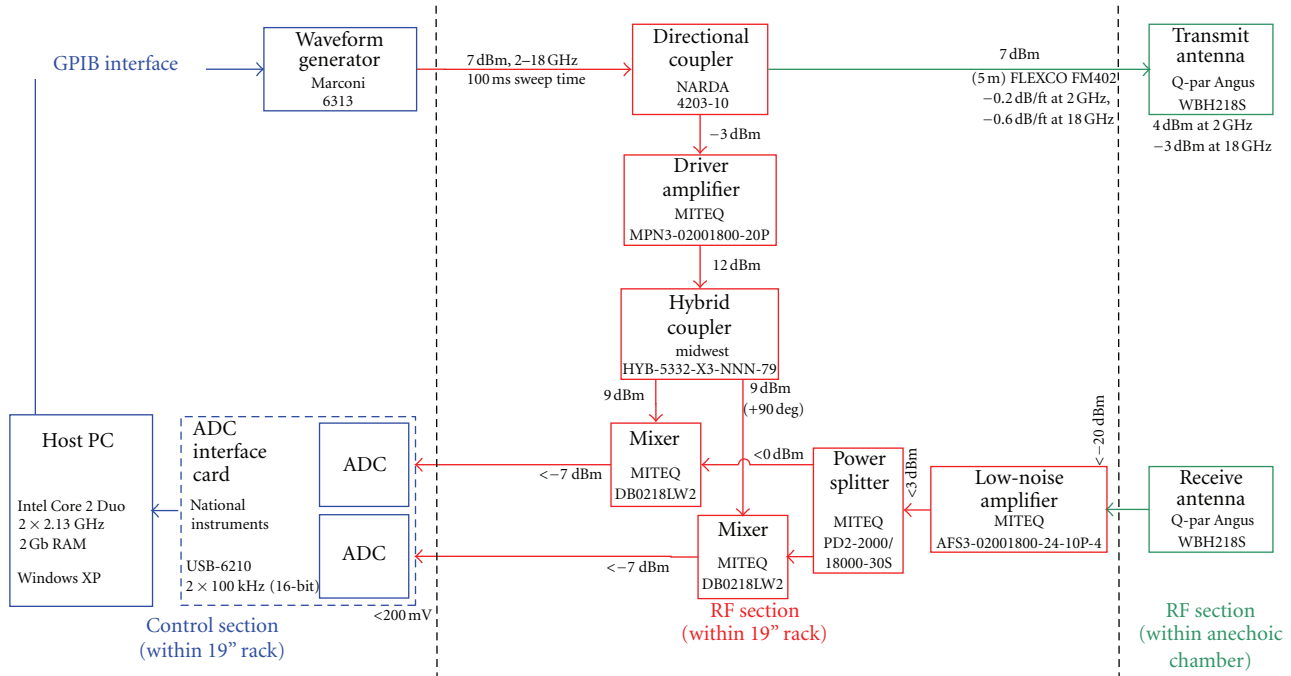


FIGURE 4: Schematic of radar hardware showing power levels detected at various points.

purified, that is, preprocessed to remove hardware-induced artefacts such as leakage signals, phase nonlinearities, and system losses. Numerous methods exist to linearise the frequency chirp in hardware prior to transmission. These are generally based on Phase Locked Loops (PLLs) and/or false-target calibration [18]; however, these methods are still hardware-bandwidth-limited and can only provide a certain level of improvement. Also, although many of our radar's hardware components operate over the full 2–18 GHz band, there are no commercially available oscillators that can sweep continuously over this region, and the switching between oscillators introduces severe nonlinearities that cannot be corrected by a PLL. Indeed, over such a large swept bandwidth, nonlinearities in both the antennas and cables emerge that cannot be corrected for in hardware, therefore a software linearisation solution must be found. Other aspects of chamber calibration that should be taken into account relate to imperfections in the geometry of the measurement system. These include variations in the curvature of the steel arc on which the transmit- and receive-antenna trolleys translate, inertial sensor errors due to timing belt slippage on both of the antenna trolleys and the turntable, and the possible misalignment of the turntable beneath the centre of the steel arc.

The flowchart in Figure 5 describes the processing steps required to obtain a set of consistent, linearised radar samples.

3.1. Individual Sweep Extraction/Empty Chamber Subtraction.

Despite the use of a RAM baffle installed on the receive antenna, the direct-path leakage signal between the transmit and receive antenna dominates the measured data and must be removed prior to the subsequent preprocessing steps. This is a common technique, often employed in the form of a

reflective power canceller, as described in [19]. Because the leakage signal remains constant irrespective of the sample within the chamber, it provides a convenient measure of both the consistency of empty-chamber-subtraction for a fixed antenna configuration, and a means of relocating a particular bistatic configuration to great accuracy. The relative positions of the transmit and receive antennas along the steel arc are measured by optical encoders on the pulley wheel that drives each trolley along the timing belt affixed to the steel-arc itself. However, due to the weight of the trolleys and the steepness of the incline in places, it is not unknown for the pulley to slip on the timing belt, which goes unnoticed by the proprioceptive sensor. To account for this, *empty chamber subtraction* is employed to measure the bistatic leakage distance and accurately locate the receive antenna (assuming a fixed transmit antenna position). The graph in Figure 6 is made up of range profiles corresponding to 350 receiver positions over a range of 70° , that is, steps of 0.2° , with the transmitter fixed at the end-stop of the arc. The receive antenna can then be relocated to any of these 350 positions by determining the best level of leakage-signal suppression through empty chamber subtraction. The system of antenna localisation was found to be accurate to within $\pm 0.1^\circ$ of arc as described. Whilst having cm-level two-target resolution, it was found that after phase-linearisation the system could follow the phase progression of a single dominant target to sub-mm accuracy.

3.2. *Bandpass Filtering.* To further improve the subsequent nonlinearity-measurement and normalisation steps, the “*chamber-subtracted*” signal is bandpass filtered to isolate the region of interest defined by the range-extent of the turntable.

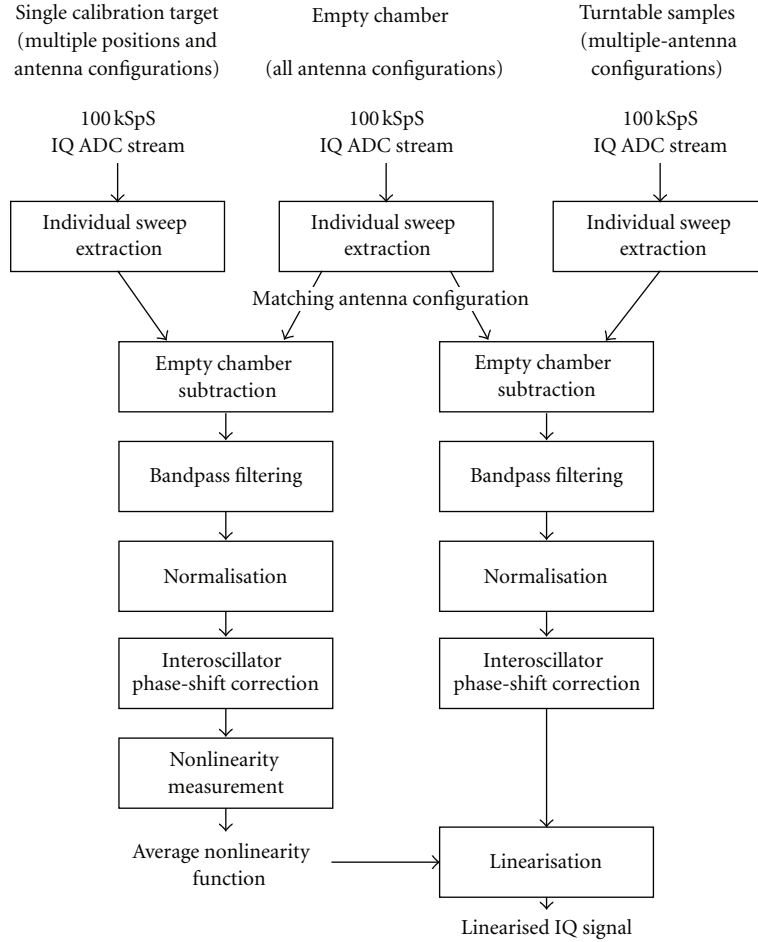


FIGURE 5: Flowchart of signal linearisation process.

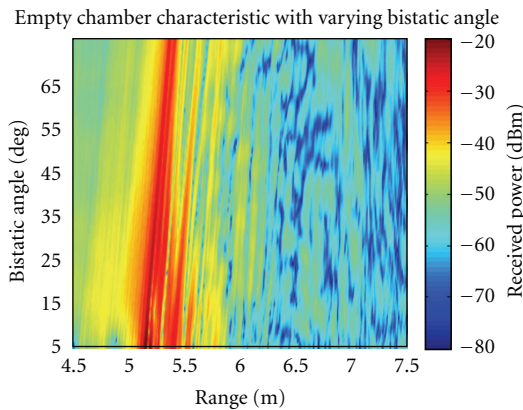


FIGURE 6: Empty chamber measurements for varying bistatic angles. Colour represents signal intensity in dBm.

3.3. *Normalisation.* Following an analysis of cable and antenna losses between 2 and 18 GHz, as described in [15], a log-linear power gain-correction factor of 0–25 dB is applied to the filtered signal at this point. Quantisation noise then reduces the *effective-number-of-bits* (ENOB) of the ADC to

~8.5 bits at 18 GHz; however, this is still adequate for the subsequent linearisation stage.

3.4. *Interoscillator Phase-Shift Correction.* The Marconi 6313 sweep generator is made up of a number of *yttrium-iron-garnet* (YIG) tuned oscillators [20], which although inherently linear, experience a band switching delay of 0.5 μ sec. This switching between oscillator sections leads to a significant, although consistent, non-linearity in phase that can initially be dealt with by applying a constant phase shift to data within each of the upper (8–12.4 GHz and 12.4–18 GHz) oscillator bands.

A technique has recently been put forward in the SAR literature by Meta et al. [21], claiming to solve the non-linearity problem entirely in software, although it does require precise knowledge of the original non-linearity. For the case of the anechoic environment, this can be extracted from an isolated test target (such as a sphere). The signal-phase from this target is then unwrapped (following the pre-processing steps described above), which is a simple matter for a strong complex signal, and a linear fit of the result removed to produce a residual phase characteristic as seen in Figure 7. Because this signal includes the effects of target location and

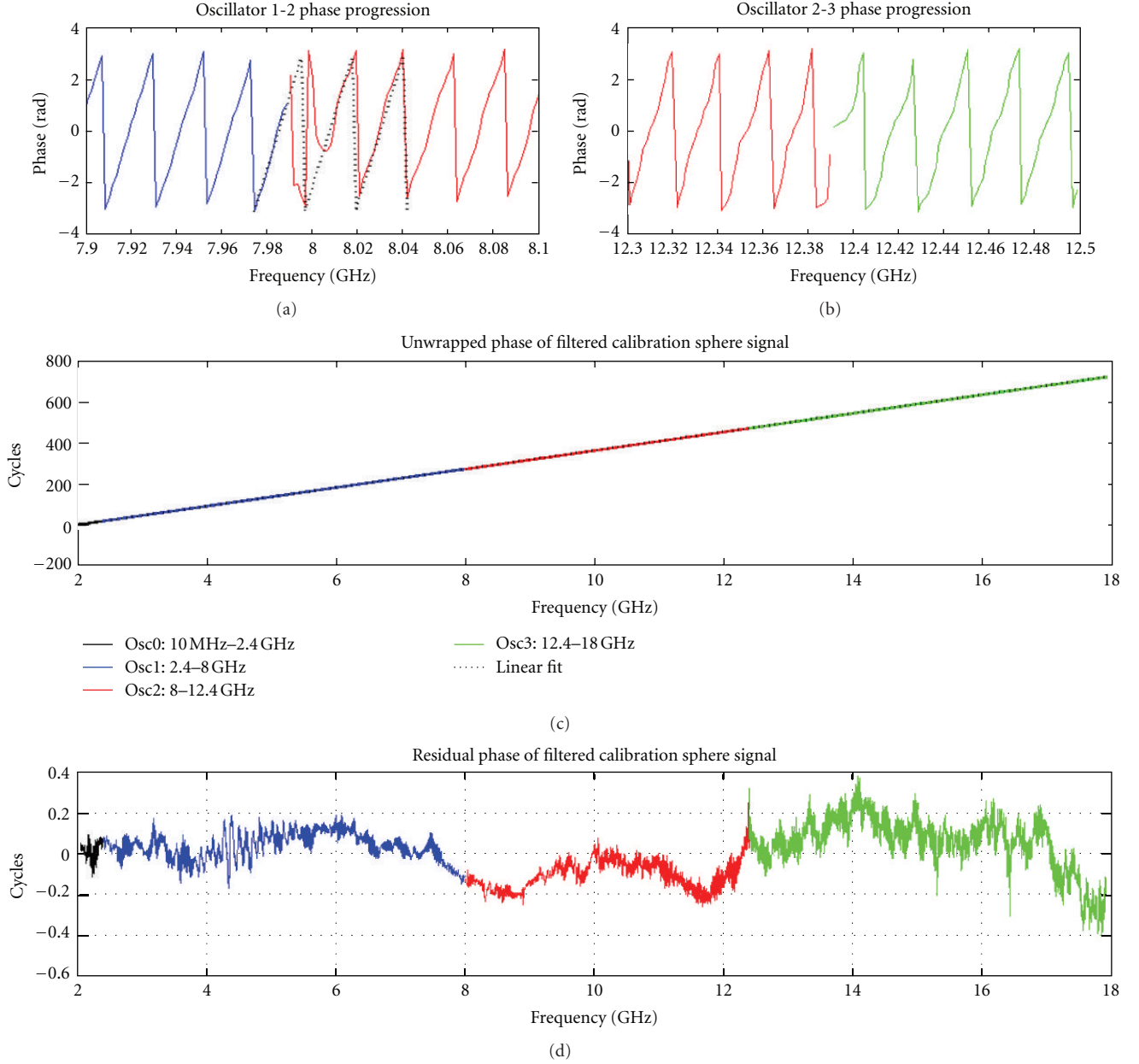


FIGURE 7: Determination of LFM-CW system non-linearity using phase fill-in and unwrapping applied to an isolated target.

antenna configuration, this process is repeated for a number of movements and an average non-linearity is derived.

After the *interscillator phase-shift correction* process, there then remains a period of irregular phase caused by variations in amplitude as the oscillators are switched, which is too nonlinear to be dealt with by Meta's algorithm. However, by applying a phase fill-in procedure, as depicted in Figure 7, that is, replacing the irregular phase section by a signal with a linear phase variation based on the well-behaved portion of the signal.

The Meta technique then expresses the nonlinear beat signal of a target received after a time delay, τ , as the product of the ideal linear beat signal, $s_{if,lin}(t)$, and the

non-linear error function, $s_{\epsilon}(t)$, applied both on transmission and reception:

$$\begin{aligned}
 s_{if}(t) &= e^{j2\pi(f_c\tau + \alpha t\tau + (1/2)\alpha t^2 + \epsilon(t) - \epsilon(t-\tau))} \\
 &= e^{j2\pi(f_c\tau + \alpha t\tau + (1/2)\alpha t^2)} e^{j2\pi\epsilon(t)} e^{-j2\pi\epsilon(t-\tau)} \quad (1) \\
 &= s_{if,lin}(t) s_{\epsilon}(t) s_{\epsilon}(t-\tau)^*,
 \end{aligned}$$

where (i) f_c ; The central carrier frequency of the transmitted signal. (ii) α ; The slope of the frequency chirp (Hz/s). (iii) $\epsilon(t)$; The time dependent non-linearity applied to the voltage ramp.

Assuming the error function, $s_{\epsilon}(t)$, is well known, the ideal linear beat signal can be recovered by a 3-step process:

- (1) multiplying the non-linear beat signal by the conjugate of the error function, $s_\epsilon(t)^*$, to remove the effects of the transmitted non-linearity;
- (2) applying a range-dependent time shift to the received signal to remove the range/time dependence of the received non-linearity. This is performed by a *residual video phase* (RVP) removal filter in Fourier space;
- (3) multiplying the filtered signal by the conjugate of the error function after it too has been passed through the RVP filter.

The process described in the flowchart of Figure 5 is now shown for the example of two metallic spheres placed in isolation within the anechoic chamber. In Figure 8, each step of the phase-linearisation process is shown with the final result that the two spheres, with a bistatic range separation of 100 mm, can be seen clearly 15 dB above the next spurious peak. Here, values in dBm relate to the direct measurement made into a 50 Ω load, and changes in antenna gain and cable losses with frequency are subsumed into the empty chamber subtraction step.

The two spheres shown in Figure 9(a) have then moved to produce a closer bistatic range separation of 20 mm and still have clearly separated peaks as seen in Figure 9(b), although there is a 3 dB difference in intensity caused by the variation in gain of both the transmitter and receiver [22].

It should be noted that a side-effect of the Meta linearisation technique is to add ~ 2 dBm to all dominant targets, as energy from the error function is essentially added in to the linearised result. This can be seen in both Figure 8 (inset) and Figure 9(b).

4. A Coherent Multistatic Near-Field Imaging Algorithm for Point Targets

This section provides a brief overview of the bistatic SWISAR imaging algorithm for point targets, with an accompanying metric of performance for the case of a set of disparate sized spheres. Further details of the monostatic point-target algorithm can be found in [5], whilst the 3D multi/bistatic imaging algorithm applied to a selection of rocks has been previously presented in [14, 23].

Figure 10 depicts a *bistatic* (BS) SWISAR geometry, but can equally be employed to visualise the *monostatic* (MS), or *quasi-monostatic* (QMS) in which case a single, or pair of, antenna(s) centred on ‘‘Tx’’ will simply use $R = R_t$ in the formulae for the *spatially variant matched filter* (SVMF), F , for each voxel in the cylindrical-polar imaging coordinate system, following Fortuny [4]:

$$I(\rho, \phi, z) = \frac{8}{c^3} \int_f f^2 \int_\theta \sin \theta \times \int_{\phi'} E_s(f, \phi', \theta) F(\rho, \phi - \phi', z; f, \theta) df d\theta d\phi', \quad (2)$$

where

$$F(\rho, \phi, z; f, \theta) = \left(\frac{R}{R_a} \right)^2 \exp[jk_f(R - R_a)], \quad (3)$$

$$R = \sqrt{R_a^2 + \rho^2 + z^2 - 2R_a[\rho \sin \theta \cos \phi + z \cos \theta]}. \quad (4)$$

Equation, (2) describes a circular convolution and can therefore be calculated by a 1D azimuth *discrete-Fourier-transform* (DFT) and matched-filter multiply. Fortuny observed that the azimuth Fourier transform of (3) can be rewritten (for fixed f and θ) in the form of a 1D *Fourier-integral-operator* (FIO) focussing function, $\mathcal{F}(\cdot)$:

$$\mathcal{F}(\rho, k_\phi, z; f, \theta) = \int_{-\pi}^{\pi} \left(\frac{R(\phi)}{R_a} \right)^2 \exp[jp(\phi)] d\phi, \quad (5)$$

where, for the monostatic case, $R(\phi) = R_{MS}(\phi)$ and $p(\phi) = p_{MS}(\phi)$

$$p_{MS}(\phi) = A[R_{MS}(\phi) - R_a] - k_\phi \phi, \quad (6)$$

$$R_{MS}(\phi) = \sqrt{B - C \cos \phi},$$

$$A = k_f = \frac{4f}{c},$$

$$B = R_a^2 + \rho^2 + z^2 - 2R_a z \cos \theta_{MS}, \quad (7)$$

$$C = 2R_a \rho \sin \theta_{MS}.$$

The MoSP can then be used to determine analytically the asymptotic approximation to this azimuth DFT, as for a rapidly oscillating FIO, such that describing the phase history of a point target on a rotating turntable, the major contribution to the integral comes from the regions around the stationary phase points.

For the case when two 1st-order stationary phase points are present at ϕ_- and ϕ_+ ,

$$p'_{MS}(\phi_-) = \left. \frac{\partial p_{MS}(\phi)}{\partial \phi} \right|_{\phi_-} = A \frac{C \sin \phi_-}{2\sqrt{B - C \cos \phi_-}} - k_\phi = 0, \\ p'_{MS}(\phi_+) = \left. \frac{\partial p_{MS}(\phi)}{\partial \phi} \right|_{\phi_+} = A \frac{C \sin \phi_+}{2\sqrt{B - C \cos \phi_+}} - k_\phi = 0. \quad (8)$$

This can be solved algebraically to give

$$\phi_\pm = \arccos \left[\frac{2\alpha^2 \pm \sqrt{\beta^2 - 4\alpha^2(1 - \alpha^2)}}{\beta} \right], \quad (9)$$

where

$$\alpha = \frac{k_\phi}{A\sqrt{B}}, \quad \beta = \frac{C}{B}. \quad (10)$$

Above a certain threshold of k_ϕ , the two stationary phase points given in (9) coalesce to a single point ϕ_0 given by:

$$\phi_0 = \arccos \left[\frac{1 - \sqrt{1 - \beta^2}}{\beta} \right]. \quad (11)$$

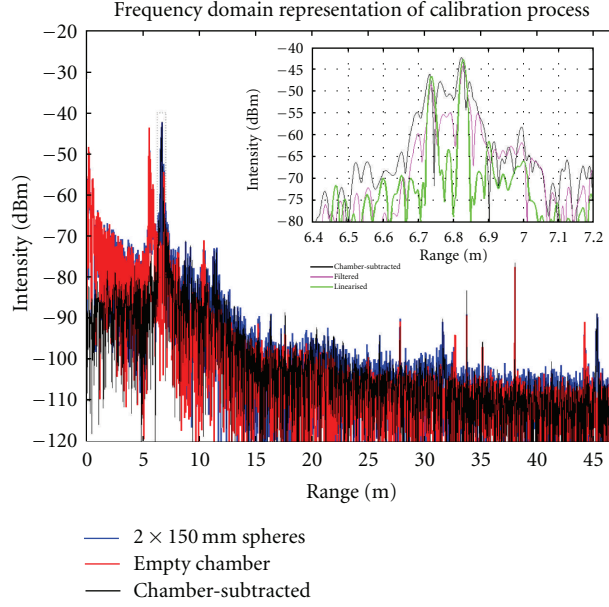


FIGURE 8: Signal linearisation of two targets closely separated in range.

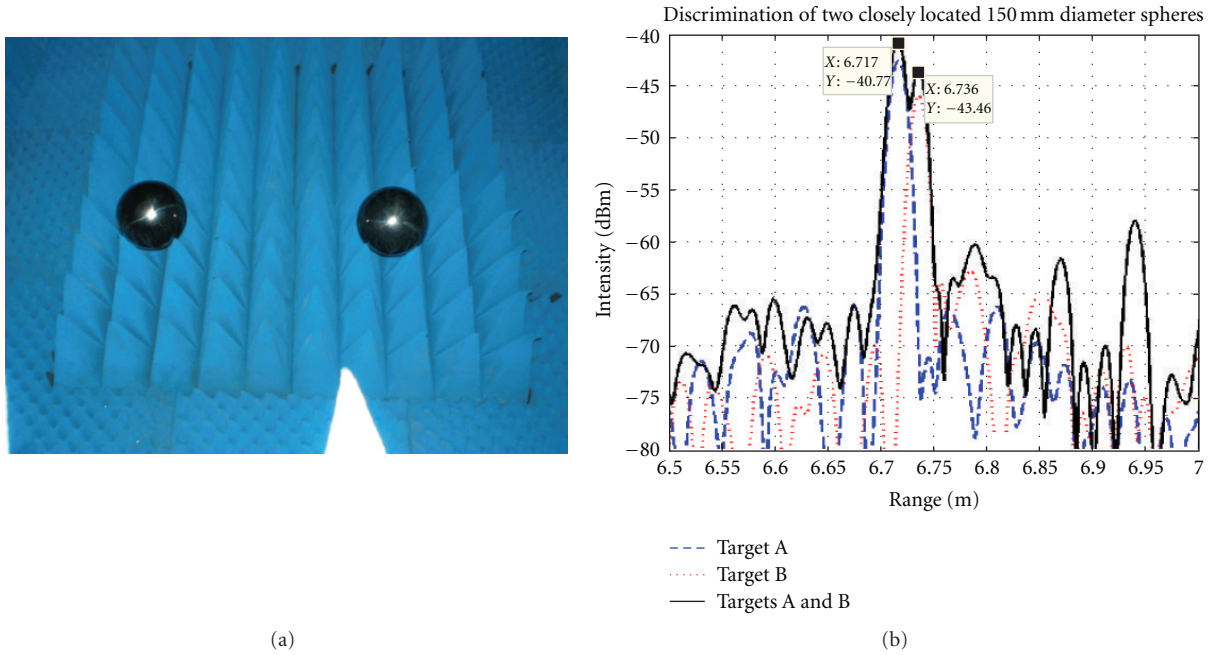


FIGURE 9: (a) Two 150 mm spherical targets within an otherwise empty chamber. (b) Linearised results of both targets in isolation, and together.

These expressions can then be resubstituted when equating the higher derivatives of $p_{MS}(\phi)$ at the stationary phase points, as they relate to the asymptotic approximations for the focussing template of (5):

$$\mathcal{F}_{MS}(\rho, k_\phi, z; f, \theta) \approx \frac{\sqrt{j2\pi}}{R_a^2} \left(\frac{R_{MS}^2(\phi_-)}{p_{MS}''(\phi_-)} e^{jp_{MS}(\phi_-)} + \frac{R_{MS}^2(\phi_+)}{p_{MS}''(\phi_+)} e^{jp_{MS}(\phi_+)} \right),$$

$$\mathcal{F}_{MS}(k_\phi) \approx 2\pi e^{jp(\phi_0)} \left(\frac{R_{MS}(\phi)^2}{R_a^2} \right) \left(\frac{2}{|p_{MS}'''(\phi_0)|} \right)^{1/3} \times Ai \left(- \left[\frac{2}{|p_{MS}'''(\phi_0)|} \right]^{1/3} p_{MS}'(\phi_0) \right), \quad (12)$$

where $Ai(\cdot)$ denotes the Airy function [24]. An extended description of this derivation can be found in the Appendix A

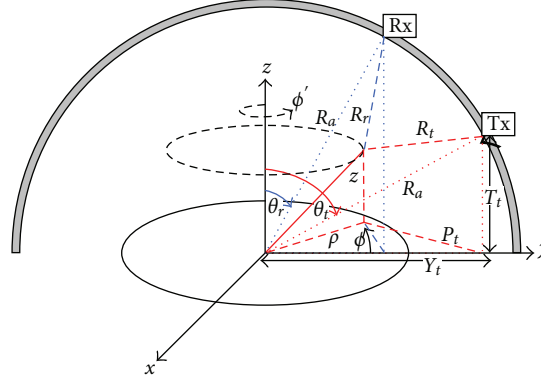


FIGURE 10: Bistatic SWISAR geometry (for which the monostatic geometry is a subset).

of [15]. Because these expressions involve only A , B , and C , they are independent of any target properties and need only be regenerated if the sensing geometry is altered.

The meaning of the two regions of k_ϕ in (12) can be explained with reference to Figures 11–13 below.

Figure 11 depicts the four time/frequency domain combinations available for SAR processing. The top-left “Fourier domain” matched-filter template corresponds to a target at a particular position as seen in the bottom-right. Also obvious, is a triangular region, that is itself a subset of a rectangular region (which for the most part is some 50 dB weaker).

Targets positioned at points A1 and A2 in Figure 12 will fall along the line $k_\phi = 0$, whilst the points B1 and B2 refer to an area within the triangular region itself.

The boundary of the triangular region in Figure 11(a) relates to the point $k_\phi \leq \hat{k}_\phi$. If the antenna was in the plane $z = 0$, that is, $\theta = 90^\circ$, then this would correspond to the maximum spatial bandwidth of the geometry and the point C in Figure 12. Outside of this triangular region, $k_\phi > \hat{k}_\phi$ would then correspond to an evanescent-wave region and hence provide negligible response for ranges much greater than the wavelength of the radar. Because we are dealing with a slant-plane circular-SAR geometry, however, this region does have an affect on the subsequent time-domain solution, as seen in Figure 13.

When the transmitter and receiver are separated along the arc, as seen in Figure 10, applying the *monostatic to bistatic equivalence theorem* (MBET) works well for small bistatic angles, that is, $\lesssim 6^\circ$ [25]. that is, by assuming that the bistatic-bisector angle, θ_b , can be used to provide a *quasimonostatic* (QMS) estimation of θ in (5). For larger bistatic separations, this assumption can no longer be made.

Figure 14 and Table 1 describe two equivalent experimental setups, which will be used to explain and in the subsequent text demonstrate a full bistatic SWISAR formulation.

In the bistatic SWISAR context, to produce a dataset equivalent to the QMS antenna-pair measurements shown in Figure 14(a), for which a pair of antennas are moved synchronously across the arc, requires the experimental geometry of Figure 14(b), using a fixed transmitter and a receiver moved at twice the angular-increments. In the most extreme

TABLE 1: Parameters for simulated and experimental SWISAR imaging.

Parameter	Symbol	Value
Number of MS/BS antenna configurations	N	12
<i>Experiment 1: (Quasi-) Monostatic configuration</i>		
MS _n Tx antenna angular range ($n = 1:12$)	$\theta_{t,MSn}$	$39^\circ : -2^\circ : 17^\circ$
MS _n Rx antenna angular range ($n = 1:12$)	$\theta_{r,MSn}$	$33^\circ : -2^\circ : 11^\circ$
QMS1_n-equivalent angle = $(\theta_{t,MSn} + \theta_{r,MSn})/2$	$\theta_{QMS1,n}$	$36^\circ : -2^\circ : 14^\circ$
<i>Experiment 2: Bistatic configuration</i>		
BS ₀ Tx antenna angle (fixed)	$\theta_{t,BS0}$	39° (fixed)
BS _n Rx antenna angular range ($n = 1:12$)	$\theta_{r,BSn}$	$33^\circ : -4^\circ : -11^\circ$
QMS2_n-equivalent angle = $(\theta_{t,BS0} + \theta_{r,BSn})/2$	$\theta_{QMS2,n}$	$36^\circ : -2^\circ : 14^\circ$
<i>Other parameters:</i>		
Frequency range	f	2–18 GHz
Turntable angular range	ϕ	$0^\circ : 0.5^\circ : 359.5^\circ$
Radial coordinate range	ρ	$0 : 0.01 : 0.7$ m
Height coordinate range	z	$-0.2 : 0.01 : 0.4$ m
Cartesian coordinate range	x, y	$-1 : 0.01 : 1$ m

case, with values of $\theta_{t,BS0} = +39^\circ$ and $\theta_{r,BS12} = -11^\circ$ (with $\theta = 0$ at the zenith), the bistatic pair of antennas span the centre of the arc with a bistatic-angle of 50° . This is a fairly reasonable requirement if an eventual multi-static radar is required to obtain measurements over a wide θ -range, operating with multiple static receivers rather than the single dynamic unit used by the prototype. The validity of applying a *point-target* approximation over this large bistatic angle is discussed later.

To form a bistatic asymptotic expansion for the focussing function, \mathcal{F}_{BS} , similar to that given in (12) for the (quasi-) monostatic case, \mathcal{F}_{MS} , requires that the stationary phase points (ϕ_\pm or ϕ_0 , depending on the size of k_ϕ) be obtained in an accurate and efficient manner. For the bistatic case, (5)

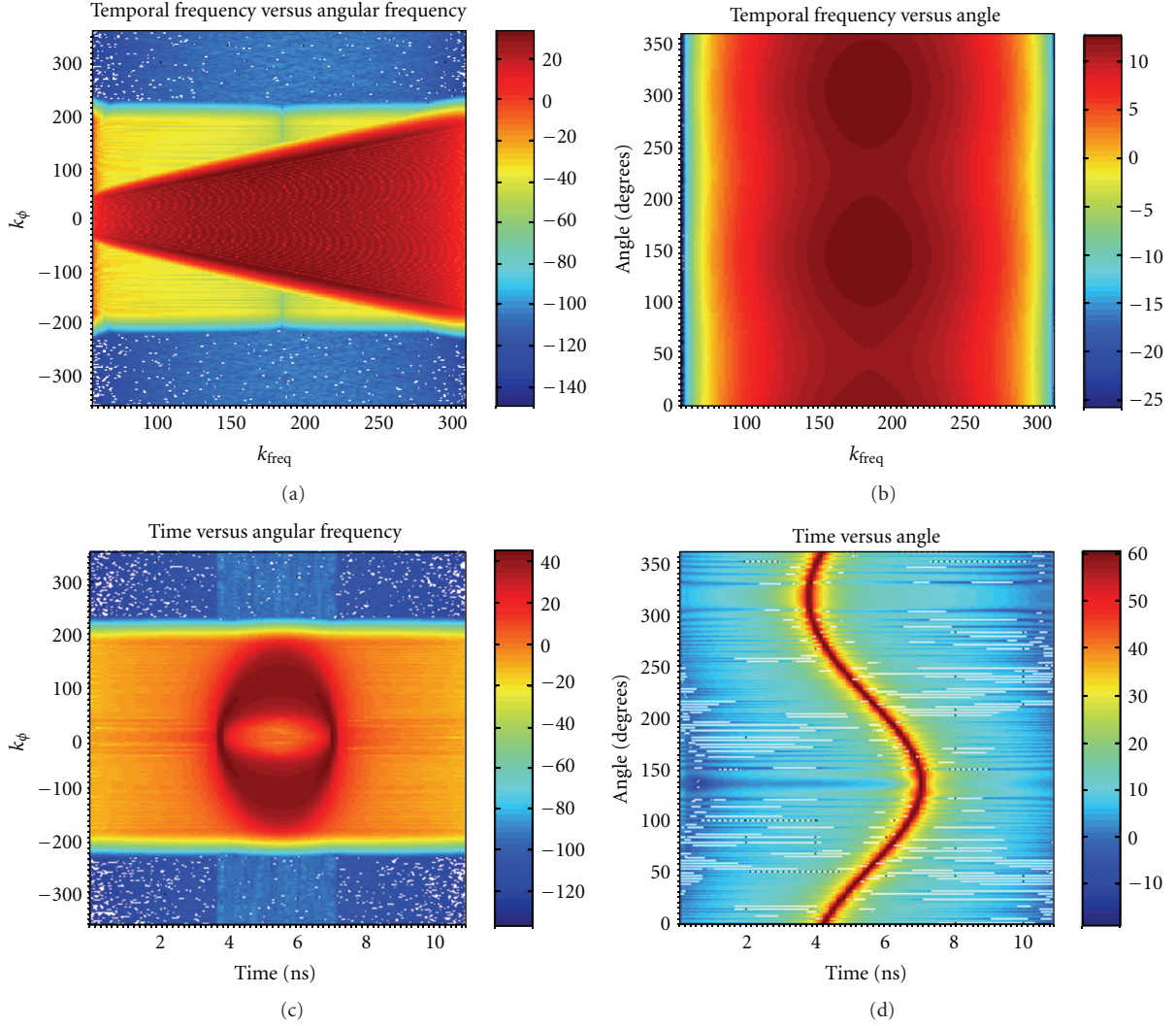


FIGURE 11: Four representations of data corresponding to a single simulated point target from a single bistatic antenna pair: (a) the “Fourier” domain, (b) the “raw-data” domain, (d) the “time” domain, and (c) shown for completeness but not used anywhere.

still applies; however, (6) must be adjusted to take the full bistatic geometry into account:

$$p_{\text{BS}}(\phi) = A \left[\frac{R_t(\phi)}{2} + \frac{R_r(\phi)}{2} - R_a \right] - k_{\phi} \phi, \quad (13)$$

$$R_{t,r}(\phi) = \sqrt{B_{t,r} - C_{t,r} \cos \phi},$$

where

$$B_{t,r} = R_a^2 + \rho^2 + z^2 - 2R_a z \cos \theta_{t,r}, \quad (14)$$

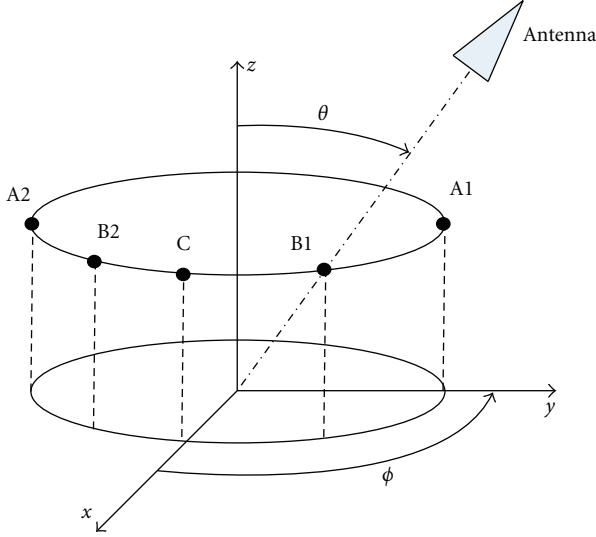
$$C_{t,r} = 2R_a \rho \sin \theta_{t,r}.$$

Splitting $p(\phi)$ into the contributions from each antenna has the effect of complicating the solution of the stationary-phase points in the bistatic case, as the first-order derivative then has $\sin \phi$ terms for both transmitter and receiver simultaneously. In fact, within the region of K_{ϕ} -space corresponding to two unique stationary points, these must be solved by a 6th-order polynomial equation in ϕ , whose full expansion has been shown in [15].

Clearly the calculation of the polynomial coefficients adds to the complexity of the bistatic SWISAR algorithm compared to the monostatic case, particularly as the roots must then be solved approximately by *eigenvalue-analysis* [26] and then verified for consistency by substitution into the first-order derivative equation:

$$p'_{\text{BS}} = \frac{A}{2} \left[\frac{C_t \sin \phi_{\pm}}{2\sqrt{B_t - C_t \cos \phi_{\pm}}} + \frac{C_r \sin \phi_{\pm}}{2\sqrt{B_r - C_r \cos \phi_{\pm}}} \right] - k_{\phi} < \delta p', \quad (15)$$

where $\delta p'$ is an arbitrarily small threshold. The result of this procedure is, however, considerably more accurate than the QMS solution, as seen in Figure 15, and is significantly faster than computing the full DFT, particularly if the resolution in the ϕ domain is high, as is required by a large radial dimension.

FIGURE 12: Geometric description of boundaries of k -space.

In the instance where no results for $\phi_{\pm} < \delta p'$ can be found from the sixth-order polynomial, the second-order derivative of the “phase” term tends to zero at a single root as before, which for the bistatic geometry now becomes

$$p_{BS}(\phi)'' = A \left(-\frac{C_t^2 \sin^2 \phi}{8R_t(\phi)^3} + \frac{C_t \cos \phi}{4R_t(\phi)} - \frac{C_r^2 \sin^2 \phi}{8R_r(\phi)^3} + \frac{C_r \cos \phi}{4R_r(\phi)} \right) = 0. \quad (16)$$

Following the same procedure as before, (16) has a seventh-order polynomial-root solution, allowing the second- and third-order phase derivatives to be calculated explicitly at these points.

The algorithm then proceeds as before, with the appropriate bistatic terms substituting those for the monostatic case in (12) to form the focussing template, \mathcal{F}_{BS} for each frequency, f , and look-angle, θ_b (which does still make use of the bistatic bisector angle, without any noticeable side-effects). The reflectivity of the target volume in cylindrical-polar coordinates can then be recovered as follows:

$$I_{BS}(\rho, \phi, z) = \frac{8}{c^3} \text{IFFT}_{k_\phi} \left[\sum_f f^2 \sum_{\theta_b} \sin \theta_b \text{FFT}_\phi [E_{BS}(f, \phi, \theta_b)] \times [\mathcal{F}_{BS}]_{k_\phi} \right] \Delta f \Delta \theta_b \Delta \phi, \quad (17)$$

where $[\mathcal{F}_{BS}]_{k_\phi} = \mathcal{F}_{BS}(\rho, k_\phi, z; f, \theta_t, \theta_r)$ for $K_\phi = -N_\phi/2, -N_\phi/2 + 1, \dots, N_\phi/2 - 1$.

To demonstrate the improvement in applying the *bistatic* (BS) approach to determine \mathcal{F}_{BS} , over the existing \mathcal{F}_{MS} approach used in [4], the example shown in Figure 15 uses the extreme Tx/Rx positions listed previously.

The uppermost phase plot in Figure 15 is formed with a full expansion of the DFT described by (5), (13), and

TABLE 2: Parameters of spherical targets used in point target simulations. based on the graphically estimated true target positions seen in Figure 16.

Target no.	X, m	Y, m	Z, m	Diameter, m
1	-0.2	-0.11	0.15	0.15
3	0.11	0.09	0.125	0.10
8	0.065	-0.165	0.1	0.05

(14). The blue lines in the remaining plots are then simple derivatives of this term, while the red line in the 2nd plot shows the value of the phase derivative assuming that the bistatic-bisector angle, θ_b , is used to provide a quasimonostatic approximation to the geometry. Admittedly this is far outside the expected region of validity for the bistatic angle of 6° given by the MBET. For the particular values of $k_\phi = 25$, and $f = 10$ GHz, two 1st-order stationary points can be seen, requiring the solution and validation of 6th-order polynomial roots. The dashed black line in the 2nd plot then shows a 6th order polynomial expansion of (15), two roots of which, shown by the blue markers, correspond exactly with the DFT solution. The variation in position of these stationary-phase points with the (red) QMS phase derivative is obvious from the markers.

As stated previously, in order to test the volumetric imaging performance of the full Bistatic-SWISAR algorithm, the prototype ISAR system was configured with two geometries as described by Table 1 and Figure 14. A set of spherical targets was then placed within the anechoic chamber as seen in Figure 16 and described by Table 2. Simulation and experimental results relating to these two geometries and common target set are then shown in Figures 17, 18, 19.

A summary of the experiments and a brief analysis of their main features are shown in Table 3.

The (white) “dead-pixels” seen both at the X-Y origin and for large values of both X and Y in all images are due to the postprocessing interpolation from cylindrical-polar to Cartesian coordinates. The limited variation in θ also leads to strong sidelobes forming *annuli* above and below the target.

When the point target SWISAR algorithm is applied to nonpoint targets, the energy is distributed around the surface of that target (corresponding to the specular region of that target at each rotation angle).

To allow these algorithms to be compared more accurately, a metric is required that determines how closely the imaged data conforms to “ground-truth.” Such a metric is given by the average power density over concentric spheres whose origins correspond to the targets of the multi-ball scenario, as seen in Figure 16.

The results of applying this metric are seen in Figure 20. The simulated MS and BS results correctly place the peak intensity at the desired result (within measurement error). The simulated QMS results meanwhile show that the classified spherical radius, as determined by the peak intensity, is overestimated by 5–10 mm for each target. The peak-responses for the MS and BS results are also significantly narrower than the equivalent QMS results (by $\sim 50\%$). The hump in intensity for a spherical radius of approximately

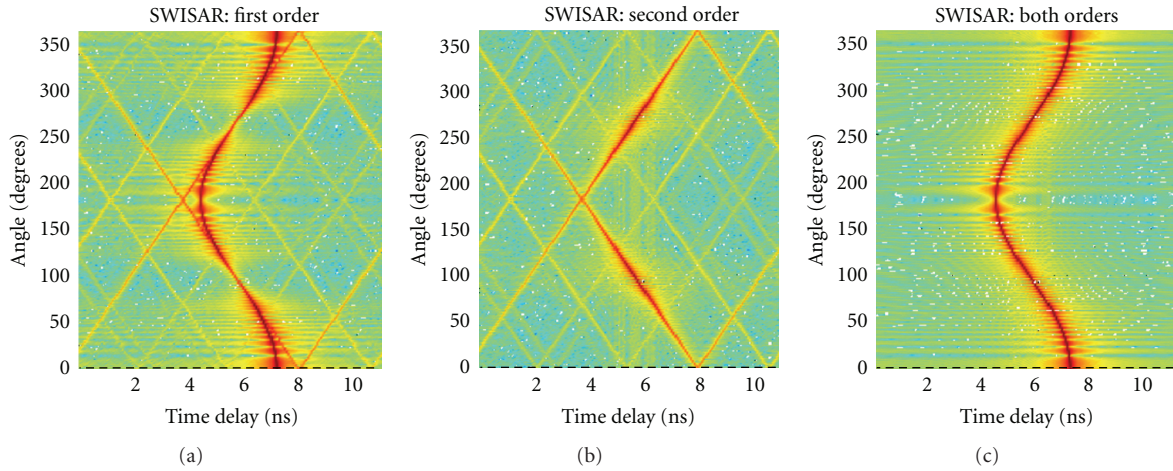


FIGURE 13: Time domain solutions for a single-simulated point target corresponding to the use of (a): $\text{IFFT}_{k_\phi, k_f}$ of first-order ($K_\phi \leq \hat{K}_\phi$) Fourier domain region only, (b): $\text{IFFT}_{k_\phi, k_f}$ of second-order ($K_\phi > \hat{K}_\phi$) Fourier domain region only and, (c): $\text{IFFT}_{k_\phi, k_f}$ of full k_ϕ Fourier domain regions. (The units, although not important to the figure, are nanoseconds on the x -axis and degrees on the y -axis.)

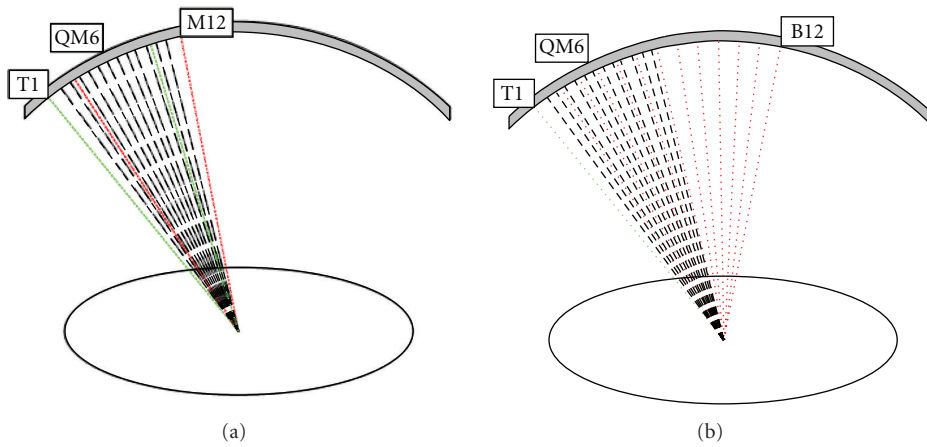


FIGURE 14: Equivalent QMS paths shown for (a) a pair of closely located antennas moving in sync across the arc and (b) a stationary transmitter and a moving bistatic receiver.

TABLE 3: Description for point-target SWISAR experiments.

	Simulated point target at [X, Y, Z] = [0, 0.5, 0.05]	Simulated spherical targets	Experimental spherical targets
Mono Static (MS) $\theta_t = 39^\circ : -2^\circ : 17^\circ$ $\theta_r = 33^\circ : -2^\circ : 11^\circ$ $\theta_{MS} = 36^\circ : -2^\circ : 14^\circ$ Computation time = 34 mins	Figure 17(a) Focussed to a single point. Effects of limited aperture in θ clearly visible.	Figure 18(a) Clear correspondence to upper (visible) surface of spheres Some residual energy in annuli	Figure 19(a) Clear correspondence to upper (visible) surface of spheres
Quasi Mono Static (QMS) $\theta_t = 39^\circ : -2^\circ : 17^\circ$ $\theta_r = 33^\circ : -2^\circ : 11^\circ$ $\theta_{MS} = 36^\circ : -2^\circ : 14^\circ$ Computation time = 34 mins	Figure 17(b) Poorly focussed	Figure 18(b) Smearred target response Greater residual energy in annuli.	Figure 19(b) Peak energy density away from target surface
Bi Static (BS) $\theta_t = 39^\circ$ (fixed) $\theta_r = 33^\circ : -4^\circ : -11^\circ$ $\theta_{BS} = 36^\circ : -2^\circ : 14^\circ$ Computation time = 7.5 hrs	Figure 17(c) Result "as good as" that of MS	Figure 18(c) Result "as good as" that of MS	Figure 19(c) Result "as good as" that of MS

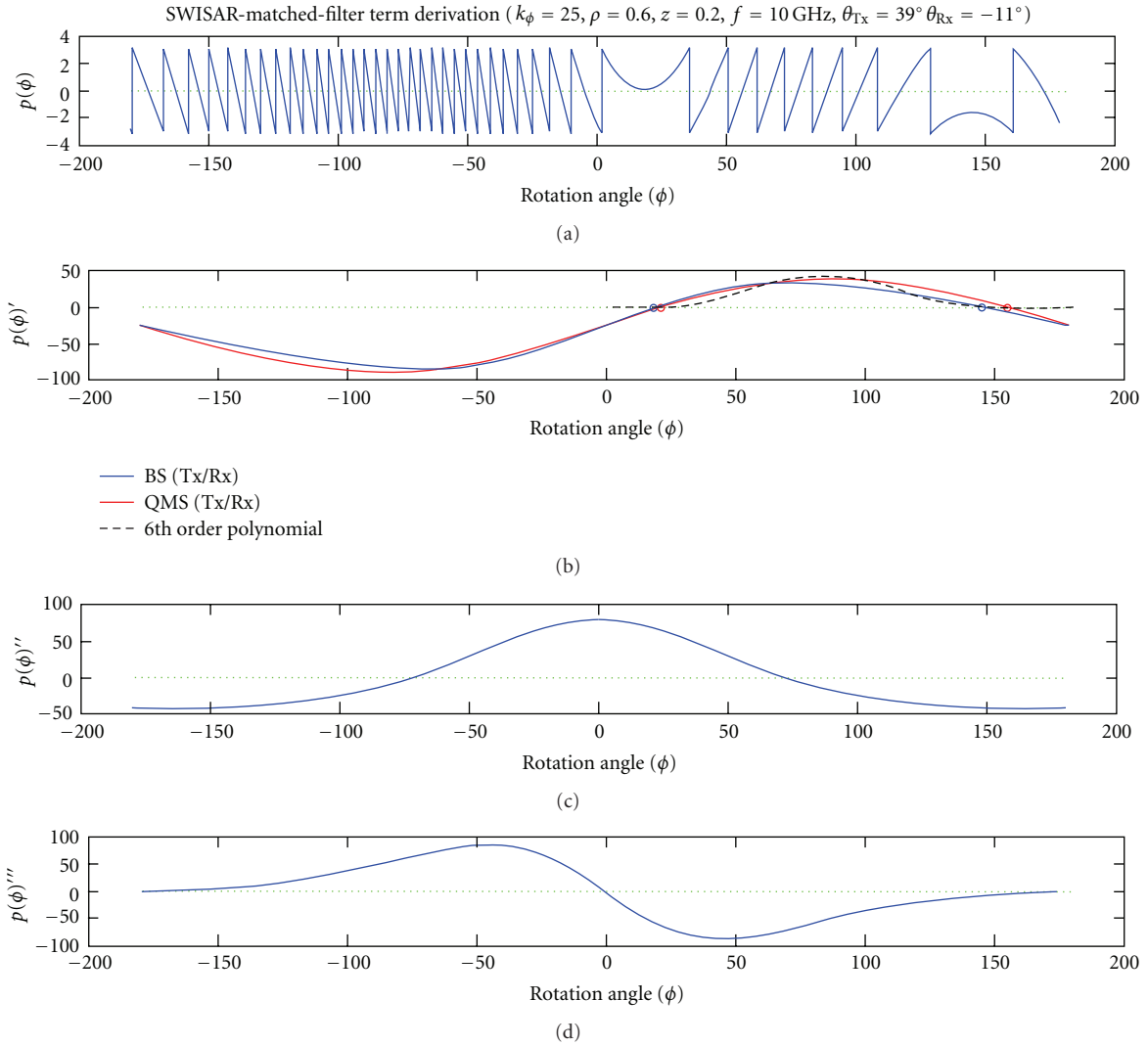


FIGURE 15: SVMF phase (and derivatives) for a large bistatic angle.

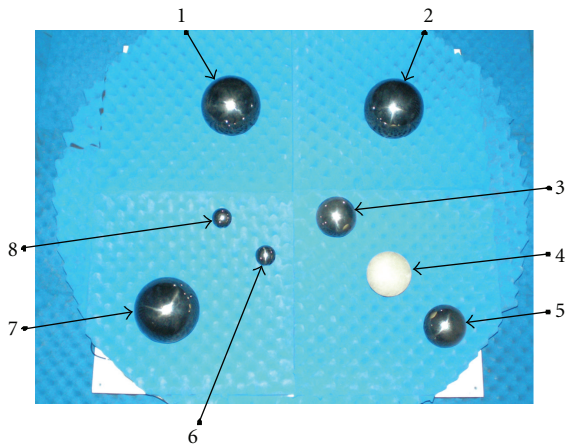


FIGURE 16: Experimental setup used to test monostatic (MS), quasimonostatic (QMS), and bistatic (BS) SWISAR algorithms, and the basis for equivalent simulated results.

0.25 m, for all MS and BS simulated targets, is believed to be due to the annuli artefacts earlier discussed, and not the other targets in the image.

Simulated data for targets 1, 3 and 8 (on the left) are compared to the experimental results for all 8 targets (on the right). These results correspond to concentric spheres whose radii increase in increments of 5 mm. The small (high-frequency) oscillations seen in the plots are, therefore, due to the discrete nature of the imaged data on a 10 mm voxel 3D grid.

5. A Coherent Multistatic Near-Field Imaging Algorithm for Spherical Targets

For a fixed geometry, determining focussing templates “on the fly” is a far more time consuming process than retrieving precomputed templates from a memory store (by up to three orders of magnitude). This being the case, the templates

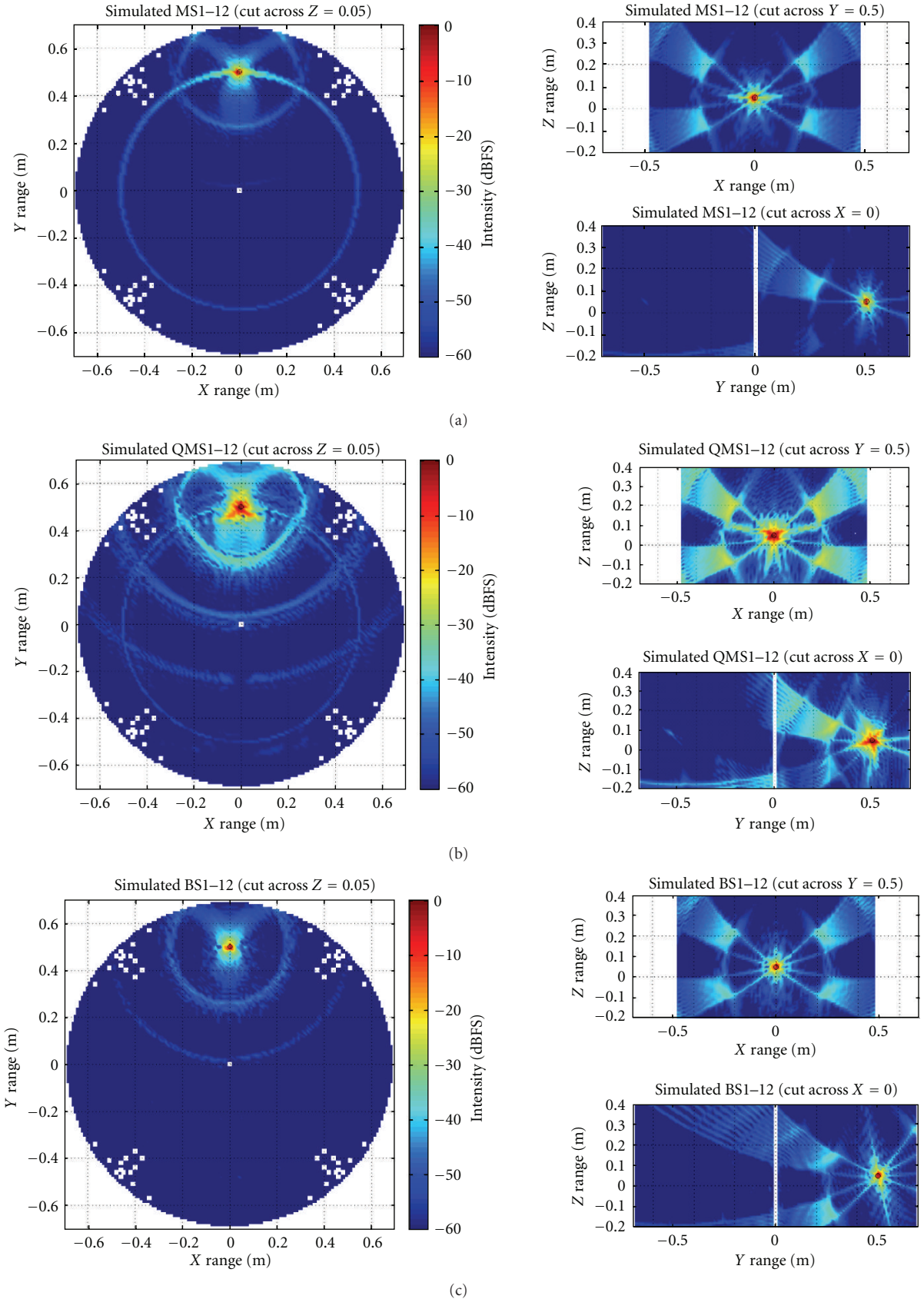


FIGURE 17: Simulated point-spread-function results for a single target at $[X, Y, Z] = [0, 0.5, 0.05]$ cut through each plane. (a) (Q)MS antennas, (Q)MS algorithm. (b) BS antennas, (Q)MS algorithm. (c): BS antennas, BS algorithm.

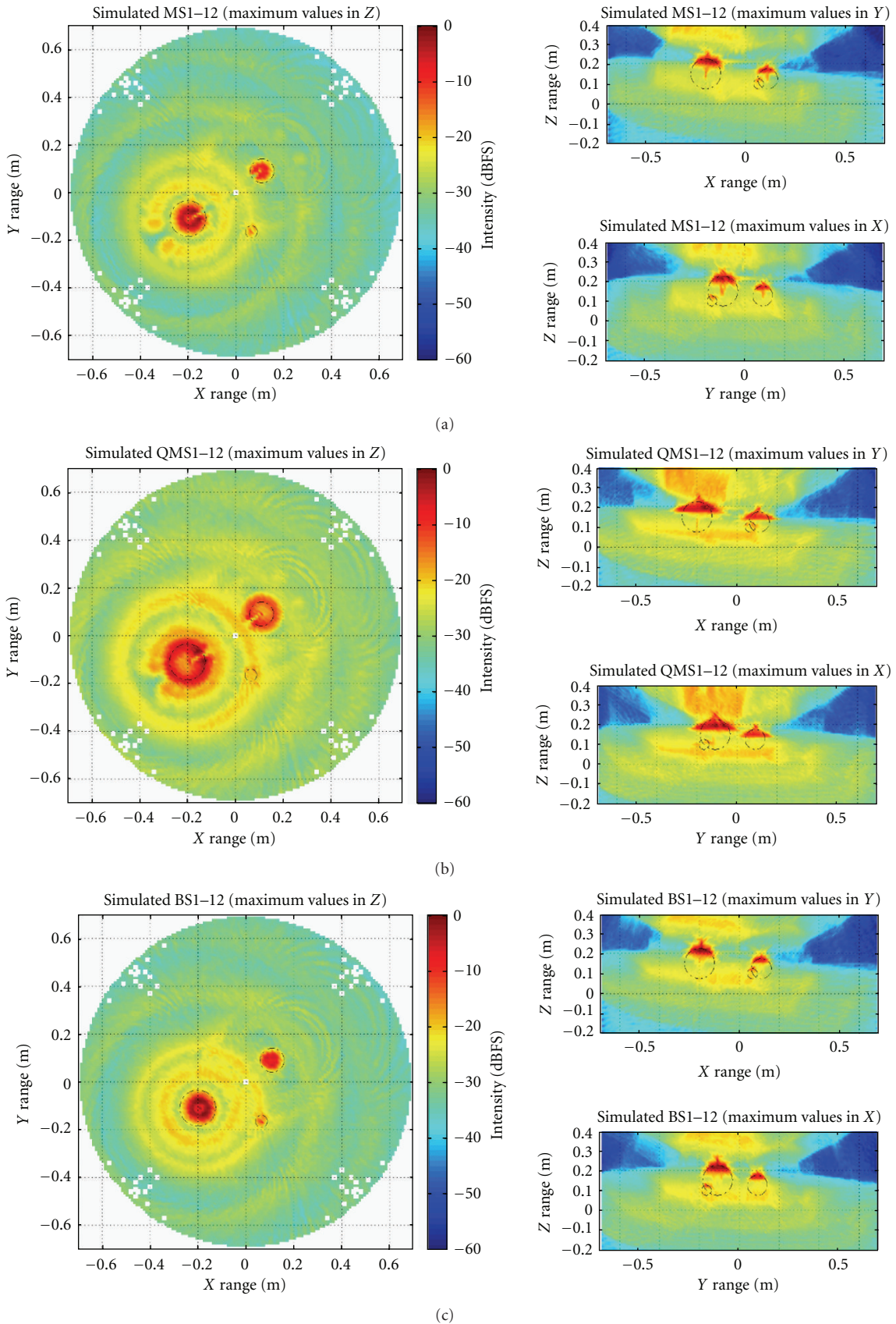


FIGURE 18: *Simulated* tomographic reconstruction of the spherical targets listed in Table 2. (a) (Q)MS antennas, (Q)MS algorithm. (b): BS antennas, (Q)MS algorithm. (c) BS antennas, BS algorithm.

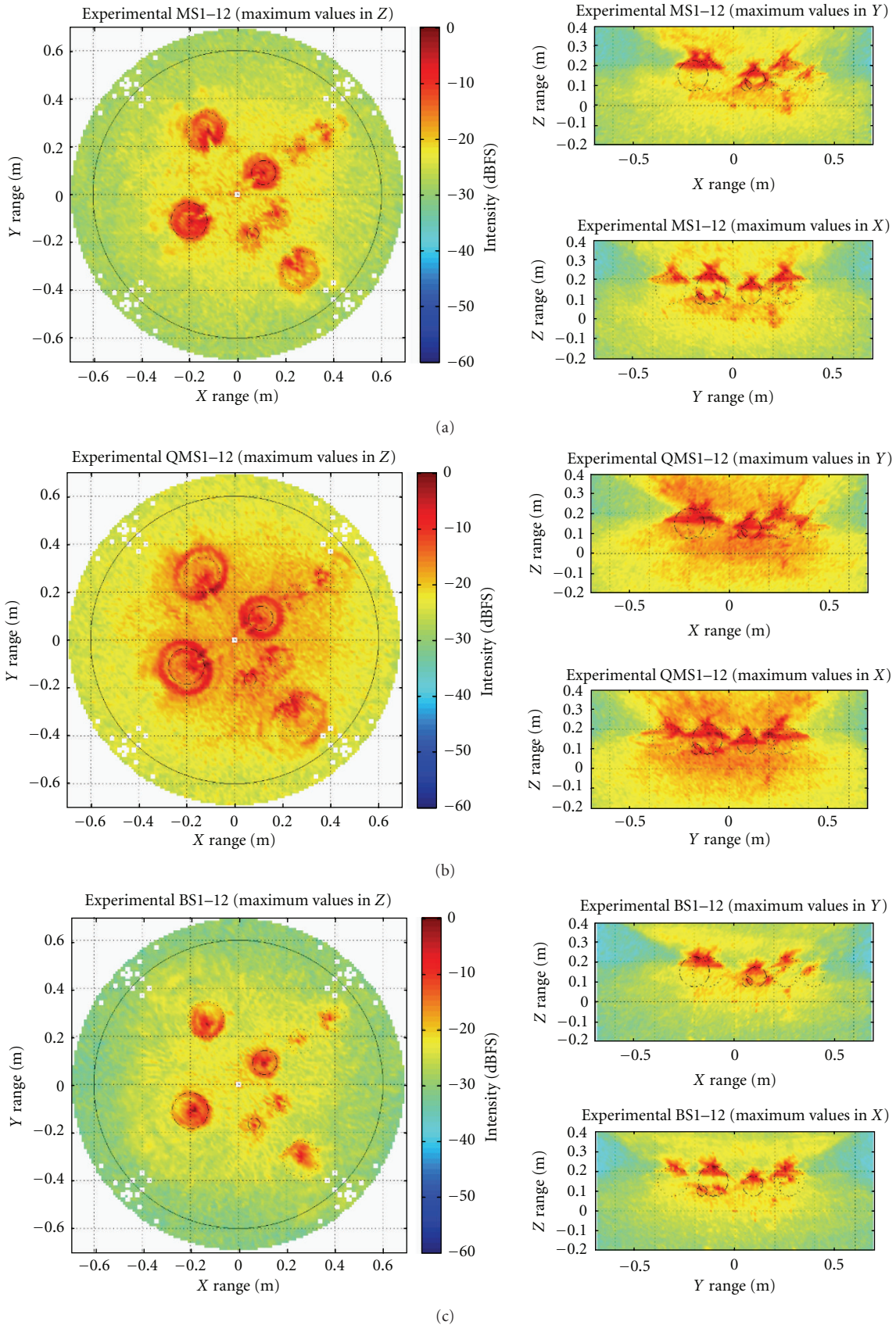


FIGURE 19: Experimental tomographic reconstruction of the targets seen in Figure 16. (a) (Q)MS antennas, (Q)MS algorithm. (b) BS antennas, (Q)MS algorithm. (c): BS antennas, BS algorithm.

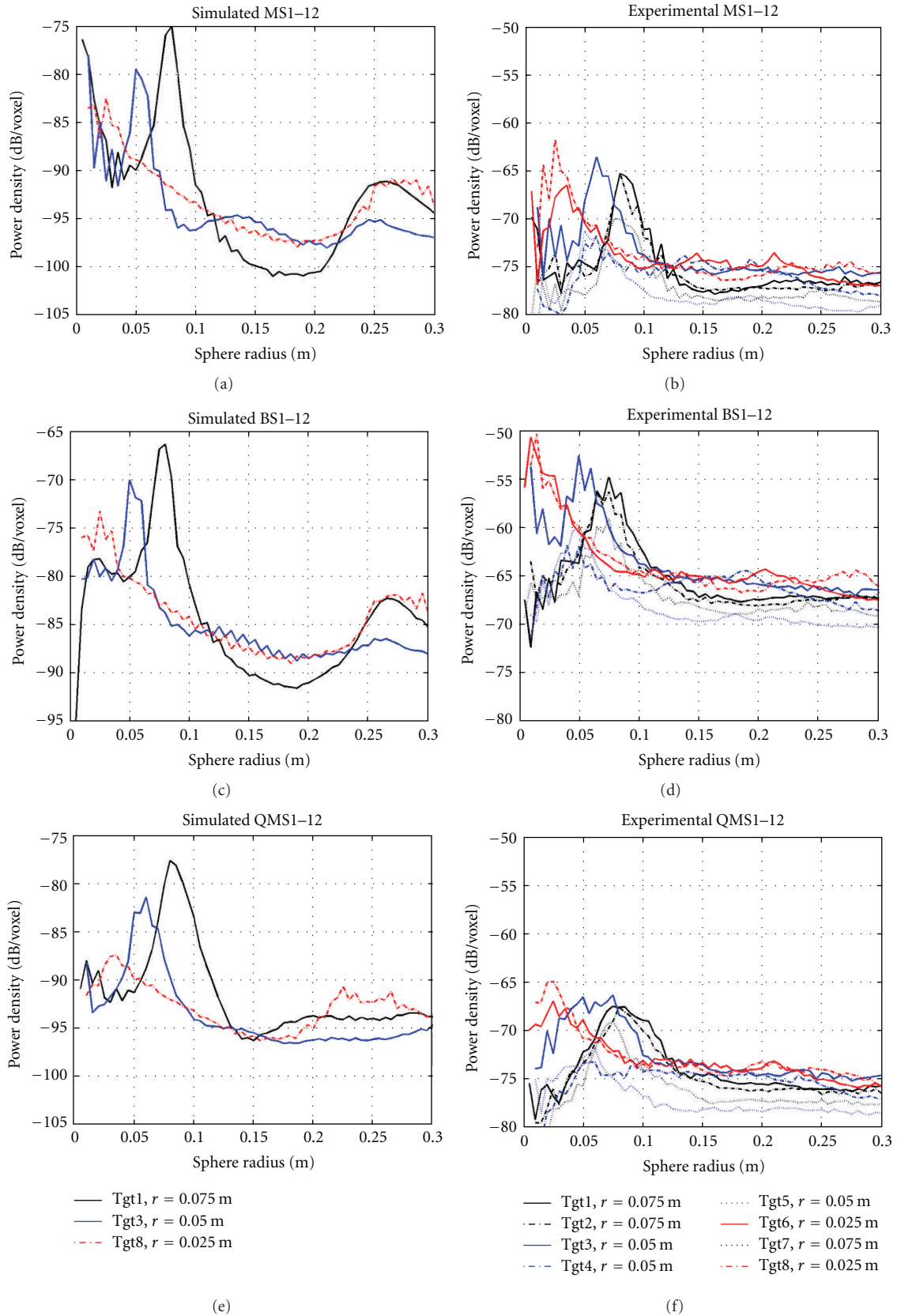


FIGURE 20: Spherical-surface classification performance of point-target SWISAR algorithms. Left: simulated and, Right: experimental data. (a, b) (Q)MS antennas, (Q)MS algorithm. (c, d) BS antennas, (Q)MS algorithm. (e, f) BS antennas, BS algorithm.

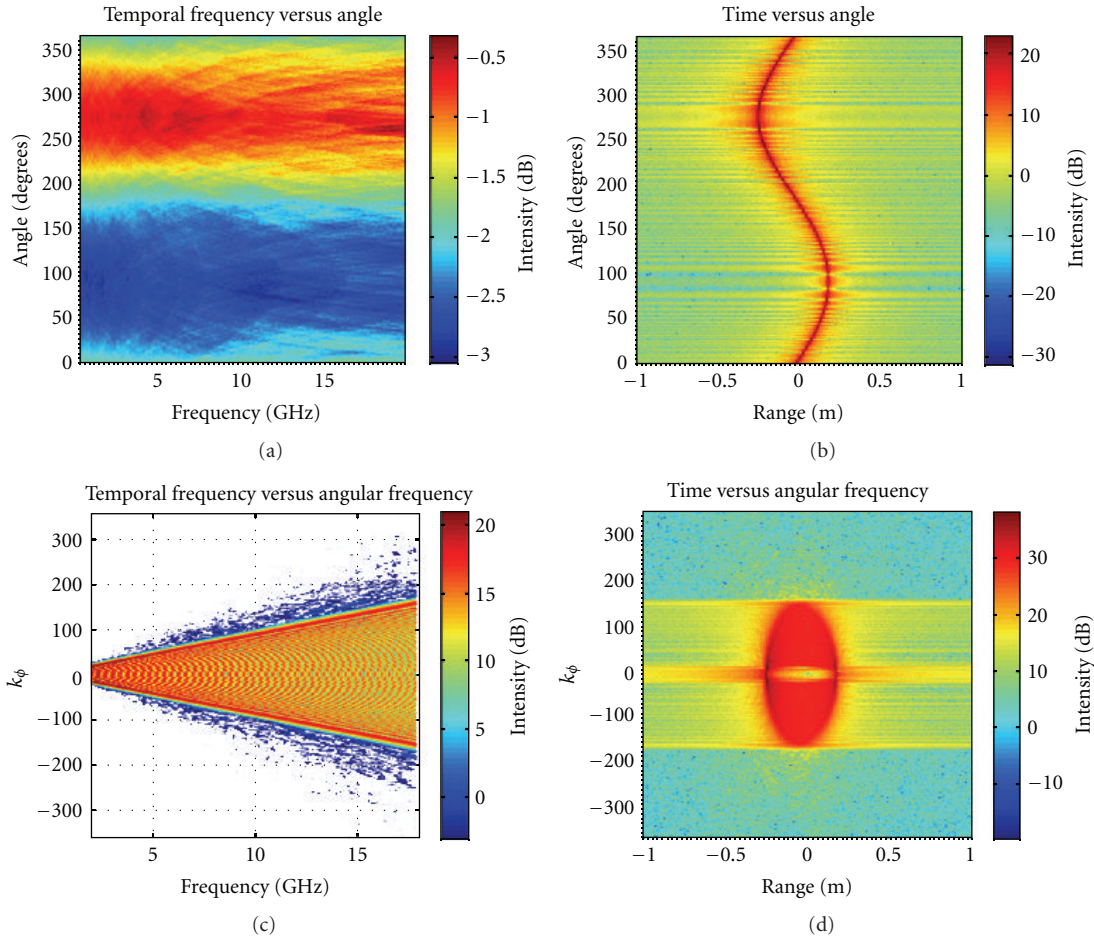


FIGURE 21: Four representations of the false-target-generated focussing template revolution data for a single antenna pair (BS_6): (a) the “raw-data” domain, (b) the “time” domain, (c) the “Fourier” domain, and (d) shown for completeness but not otherwise used.

may as well be created by any tractable means. Taking this into consideration, the simulator used to test the SWISAR algorithm in the previous section was extended to allow the formation of templates corresponding to arbitrary shapes placed anywhere within the target volume. A spherical target, made up of distributed point-elements, is simulated at each required rotation angle around the turntable, and the (geometric optics) phase contributions calculated from the individual elements located within the frequency-dependent cophase region, that is, those points on the sphere, at each angle and frequency, whose bistatic range fall within a half-wavelength of the shortest path. This, therefore, forms a numerical approximation to the “wavefront-set” of the target, as recognised by microlocal-analysis, and can be easily calculated for a large number of scatterers. It can also be computed for any antenna configuration, and if necessary, arbitrary trajectories. A bank of generic SVMFs based on spherical false-targets can then be built-up to determine locally coherent scattering regions on complex experimental targets. The Fourier-domain matched filter template, equivalent to that produced by (2), is then formed by a 1D azimuth FFT of the simulated frequency/angle data, which can then be applied to detect the location of any target within the

cylindrical-polar coordinate space. The simulation process is then repeated for targets of arbitrary size, under all required antenna-pair configurations. An example of the focussing template, that is produced for a 50 mm diameter sphere located at $[X, Y, Z] = [0, 0.5, 0.05]$ m (or $[\rho, \phi, z] = [0.5, 0, 0.05]$), is shown in Figure 21 for the bistatic antenna pair: $\theta_{Tx} = 39^\circ$, $\theta_{Rx} = 13^\circ$.

One additional point to note is that although a focussed intensity peak is obtained at the centre of a sphere, most targets are not perfect spheres and will, therefore, have a variable local curvature, which will lead to defocussing of the peak intensity. Whilst windowing of the focussing templates may be employed to highlight angular subregions of certain curvature, this remains an area of future work.

Focus templates were generated for a range of spherical radii from 0 to 100 mm in steps of 5 mm. As an example, the maximum intensity values for the mid-range value of $r_s = 50$ mm are shown in Figure 22. While the false-target template generation method is also amenable to antenna gain-correction, this was not applied in keeping with previous results.

These results show that when the data are correctly focussed at the centre of the 100 mm diameter “Target 3”,

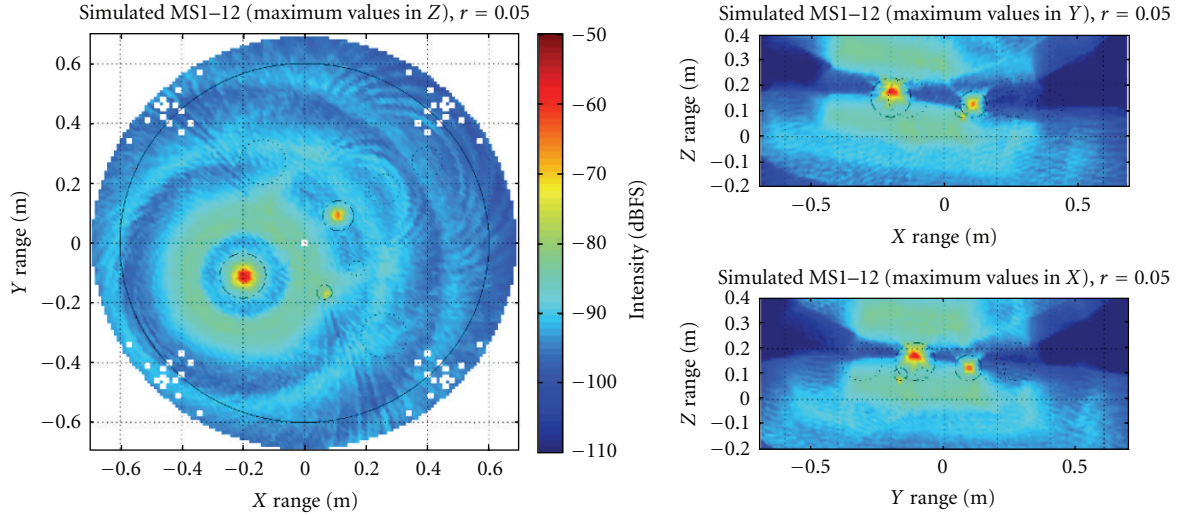


FIGURE 22: Maximum intensity in X, Y, Z dimensions for the 3 spherical targets described in Table 2, when imaged by the MS spherical-target SWISAR algorithm.

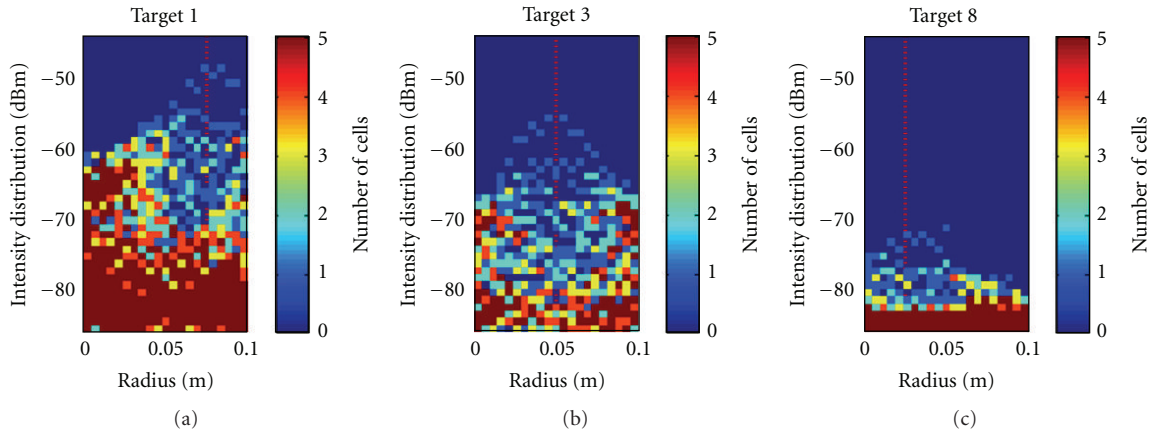


FIGURE 23: Intensity distribution per voxel within the proximity of simulated targets 1, 3 and 8.

the intensity remains off-centre for both the smaller and larger targets; indeed the main effect seems to be merely to push the intensity peak downwards in z as r_s is increased. This can be expected due to the limited extent in θ .

Also, whilst the intensity relating to each sphere increases to a peak as the correct radius is reached, the total energy remains distributed as for the original data, that is, the peak intensity for any search radius corresponds to the signal from the largest sphere, while the signal from the smallest remains at all times the weakest. This is most clearly summarised in the intensity distribution plots shown in Figure 23.

Here, the distribution of power within a subset of the target volume (for each target, a histogram of voxel intensity is applied over a subvolume defined by ground truth position ± 75 mm in X and Y and over the full range in Z) is plotted against spherical radius to highlight the fact that

- (i) the energy related to each target is focussed towards a peak at the correct radius, which typically occurs within a single voxel of the target volume, and is

approximately 10 dB greater than the energy in the surrounding cells;

- (ii) the energy from large targets is significantly greater than for smaller targets, even when the radius is far from its true value, as the SWISAR algorithm continues to focus data as a mismatched filter;
- (iii) the noise floor of large targets is significantly higher than the peak of smaller targets due to the imaging artefacts previously discussed.

For the experimental results, the choice of ground-truth origin for each sphere plays an important part in determining the algorithm’s performance and in practice must be determined from the data as the target structure is “unknown.” In this instance, the spherical origin was chosen by clustering regions of high intensity and choosing the peak intensity of each cluster. As can be seen from the results in Figure 24, this is an area for improvement.

Reconstruction may then be performed by rebuilding complex targets as the sum of spheres of different sizes. This

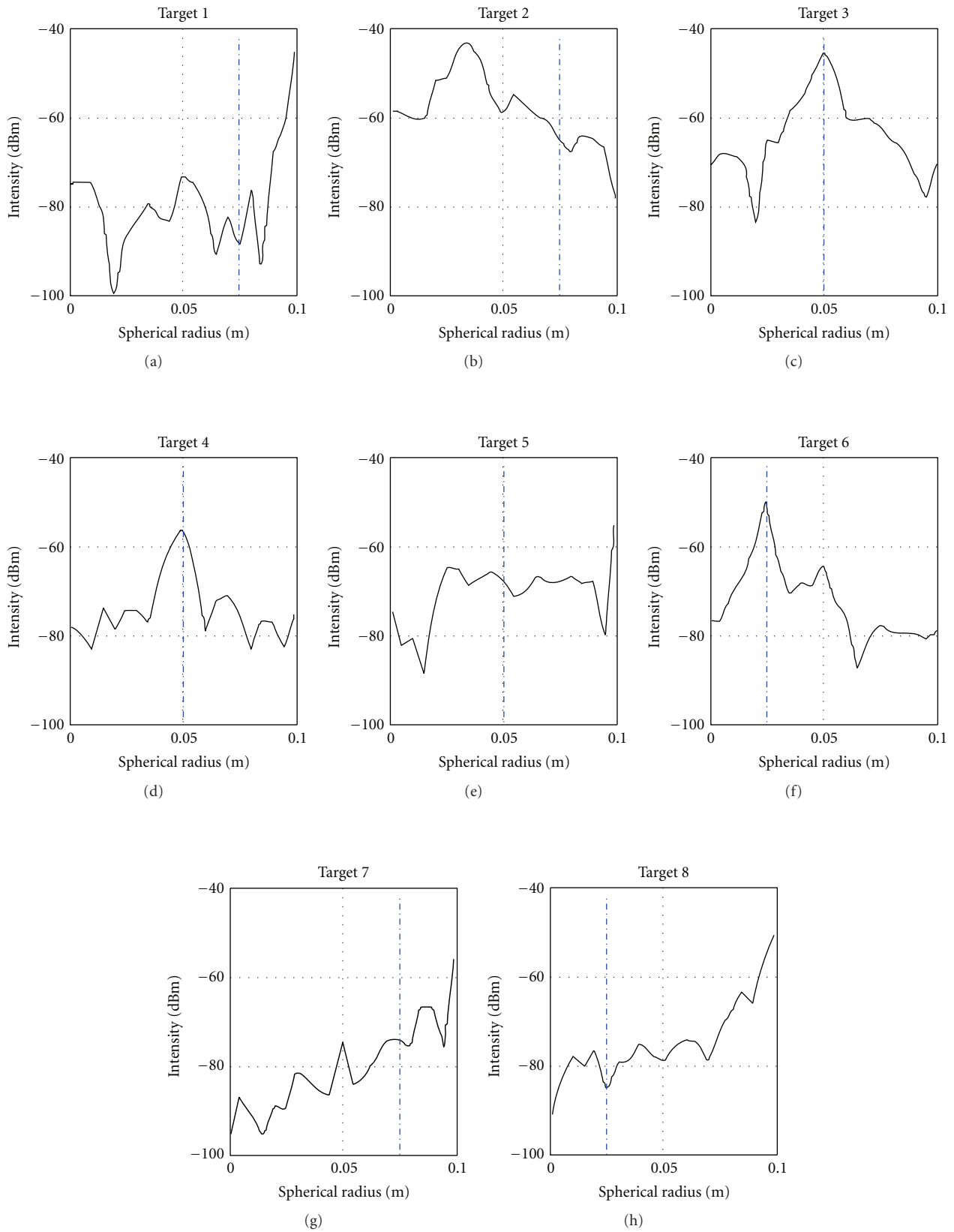


FIGURE 24: Variation in intensity versus spherical search radius for each target. The origin of each target was determined by peak intensity of each target cluster. Actual target radii are indicated by the dashed/dotted lines.

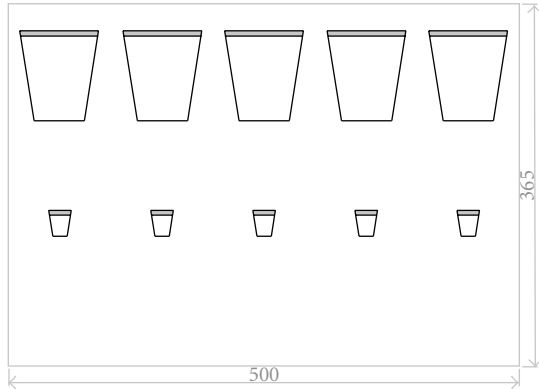


FIGURE 25: Mitre joint cutting template for 300 mm tall, 100 mm unit-square base, pyramidal RAM (must be scaled to indicated dimensions prior to use).

is a time-consuming process but has the benefit of identifying both large specular regions, as well as smaller textural features. This work has been reported in [23].

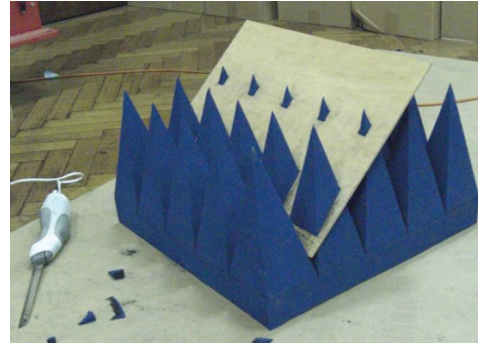
6. Conclusions

A prototype 3D imaging radar system has been developed utilising software linearisation and the highest available component bandwidth of 2–18 GHz. This bandwidth requires multiple YIG oscillator sections, which have been linearised to one another to reduce phase noise and achieve close to theoretical range resolutions. Two-target range discrimination performance of better than 20 mm has been obtained for a single FMCW measurement within a custom anechoic test environment.

Bistatic antennas in an ISAR configuration have been used to demonstrate the concept of a multistatic spherical SAR system. The Fourier domain point-target focussing templates for this bistatic antenna configuration have been derived using the MoSP. Due to the differing trigonometric terms for two antennas, the phase derivative terms must be solved using polynomial root equations, which although quicker than a full DFT expansion are considerably slower than the equivalent QMS calculation. Results, however, are considerably improved, particularly when the bistatic antenna separation crosses the spherical-polar coordinate system's zenith.

When the point target SWISAR algorithm is applied to nonpoint targets, the imaged intensity is distributed around the surface of that target, but the shallow drop-off in power away from the surface makes size discrimination difficult. A MS spherical-target SWISAR algorithm has, therefore, been developed, acting as a matched filter for targets of a particular radius.

Applying the MoSP to the detection of spherical targets in a bistatic antenna configuration is intractable due to the high number of polynomial root equations that must be solved. Alternatively, the Fourier-domain focussing templates for a spherical target can be precomputed using a geometric-optics false-target model, based on numerical rather



(a)



(b)

FIGURE 26: (a) Indicative use of mitre-cutting template and recommended cutting tool. (b) Recommended means of supporting ceiling panels while (3 M 90) adhesive cures.

than asymptotic-analytic integration of elements within the wavefront-set of the target.

Experimental results show that while the MS and BS methods provide positive identification of spherical targets of varying diameter, applying the MS algorithm to the BS antenna dataset (i.e., QMS-mode) has significantly poorer results.

While further work remains to achieve the original aim of producing size-distributions of blasted rock fragments, this work has then been extended to the 3-D reconstruction of more regular rocks as reported in [14, 23]. It also remains to incorporate the frequency-dependent antenna gain variation, inherent with multioctave measurements, which might otherwise lead to suboptimal image fidelity.

Appendix

Anechoic Chamber Construction Tips

When correctly scaled and transferred to an appropriate material (such as 3 mm plywood), the template shown in Figure 25 will fit over a 500 × 500 mm square RAM tile at 45° to enable the cutting of mitre-joints with an electric carving knife, as seen in Figure 26(a). “3 M 90 Hi-Strength Spray Adhesive” is recommended for affixing the RAM to the walls and ceiling, whilst “Acrow props” and a 2nd tile provide

a simple means of holding tiles in place until the glue dries (~15 minutes), as seen in Figure 26(b).

Acknowledgment

The author wishes to thank the CRC Mining for funding this paper.

References

- [1] T. Derham, S. Doughty, C. Baker, and K. Woodbridge, "Ambiguity functions for spatially coherent and incoherent multistatic radar," *IEEE Transactions on Aerospace and Electronic Systems*, vol. 46, no. 1, pp. 230–245, 2010.
- [2] L. H. Hemming, *Electromagnetic Anechoic Chambers*, Wiley-Interscience, New York, NY, USA, 2002.
- [3] D. P. Ray and J. Green, "Trials and tribulations of building a modern EMC facility," in *Proceedings of the IEEE International Symposium on Electromagnetic Compatibility*, pp. 275–280, August 2000.
- [4] J. Fortuny, *Efficient algorithms for three-dimensional near-field synthetic aperture radar imaging*, Ph.D. thesis, Faculty of Electrical Engineering, University of Karlsruhe, Karlsruhe, Germany, 2001.
- [5] J. Fortuny, "An efficient 3-D near-field ISAR algorithm," *IEEE Transactions on Aerospace and Electronic Systems*, vol. 34, no. 4, pp. 1261–1270, 1998.
- [6] A. Papoulis, *Signal Analysis*, McGraw Hill, New York, NY, USA, 1977.
- [7] F. Natterer and F. Wübbeling, *Mathematical Methods in Image Reconstruction*, Society for Industrial and Applied Mathematics, Philadelphia, Pa, USA, 2001.
- [8] B. Borden and M. Cheney, "Microlocal ISAR for low signal-to-noise environments," in *Proceedings of the IEEE Radar Conference*, pp. 829–834, April 2006.
- [9] M. Cheney and B. Borden, "Microlocal analysis of GTD-based SAR models," in *Proceedings of the 12nd Algorithms for Synthetic Aperture Radar Imagery*, p. 15, Orlando, Fla, USA, 2005.
- [10] C. J. Nolan and M. Cheney, "Synthetic aperture inversion for arbitrary flight paths and nonflat topography," *IEEE Transactions on Image Processing*, vol. 12, no. 9, pp. 1035–1043, 2003.
- [11] V. Krishnan, J. Swoboda, C. E. Yarman, and B. Yazici, "Multistatic synthetic aperture radar image formation," *IEEE Transactions on Image Processing*, vol. 19, no. 5, pp. 1290–1306, 2010.
- [12] C. E. Yarman, B. Yazic, and M. Cheney, "Bistatic synthetic aperture radar imaging for arbitrary flight trajectories," *IEEE Transactions on Image Processing*, vol. 17, no. 1, pp. 84–93, 2008.
- [13] D. Blacknell, D. Andre, C. Finch, M. Nottingham, and D. Muff, "Life in the frequency domain: SAR CCD over mountains and the physics of vibrating targets," in *Proceedings of the Defense Applications of Signal Processing (DASP '11)*, Sunshine Coast, Australia, 2011.
- [14] D. Johnson, "Complex scatterer reconstruction using multistatic spherical wave ISAR Fourier template matching," in *Proceedings of the International Conference on Electromagnetic Advanced Applications (ICEAA '09)*, Turin, Italy, 2009.
- [15] D. Johnson, *Complex target reconstruction using near-field synthetic aperture radar*, Ph.D. thesis, University of Sydney, 2009.
- [16] Austec-Panel-Systems-Australia-Pty-Ltd. Panelex datasheet, <http://www.austecpanels.com.au/>.
- [17] D. G. Johnson, "Development of a high resolution MMW radar employing an antenna with combined frequency and mechanical scanning," in *Proceedings of the IEEE Radar Conference (RADAR '08)*, May 2008.
- [18] D. G. Johnson and G. M. Brooker, "4GHz bandwidth closed loop linearisation of a millimetre-wave, linear frequency modulated radar," in *Proceedings of the 2nd International Conference on Sensing Technology*, Pamerston North, New Zealand, 2007.
- [19] A. G. Stove, "Linear FMCW radar techniques," *IEE Proceedings F*, vol. 139, no. 5, pp. 343–350, 1992.
- [20] Marconi 6311, "Programmable sweep generator, operating manual," 1989.
- [21] A. Meta, P. Hoogeboom, and L. P. Ligthart, "Range non-linearities correction in FMCW SAR," in *Proceedings of the IEEE International Geoscience and Remote Sensing Symposium (IGARSS '06)*, pp. 403–406, August 2006.
- [22] D. Baumann, C. Fumeaux, P. Leuchtman, and R. Vahldieck, "Finite-volume time-domain (FVTD) modelling of a broadband double-ridged horn antenna," *International Journal of Numerical Modelling*, vol. 17, no. 3, pp. 285–298, 2004.
- [23] D. Johnson, "Extended scatterer reconstruction using multistatic spherical wave ISAR Fourier template matching," in *Proceedings of the Australian Mining Technology Conference*, Perth, Australia, 2010.
- [24] M. Abramowitz and I. A. Stegun, *Handbook of Mathematical Functions*, National Bureau of Standards (US), 1964.
- [25] C. J. Bradley, P. J. Collins, D. G. Falconer, J. Fortuny-Guasch, and A. J. Terzuoli, "Evaluation of a near-field monostatic-to-bistatic equivalence theorem," *IEEE Transactions on Geoscience and Remote Sensing*, vol. 46, no. 2, pp. 449–456, 2008.
- [26] G. H. Golub and C. F. Van Loan, *Matrix Computations*, John Hopkins University Press, Baltimore, Md, USA, 3rd edition, 1996.

Research Article

Examination of Far-Field Mathematical Absorber Reflection Suppression through Computational Electromagnetic Simulation

S. F. Gregson, A. C. Newell, and G. E. Hindman

Nearfield Systems Inc., 19730 Magellan Drive, Torrance, CA 90502, USA

Correspondence should be addressed to S. F. Gregson, sgregson@nearfield.com

Received 13 October 2011; Accepted 11 March 2012

Academic Editor: Lars Jacob Foged

Copyright © 2012 S. F. Gregson et al. This is an open access article distributed under the Creative Commons Attribution License, which permits unrestricted use, distribution, and reproduction in any medium, provided the original work is properly cited.

The mathematical absorber reflection suppression (MARS) technique has been used to identify and then suppress the effects of spurious scattering within spherical, cylindrical, and planar near-field antenna measurement systems, compact antenna test ranges (CATRs), and far-field measurement facilities for some time now. The recent development of a general-purpose three-dimensional computational electromagnetic model of a spherical antenna test system has enabled the MARS measurement and postprocessing technique to be further investigated. This paper provides an overview of the far-field MARS technique and presents an introduction to the computational electromagnetic range model. Preliminary results of computational electromagnetic range simulations that replicate typical MARS measurement configurations are presented and discussed which, for the first time, confirm through simulation many of the observations that have previously been noted using purely empirical techniques.

1. Introduction to Far-Field MARS

Reflections in antenna test ranges can often be the largest source of measurement error within the error budget of a given facility [1] with direct collimating ranges being perhaps the most susceptible to these contaminants [2]. Considerable attention has been paid to range multipath suppression in the open literature with significant effort, ingenuity and resourcefulness having been devoted to quantifying and subsequently correcting multipath contaminated measurements by means of hardware or software time gating, background subtraction, complex plane circular least squares fitting, and signal-encoding-based techniques. However, until very recently, the frequency domain mode orthogonalisation and filtering techniques that have proved so overwhelmingly successful in near-field measurements (i.e., spherical [3–6], cylindrical [7–9], planar [10–12], and more generally [13]) have not been applied to one-dimensional far-field measurements. Far-field MARS (F-MARS) [14, 15] is very closely related to the well-established spherical and cylindrical MARS implementations with processed results being obtained from only a single one-dimensional far-field pattern cut. This is significant, as one of the most appealing attributes of the far-field methodology has been its ability to

provide a single antenna pattern cut, thereby, minimising the required measurement time and complexity. However, one of the more widely acknowledged shortcomings of making direct far-field antenna pattern measurements is that range multipath can degrade the accuracy of the measurement results [2]. This is especially true for outdoor far-field measurements where, in general, far less control is obtained over the test environment. The F-MARS measurement and post-processing technique was specifically conceived for use with far-field ranges to combat exactly this issue where only one-dimensional single frequency far-field antenna pattern data is acquired.

F-MARS is entirely generic in nature, and can be applied to a variety of different antenna types with no *a priori* assumptions being made about the excitation or distribution of currents sources. Previously [14, 15], empirical test campaigns have been used to verify that the F-MARS technique is able to suppress spurious range reflections whilst preserving the integrity of the underlying antenna pattern function. This verification has been accomplished by establishing the degree of repeatability between successive F-MARS processed measurements where only a single parametric change had been introduced into the experimental configuration. That parametric change comprised the installation of a single

large scattering object into the test environment. During that investigation, it was found that like other implementations of the MARS technique, displacing the antenna under test (AUT) away from the centre of rotation was crucial to the success of the technique, and rules for optimising this offset were developed. The purpose of this paper is to present the results of a computational electromagnetic simulation that attempted to recreate the previously used experimental configuration and procedure in order to obtain further independent verification of the F-MARS technique. Whilst a detailed description of the theoretical basis and practical verification of F-MARS can be found presented in the open literature [14, 15] and is not the primary subject of this paper, the following summary of the F-MARS measurement and data postprocessing may be of some utility to the reader in understanding the chosen simulation configuration described herein.

- (1) Take a direct acquisition of the one-dimensional far electric field amplitude and phase pattern function with the AUT offset from the origin (a single far-field component is sufficient).
- (2) Apply a differential phase change to mathematically translate the AUT to the origin of the measurement coordinate system.
- (3) Obtain the translated mode coefficients of the AUT for an AUT conceptually located at the origin of the measurement coordinate system using the inverse fast Fourier transform (FFT).
- (4) Apply band-pass mode filtering function to suppress unwanted higher order cylindrical mode coefficients (CMC) where the properties of the filter function are determined from the physical size of the AUT and the free space propagation number.
- (5) Compute the complete far electric field pattern from the filtered mode coefficients using the FFT to obtain the MARS filtered antenna pattern function.

Here, since these transformations and their inverse operations can be evaluated using the one-dimensional fast Fourier transform (FFT) algorithm, this insures that F-MARS processing is very efficient in terms of computational effort and resources.

The development of general-purpose tools for the simulation of near-field or far-field antenna measurements is of interest for several reasons. Such a tool would enable one to plan and optimise a measurement campaign before committing valuable facility time or resources or to assess individual error terms within the facility level error budget and to verify correction algorithms. In this instance it was the impact of spurious range multipath that was being assessed together with the effectiveness of correction techniques. In general, it is difficult to obtain closed form functional solutions for the electromagnetic (EM) field at an arbitrary point in space from knowledge of the tangential electric and/or tangential magnetic fields over a closed surface for anything but the simplest of configurations. This is especially true when the closed surface is not coincident with the

aperture of the radiating structure, as is the case for near-field or MARS type antenna measurements. As such, recourse to alternative, typically numerical-based techniques becomes unavoidable.

In essence, any antenna measurement can be simulated by evaluating the complex coupling coefficient between the AUT and the field probe (or remote source antenna). This must be accomplished for each point within the simulated acquisition surface, for each sampled polarisation, and for each frequency at which the measurement is to be taken. In principle then, it would be possible to obtain the mutual coupling coefficient, S_{21} , between a given mode in the waveguide port in the AUT and a given mode in the waveguide port on the scanning probe (or remote source antenna) from a three-dimensional computational electromagnetic (CEM) full wave solver. This approach would have the advantage of, potentially, introducing the least number of assumptions and approximations and therefore could in principle yield the most accurate predictions. Unfortunately, at the present time, although many solvers are available employing, say, the finite difference time domain (FDTD) method, the finite element method (FEM), the method of moments (MoM), and so forth, these are generally considered inappropriate for simulating problem spaces as electrically large as those needed to enclose a complete near- or far-field measurement system, especially when that model extends to include positioners, absorber, cranes, and lights. This limitation is merely a consequence of the extended processing times and the large amounts of computer resources that are typically required. Hence, alternative, perhaps less generally applicable, but more computationally efficient techniques are required. One possible strategy for accomplishing this is introduced in the following section.

2. Overview of Simulation Technique

The computational electromagnetic simulation of a direct far-field range measurement was based on physical optics, and specifically on the Kirchhoff-Huygens principle which enables fields specified over one closed surface to be propagated to another point in space. The Kirchhoff-Huygens principle is a powerful technique for determining the field in a source free region outside a closed surface from the knowledge of the electromagnetic field distributed across that surface. This method is applicable to arbitrary shaped surfaces over which both the electric and magnetic fields are known. The form of the Huygens principle which is used can be derived from the integral form of the Stratton Chu equations [16] which represents an integral form of Maxwell's equations. When expressed mathematically, the electric field at a point P radiated by a closed, but arbitrary, Huygens surface S is

$$\underline{E}_p = \frac{1}{4\pi} \int_S -[j\omega\mu(\underline{n} \times \underline{H})\psi + (\underline{n} \times \underline{E}) \times \nabla_0\psi + (\underline{n} \cdot \underline{E})\nabla_0\psi]ds_0. \quad (1)$$

Here, \underline{E} and \underline{H} are the electric and magnetic fields, respectively, and are specified over the enclosing surface, and ψ denotes the first order spherical function,

$$\psi = \frac{e^{-jk_0 r'}}{r'}. \quad (2)$$

Here r' is the displacement of the field point from the elemental source and is related to the coordinates of the elemental Huygens source \underline{r}_0 and the coordinates of the field point \underline{r} through,

$$r' = |\underline{r} - \underline{r}_0|. \quad (3)$$

ω is the angular frequency and is related to the frequency f by $\omega = 2\pi f$; k_0 is the free space propagation constant and is related to the wavelength by $k_0 = 2\pi/\lambda$; \underline{n} is the outward pointing unit normal and, respectively; ϵ and μ are the permittivity and permeability of the medium through which the fields are propagating. In general, these are complex tensors that are a function of the field strength; however, here it is assumed that the region of space under consideration is free space comprising a homogeneous isotropic linear dielectric medium, and thus ϵ and μ can be approximated by real constants. j is the imaginary unit, and ∇_0 is the differential vector operator expressed in the source coordinate system. The geometry of this statement of the Kirchhoff-Huygens formula can be found illustrated in its conventional form in Figure 1.

Expanding $\nabla_0 \psi$ obtains [17]

$$\nabla_0 \psi = \left(jk_0 + \frac{1}{r'} \right) \hat{\underline{r}}' \psi. \quad (4)$$

Thus, the general vector Kirchhoff-Huygens formula can be expressed as [15]

$$\begin{aligned} \underline{E}_p = \frac{1}{4\pi} \int_S & - \left[j\omega\mu(\underline{n} \times \underline{H}) + \{(\underline{n} \times \underline{E}) \times \hat{\underline{r}}' + (\underline{n} \cdot \underline{E})\hat{\underline{r}}'\} \right. \\ & \left. \times \left(jk_0 + \frac{1}{r'} \right) \right] \times \frac{e^{-jk_0 r'}}{r'} ds. \end{aligned} \quad (5)$$

These expressions yield the vector electric field function from an integral of the electric and magnetic fields over the closed surface S where dS is an elemental portion of the that surface. Equivalent expressions can be obtained for the magnetic field [16–18]. These expressions are amenable for evaluating the field at any point in space outside of S and as such can be used to create near- and far-field simulations alike. The use of these expressions enables commercially available full-wave three-dimensional CEM simulation tools to be used to solve the fields around some, comparatively small tractable, radiating structure whereupon the Kirchhoff-Huygens method can be used to calculate the fields resulting from this radiator throughout a much larger problem space. In this way, measurement simulations of great accuracy can be produced comparatively simply and easily using essentially rigorous, but computationally intensive, near-field solvers.

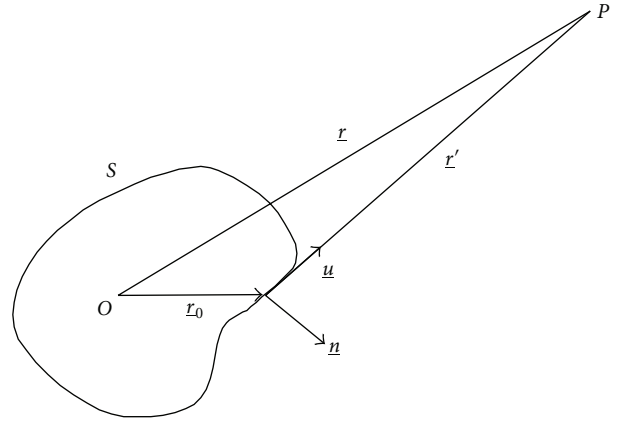


FIGURE 1: Geometry of Kirchhoff-Huygens formula, that is, (5), for the propagation of electromagnetic fields from Huygens surface S to point P .

Typically, when using (5) to compute the far-field pattern of an antenna from knowledge of the corresponding near-fields, the vector \underline{r} would be chosen so that the evaluation of the integral would produce the antenna diagram for a specified angular direction, as for example,

$$\begin{aligned} \hat{\underline{r}} = \sin(Az) \cos(El) \hat{\underline{e}}_x + \sin(El) \hat{\underline{e}}_y \\ + \cos(Az) \cos(El) \hat{\underline{e}}_z. \end{aligned} \quad (6)$$

Here, Az and El are the azimuth and elevation angles, respectively, and describe a conventional azimuth over elevation spherical positioning system [17, 19]. However, when simulating an antenna measurement facility, it is perhaps simpler to rotate the AUT, that is, the closed Huygens surface, using an isometric rotation and then to evaluate the far fields in a single direction, which more closely mimics the antenna measurement process and allows chamber scatterer to be introduced into the model in a direct way. In this case, \underline{r} would be held fixed for all measurement angles such that

$$\hat{\underline{r}} = 1 \hat{\underline{e}}_z. \quad (7)$$

Such isometric rotations are easily implemented using transformation matrices to rotate the fields and coordinates. Transformation matrices are matrices that post-multiply a column point vector to produce a new column point vector. A series of transformation matrices may be concatenated into a single matrix using matrix multiplication. A transformation matrix may represent each of the operations of translation, scaling, and rotation. However, if A is a three by three orthogonal, normalised square matrix, it may be used to specify an isometric rotation that can be used to relate two frames of reference, that is, two coordinate systems. Here, an isometric rotation is taken to mean a transformation in which the distance between any two points on an object remain invariant under the transformation. Any number of angular definitions for describing the relationship between the two coordinate systems exists. However, if the angles azimuth and elevation are used, where the rotations are applied in this order, we may write that a point in one frame

of reference can be specified in terms of a point in the other frame of reference as [17, 19]

$$\begin{bmatrix} u' \\ v' \\ w' \end{bmatrix} = [A] \cdot \begin{bmatrix} u \\ v \\ w \end{bmatrix}. \quad (8)$$

Here primed coordinates are used to denote the rotated frame of reference. In this case, in order that a far-field system comprising an azimuth over elevation positioning system is utilised, then A can be constructed by applying a rotation of elevation about the positive x -axis and a negative azimuth rotation about the positive y -axis where the rotations are applied in this order [17, 19]. Thus, by fixing $\hat{r} = 1\hat{e}_z$ and using (8) to rotate the electric and magnetic fields, the position vector \underline{r}_0 , the unit surface normal, and the AUT can be positioned within the range as though they were installed on a conventional azimuth over elevation positioning system. As a central constituent of the MARS measurement process is to offset the AUT from the centre of rotation, this can be easily incorporated within the simulation by applying an offset to the Cartesian components of the position vector that determines the location of the radiating Huygens surface. This translation is applied prior to applying the aforementioned rotation. Once evaluated using the Kirchhoff-Huygens method, the resulting far-fields can be resolved from the range coordinate system back onto the antenna coordinate system by applying the inverse rotation to the far electric (and magnetic) fields where the results have been found to be in agreement with those produced using conventional processing. Crucially, when introducing a given scatterer into the range simulation, the position and orientation of the scatterer is by definition specified in the range coordinate system and will therefore be fixed, irrespective of the particular far-field antenna pattern angle being computed. Thus, working in terms of the range coordinate system as outlined above significantly simplifies the computational processing.

The inclusion of an arbitrarily located and shaped perfectly conducting (i.e., worst case) scattering object can be introduced by using the Kirchhoff-Huygens field propagation method described above together with the generalised law of reflection. By definition, an elemental Huygens source is considered to be infinitesimally small, and so it will radiate a spherical wave. However, as the observation point on the reflecting plate is finitely far removed from the source, that is, more than a few wavelengths away, the reflecting plate will be in the far field of the elemental Huygens source. Locally therefore, at the observation point, the field will be of the form of a TEM plane wave propagating in the direction \underline{r}' . As the field is a local plane wave and assuming that the reflecting surface is locally, planar and is made from a perfectly conducting (PEC) material, the normal electric field component will be unchanged upon reflection. Thus, if a homogeneous plane wave is incident on a perfect electrical conducting (PEC) flat surface of infinite extent, the reflected elemental electric field constitutes a similar plane wave and

the reflected field can be obtained from the incident field using [18]

$$\underline{E}_r = 2(\hat{n} \cdot \underline{E}_i)\hat{n} - \underline{E}_i. \quad (9)$$

The law of reflection states that the angle of incidence equals the angle of reflection. Thus, when expressed mathematically this becomes,

$$\theta = \arccos(\hat{n} \cdot \hat{\underline{u}}_i) = \arccos(\hat{n} \cdot \hat{\underline{u}}_r). \quad (10)$$

Thus it is possible to write the general statement of reflection as [18],

$$\hat{\underline{u}}_r = \hat{\underline{u}}_i - 2(\hat{n} \cdot \hat{\underline{u}}_i)\hat{n}. \quad (11)$$

Here, $\hat{\underline{u}}_i$ denotes the direction of propagation of the incident plane wave, and $\hat{\underline{u}}_r$ represents the direction of propagation of the reflected, specular plane wave. This can be taken to represent the general form of the law of reflection with the scattered field being a plane wave as the material is assumed to be infinite in extent in the tangential direction, and the material properties do not vary across this surface. As the reflected elemental electric field correspond to a plane wave propagating in the direction $\hat{\underline{u}}_r$, the elemental magnetic field can be obtained from the elemental electric field using the TEM, that is, plane wave condition thus [17, 18]

$$d\underline{H}_r = \frac{1}{Z_0} \hat{\underline{u}}_r \times \underline{E}_r ds. \quad (12)$$

Here, Z_0 is the plane wave impedance, or characteristic impedance, of free space where $Z_0 = c\mu_0$. The total reflected electric and magnetic fields at each point on the surface of the reflector can be obtained by summing all of the contributions from the many elemental Huygens sources infinitely radiated from S . The far scattered field can again be obtained using the Kirchhoff-Huygens method by integrating over the surface of the reflector and thereby evaluating the far scattered fields. The total measured far field for a particular pattern angle can be obtained by taking the linear superposition of the direct and scattered fields where, in agreement with theory, the remote source antenna is assumed to be an infinitesimal Hertzian dipole. As a quasifar-field measurement is being simulated, probe pattern effects are unimportant in this analysis providing that the range length is sufficiently large to insure that the pattern of the far-field range illuminator is essentially constant across the AUT during the measurement [20]. Thus, by following this process, a simulation of a typical MARS type far-field measurement can be created with almost complete freedom to choose the AUT, the measurement geometry, and the location of the scattering object in order to test the existing far-field MARS technique. Far-field predictions obtained from this simulation technique together with results of the far-field MARS processing can be found presented within the following sections.

3. Results

In order that the F-MARS measurement and postprocessing technique could be further verified, a far-field measurement

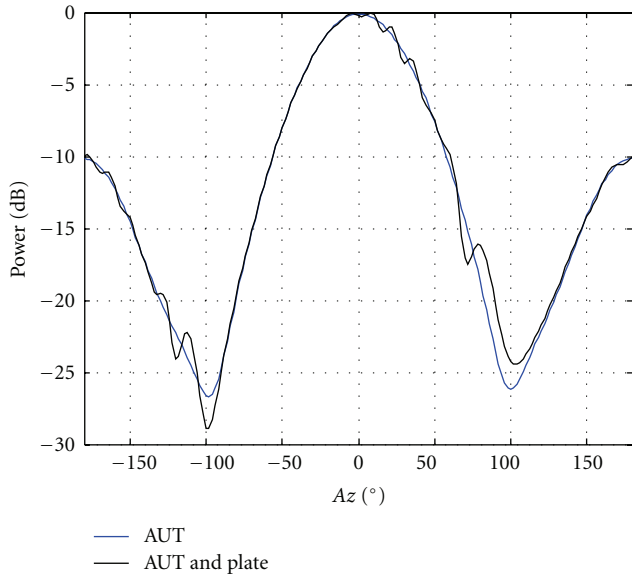


FIGURE 2: Far-field amplitude pattern of OEWG with and without plate. AUT offset = 10 cm.

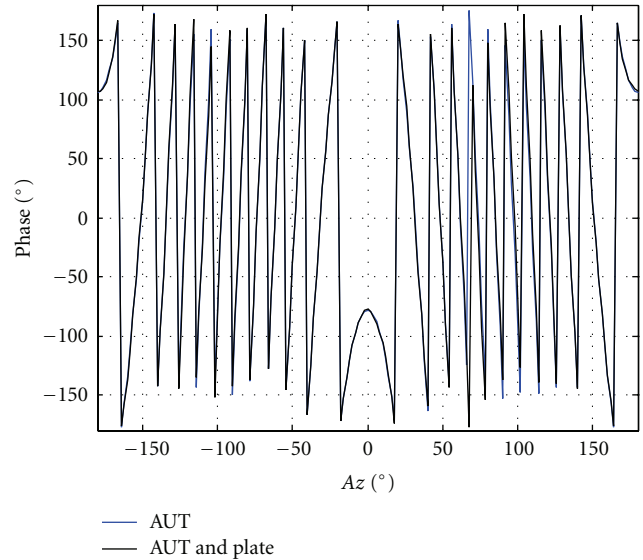


FIGURE 3: Far-field phase pattern of OEWG with and without plate. AUT offset = 10 cm.

was simulated that recreated a typical F-MARS configuration. A commercially available three-dimensional full-wave CEM solver was used to simulate the near fields radiated by a WR90 open-ended rectangular waveguide (OEWG) section that was excited by a TE₁₀ mode. The Cartesian components of the electric and magnetic fields were obtained at 10 GHz and were specified over the surface of an ellipsoid that tightly bounded the radiating aperture. The maximum radial extent of this ellipsoid when displaced from the origin was 0.08 m. The aperture of the OEWG section was displaced from the origin of the range measurement coordinate system, that is, the centre of rotation, by 0.1 m in the AUT z-axis, which was specified as being at a normal to the waveguide aperture plane. A square reflecting plate of side length 0.3 m was introduced into the simulation located with its centre at $x = -0.1$ m, $y = 0$ m, and $z = 1.0$ m with its unit normal directed in the positive x -axis and the sides of the plate being parallel with the y - and z -axes. This configuration closely mimicked the experimental arrangement that had previously been used to verify the F-MARS technique, compare [14, 15]. The physical-optics-based simulation was then used to obtain the far-electric field great circle azimuth cut with a range length of 200 m which placed the AUT in the far field for all of the simulations. The results of this simulation can be found presented in Figure 2, which contains the amplitude antenna diagram plotted together with the equivalent ideal far-field pattern (i.e., the far-field pattern of antenna in the absence of the reflecting flat plate). Figure 3 contains an equivalent plot that shows the far-field great circle phase pattern.

Typically, an antenna is installed within a near, or far-field facility such that it is displaced in space as little as possible during the course of a measurement. As range multipath tends to disturb the fields illuminating the test antenna, the purpose of this strategy is to ensure that the field illuminating the test antenna changes as little as possible during the course of the acquisition, thereby minimising the impact of

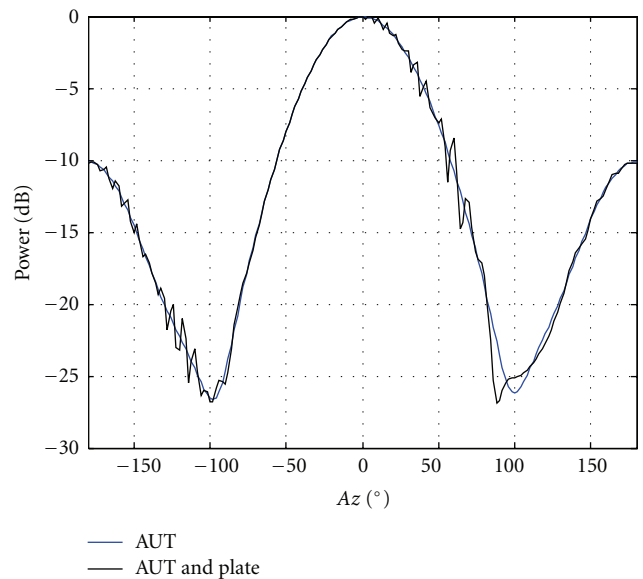


FIGURE 4: Far-field amplitude pattern of OEWG with and without plate. AUT offset = 30 cm.

scattering on the measurements. However, as modelled above, the MARS measurement technique deliberately displaces the AUT away from the centre of rotation. This has the effect of making the differences in the illuminating field far more pronounced than would otherwise be the case, and it is this greater differentiation that makes the identification of scattered fields and their subsequent removal viable. In order that this effect could be further investigated, the simulation was repeated with an AUT offset of 0.3 m and 0.5 m. The results of these simulations can be found presented in Figures 4 and 5 and Figures 6 and 7, respectively. It is well known that as an antenna is moved away from the centre of rotation

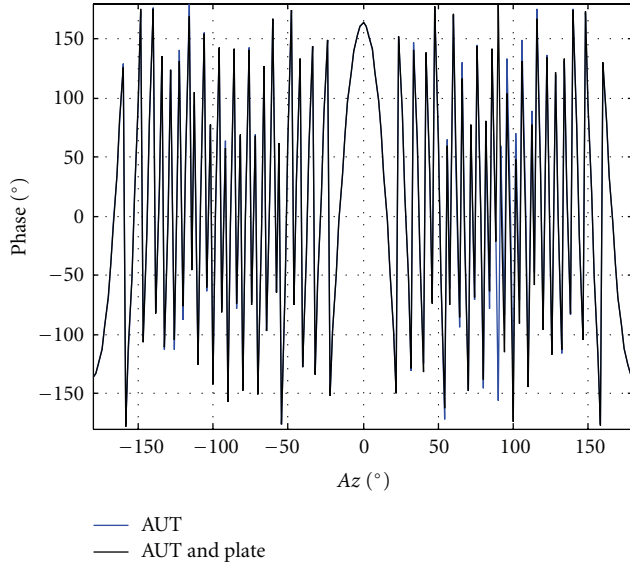


FIGURE 5: Far-field phase pattern of OEWG with and without plate. AUT offset = 30 cm.

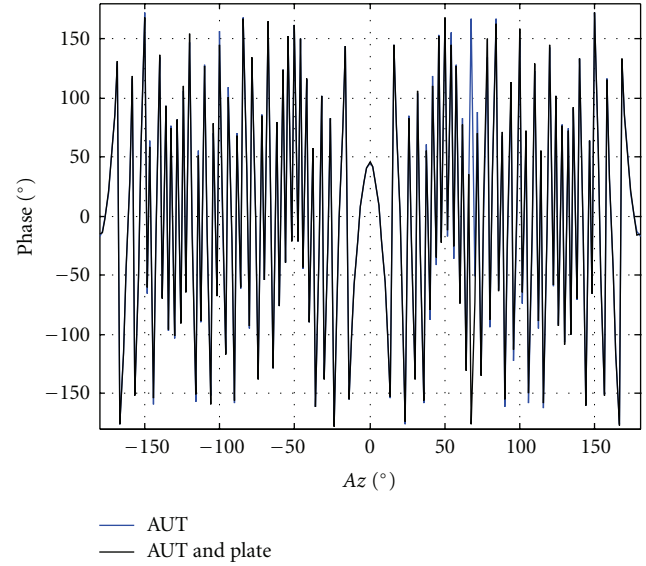


FIGURE 7: Far-field phase pattern of OEWG with and without plate. AUT offset = 50 cm.

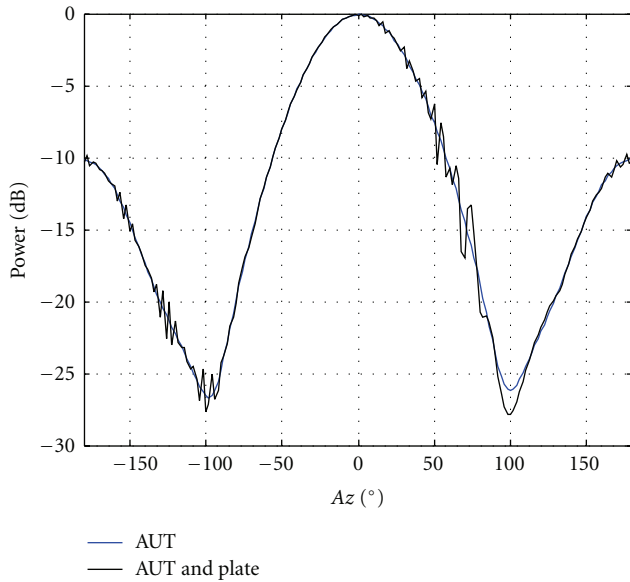


FIGURE 6: Far-field amplitude pattern of OEWG with and without plate. AUT offset = 50 cm.

of the measurement system, in the true far field, the phase function of the AUT changes such that [17]

$$\underline{E}_t(r \rightarrow \infty, \theta, \phi) = \underline{E}(r \rightarrow \infty, \theta, \phi) e^{jk_0 \cdot \underline{r}}. \quad (13)$$

Here, \underline{r} denotes the displacement vector between the centre of the measurement coordinate system and the centre of the current sources, for example, the aperture of the AUT. If a displacement is made purely in the AUT z -axis, this reduces to

$$\underline{E}_t(r \rightarrow \infty, \theta, \phi) = \underline{E}(r \rightarrow \infty, \theta, \phi) e^{jk_0 \cos \theta \Delta z}. \quad (14)$$

Here Δz was 0.1, 0.3, and 0.5 m, respectively for the three simulations presented above. As can be seen from the inspection of Figures 3, 5, and 7 it is clear that a parabolic phase function has been introduced onto the far-field patterns. This feature was not introduced explicitly within the simulation and is an artefact of the geometry of the simulation and the due regard to the phase, that is, inherent within the Kirchhoff-Huygens formula.

The effects of the reflecting plate can be clearly seen on the far-field great circle cuts with disturbances evident primarily around the $0^\circ < \theta < 90^\circ$ angular region with some scattering also being evident on the back lobes of the antenna. This ripple is a result of the direct and indirect (scattered) signals adding in and out of phase as the AUT is progressively rotated. Clearly, the further the AUT is displaced across the range quiet zone during the measurement simulation the more rapidly the signals will beat in and out of phase as the difference in the electrical paths becomes larger and the higher the angular frequency of the resulting ripple will be observed on the measured antenna pattern. Again, this is in agreement with what is generally observed when taking an F-MARS measurement, compare [15, Figures 2, 4, and 6].

It is well known that the electromagnetic fields outside an arbitrary test antenna radiating into free space can be expanded into a set of orthogonal cylindrical mode coefficients (CMC) and that these modes and coefficients can then be used to obtain the electric and magnetic fields everywhere in space outside of a conceptual cylindrical surface which encloses the radiator, that is, which encloses the majority of the current sources [7–9, 14, 15]. The success of F-MARS processing is predicated upon the ability to deduce these CMCs and, on the characteristics of the distribution of those modes once they have been obtained. Thus, in order that this could be investigated in detail, far-field antenna pattern data was simulated for the AUT with

the aperture located at several different offsets from the origin of the measurement coordinate system to illustrate the effect of the offset on the equivalent CMC, and thus on the MARS correction itself. Figures 8, 10, and 12 show the ideal modelled far-field patterns (red trace) plotted together with the scattering contaminated far-field equivalent plots (blue trace) and the F-MARS processed pattern (black trace) for the cases where the AUT was displaced by 10 cm, 30 cm, and 50 cm. Here, it is clear that as the displacement becomes larger, the agreement between the ideal pattern and the F-MARS processed pattern is in increasingly encouraging agreement. Figures 9, 11, and 13 contain the equivalent CMC plots with (blue trace) and without (red trace) MARS filtering. It is clear from the inspection of these plots that the displacement of the spectral peak of the scattered fields to increasingly higher order modes with increasing AUT offset corresponds to the change in the appearance of the measured far-field patterns, compare [15]. Note that as the offset is increased, the spectral peak representing multipath energy tends to move further away (towards higher order mode numbers) from the AUT spectral peak (shown in the centre of the plot at $n = 0$). In addition, note that the multipath spectrum becomes wider as the offset is increased. It can be seen that in the small 10 cm offset case, the multipath and AUT modes are mostly coincident, and thus MARS processing provides less immunity to range multipath. In the case where the offset is larger, that is, 30 cm and 50 cm it is clear that the MARS provides far great immunity from multipath as the CMCs that are associated with field reflected from the reflecting plate can now be clearly resolved from the antenna coefficients, which are closely distributed about the lowest order mode. Here, MARS processing provides a clear view of the AUT pattern throughout the range of angles where range multipath had the greatest effect. These observations are in agreement with what has been noted while taking actual range measurements [15].

The minimum conceptual maximum radial extent (MRE) which is used by the MARS cylindrical mode coefficient filter function to exclude scattering from the measurements must be sufficiently large to create a conceptual cylinder that is coaxial with the rotation axis and which encloses the majority of the current sources. As the AUT was a low gain, OEWG inspection of the near-field simulation showed that significant currents flowed down the exterior surfaces of the waveguide walls. For this reason, this antenna is not a true aperture-type antenna as the excitation current distribution extends in all three Cartesian axes. These currents contribute to the far-field pattern, particularly to the wide angle sidelobes, and therefore should not be excluded from the measurement by the F-MARS processing. Thus, during this processing a conservative radius of 8 cm was employed (which was far larger than suggested by the maximum diagonal dimension of the aperture, which was 2.5 cm) as this retained many more of these exterior fields. Thus far, only rectangular brick-wall band-pass filter functions have been used to filter the CMCs when applying far-field MARS. As the exclusion of modes is based upon a consideration of the physical (and therefore electrical) extent of the source, this technique will preserve the integrity of the

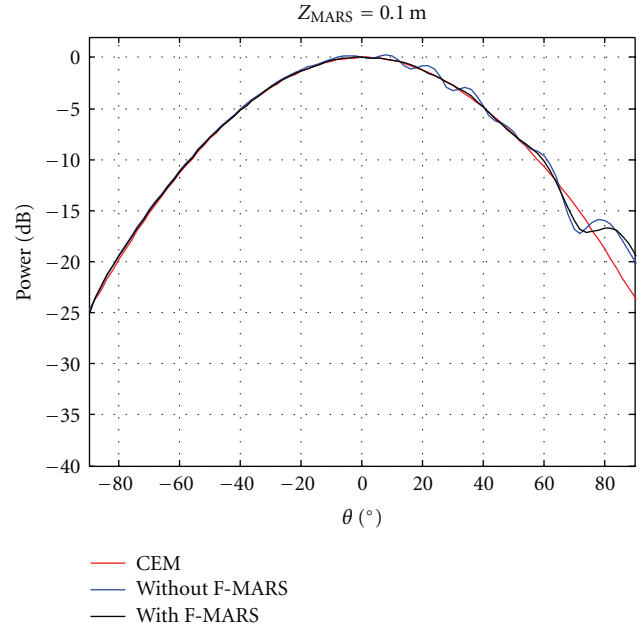


FIGURE 8: Far-field cut with and without MARS processing. Displacement of 10 cm.

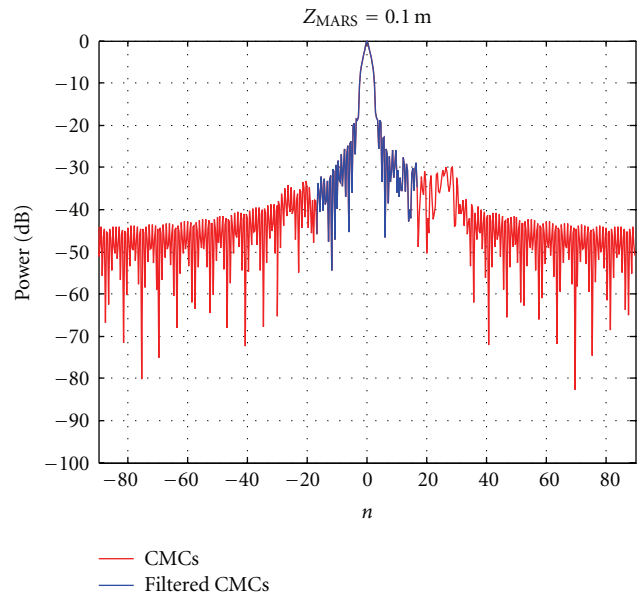


FIGURE 9: Equivalent CMCs with AUT displacement of 10 cm.

underlying pattern function. In an attempt to minimise the likelihood of introducing transform leakage, which would result in a spurious ripple being superimposed on the F-MARS filtered far-field pattern, since this is a second-order effect, and as the ideal antenna pattern was known a priori from the CEM simulation for the first time, these effects could be assessed critically.

As there are almost infinite number of possible windowing functions that could be examined, it was decided that merely establishing the effectiveness that this approach has in enabling a tighter band-pass filter functions to be employed

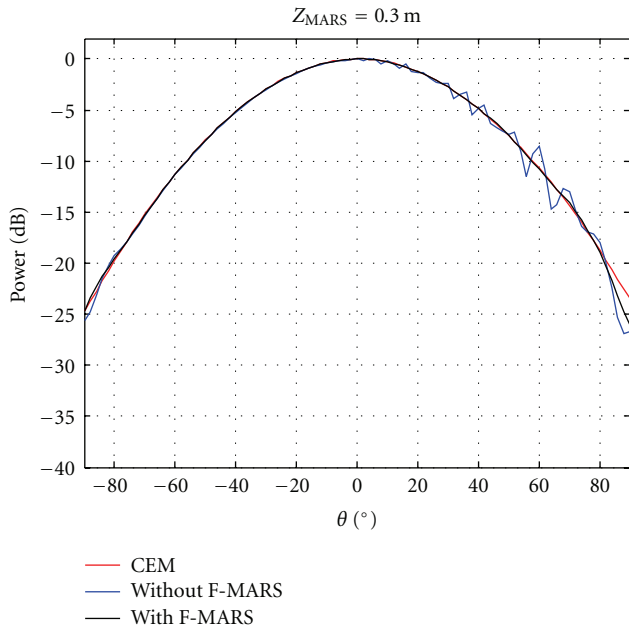


FIGURE 10: Far-field cut with and without MARS processing. Displacement of 30 cm.

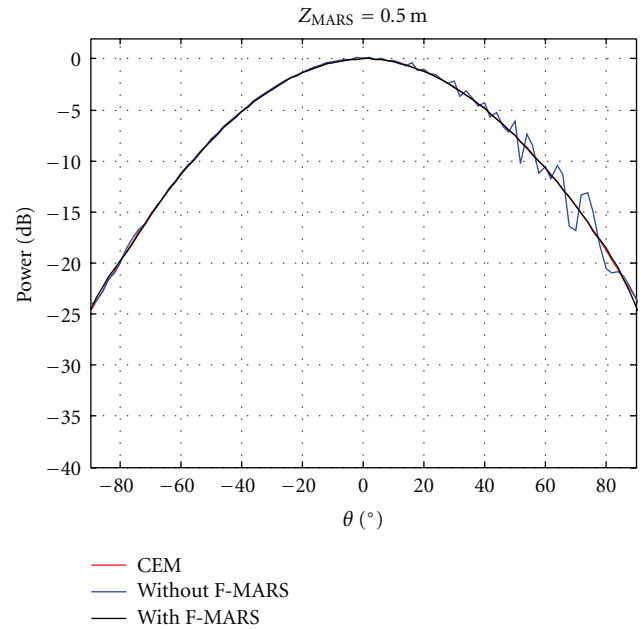


FIGURE 12: Far-field cut with and without MARS processing. Displacement of 50 cm.

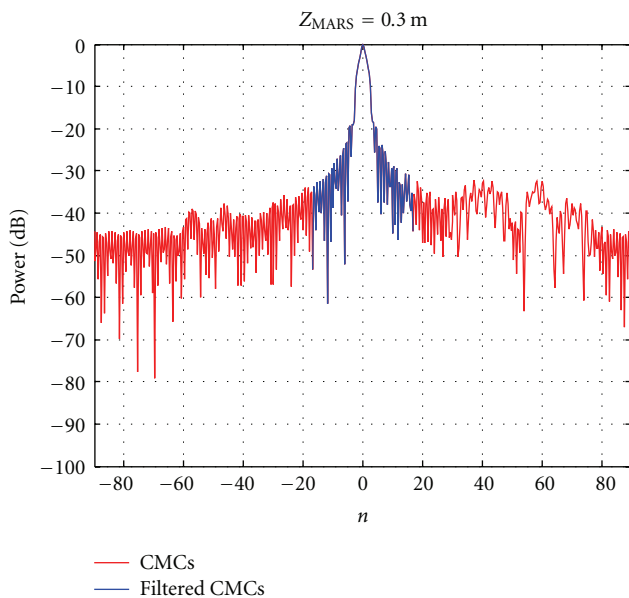


FIGURE 11: Equivalent CMCs with AUT displacement of 30 cm.

was thought sufficient to justify a more exhaustive investigation at a future time. Figure 14 contains an equivalent CMC plot to that shown in Figure 11, only here, a cosine squared windowing function has been applied to filter out higher order modes whilst attempting to match the function and as many of its derivatives to zero at the boundary of the transform domain so as to minimise ripple in the transformed domain. As can be seen from the inspection of Figure 15, the ideal CEM pattern and the F-MARS filtered pattern are in very encouraging agreement. Furthermore, the degree of agreement is clearly an improvement over the

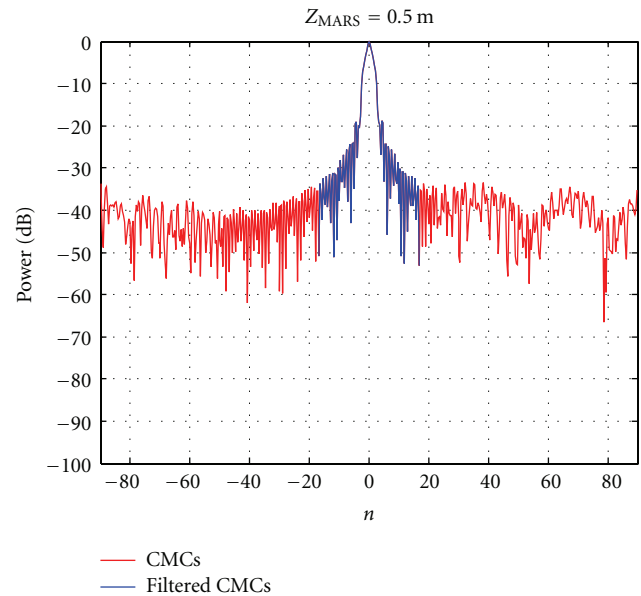


FIGURE 13: Equivalent CMCs with AUT displacement of 50 cm.

previous case, compare Figure 10, where a rectangular filter function had been employed. This demonstrates the validity of this future line of research.

4. Summary and Conclusions

A new physical-optics-based antenna measurement model that can be used to investigate the impact of various error terms within the facility level error budget of a given spherical near- or far-field range has been introduced. A traditional objection to the implementation of physical-optics-based software modelling tools has been the long

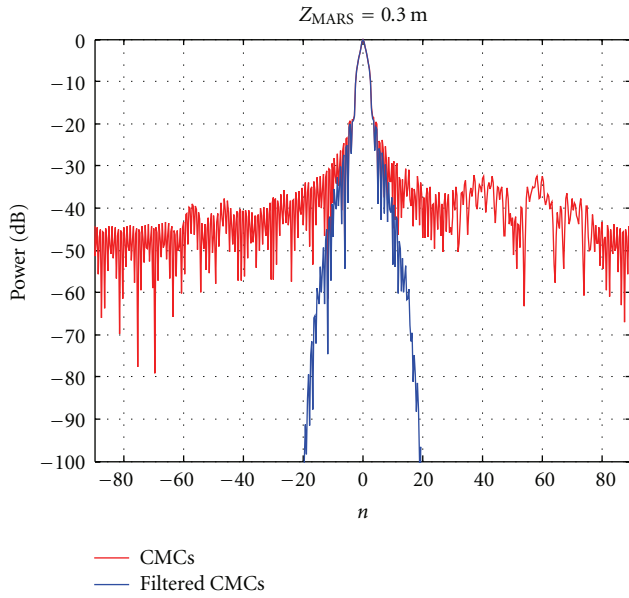


FIGURE 14: Equivalent CMCs with AUT displacement of 30 cm. Cosine squared filter applied.

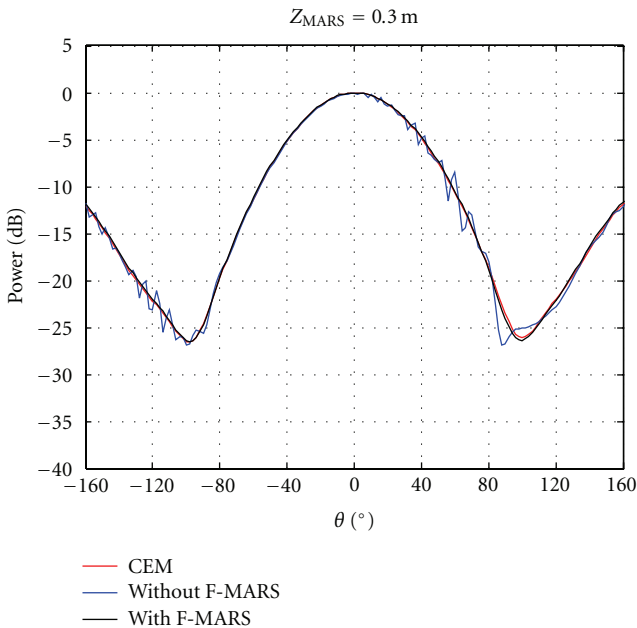


FIGURE 15: Far-field cut with and without MARS processing. Displacement of 30 cm.

run times; however, with the advent of high-CPU-power computers this objection has been largely nullified. This tool has been used to model a conventional F-MARS measurement whereupon similar phenomena have been observed in the CEM model as seen in actual range measurements. Specifically these are as follows: (1) parabolic phase function is imposed on far-field phase pattern that is dependent upon displacement of AUT from measurement origin, (2) the effects of scattering on a far-field pattern depend upon the AUT displacement with greater displacement resulting

in higher angular frequency ripple on the far-field pattern, (3) CMCs resulting from scattering are displaced to higher order modes AUT modes are displaced to lower order modes once the AUT is mathematically displaced back to the origin of the measurement coordinate system, (4) the amount of separation between mode distributions associated with scattering and those associated with the AUT increases as the displacement increases, and (5) F-MARS is capable of effectively suppressing scattering providing that the magnitude of the displacement is sufficiently large.

Thus, the CEM model has been able to provide further confirmation of the effectiveness of the far-field MARS technique, and hence F-MARS processing can be used with a very high degree of confidence since all the steps in the measurement and analysis are consistent with the well-established principles of the standard cylindrical near-field theory and measurement technique, and all comparisons to date have proved to be overwhelmingly positive. The offset of the AUT and the resulting smaller data point spacing are valid if the data point spacing satisfies the sampling criteria. The translation of the far-field pattern to the origin with the application of a differential phase change is rigorous. The selection of the mode cutoff for the translated pattern is based on the physical dimensions of the AUT and its translated location.

Acknowledgment

The authors extend their gratitude to the reviewers for their very detailed and constructive comments and suggestions.

References

- [1] A. C. Newell, "Error analysis techniques for planar near-field measurements," *IEEE Transactions on Antennas and Propagation*, vol. 36, no. 6, pp. 754–768, 1988.
- [2] G. E. Evans, *Antenna Measurement Techniques*, Artech House, 1990.
- [3] G.E. Hindman and A.C. Newell, "Spherical near-field self-comparison measurements," in *26th AMTA Annual Meeting & Symposium*, Atlanta, Ga, USA, October 2004.
- [4] G. E. Hindman and A. C. Newell, "Reflection Suppression in a large spherical near-field range," in *27th AMTA Annual Meeting & Symposium*, Newport, RI, USA, October 2005.
- [5] G. E. Hindman and A. C. Newell, "Reflection suppression to improve anechoic chamber performance," in *AMTA Europe*, Munich, Germany, March 2006.
- [6] D. W. Hess, "The IsoFilterTM technique: extension to transverse offsets," in *AMTA Symposium*, Austin, Tex, USA, 2006.
- [7] S. F. Gregson, A. C. Newell, and G. E. Hindman, "Reflection suppression in cylindrical near-field antenna measurement systems – cylindrical MARS," in *31st AMTA Annual Meeting & Symposium*, Salt Lake City, Utah, USA, November 2009.
- [8] S. F. Gregson, A. C. Newell, and G. E. Hindman, "Reflection suppression in cylindrical near-field measurements of electrically small antennas," in *Loughborough Antennas and Propagation Conference (LAPC '09)*, pp. 393–396, November 2009.
- [9] S. F. Gregson, A. C. Newell, G. E. Hindman, and M. J. Carey, "Advances in cylindrical Mathematical Absorber Reflection

- Suppression,” in *4th European Conference on Antennas and Propagation (EuCAP '10)*, April 2010.
- [10] S. F. Gregson, A. C. Newell, G. E. Hindman, and M. J. Carey, *Extension of the Mathematical Absorber Reflection Suppression Technique to the Planar Near-Field Geometry*, AMTA, Atlanta, Ga, USA, 2010.
- [11] S. F. Gregson, A. C. Newell, G. E. Hindman, and M. J. Carey, “Application of Mathematical Absorber Reflection suppression to planar near-field antenna measurements,” in *5th European Conference on Antennas and Propagation (EUCAP '11)*, pp. 3412–3416, April 2011.
- [12] S. F. Gregson, A. C. Newell, and G. E. Hindman, *Advances in Planar Mathematical Absorber Reflection Suppression*, AMTA, Denver, Colo, USA, 2011.
- [13] O. M. Bucci, G. D’Elia, and M. D. Migliore, “A general and effective clutter filtering strategy in near-field antenna measurements,” *IEE Proceedings: Microwaves, Antennas and Propagation*, vol. 151, no. 3, pp. 227–235, 2004.
- [14] S. F. Gregson, J. Dupuy, C. G. Parini, A.C. Newell, and G. E. Hindman, “Application of mathematical absorber reflection suppression to far-field antenna testing,” in *Loughborough Antennas & Propagation Conference (LAPC '11)*, Loughborough, UK, November 2011.
- [15] S. F. Gregson, B. M. Williams, G. F. Masters, A. C. Newell, and G. E. Hindman, *Application of Mathematical Absorber Reflection Suppression to Direct Far-Field Antenna Range Measurements*, AMTA, Denver, Colo, USA, 2011.
- [16] S. Silver, *Microwave Antenna Theory and Design*, McGraw, New York, NY, USA, 1st edition, 1947.
- [17] S. F. Gregson, J. McCormick, and C. G. Parini, *Principles of Planar Near-Field Antenna Measurements*, The Institution of Engineering and Technology, UK, 2007.
- [18] R. H. Clarke and J. Brown, *Diffraction Theory and Antennas*, Ellis Horwood, 1980.
- [19] G. F. Masters and S. F. Gregson, “Coordinate system plotting for antenna measurements,” in *AMTA Annual Meeting & Symposium*, St. Louis, Mo, USA, 2007.
- [20] J. E. Hansen, Ed., *Spherical Near-Field Antenna Measurements*, IEE, UK, 1988.

Research Article

An Innovative Direct NF-FF Transformation Technique with Helicoidal Scanning

**Francesco D'Agostino, Flaminio Ferrara, Claudio Gennarelli,
Rocco Guerriero, and Massimo Migliozi**

*Department of Electronic and Computer Engineering, University of Salerno, via Ponte Don Melillo,
I-84084 Fisciano (Salerno), Italy*

Correspondence should be addressed to Claudio Gennarelli, gennar@diie.unisa.it

Received 14 September 2011; Accepted 16 February 2012

Academic Editor: Lars Jacob Foged

Copyright © 2012 Francesco D'Agostino et al. This is an open access article distributed under the Creative Commons Attribution License, which permits unrestricted use, distribution, and reproduction in any medium, provided the original work is properly cited.

A direct near-field-far-field transformation with helicoidal scanning is developed. It is based on the nonredundant sampling representation of electromagnetic fields and uses a spherical antenna modelling to determine the number of helix turns. Moreover, the number of voltage samples on each of them is fixed by the maximum transverse dimension of the antenna, both to simplify the mechanical scanning and to reduce the computational effort. This technique allows the evaluation of the antenna far field directly from a minimum set of near-field data without interpolating them. Although the number of near-field data employed by the developed technique is slightly increased with respect to that required by rigorously applying the nonredundant sampling representation on the helix, it is still remarkably smaller than that needed by the standard near-field-far-field transformation with cylindrical scanning. The effectiveness of the technique is assessed by numerical and experimental results.

1. Introduction

The techniques for the reconstruction of antenna radiation patterns from near-field (NF) measurements have been widely investigated and used for applications ranging from cellular phone antennas to large-phased arrays and complex multibeam communication satellite antennas [1–5]. They have been proved to be efficient and attractive alternatives to conventional far-field (FF) and compact range measurements. In addition, the NF measurements have the advantage to be performed in a controlled environment, such as an anechoic chamber, thus overcoming those drawbacks due to weather conditions, electromagnetic (EM) interference, and so forth, which cannot be eliminated in FF outdoor measurements. In the recent years, the researchers interested in the antenna NF measurements and in the related NF-FF transformation techniques have spent many efforts to reduce the time required for the acquisition of the NF data. As a matter of fact, this time is currently very much greater than that needed to carry out the corresponding NF-FF transformation. In this context, a significant reduction of

the number of required NF data (and, as a consequence, of the measurement time) has been obtained for all the conventional scannings [6–14] by applying the theoretical results on the nonredundant sampling representations of EM fields [15]. In particular, optimal sampling interpolation (OSI) formulas of central type [16] have been employed to efficiently recover the data required by the corresponding NF-FF transformation from the knowledge of the acquired nonredundant ones.

A more convenient way of reducing the measurement time is the use of innovative spiral scanning techniques. They have been implemented, as suggested by Yaccarino et al. in [17], by means of continuous and synchronized movements of the positioning systems of the probe and antenna under test (AUT), and are based on the aforementioned nonredundant sampling representations and OSI expansions. In particular, NF-FF transformations using the helicoidal scanning [18–20], the planar [20, 21] and spherical [20, 22] spiral scannings have been developed, by considering the AUT as enclosed in the smallest sphere able to contain it.

Then, more effective AUT modellings, that allow a further reduction of the required NF data in the case of elongated or quasiplanar antennas, have been adopted in [23–27] by properly employing the unified theory of spiral scans for nonspherical antennas [28]. These modellings allow one to consider measurement cylinders (planes) with a radius (distance) smaller than one half the AUT maximum size, thus reducing the error related to the truncation of the scanning zone. In all the cases, the NF data needed by the corresponding NF-FF transformation can be reconstructed by interpolating the nonredundant ones acquired on the spiral.

A probe uncompensated NF-FF transformation technique with planar spiral scanning has been proposed in [29], to efficiently evaluate the antenna far field directly from the acquired NF data. It uses the convolution property of the radiation integral and the fast Fourier transform (FFT) algorithm to determine the antenna far-field pattern without requiring any interpolation step. However, since such an approach does not exploit the nonredundant representations of EM fields, it needs a useless large amount of measurements. This comment holds also for the NF-FF transformation technique with helicoidal scanning proposed by the same authors in [30]. On the contrary, a direct NF-FF transformation with cylindrical scanning, based on the aforementioned nonredundant sampling representations, has been developed in [10]. It allows the evaluation of the antenna far field in any cut plane directly from the nonredundant NF data without interpolating them.

In this paper, the direct NF-FF transformation with cylindrical scanning [10] has been extended to the helicoidal one [18–20]. To this end, the approach in [10] has been reviewed in order to match the advantages of the direct cylindrical NF-FF transformation with those own of the fast helicoidal scanning. In particular, the number of helix turns is determined by the nonredundant sampling representation along a generatrix which makes use of the spherical AUT modelling, whereas the voltage samples on each of them is fixed by the AUT maximum transverse dimension.

2. Nonredundant Sampling Representations on a Cylinder from Helicoidal Samples

The nonredundant sampling representation of the probe voltage on a cylinder from NF data acquired along a helix, when adopting a spherical AUT modelling, is summarized in the following.

Let us consider a nondirective probe which scans a helix with constant angular step lying on a cylinder of radius d surrounding the AUT (see Figure 1) and adopt the spherical coordinate system (r, ϑ, φ) for denoting the observation point P in the NF region. Since the voltage V measured by this kind of probe has the same effective spatial bandwidth of the field [7], the theoretical results on the nonredundant representation of EM fields [15] can be applied to such a voltage. Accordingly, if the AUT is enclosed in a sphere of radius a (AUT ball) and the helix is described by a proper

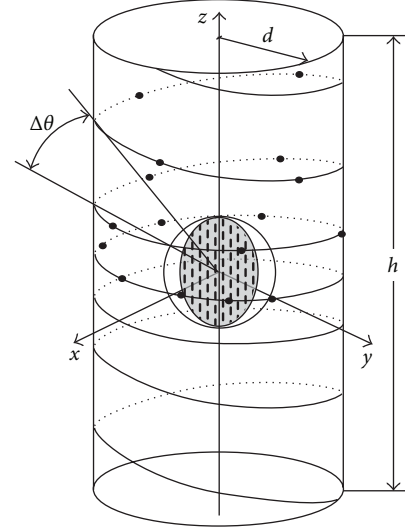


FIGURE 1: Helicoidal scanning.

analytical parameterization $\underline{r} = \underline{r}(\xi)$, the probe “reduced voltage”

$$\tilde{V}(\xi) = V(\xi)e^{j\gamma(\xi)} \quad (1)$$

can be closely approximated by a spatially band limited function [15], $\gamma(\xi)$ being a phase function to be determined. The related band limitation error becomes negligible as the bandwidth exceeds a critical value W_ξ [15], so that it can be effectively controlled by choosing a bandwidth equal to $\chi'W_\xi$, wherein the excess bandwidth factor χ' is slightly greater than unity for an electrically large AUT.

To obtain a sampling representation of the voltage on the cylinder from its nonredundant samples collected along a helix with constant angular step, it is necessary (a) to develop a nonredundant voltage representation on the helix; (b) to choose the helix step equal to the sample spacing needed to interpolate the voltage along a cylinder generatrix.

The parametric equations of the helix, when imposing its passage through a fixed point Q_0 of the generatrix at $\varphi = 0$, are $x = d \cos(\phi - \phi_i)$, $y = d \sin(\phi - \phi_i)$, $z = d \cot \theta$, where ϕ is the angular parameter describing the helix, ϕ_i is the value of ϕ at Q_0 , and $\theta = k\phi$. The parameter k is such that the angular step, determined by the consecutive intersections $Q(\phi)$ and $Q(\phi + 2\pi)$ with a generatrix, is $\Delta\theta = 2\pi k$. It is worth noting that the helix can be obtained by radially projecting on the measurement cylinder the spiral wrapping the AUT sphere with the same angular step.

As shown in [19, 20], a nonredundant sampling representation of the voltage on the helix can be obtained by using the following expressions for the optimal phase function and parameterization:

$$\gamma = \beta \int_0^r \sqrt{1 - \frac{a^2}{r'^2}} dr' = \beta \sqrt{r^2 - a^2} - \beta a \cos^{-1}\left(\frac{a}{r}\right), \quad (2)$$

$$\xi = \frac{\beta a}{W_\xi} \int_0^\phi \sqrt{k^2 + \sin^2 k\phi'} d\phi', \quad (3)$$

where β is the wavenumber.

Since the elevation step of the helix must be equal to the sample spacing required for the interpolation along a generatrix, then, according to [19, 20], $\Delta\theta = 2\pi/(2N'' + 1)$, with $N'' = \text{Int}(\chi N') + 1$ and $N' = \text{Int}(\chi' \beta a) + 1$, $\chi > 1$ being an oversampling factor controlling the truncation error [15, 16] and $\text{Int}(x)$ denoting the integer part of x . It can be easily verified that $k = 1/(2N'' + 1)$.

According to (3), ξ is proportional to the curvilinear abscissa along the spiral wrapping the sphere modelling the source. Since such a spiral is a closed curve, it is convenient to choose the bandwidth W_ξ such that ξ covers a 2π range when the whole curve on the sphere is described. As a consequence,

$$W_\xi = \frac{\beta a}{\pi} \int_0^{(2N''+1)\pi} \sqrt{k^2 + \sin^2 k\phi'} d\phi'. \quad (4)$$

According to these results, the OSI formula of central type to reconstruct the voltage at any point Q of the helix is [20]:

$$\tilde{V}(\xi) = \sum_{m=m_0-p+1}^{m_0+p} \tilde{V}(\xi_m) \Omega_M(\xi - \xi_m) D_{M''}(\xi - \xi_m), \quad (5)$$

where $m_0 = \text{Int}[(\xi - \xi(\phi_i))/\Delta\xi]$ is the index of the sample nearest (on the left) to Q , $2p$ is the number of retained samples $\tilde{V}(\xi_m)$, and

$$\xi_m = \xi(\phi_i) + m\Delta\xi = \xi(\phi_i) + \frac{2\pi m}{(2M'' + 1)} \quad (6)$$

with $M'' = \text{Int}(\chi M') + 1$ and $M' = \text{Int}(\chi' W_\xi) + 1$. Moreover,

$$D_{M''}(\xi) = \frac{\sin((2M'' + 1)\xi/2)}{(2M'' + 1) \sin(\xi/2)}, \quad (7)$$

$$\Omega_M(\xi) = \frac{T_M \left[-1 + 2 \left(\cos(\xi/2) / \cos(\bar{\xi}/2) \right)^2 \right]}{T_M \left[-1 + 2 / \cos^2(\bar{\xi}/2) \right]}$$

are the Dirichlet and Tschebyscheff sampling functions, wherein $T_M(\xi)$ is the Tschebyscheff polynomial of degree $M = M'' - M'$ and $\bar{\xi} = p\Delta\xi$.

The OSI formula (5) can be used to evaluate the ‘‘intermediate samples,’’ namely, the voltage values at the intersection points between the helix and the generatrix passing through the observation point P . Once these samples have been evaluated, the voltage at P can be reconstructed via the following OSI expansion:

$$\tilde{V}(\vartheta, \varphi) = \sum_{n=n_0-q+1}^{n_0+q} \tilde{V}(\vartheta_n) \Omega_N(\vartheta - \vartheta_n) D_{N''}(\vartheta - \vartheta_n), \quad (8)$$

where $N = N'' - N'$, $n_0 = \text{Int}[(\vartheta - \vartheta_0)/\Delta\vartheta]$, $2q$ is the number of the retained intermediate samples $\tilde{V}(\vartheta_n)$, and

$$\vartheta_n = \vartheta_n(\varphi) = \vartheta(\phi_i) + k\varphi + n\Delta\vartheta = \vartheta_0 + n\Delta\vartheta. \quad (9)$$

The described two-dimensional OSI algorithm can be properly applied to recover the NF data required by the NF-FF transformation technique [31] or [32].

3. Standard NF-FF Transformation with Cylindrical Scanning

For reader’s convenience, the key steps of the standard probe compensated NF-FF transformation technique with cylindrical scanning [31] are reported. According to such a technique, the modal coefficients a_ν and b_ν of the cylindrical wave expansion of the field radiated by the AUT are related to (i) the two-dimensional Fourier transforms I_ν^1 and I_ν^2 of the output voltage of the probe for two independent sets of measurements (the probe is rotated 90° about its longitudinal axis in the second set); (ii) the coefficients c_m, d_m , and c'_m, d'_m of the cylindrical wave expansion of the field radiated by the probe and the rotated probe, respectively, when used as transmitting antennas. The key relations are

$$a_\nu(\eta) = \frac{\beta^2}{\Lambda^2 \Delta_\nu(\eta)} \left[I_\nu^1(\eta) \sum_{m=-\infty}^{\infty} d'_m(-\eta) H_{\nu+m}^{(2)}(\Lambda d) - I_\nu^2(\eta) \sum_{m=-\infty}^{\infty} d_m(-\eta) H_{\nu+m}^{(2)}(\Lambda d) \right], \quad (10)$$

$$b_\nu(\eta) = \frac{\beta^2}{\Lambda^2 \Delta_\nu(\eta)} \left[I_\nu^2(\eta) \sum_{m=-\infty}^{\infty} c_m(-\eta) H_{\nu+m}^{(2)}(\Lambda d) - I_\nu^1(\eta) \sum_{m=-\infty}^{\infty} c'_m(-\eta) H_{\nu+m}^{(2)}(\Lambda d) \right],$$

$$I_\nu^{1,2}(\eta) = \int_{-\infty}^{\infty} \int_0^{2\pi} V^{1,2}(\varphi, z) e^{-j\nu\varphi} e^{j\eta z} d\varphi dz, \quad (11)$$

$$\Delta_\nu(\eta) = \sum_{m=-\infty}^{\infty} c_m(-\eta) H_{\nu+m}^{(2)}(\Lambda d) \times \sum_{m=-\infty}^{\infty} d'_m(-\eta) H_{\nu+m}^{(2)}(\Lambda d) - \sum_{m=-\infty}^{\infty} c'_m(-\eta) H_{\nu+m}^{(2)}(\Lambda d) \times \sum_{m=-\infty}^{\infty} d_m(-\eta) H_{\nu+m}^{(2)}(\Lambda d), \quad (12)$$

where $\Lambda = \sqrt{\beta^2 - \eta^2}$, $H_\nu^{(2)}(\cdot)$ is the Hankel function of second kind and order ν , and V^1, V^2 represent the output voltage of the probe and the rotated probe at the point of cylindrical coordinates (d, φ, z) .

Once the modal coefficients have been determined, the FF components of the electric field in the spherical coordinate system (R, Θ, Φ) , adopted to denote an observation point in the far-field region, can be evaluated by

$$\begin{aligned} E_{\Theta}(R, \Theta, \Phi) &= F_{\Theta}(\Theta, \Phi) \frac{e^{-j\beta R}}{R} \\ &= -j2\beta \frac{e^{-j\beta R}}{R} \sin \Theta \sum_{\nu=-\infty}^{\infty} j^{\nu} b_{\nu}(\beta \cos \Theta) e^{j\nu\Phi}, \\ E_{\Phi}(R, \Theta, \Phi) &= F_{\Phi}(\Theta, \Phi) \frac{e^{-j\beta R}}{R} \\ &= -2\beta \frac{e^{-j\beta R}}{R} \sin \Theta \sum_{\nu=-\infty}^{\infty} j^{\nu} a_{\nu}(\beta \cos \Theta) e^{j\nu\Phi}. \end{aligned} \quad (13)$$

4. Direct NF-FF Transformation Technique

The here proposed approach for evaluating the antenna FF pattern directly from the acquired helicoidal samples is described in the following. In particular, such a NF-FF transformation, unlike that developed in [18, 20], does not explicitly employ the OSI expansions (5) and (8), since there is no need to interpolate the nonredundant acquired data for reconstructing those needed by the classical ones [31, 32].

The starting point is the evaluation of the two-dimensional Fourier transforms of the probe output voltage in (11). By taking into account the OSI formula (8), we can rearrange the integrals (11) in the form:

$$\begin{aligned} I_{\nu}^{1,2}(\eta) &= \sum_{n \in N_r} \int_0^{2\pi} \left\{ \tilde{V}^{1,2}(\vartheta_n, \varphi) e^{-j\nu\varphi} \right. \\ &\quad \left. \times \int_{-\infty}^{\infty} D_{N''}(\vartheta(z) - \vartheta_n) Q(\vartheta(z) - \vartheta_n) e^{-j\nu(z)} e^{j\eta z} dz \right\} d\varphi, \end{aligned} \quad (14)$$

where N_r is the set of indexes of all considered NF turns, $\tilde{V}^{1,2}(\vartheta_n, \varphi)$ are the reduced voltages samples at the intersection points between the generatrix at φ and the scanning helix, and $Q = \Omega_N$, if $|\vartheta(z) - \vartheta_n| \leq q\Delta\vartheta$, or $Q = 0$, otherwise. Let us first consider the integration over z . For any fixed φ , it results

$$G_{n\eta}(\varphi) = \int_{z_i}^{z_f} D_{N''}(\vartheta(z) - \vartheta_n) \Omega_N(\vartheta(z) - \vartheta_n) e^{-j\nu(z)} e^{j\eta z} dz, \quad (15)$$

where $z_i = z(\vartheta_n + q\Delta\vartheta)$ and $z_f = z(\vartheta_n - q\Delta\vartheta)$. By taking into account (15), the relation (14) can be rewritten as follows:

$$I_{\nu}^{1,2}(\eta) = \sum_{n \in N_r} \int_0^{2\pi} \tilde{V}^{1,2}(\vartheta_n, \varphi) G_{n\eta}(\varphi) e^{-j\nu\varphi} d\varphi. \quad (16)$$

Such a relation involves an integration over φ that must be solved numerically for any $n \in N_r$, by using, from time to time, the voltage samples on the considered helix turn, whose number varies, according to the nonredundant sampling representation on the helix (see Section 2), when moving from the central to the peripheral turns and does not ensure

the convergence of the numerical integration. Moreover, the $G_{n\eta}(\varphi)$ values depend not only on the measurement cylinder and on the radius of the sphere enclosing the AUT, but also on the points at which the generatrix passing through φ intersects the scanning helix. It can be easily recognized that integration over φ can be efficiently solved by using the FFT algorithm, provided that the number of the voltage samples on each helix turn be always the same and equal to the smallest integer M_H , product of powers of 2, 3, and 5 equal or greater than $2[\text{Int}(\chi'\beta\rho_{\max}) + 1]$, ρ_{\max} being the AUT maximum transverse dimension. In such a way, the samples lying on the helix at $\varphi_m = m\Delta\varphi = 2\pi m/M_H$ with $m = 0, \dots, M_H - 1$ are all aligned. Accordingly, we get

$$\begin{aligned} &\int_0^{2\pi} \tilde{V}^{1,2}(\vartheta_n, \varphi) G_{n\eta}(\varphi) e^{-j\nu\varphi} d\varphi \\ &= \frac{2\pi}{M_H} \sum_{m=0}^{M_H-1} \tilde{V}^{1,2}(\vartheta_{m,n}, \varphi_m) G_{n\eta}(\varphi_m) e^{-j2\pi m\nu/M_H}, \end{aligned} \quad (17)$$

where

$$\vartheta_{m,n} = \vartheta_n(\varphi_m) = \vartheta(\phi_i) + k\varphi_m + n\Delta\vartheta. \quad (18)$$

The summation in (17) can be, obviously, efficiently performed via a direct FFT algorithm.

It is worthy to note that the $G_{n\eta}(\varphi_m)$ values can be calculated (once and for all) for given sets of antennas.

According to the above results, the determination of the far field is obtained through the following steps.

- (a) The samples of the probe and rotated probe voltages acquired at the constant step $\Delta\varphi$ along the scanning helix specified in Section 2 are multiplied for the phase factor $e^{j\nu}$.
- (b) For each required value of the polar angle Θ , fixing the corresponding value of η by the relation $\eta = \beta \cos \Theta$, the $G_{n\eta}(\varphi_m)$ values are computed or read, if already calculated.
- (c) For each helix turn, the FFT of the sequence $\tilde{V}^{1,2}(\vartheta_{m,n}, \varphi_m) G_{n\eta}(\varphi_m)$ is performed.
- (d) The probe voltage Fourier transforms $I_{\nu}^{1,2}(\eta)$ are evaluated by performing the summation over $n \in N_r$. The corresponding values of the cylindrical modal expansion coefficients a_{ν} and b_{ν} can be then evaluated.
- (e) The evaluation of the far field at the considered angle Θ is finally effectively achieved by performing the summations in (13) again with the FFT.

From the efficiency viewpoint, it is convenient to use this method to evaluate only the FF samples necessary to recover the antenna pattern via the following far-field OSI expansion

tailored for even numbers of samples along the meridians and parallels [10]:

$$\begin{aligned}
 & F_{\Theta, \Phi}(\Theta, \Phi) \\
 &= \frac{2N_F'' - 1}{2N_F''} \sum_{n=n_0-q+1}^{n_0+q} \left\{ \Omega_{N_F}(\Theta - \Theta_n) D_{N_F''-1}(\Theta - \Theta_n) \frac{2M_n'' - 1}{2M_n''} \right. \\
 &\quad \times \sum_{m=m_0-p+1}^{m_0+p} F_{\Theta, \Phi}(\Theta_n, \Phi_{m,n}) \\
 &\quad \times \Omega_{M_n}(\Phi - \Phi_{m,n}) \\
 &\quad \left. \times D_{M_n''-1}(\Phi - \Phi_{m,n}) \right\}, \quad (19)
 \end{aligned}$$

wherein $n_0 = \text{Int}[\Theta/\Delta\Theta]$ and $m_0 = \text{Int}[\Phi/\Delta\Phi_n]$ are the indexes of the sample nearest (on the left) to the output point, and

$$\Theta_n = n\Delta\Theta = \frac{n\pi}{N_F''}, \quad \Phi_{m,n} = m\Delta\Phi_n = \frac{m\pi}{M_n''}, \quad (20)$$

$$N_F'' = 2 \left[\text{Int} \left(\frac{\chi N'}{2} \right) + 1 \right], \quad N_F = N_F'' - N', \quad (21)$$

$$\begin{aligned}
 M_n'' &= 2^i \geq \text{Int}(\chi M_n') + 1, & M_n' &= \text{Int}[\chi^* \beta \rho_{\max} \sin \Theta_n] + 1, \\
 M_n &= M_n'' - M_n', & \chi^* &= 1 + (\chi' - 1) [\sin \Theta_n]^{-2/3}.
 \end{aligned} \quad (22)$$

The need of an OSI expansion tailored for an even number of samples along the parallels is due to the employment of an efficient power of two FFT algorithms for computing (13), whereas N_F'' has been chosen according to (21) in order to have FF samples on the equator.

It is worthy to note that there is no need to extract the phase factor from the far-field expression, since it is constant on the far-field sphere.

5. Numerical and Experimental Results

Many numerical tests have been performed to assess the validity of the presented technique. In particular, three sets of figures are reported.

The first one refers to a uniform planar circular array (see Figure 1) symmetric with respect to the plane $z = 0$ and having radius $a = 16\lambda$, λ being the wavelength. Its elements are elementary Huygens sources linearly polarized along the z -axis, radially and azimuthally spaced of 0.6λ . An open-ended WR-90 rectangular waveguide, operating at the frequency of 10 GHz, is considered as probe. The radius d of the cylinder wrapped by the scanning helix is 25λ , and its height h is 150λ .

Figures 2 and 3 show the FF pattern reconstruction in the principal planes obtained by using the direct helicoidal NF-FF transformation described in Section 4. As can be seen, the exact and recovered fields are practically indistinguishable, thus assessing the effectiveness of the technique. Moreover, a

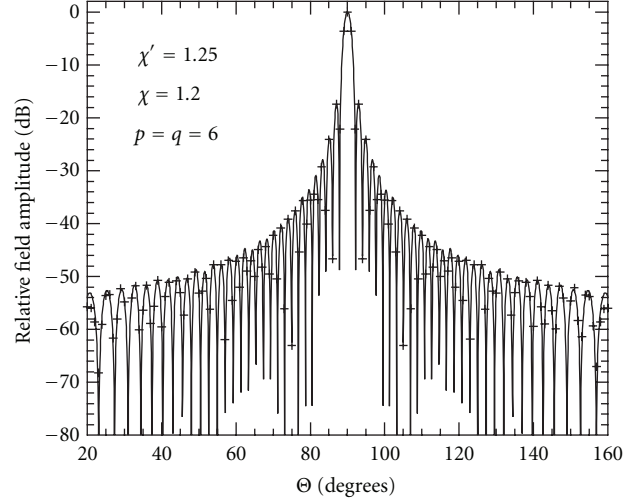


FIGURE 2: Far-field pattern in the E -plane. Solid line: exact field. Crosses: reconstructed via the direct helicoidal NF-FF transformation.

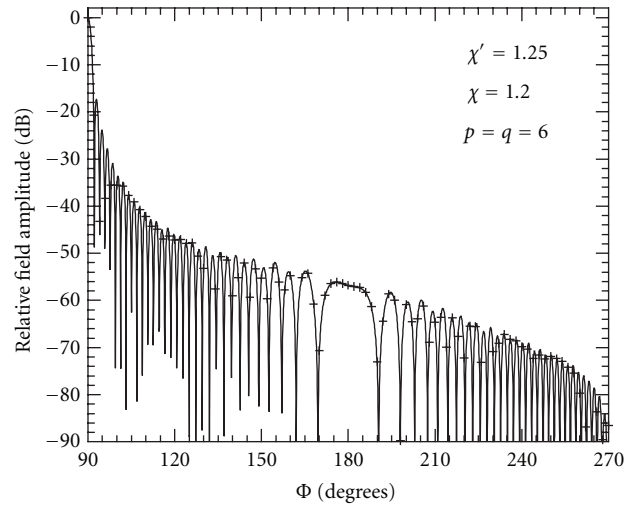


FIGURE 3: Far-field pattern in the H -plane. Solid line: exact field. Crosses: reconstructed via the direct helicoidal NF-FF transformation.

further example showing the reconstructed FF pattern in the plane at $\Phi = 60^\circ$ is reported in Figure 4, in order to show the capability of the technique to accurately reconstruct the far field in any cut-plane.

The second set of figures is relevant to a smaller antenna. It is again a uniform planar circular array of elementary Huygens sources linearly polarized along the z -axis. Its radius a is now 4.2λ , and its elements are radially and azimuthally spaced of 0.4λ . The scanning helix wraps a cylinder with height h equal to 80λ and radius $d = 15\lambda$. In order to highlight another peculiar feature of the here proposed direct helicoidal NF-FF transformation, the FF patterns in the E -plane obtained by applying such a NF-FF transformation and the standard cylindrical probe-compensated one [31] are compared with the exact FF pattern in Figures 5 and 6,

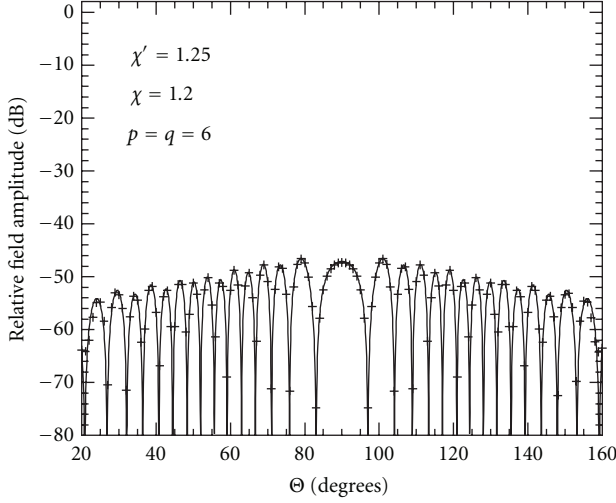


FIGURE 4: Far-field pattern in the plane at $\Phi = 60^\circ$. Solid line: exact field. Crosses: reconstructed via the direct helicoidal NF-FF transformation.

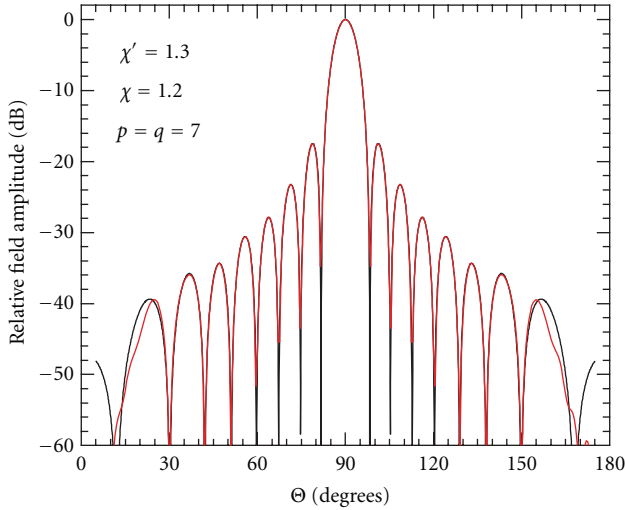


FIGURE 5: Far-field pattern in the E -plane. Black line: exact field. Red line: reconstructed via the direct helicoidal NF-FF transformation.

respectively. As can be seen, the reconstruction obtained via the proposed transformation is clearly more accurate than that achieved by the standard one, since the characteristic ripple caused by the discontinuity of the near field at the edge of the scanning surface is not present. This is due to the different method employed to evaluate the two-dimensional Fourier transforms I_y^1 and I_y^2 of the probe voltage. As a matter of fact, in the standard transformation technique [31], they are computed via FFT by taking into account only the NF data falling in the measurement area so that the integration over z results truncated to the cylinder height. When the evaluation of I_y^1 and I_y^2 is carried out according to the proposed technique, the effect of each NF sample is considered (see (15)) in the range $[z_i, z_f]$, so that the peripheral samples can affect the evaluation even far from the scanning area. Thus, the proposed technique intrinsically

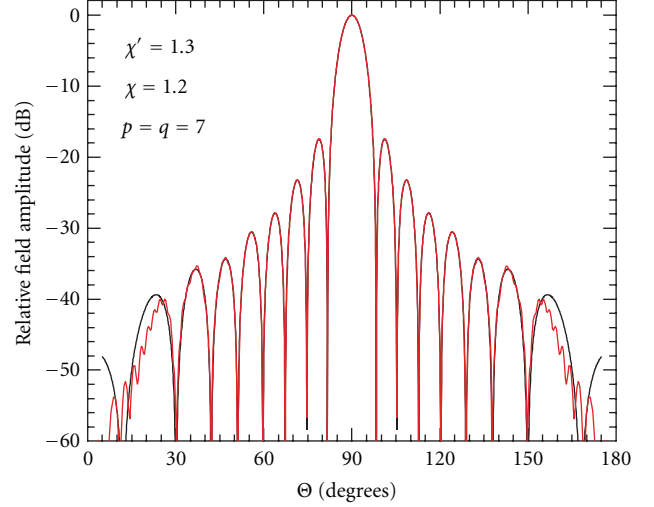


FIGURE 6: Far-field pattern in the E -plane. Black line: exact field. Red line: reconstructed via the standard cylindrical NF-FF transformation [31].

eliminates the field discontinuity at the edges of the scanning surface, without using any windowing function, that, as well known, reduces the ripple as well as the zone of good far-field reconstruction.

The third set of figures refers to the experimental validation of the direct helicoidal NF-FF transformation. Such a validation has been carried out in the anechoic chamber of the UNISA Antenna Characterization Lab. The chamber is equipped with a rotating table and a vertical scanner supplied by MI Technologies. The amplitude and phase measurements are performed by means of a vectorial network analyzer. An open-ended WR90 rectangular waveguide is used as probe. The considered antenna is a MI-12-8.2 standard gain horn with aperture $19.4 \text{ cm} \times 14.4 \text{ cm}$, located on the plane $y = 0$ of the adopted reference system and operating at the frequency of 10 GHz. Such an AUT has been considered as enclosed in a spherical surface having radius equal to 12.6 cm. The probe output voltages have been collected along a helix lying on cylinder with $d = 45 \text{ cm}$ and $h = 240 \text{ cm}$.

It must be stressed that the proposed NF-FF transformation incorporates the probe characterization. Therefore, first of all, the employed probe has been characterized according to [33] as done in the software package MI-3000 implementing the standard probe compensated NF-FF transformation with cylindrical scanning [32]. Then, it has been verified that practically identical results are obtained when the same NF data are transformed by using the MI package and the so developed version of the probe compensated NF-FF transformation [31]. Afterwards, the FF pattern in the principal planes E and H reconstructed by using the direct helicoidal NF-FF transformation has been compared with that obtained via the MI software (reference 1). These reconstructions are shown in Figures 7 and 8. As can be seen, there is a good agreement save for the zones characterized by very low field levels, wherein the discrepancies are due to the fact that two different NF data

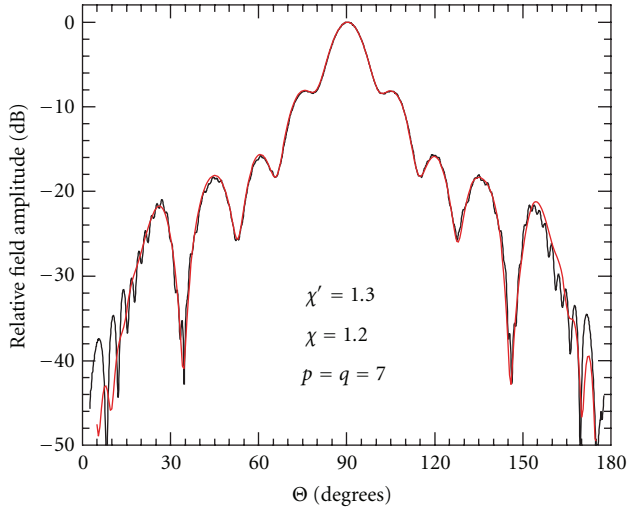


FIGURE 7: Far-field pattern in the E -plane. Black line: reference 1. Red line: reconstructed via the direct helicoidal NF-FF transformation.

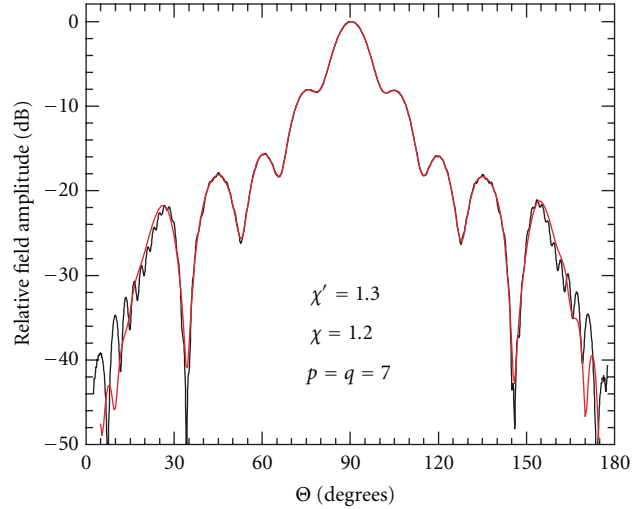


FIGURE 9: Far-field pattern in the E -plane. Black line: reference 2. Red line: reconstructed via the direct helicoidal NF-FF transformation.

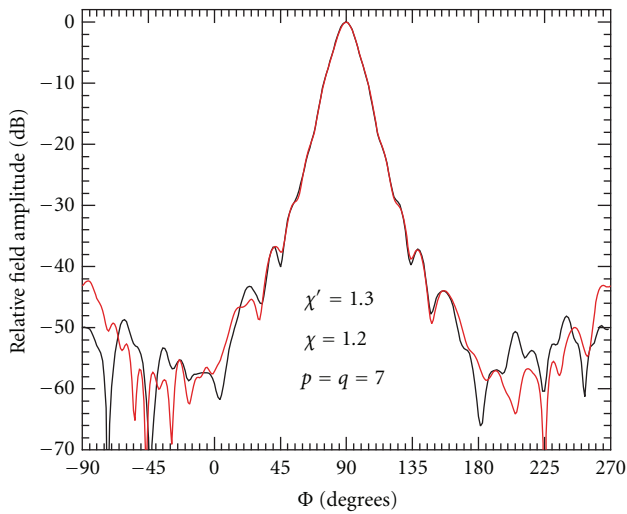


FIGURE 8: Far-field pattern in the H -plane. Black line: reference 1. Red line: reconstructed via the direct helicoidal NF-FF transformation.

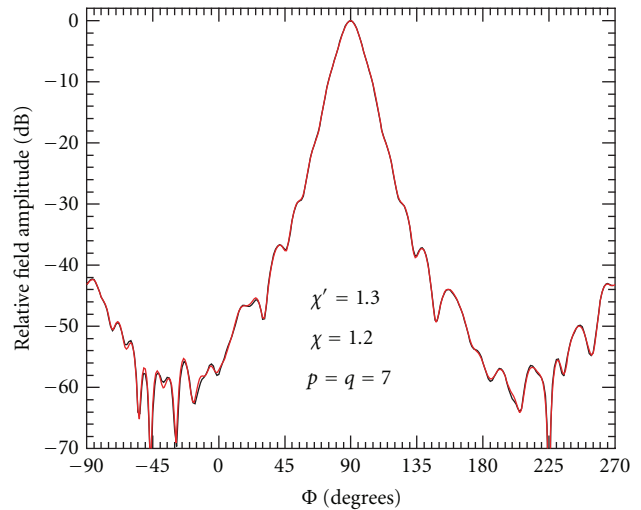


FIGURE 10: Far-field pattern in the H -plane. Black line: reference 2. Red line: reconstructed via the direct helicoidal NF-FF transformation.

sets have been employed. As expected, a better agreement results (see Figures 9 and 10) when the NF data used by the direct helicoidal NF-FF transformation are employed to obtain via a proper interpolation expansion those needed by the software package MI-3000, thus getting a new FF pattern (reference 2). The last reconstruction example (Figure 11) is relevant to the FF pattern in the plane at $\Phi = 60^\circ$.

As can be seen, the experimental results relevant to the FF reconstructions in the E -plane and in the plane at $\Phi = 60^\circ$ confirm the particular property of the developed technique to eliminate the ripple caused by the discontinuity of the near field at the edges of the scanning surface.

It can be interesting to compare the number of NF data used by the direct NF-FF transformation (31 044 for the first example and 2 417 for the other two) with those (67 725 for the first example and 11 592 for the other two) needed by the MI software and by the helicoidal NF-FF transformation technique [30].

For what concerns the time needed for the NF data acquisition, the technique in [30] is certainly quicker than the traditional one, since the acquisition is performed by continuous and synchronized movements of the positioning systems. Accordingly, it is enough to compare the here developed technique only with the one in [30]. In such a case,

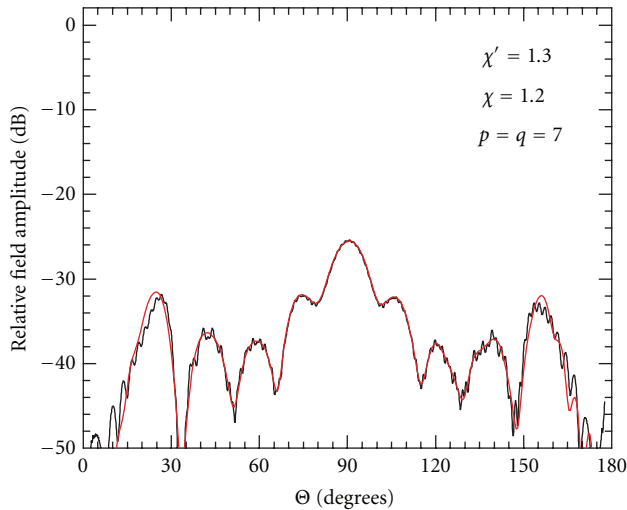


FIGURE 11: Far-field pattern in the plane at $\Phi = 60^\circ$. Black line: reference 2. Red line: reconstructed via the direct helicoidal NF-FF transformation.

it can be easily realized that the measurement times are directly proportional to the numbers of needed samples.

6. Conclusions

A direct NF-FF transformation with helicoidal scanning, which allows one to evaluate the antenna far field in any cut plane directly from a minimum set of NF data without interpolating them, has been developed in this paper. To this end, the approach in [10] has been reviewed in order to match the advantages of the direct cylindrical NF-FF transformation with those own of the fast helicoidal scanning. In particular, the NF sampling arrangement is obtained by determining the number of helix turns according to the nonredundant sampling representation along a generatrix which makes use of the spherical AUT modelling and the voltage samples on each of them according to the AUT maximum transverse dimension. Many numerical tests have assessed the validity of the presented technique and its capability to eliminate the ripple caused by the discontinuity of the near field at the edges of the scanning surface. Moreover, the technique effectiveness has been further confirmed by the experimental results. At last, it has been shown that, although the number of NF data employed by the developed technique is slightly increased with respect to that required by rigorously applying the nonredundant sampling representation on the helix, it remains still remarkably smaller than that needed by the standard NF-FF transformation with cylindrical scan. It is worthy to note that the proposed technique, as well as all those using the spiral scannings, allow also the frequency extension of existing near-field ranges, since both measurement axes are used simultaneously hence reducing the effect of backlash.

References

- [1] "Special Issue on near-field scanning techniques," *IEEE Transactions on Antennas and Propagation*, vol. AP-36, no. 6, pp. 727–901, 1988.
- [2] A. D. Yaghjian, "An overview of near-field antenna measurements," *IEEE Transactions on Antennas and Propagation*, vol. AP-34, no. 1, pp. 30–45, 1986.
- [3] C. Gennarelli, G. Riccio, F. D'Agostino, and F. Ferrara, *Near-Field—Far-Field Transformation Techniques*, vol. 1, CUES, Salerno, Italy, 2004.
- [4] D. Slater, *Near-Field Antenna Measurements*, Artech House, Boston, Mass, USA, 1991.
- [5] C. A. Balanis, *Modern Antenna Handbook*, John Wiley & Sons, Hoboken, NJ, USA, 2008.
- [6] O. M. Bucci, C. Gennarelli, G. Riccio, and C. Savarese, "Near-field—far-field transformation from nonredundant plane-polar data: effective modellings of the source," *IEE Proceedings on Microwaves, Antennas and Propagation*, vol. 145, no. 1, pp. 33–38, 1998.
- [7] O. M. Bucci, G. D'Elia, and M. D. Migliore, "Advanced field interpolation from plane-polar samples: experimental verification," *IEEE Transactions on Antennas and Propagation*, vol. 46, no. 2, pp. 204–210, 1998.
- [8] O. M. Bucci, F. D'Agostino, C. Gennarelli, G. Riccio, and C. Savarese, "NF-FF transformation with plane-polar scanning: ellipsoidal modelling of the antenna," *Automatika*, vol. 41, no. 3-4, pp. 159–164, 2000.
- [9] F. D'Agostino, C. Gennarelli, G. Riccio, and C. Savarese, "Data reduction in the NF-FF transformation with bi-polar scanning," *Microwave and Optical Technology Letters*, vol. 36, no. 1, pp. 32–36, 2003.
- [10] O. M. Bucci, C. Gennarelli, G. Riccio, V. Speranza, and C. Savarese, "Nonredundant representation of the electromagnetic fields over a cylinder with application to the near-field far-field transformation," *Electromagnetics*, vol. 16, no. 3, pp. 273–290, 1996.
- [11] O. M. Bucci, C. Gennarelli, G. Riccio, and C. Savarese, "NF-FF transformation with cylindrical scanning: an effective technique for elongated antennas," *IEE Proceedings on Microwaves, Antennas and Propagation*, vol. 145, no. 5, pp. 369–374, 1998.
- [12] F. D'Agostino, F. Ferrara, C. Gennarelli, G. Riccio, and C. Savarese, "NF-FF transformation with cylindrical scanning from a minimum number of data," *Microwave and Optical Technology Letters*, vol. 35, no. 4, pp. 264–268, 2002.
- [13] O. M. Bucci, F. D'Agostino, C. Gennarelli, G. Riccio, and C. Savarese, "Data reduction in the NF-FF transformation technique with spherical scanning," *Journal of Electromagnetic Waves and Applications*, vol. 15, no. 6, pp. 755–775, 2001.
- [14] F. D'Agostino, F. Ferrara, C. Gennarelli, R. Guerriero, and M. Migliozzi, "Effective antenna modellings for NF-FF transformations with spherical scanning using the minimum number of data," *International Journal of Antennas and Propagation*, vol. 2011, Article ID 936781, 11 pages, 2011.
- [15] O. M. Bucci, C. Gennarelli, and C. Savarese, "Representation of electromagnetic fields over arbitrary surfaces by a finite and nonredundant number of samples," *IEEE Transactions on Antennas and Propagation*, vol. 46, no. 3, pp. 351–359, 1998.
- [16] O. M. Bucci, C. Gennarelli, and C. Savarese, "Fast and accurate near-field-far-field transformation by sampling interpolation of plane-polar measurements," *IEEE Transactions on Antennas and Propagation*, vol. 39, no. 1, pp. 48–55, 1991.

- [17] R. G. Yaccarino, L. I. Williams, and Y. Rahmat-Samii, "Linear spiral sampling for the bipolar planar near-field antenna measurement technique," *IEEE Transactions on Antennas and Propagation*, vol. 44, no. 7, pp. 1049–1051, 1996.
- [18] O. M. Bucci, C. Gennarelli, G. Riccio, and C. Savarese, "Nonredundant NF-FF transformation with helicoidal scanning," *Journal of Electromagnetic Waves and Applications*, vol. 15, no. 11, pp. 1507–1519, 2001.
- [19] F. D'Agostino, F. Ferrara, C. Gennarelli, R. Guerriero, and M. Migliozi, "Experimental results validating the near-field to far-field transformation technique with helicoidal scan," *The Open Electrical & Electronic Engineering Journal*, vol. 4, pp. 10–15, 2010.
- [20] F. D'Agostino, C. Gennarelli, G. Riccio, and C. Savarese, "Theoretical foundations of near-field-far-field transformations with spiral scannings," *Progress in Electromagnetics Research*, vol. 61, pp. 193–214, 2006.
- [21] O. M. Bucci, F. D'Agostino, C. Gennarelli, G. Riccio, and C. Savarese, "Probe compensated far-field reconstruction by near-field planar spiral scanning," *IEE Proceedings: Microwaves, Antennas and Propagation*, vol. 149, no. 2, pp. 119–123, 2002.
- [22] O. M. Bucci, F. D'Agostino, C. Gennarelli, G. Riccio, and C. Savarese, "Near-field-far-field transformation with spherical spiral scanning," *IEEE Antennas and Wireless Propagation Letters*, vol. 2, pp. 263–266, 2003.
- [23] F. D'Agostino, F. Ferrara, C. Gennarelli, R. Guerriero, and M. Migliozi, "Near-field-far-field transformation technique with helicoidal scanning for elongated antennas," *Progress in Electromagnetics Research B*, vol. 4, pp. 249–261, 2008.
- [24] F. D'Agostino, F. Ferrara, J. A. Fordham et al., "An effective near-field-far-field transformation technique for elongated antennas using a fast helicoidal scan," *IEEE Antennas and Propagation Magazine*, vol. 51, no. 4, Article ID 5338700, pp. 134–141, 2009.
- [25] F. D'Agostino, F. Ferrara, C. Gennarelli, R. Guerriero, and M. Migliozi, "Laboratory tests assessing the effectiveness of the NF-FF transformation with helicoidal scanning for electrically long antennas," *Progress in Electromagnetics Research*, vol. 98, pp. 375–388, 2009.
- [26] F. D'Agostino, F. Ferrara, C. Gennarelli, R. Guerriero, and M. Migliozi, "An effective NF-FF transformation technique with planar spiral scanning tailored for quasi-planar antennas," *IEEE Transactions on Antennas and Propagation*, vol. 56, no. 9, pp. 2981–2987, 2008.
- [27] F. D'Agostino, F. Ferrara, C. Gennarelli, R. Guerriero, M. Migliozi, and G. Riccio, "A nonredundant near-field to far-field transformation with spherical spiral scanning for nonspherical antennas," *The Open Electrical & Electronic Engineering Journal*, vol. 3, pp. 1–8, 2009.
- [28] F. D'Agostino, F. Ferrara, C. Gennarelli, R. Guerriero, and M. Migliozi, "The unified theory of near-field-far-field transformations with spiral scannings for nonspherical antennas," *Progress In Electromagnetics Research B*, no. 14, pp. 449–477, 2009.
- [29] S. Costanzo and G. Di Massa, "Near-field to far-field transformation with planar spiral scanning," *Progress in Electromagnetics Research*, vol. 73, pp. 49–59, 2007.
- [30] S. Costanzo and G. Di Massa, "Far-field reconstruction from phaseless near-field data on a cylindrical helix," *Journal of Electromagnetic Waves and Applications*, vol. 18, no. 8, pp. 1057–1071, 2004.
- [31] W. M. Leach and D. T. Paris, "Probe compensated near-field measurements on a cylinder," *IEEE Transactions on Antennas and Propagation*, vol. AP-21, no. 4, pp. 435–445, 1973.
- [32] A. D. Yaghjian, "Near-field antenna measurement on a cylindrical surface: a source scattering matrix formulation," NBS Technical Note 696, U.S. Government Printing Office, Washington, DC, USA, 1977.
- [33] A. D. Yaghjian, "Approximate formulas for the far field and gain of open-ended rectangular waveguide," *IEEE Transactions on Antennas and Propagation*, vol. AP-32, no. 4, pp. 378–384, 1984.

Application Article

Using Truncated Data Sets in Spherical-Scanning Antenna Measurements

Ronald C. Wittmann, Carl F. Stubenrauch, and Michael H. Francis

Electromagnetics Division, National Institute of Standards and Technology, 325 Broadway, Boulder, CO 80305, USA

Correspondence should be addressed to Ronald C. Wittmann, wittmannrc@gmail.com

Received 12 October 2011; Accepted 8 February 2012

Academic Editor: Amedeo Capozzoli

Copyright © 2012 Ronald C. Wittmann et al. This is an open access article distributed under the Creative Commons Attribution License, which permits unrestricted use, distribution, and reproduction in any medium, provided the original work is properly cited.

We discuss the mitigation of truncation errors in spherical-scanning measurements by use of a constrained least-squares estimation method. The main emphasis is the spherical harmonic representation of probe transmitting and receiving functions; however, our method is applicable to near-field measurement of electrically small antennas for which full-sphere data are either unreliable or unavailable.

1. Introduction

The transmitting function of an electrically small probe tends to be very broad, so that full-sphere data are needed to compute the spherical-harmonic representation of the pattern by use of standard methods [1]. Unfortunately, backward-hemisphere data are often unavailable or at best unreliable due to support-structure blockage. Simply setting the backward-hemisphere data to zero leads to ringing effects that degrade the accuracy of the probe-pattern representation in the forward hemisphere. In this paper, we approximate the spherical-harmonic expansion of transmit/receive functions using only forward hemisphere data. The solution presented is a least-squares fit with energy constraints (to limit backward-hemisphere radiation) and proper weighting of measurements (to compensate for clustering near the poles). The energy constraint is specified using an estimated value of directivity. Results are given that compare pattern representations obtained using both full-sphere and half-sphere data.

Others have also considered truncation error mitigation in various near-field measurement contexts [2–5].

2. Theory

We wish to approximate a physical quantity \mathbf{b} by a spherical-harmonic expansion

$$\mathbf{b}(\theta, \varphi) = b^\theta(\theta, \varphi)\hat{\boldsymbol{\theta}} + b^\varphi(\theta, \varphi)\hat{\boldsymbol{\varphi}} \approx \hat{\mathbf{b}}(\theta, \varphi), \quad (1)$$

$$\hat{\mathbf{b}}(\theta, \varphi) = \sum_{\mu=-M}^M \sum_{\nu=n(\mu)}^N [a_{\nu\mu}^1 \mathbf{X}_{\nu\mu}(\theta, \varphi) + a_{\nu\mu}^2 \mathbf{Y}_{\nu\mu}(\theta, \varphi)], \quad (2)$$

$$n(\mu) = \max(1, |\mu|), \quad |M| \leq N.$$

Here, \mathbf{X}_{nm} and $\mathbf{Y}_{nm} = \hat{\mathbf{r}} \times \mathbf{X}_{nm}$ are vector spherical harmonics [6, chapter 16]. For example, $\mathbf{b}(\theta, \varphi)$ might be the measured transmitting or receiving pattern of a probe, or it might be the “measurement vector” $\mathbf{w}(\theta, \varphi)$ for a spherical near-field scanning measurement [1, 7–9].

When full-sphere data are available, the orthogonality of vector spherical harmonics can be used to determine the coefficients $a_{\nu\mu}^1$ and $a_{\nu\mu}^2$ from discrete measurements of $\mathbf{b}(\theta, \varphi)$ gathered on a uniform grid in θ and φ . When so determined, $\hat{\mathbf{b}}(\theta, \varphi)$ is optimal in the sense that

$$\int_0^\pi \sin \theta d\theta \int_0^{2\pi} |\mathbf{b}(\theta, \varphi) - \hat{\mathbf{b}}(\theta, \varphi)|^2 d\varphi \quad (3)$$

is minimal.

In this paper, we assume that data are available only in the forward hemisphere $\theta \leq \pi/2$ on the grid

$$\begin{aligned}\theta_n &= \frac{\pi}{2P'}n, \quad 0 \leq n \leq P', \\ \varphi_m &= \frac{2\pi}{Q}m, \quad 0 \leq m < Q,\end{aligned}\quad (4)$$

with

$$\begin{aligned}P' &> N, \\ Q &> 2M.\end{aligned}\quad (5)$$

Requirement (5) preserves the standard number of measurement points by halving the maximum sample interval in θ . Ideally, P' and Q are products of small primes to allow efficient application of the fast Fourier transform (FFT) algorithm; however, factorization may not be important when antennas are “electrically small.” Our goal is to minimize the discrepancy

$$\Delta = \sum_{n=0}^{P'} w_n \int_0^{2\pi} \left| \mathbf{b}(\theta_n, \varphi) - \hat{\mathbf{b}}(\theta_n, \varphi) \right|^2 d\varphi, \quad (6)$$

where the w_n are positive weights. Equation (6) may be viewed as an adaptation of (3). Because the sampling theorem has been satisfied, the φ integral can be readily evaluated analytically. The θ integral, however, has been discretized. (We generally set $w_n = \sin \theta_n$.)

The discrepancy Δ is minimized subject to the “energy” constraint

$$E = \sum_{\nu\mu} \left(\left| a_{\nu\mu}^1 \right|^2 + \left| a_{\nu\mu}^2 \right|^2 \right), \quad (7)$$

in order to limit the power radiated into directions where there are no measurements. When $\mathbf{b}(\hat{\mathbf{r}})$ is proportional to the transmitting pattern of the test antenna, we have

$$E = \frac{4\pi \left| \mathbf{b}(\hat{\mathbf{r}}) \right|^2}{D(\hat{\mathbf{r}})}, \quad (8)$$

so that E may be chosen using an estimate of the directivity D in some measurement direction $\hat{\mathbf{r}}$. (Directivity and gain are approximately equal when ohmic losses are small).

Avoiding details for the moment, we write

$$\mathbf{b} \approx \hat{\mathbf{b}} = \mathbf{A}\mathbf{x}, \quad (9)$$

where \mathbf{b} and $\hat{\mathbf{b}}$ are vectors of measurements and predicted values, \mathbf{x} is a vector of coefficients to be determined, and the matrix \mathbf{A} represents a known linear relationship. We choose \mathbf{x} to minimize $\Delta = (\mathbf{b} - \mathbf{A}\mathbf{x})^* \boldsymbol{\kappa} (\mathbf{b} - \mathbf{A}\mathbf{x})$ subject to the constraint $E = \|\mathbf{x}\|^2$. Here, $\boldsymbol{\kappa}$ is a diagonal matrix of positive weights, and an asterisk implies Hermitian transpose. It is easy to show that this \mathbf{x} is determined by the equations

$$\mathbf{A}^* \boldsymbol{\kappa} \mathbf{A} \mathbf{x} - \lambda \mathbf{x} = \mathbf{A}^* \boldsymbol{\kappa} \mathbf{b}, \quad (10)$$

$$\mathbf{x}^* \mathbf{x} = E \quad (11)$$

The significance of the Lagrange multiplier λ is seen in the relation

$$|\lambda| = \frac{\|\mathbf{A}^* \boldsymbol{\kappa} \mathbf{A} \mathbf{x} - \mathbf{A}^* \boldsymbol{\kappa} \mathbf{b}\|}{\sqrt{E}} \quad (12)$$

that is, $|\lambda|$ is a measure of the residual of the fit. In the absence of the energy constraint (7) of course, we can choose \mathbf{x} to be the solution of the normal equations $\mathbf{A}^* \boldsymbol{\kappa} \mathbf{A} \mathbf{x} = \mathbf{A}^* \boldsymbol{\kappa} \mathbf{b}$.

Since $\mathbf{A}^* \boldsymbol{\kappa} \mathbf{A}$ is Hermitian nonnegative definite, we have the singular-value decomposition (SVD)

$$\mathbf{A}^* \boldsymbol{\kappa} \mathbf{A} = \mathbf{S} \mathbf{D} \mathbf{S}^*, \quad (13)$$

where \mathbf{S} is unitary, $D_{ij} = d_i \delta_{ij}$, and $d_i \geq 0$. From (13), (10), and (11), we are led to

$$E = \sum_i \frac{|f_i|^2}{(d_i - \lambda)^2}, \quad (14)$$

$$\mathbf{f} \equiv \mathbf{S}^* \mathbf{A}^* \boldsymbol{\kappa} \mathbf{b}.$$

The right side of (14) tends to 0 as $|\lambda| \rightarrow \infty$, and because of poles at the singular values d_i , there may be numerous solutions for λ . According to (12), the best choice corresponds to the unique solution for which $\lambda < d_1$, where d_1 is the smallest singular value. In general, $\lambda < 0$, since the constrained solution is expected to have lower energy than the unconstrained solution. Finally, given λ , we may compute \mathbf{x} ,

$$x_i = \sum_j \frac{S_{ij} f_j}{d_j - \lambda}. \quad (15)$$

Numerical methods used in this paper are discussed in greater detail in [10].

At this point, we have discussed the main ideas of this paper. What follows are some rather unpleasant details that we summarize dutifully and concisely. To begin with, (1) can be written as a Fourier series

$$\mathbf{b}(\theta, \varphi) = \sum_{\mu=-M}^M \left[b_{\mu}^{\theta}(\theta) \hat{\boldsymbol{\theta}} + b_{\mu}^{\varphi}(\theta) \hat{\boldsymbol{\varphi}} \right] \exp(i\mu\varphi), \quad (16)$$

where the coefficients may be computed from the data with a discrete Fourier transform

$$b_{\mu}^{\theta, \varphi}(\theta) = \frac{1}{Q} \sum_{m=0}^{Q-1} b^{\theta, \varphi}(\theta, \varphi_m) \exp\left(-i \frac{2\pi}{Q} m\mu\right). \quad (17)$$

Similarly, for (2),

$$\hat{\mathbf{b}}(\theta, \varphi) = \sum_{\mu=-M}^M \left[\hat{b}_{\mu}^{\theta}(\theta) \hat{\boldsymbol{\theta}} + \hat{b}_{\mu}^{\varphi}(\theta) \hat{\boldsymbol{\varphi}} \right] \exp(i\mu\varphi), \quad (18)$$

$$\hat{b}_{\mu}^{\theta, \varphi}(\theta) = \sum_{\nu=n(\mu)}^N \left[a_{\nu\mu}^1 X_{\nu\mu}^{\theta, \varphi}(\theta, 0) + a_{\nu\mu}^2 Y_{\nu\mu}^{\theta, \varphi}(\theta, 0) \right],$$

$$\mathbf{X}_{\nu\mu} = X_{\nu\mu}^{\theta} \hat{\boldsymbol{\theta}} + X_{\nu\mu}^{\varphi} \hat{\boldsymbol{\varphi}}, \quad (19)$$

$$\mathbf{Y}_{\nu\mu} = Y_{\nu\mu}^{\theta} \hat{\boldsymbol{\theta}} + Y_{\nu\mu}^{\varphi} \hat{\boldsymbol{\varphi}},$$

$$Y_{\nu\mu}^{\theta} = -iX_{\nu\mu}^{\varphi}, \quad Y_{\nu\mu}^{\varphi} = iX_{\nu\mu}^{\theta}.$$

With substitution of (16) and (18), the discrepancy (6) becomes

$$\Delta = 2\pi \sum_{n=0}^{P'} w_n \sum_{\mu=-M}^M \left[\left| b_{\mu}^{\theta}(\theta_n) - \hat{b}_{\mu}^{\theta}(\theta_n) \right|^2 + \left| b_{\mu}^{\varphi}(\theta_n) - \hat{b}_{\mu}^{\varphi}(\theta_n) \right|^2 \right]. \quad (20)$$

This may be rewritten in the form

$$\Delta = 2\pi \sum_{\mu=-M}^M (\mathbf{b}_{\mu} - \mathbf{A}_{\mu} \mathbf{x}_{\mu})^* \boldsymbol{\kappa}_{\mu} (\mathbf{b}_{\mu} - \mathbf{A}_{\mu} \mathbf{x}_{\mu}). \quad (21)$$

Here

$$\begin{aligned} \mathbf{x}_{\mu} &= \begin{pmatrix} \mathbf{x}_{\mu}^1 \\ \mathbf{x}_{\mu}^2 \end{pmatrix}, & \mathbf{b}_{\mu} &= \begin{pmatrix} \mathbf{b}_{\mu}^{\theta} \\ \mathbf{b}_{\mu}^{\varphi} \end{pmatrix}, \\ \mathbf{x}_{\mu}^{1,2} &= \begin{pmatrix} a_{n(\mu),\mu}^{1,2} \\ \vdots \\ a_{N\mu}^{1,2} \end{pmatrix}, & \mathbf{b}_{\mu}^{\theta,\varphi} &= \begin{pmatrix} b_{\mu}^{\theta,\varphi}(\theta_0) \\ \vdots \\ b_{\mu}^{\theta,\varphi}(\theta_{P'}) \end{pmatrix}, \\ \mathbf{A}_{\mu} &= \begin{pmatrix} \boldsymbol{\alpha}_{\mu} & \boldsymbol{\beta}_{\mu} \\ i\boldsymbol{\beta}_{\mu} & i\boldsymbol{\alpha}_{\mu} \end{pmatrix}, \\ \boldsymbol{\alpha}_{\mu} &= \begin{pmatrix} X_{n(\mu),\mu}^{\theta}(\theta_0, 0) & \cdots & X_{N\mu}^{\theta}(\theta_0, 0) \\ \vdots & \ddots & \vdots \\ X_{n(\mu),\mu}^{\theta}(\theta_{P'}, 0) & \cdots & X_{N\mu}^{\theta}(\theta_{P'}, 0) \end{pmatrix}, \\ \boldsymbol{\beta}_{\mu} &= -i \begin{pmatrix} X_{n(\mu),\mu}^{\varphi}(\theta_0, 0) & \cdots & X_{N\mu}^{\varphi}(\theta_0, 0) \\ \vdots & \ddots & \vdots \\ X_{n(\mu),\mu}^{\varphi}(\theta_{P'}, 0) & \cdots & X_{N\mu}^{\varphi}(\theta_{P'}, 0) \end{pmatrix}, \\ \boldsymbol{\kappa}_{\mu} &= \begin{pmatrix} \mathbf{w} & \mathbf{0} \\ \mathbf{0} & \mathbf{w} \end{pmatrix}, \\ \mathbf{w} &= \begin{pmatrix} w_0 & 0 & \cdots & 0 \\ 0 & w_1 & \ddots & \vdots \\ \vdots & \ddots & \ddots & 0 \\ 0 & \cdots & 0 & w_{P'} \end{pmatrix}. \end{aligned} \quad (22)$$

Finally, with the definitions

$$\mathbf{A} = \begin{pmatrix} \mathbf{A}_{-M} & \mathbf{0} & \cdots & \mathbf{0} \\ \mathbf{0} & \mathbf{A}_{-M+1} & \ddots & \vdots \\ \vdots & \ddots & \ddots & \mathbf{0} \\ \mathbf{0} & \cdots & \mathbf{0} & \mathbf{A}_M \end{pmatrix},$$

$$\boldsymbol{\kappa} = \begin{pmatrix} \boldsymbol{\kappa}_{-M} & \mathbf{0} & \cdots & \mathbf{0} \\ \mathbf{0} & \boldsymbol{\kappa}_{-M+1} & \ddots & \vdots \\ \vdots & \ddots & \ddots & \mathbf{0} \\ \mathbf{0} & \cdots & \mathbf{0} & \boldsymbol{\kappa}_M \end{pmatrix},$$

$$\mathbf{x} = \begin{pmatrix} \mathbf{x}_{-M} \\ \vdots \\ \mathbf{x}_M \end{pmatrix}, \quad \mathbf{b} = \begin{pmatrix} \mathbf{b}_{-M} \\ \vdots \\ \mathbf{b}_M \end{pmatrix}, \quad (23)$$

we have

$$\begin{aligned} \mathbf{b} &\approx \hat{\mathbf{b}} = \mathbf{A} \mathbf{x}, \\ E &= \|\mathbf{x}\|^2, \end{aligned} \quad (24)$$

$$\Delta = (\mathbf{A} \mathbf{x} - \mathbf{b})^* \boldsymbol{\kappa} (\mathbf{A} \mathbf{x} - \mathbf{b}).$$

Thus, the measurement truncation problem has been reduced, explicitly, to the constrained least-square optimization problem discussed earlier. In particular, (10) and (11) can be written as

$$\mathbf{A}_{\mu}^* \boldsymbol{\kappa}_{\mu} \mathbf{A}_{\mu} \mathbf{x}_{\mu} - \lambda \mathbf{x}_{\mu} = \mathbf{A}_{\mu}^* \boldsymbol{\kappa}_{\mu} \mathbf{b}_{\mu}, \quad -M \leq \mu \leq M, \quad (25)$$

$$E = \sum_{\mu=-M}^M \|\mathbf{x}_{\mu}\|^2. \quad (26)$$

Because of the block-diagonal structure, the overall SVD can be broken into smaller parts, one μ at a time, resulting in an algorithm with computational complexity $\mathcal{O}(N^4)$. Comparing unfavorably with the $\mathcal{O}(N^3)$ complexity for the full-sphere case, our method may be less useful for larger antennas. The order of \mathbf{A}_{μ} is $2(P' + 1) \times 2(N - n(\mu) + 1)$, so there will be more equations than unknowns in every block $|\mu| \leq M$ as long as $P' \geq N$. Actually, there is always a unique solution to our constrained optimization problem; however, the quality of this solution is observed to degrade dramatically as P' is decreased below the threshold $P' = N$.

3. Experimental and Simulated Results

To investigate the utility of our least-squares technique for reducing the truncation error that results from zero filling in the rear hemisphere, we examined a number of typical probes for which full-sphere far-field patterns are available. In each case, we computed the far-field pattern using the spherical mode expansion obtained (a) from the standard algorithm with *full-sphere* data, (b) from the standard algorithm with *zero-fill* in the backward-hemisphere, and finally, (c) from the constrained *least-squares* fit to forward-hemisphere measurements described previously. Ideally, the far-field pattern calculated from the spherical-mode expansion should agree with the original pattern. For the *full-sphere* modal calculation, this is of course the case if the sampling theorem is satisfied. We show E-plane results only,

since truncation effects are more important because the patterns tend to be broader. For all cases, the sampling is 2° in θ and 5° in ϕ .

3.1. High-Gain Symmetric Probe. In this case, the input data were simulated using a far-field pattern calculated from a specified set of ($m = \pm 1$) modal coefficients. For this antenna, we used $N = 10$, $M = 5$. The directivity of 15.44 dB was used in (8) to determine the energy constraint. Figures 1 and 2 indicate excellent agreement between the *full-sphere* and *least-squares* techniques in the forward hemisphere.

In this example, the *constrained least-squares* technique also performs well in the backward-hemisphere if the correct energy is specified. This is not necessarily true in the presence of noise. As a test, we added random errors with an RMS value of 0.1% relative to the noise-free RMS pattern level. An *unconstrained* fit resulted in an on-axis directivity of -32 dB. In other words, the back hemisphere overwhelmed the forward hemisphere. On the other hand, a *constrained* fit forced the back hemisphere pattern to remain at a reasonable level even though the details were incorrect. Although an *unconstrained* fit may be somewhat better in the forward directions, a *constrained* fit is undoubtedly more reasonable given our knowledge of the directivity of the test antenna.

In probe-corrected spherical near-field measurements, for example, the complete probe pattern is required. We often argue that the forward hemisphere pattern is most important, but all bets are off when the back hemisphere pattern dwarfs the forward hemisphere pattern.

3.2. NIST Circularly Cylindrical Waveguide Probe. This cylindrical waveguide probe was designed and built for spherical near-field measurements at 3.3 GHz. The far-field pattern was measured over the entire sphere, although support-structure blockage limits the value of backward-hemisphere information. In this case, we used $N = 17$, $M = 17$. A directivity of 7.87 dB was calculated using the *full-sphere* data. Deviations (Figure 3) between the *full-sphere* and *zero-fill* methods will lead to significant errors when the *zero-fill* results are used in spherical scanning measurements. Within the range $\pm 75^\circ$, the maximum error in the *zero-fill* result is about 0.6 dB, while the *least-squares* technique has a maximum error of 0.08 dB. Figure 4 shows how the *full-sphere*, *zero-fill*, and *least-squares* results compare in the backward-hemisphere. In this case, the truncation level is as high as -12 dB, which causes a greater discrepancy between the *zero-fill* and *full-sphere* patterns than observed in the previous example.

3.3. Rectangular Waveguide Probe. This probe is a section of WR-284 rectangular waveguide. Far-field patterns were obtained over the entire sphere at 3.3 GHz. In this case, we used $N = 17$, $M = 17$. Strictly speaking, rectangular waveguide probes do not have the correct symmetry for spherical near-field scanning applications; however, they often perform satisfactorily when the scan radius is more than about an antenna diameter. Thus, we include results for this type of probe. A directivity of 7.12 dB, calculated from the *full-sphere* modal expansion, was used to determine the

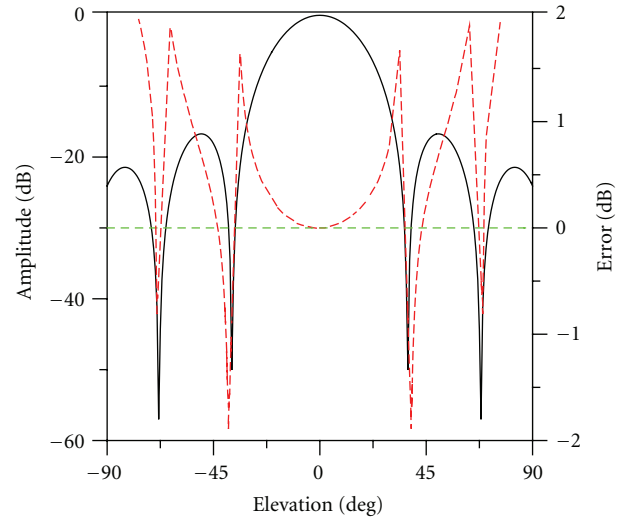


FIGURE 1: Simulated probe: deviations from the *full-sphere* pattern (errors) are shown for the *zero-fill* (long dash) and *least-squares* (short dash) techniques. The *full-sphere* pattern is shown as a solid line.

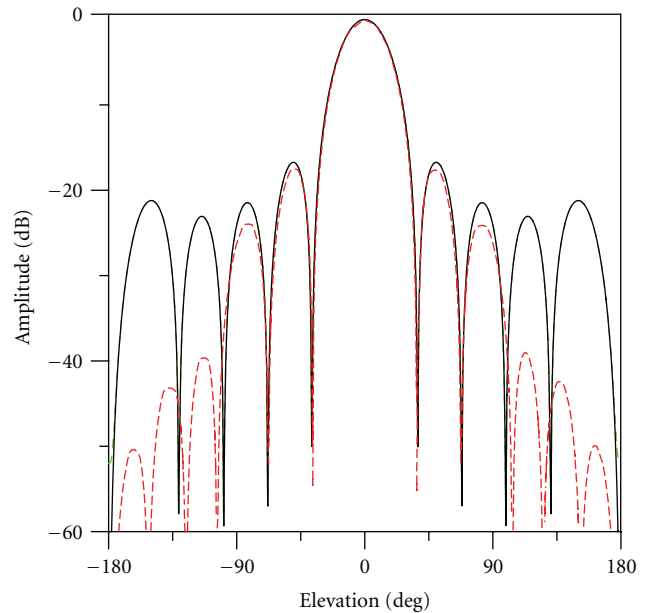


FIGURE 2: Simulated probe: comparison of the *full-sphere* E-plane far-field patterns obtained using *zero-fill* (long dash) and *least-squares* (short dash) techniques. The *full-sphere* pattern is shown as a solid line. The *least-squares* and *full-sphere* patterns are indistinguishable at this scale.

energy constraint. Measured gain was 6.7 dB. The results are similar to those for the cylindrical waveguide case. As evident in Figure 5, within the angular range $\pm 75^\circ$, the *zero-fill* error is greatest at about 40° , where it is 0.66 dB. The error is only about 0.11 dB for the *least-squares* technique at this angle. In the forward hemisphere, the *zero-fill* technique exhibits large errors, while the *least-squares* technique errors remain

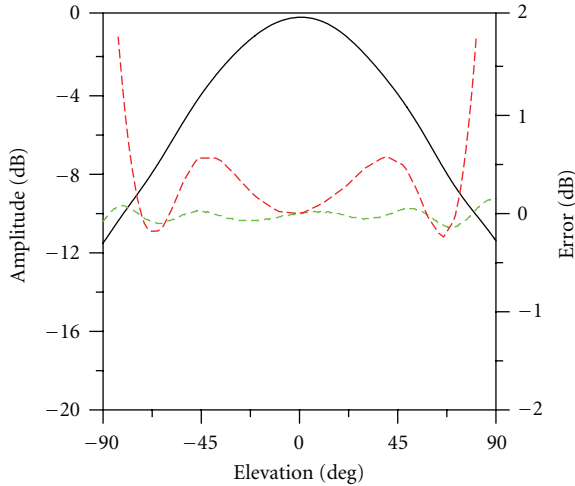


FIGURE 3: Cylindrical waveguide probe: deviations from the *full-sphere* pattern (errors) are shown for the *zero-fill* (long dash) and *least-squares* (short dash) techniques. The *full-sphere* pattern is shown as a solid line.

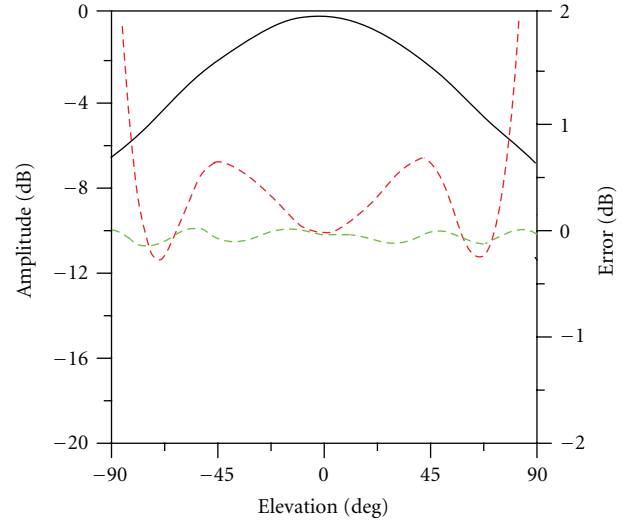


FIGURE 5: Rectangular waveguide probe: deviations from the *full-sphere* pattern (errors) are shown for the *zero-fill* (long dash) and *least-squares* (short dash) techniques. The *full-sphere* pattern is shown as a solid line.

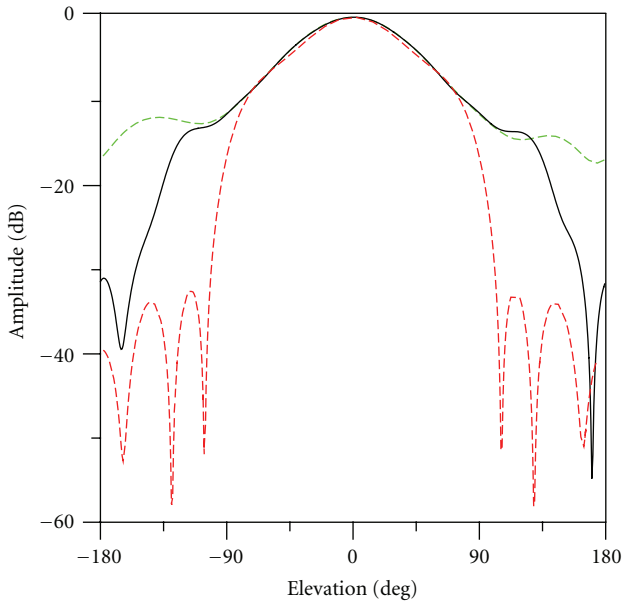


FIGURE 4: Cylindrical waveguide probe: comparison of the full-sphere E-plane far-field patterns obtained using the *zero-fill* (long dash) and the *least-squares* (short dash) techniques. The *full-sphere* pattern is shown as a solid line.

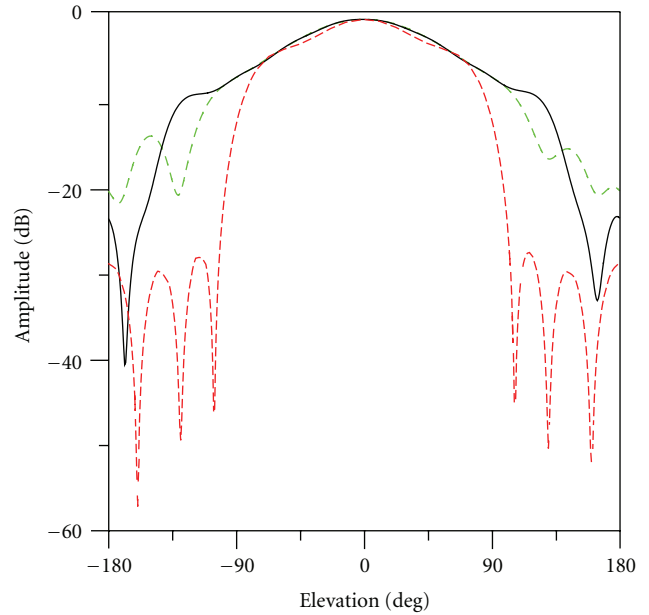


FIGURE 6: Rectangular waveguide probe: comparison of the full-sphere E-plane far-field patterns obtained using the *zero-fill* (long dash) and the *least-squares* (short dash) techniques. The *full-sphere* pattern is shown as a solid line.

relatively small. Figure 6 provides a full-sphere comparison of the three techniques.

3.4. *Choice of E.* Several tests indicate that the quality of the *least-squares* fit in the forward hemisphere is relatively insensitive to the choice of E . In a typical case with $0.9E_0 \leq E \leq 1.1E_0$, the errors observed in the results were generally much less than 0.15 dB within 20° of the on-axis direction. (Here, E_0 is the correct value). When gain is used to

approximate directivity, experience indicates that the error in E usually will be less than 10%.

4. Summary and Future Work

We have demonstrated a constrained *least-squares* technique for calculating the spherical mode coefficients of a small antenna from forward-hemisphere far-field data. This technique can significantly reduce truncation errors that arise

when the standard algorithm is used with *zero-fill* in the backward-hemisphere. While the *least-squares* algorithm is not especially efficient, computational times are still acceptable for small antennas.

Our technique can also be used to process near-field data when reliable full-sphere measurements are not available. The method may be adapted to serve when measurements are made in the range $0 \leq \theta \leq \theta_0$, where θ_0 is not restricted to 90° . We are considering an iterative algorithm to find both \mathbf{x} and λ simultaneously. For well-conditioned systems, this could effectively reduce the computational complexity to $O(N^3)$. By beginning with a spherical-wave expansion and projecting onto a scanning surface, our method should be useful for mitigation of truncation error in planar and cylindrical scanning measurements, as well.

Acknowledgments

The authors thank Allen Newell, consultant, for bringing this problem to our attention. They also thank Brad Alpert of NIST for insightful discussions concerning the numerical methods employed in this work.

References

- [1] M. H. Francis and R. C. Wittmann, "Near-field scanning measurements: theory and practice," in *Modern Antenna Handbook*, C. A. Balanis, Ed., chapter 19, John Wiley & Sons, New York, NY, USA, 2008.
- [2] E. B. Joy, C. A. Rose et al., "Windows 96 for planar near-field measurements," in *Proceedings of the 18th AMTA Annual Meeting & Symposium*, pp. 80–85, October 1996.
- [3] P. R. Rousseau, "The development of a near-field data window function for measuring standard gain horns," in *Proceedings of the 19th AMTA Annual Meeting & Symposium*, pp. 96–101, November 1997.
- [4] O. M. Bucci and M. D. Migliore, "A new method for avoiding the truncation error in near-field antennas measurements," *IEEE Transactions on Antennas and Propagation*, vol. 54, no. 10, pp. 2940–2952, 2006.
- [5] K. T. Kim, "Slepian transverse vector spherical harmonics and their application to near-field scanning," in *Proceedings of the IEEE Antennas and Propagation Society, AP-S International Symposium*, pp. 2138–2141, Spokane, Wash, USA, July 2011.
- [6] J. D. Jackson, *Classical Electrodynamics*, John Wiley & Sons, New York, NY, USA, 2nd edition, 1975.
- [7] R. C. Wittmann, B. K. Alpert, and M. H. Francis, "Near-field, spherical-scanning antenna measurements with nonideal probe locations," *IEEE Transactions on Antennas and Propagation*, vol. 52, no. 8, pp. 2184–2186, 2004.
- [8] R. C. Wittmann and C. F. Stubenrauch, "Spherical near-field scanning: Experimental and theoretical studies," NISTIR 3955, National Institute of Standards and Technology, 1990.
- [9] R. C. Wittmann, C. F. Stubenrauch, and M. H. Francis, "Spherical scanning measurements using truncated data sets," in *Proceedings of the 24th AMTA Annual Meeting & Symposium*, pp. 279–283, November 2002.
- [10] G. H. Golub and C. F. Van Loan, *Matrix Computations*, The Johns Hopkins University Press, Baltimore, Md, USA, 1989.

Research Article

A Probe-Compensated Helicoidal NF-FF Transformation for Aperture Antennas Using a Prolate Spheroidal Expansion

**Amedeo Capozzoli,¹ Claudio Curcio,¹ Giuseppe D'Elia,¹ Flaminio Ferrara,²
Claudio Gennarelli,² Rocco Guerriero,² and Angelo Liseno¹**

¹*Dipartimento di Ingegneria Biomedica, Elettronica e delle Telecomunicazioni, Università di Napoli Federico II, Via Claudio 21, 80125 Napoli, Italy*

²*Dipartimento di Ingegneria Elettronica ed Ingegneria Informatica, Università di Salerno, via Ponte Don Melillo, Salerno, 84084 Fisciano, Italy*

Correspondence should be addressed to Claudio Gennarelli, gennar@diie.unisa.it

Received 10 October 2011; Accepted 23 January 2012

Academic Editor: Jeff Fordham

Copyright © 2012 Amedeo Capozzoli et al. This is an open access article distributed under the Creative Commons Attribution License, which permits unrestricted use, distribution, and reproduction in any medium, provided the original work is properly cited.

A new probe-compensated near-field-far-field (NF-FF) transformation for aperture antennas in a cylindrical scanning geometry is presented. Such a technique takes the advantage of the NF data acquisition made according to a very efficient sampling strategy along a helix and exploits a proper aperture field expansion based on the use of the prolate spheroidal wave functions (PSWFs), accounting for the a priori information on shape and size of the antenna under test. The unknown aperture field expansion coefficients of the PSWFs are evaluated from the acquired voltage samples by an inversion process using a regularized version of the singular value decomposition method. Experimental results on connected and disconnected radiating aperture antennas, including sum and difference patterns, show the effectiveness of the approach and, in particular, how it enables a serious reduction of the measurement points without impairing the FF estimation accuracy.

1. Introduction

As well known, near-field-far-field (NF-FF) transformations represent nowadays a widely used technique for antenna characterization as an alternative to measurements directly performed in the far zone of the radiating system [1–4]. Moreover, the pattern evaluation from NF measurements, carried out in a controlled environment (anechoic chamber), allows overcoming those drawbacks which make the measurement of the radiation pattern in a conventional FF range unpractical for electrically large antennas. In this framework, reducing the NF acquisition time is assuming an ever growing relevance for the antenna measurement community. In fact, such a time is currently very much greater than that needed to perform the corresponding NF-FF transformation.

An effective way to reduce the measurement time in a NF cylindrical facility is the use of the innovative helicoidal scanning technique [5–9], which can be accomplished by means of continuous and synchronized movements of the

positioning systems of the probe and antenna under test (AUT), as suggested by Yaccarino et al. in [10]. The technique in [5–9] relies on the “nonredundant sampling representations” of electromagnetic (EM) fields in [11] and uses optimal sampling interpolation (OSI) formulas to reconstruct the NF data required by the standard NF-FF transformation with cylindrical scanning [12, 13]. The drastic time saving so achieved is due both to the use of continuous movements and to the significantly reduced number of needed NF data. The resulting NF-FF transformation has proved to be accurate, stable, and efficient. In particular, effective AUT modellings [7–9] have been used when dealing with antennas having a predominant dimension and allowed a further reduction of needed NF data with respect to the spherical AUT modelling [5, 6]. However, when dealing with aperture antennas, such an additional a priori information available on the AUT can be conveniently exploited to provide the aperture field with an effective representation, suitably accounting for its shape and size as well as for its radiating features, thus further

reducing the overall number of parameters to be sought for and improving the achievable accuracy [14–16].

Following the approach in [16], herewithin, we present an approach to the near-field characterization of aperture antennas in a cylindrical geometry based on the joint use of a proper helicoidal scanning and an efficient modal representation of the aperture field leading back the NF-FF transformation to an inversion step and a prompt subsequent radiation step. More in detail,

- (i) the measurement voltages are acquired along a helicoidal curve determined according to the above-quoted approaches [6–9];
- (ii) the prolate spheroidal wave functions (PSWFs) [17, 18], which are able to represent the radiative aperture field by a well-defined subspace, are employed in this paper;
- (iii) the unknown aperture field expansion coefficients are evaluated from the measured voltages by an inversion process carried out by means of a regularized version of the singular value decomposition (SVD) approach (first step of the NF-FF transformation);
- (iv) the radiated field is then evaluated by exploiting the link between the subspace spanned by the basis functions used to represent the aperture field and their Fourier transforms (second step of the NF-FF transformation).

It should be noticed that previous efforts have been already pursued in the literature to use the SVD in NF-FF transformations [19]. However and as well known [14], the *sinc* sampling representation of the plane wave spectrum (PWS) radiated by the source is significantly suboptimal as compared to the PSWFs representation.

In contrast with [16], the method is here presented in its complete formulation accounting also for the probe compensation, and the performance is evaluated against experimental tests involving different aperture antenna configurations, enhancing key aspects related, among others, to disconnected aperture domains and field polarization. The experimental results show the effectiveness of the technique and how much it enables to reduce the number of measurement points, leaving the performance unchanged.

The paper is organized in six sections and two appendices.

Section 2 describes the sampling strategy in [6–9] for the helicoidal scanning using effective AUT modellings. Section 3 introduces the PSWF-based representation [15, 16] to be exploited in the case of connected and disconnected rectangular apertures. Section 4 describes the probe-compensated inversion technique using the SVD method and the radiation procedure (steps 1 and 2). In Section 5, the experimental results obtained via the proposed technique are compared with those relevant to the helicoidal NF-FF transformations [6, 8] and to the standard NF-FF cylindrical transformation [12, 13]. Finally, in Section 6, conclusions are drawn and future developments sketched.

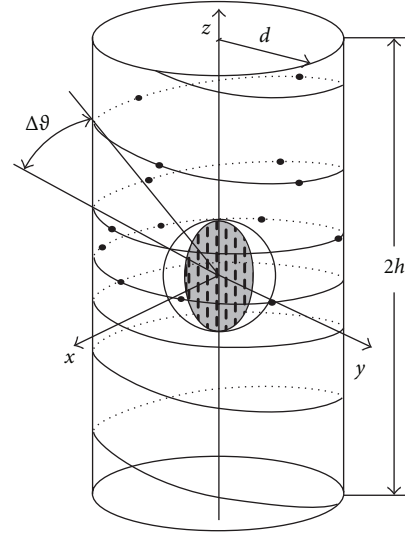


FIGURE 1: Helicoidal scanning.

2. Helicoidal Sampling Strategy

The voltage sampling representation on a cylinder from its samples acquired along a helix (see Figure 1) is summarized in the following.

Let us consider an AUT, enclosed in a convex domain bounded by a surface Σ with rotational symmetry and a nondirective probe scanning a proper helix lying on a cylinder of radius d . The spherical coordinate system (r, ϑ, φ) is adopted to denote an observation point P . Since the voltage measured by a nondirective probe has the same effective spatial bandwidth of the AUT field [20], the “nonredundant sampling representation” of EM fields [11] can be applied to it. Accordingly, when dealing with the voltage representation on an observation curve C , it is convenient to adopt a proper analytical parameterization $\underline{r} = \underline{r}(\eta)$ for describing C and to introduce the “reduced voltage”

$$\tilde{V}(\eta) = V(\eta)e^{j\psi(\eta)}, \quad (1)$$

where $V(\eta)$ is the measured probe voltage and $\psi(\eta)$ is a proper phase function. The band limitation error, occurring when $\tilde{V}(\eta)$ is approximated by a spatially bandlimited function, becomes negligible as the bandwidth exceeds a critical value W_η [11]. Therefore, such an error can be effectively controlled by choosing a bandwidth equal to $\chi' W_\eta$, where $\chi' > 1$ is the bandwidth enlargement factor.

The unified theory of spiral scanings for nonspherical antennas [21], obtained by paralleling the corresponding procedure based on the spherical AUT modelling [22], allows the development of the voltage representation on the cylinder from a minimum number of its samples on the helix. To this end, it is necessary

- (a) to choose the step of the helix coincident with that needed for the interpolation along a generatrix;
- (b) to determine an effective sampling representation along the helix.

In particular, according to [21], the bandwidth W_η and parameterization η relevant to a generatrix and the corresponding phase function ψ are given by

$$\begin{aligned} W_\eta &= \frac{\beta \ell'}{2\pi}, \\ \psi &= \frac{\beta}{2} [R_1 + R_2 + s'_1 - s'_2], \\ \eta &= \frac{\pi}{\ell'} [R_1 - R_2 + s'_1 + s'_2], \end{aligned} \quad (2)$$

where β is the wavenumber, ℓ' is the length of C' (intersection curve between the meridian plane and Σ), $s'_{1,2}$ are the arclength coordinates of the two tangency points $P_{1,2}$ between the cone of vertex at the observation point P and C' , and $R_{1,2}$ are the distances from P to $P_{1,2}$.

The helix can be obtained by projecting on the scanning cylinder a proper spiral wrapping the surface Σ . The projection is obtained via the curves at $\eta = \text{const}$ [21]. The helix step, determined by two consecutive intersections with a generatrix, is equal to the sample spacing $\Delta\eta = 2\pi/(2N'' + 1)$ relevant to a generatrix. Note that $N'' = \text{Int}(\chi N') + 1$ ($\text{Int}(x)$ denotes the integer part of x), $N' = \text{Int}(\chi' W_\eta) + 1$, and $\chi > 1$ is an oversampling factor [11], which controls the truncation error. Accordingly, the parametric equations of the helix, when imposing its passage through a given point Q_0 of the generatrix at $\varphi = 0$, are

$$\begin{aligned} x &= d \cos(\phi - \phi_s), \\ y &= d \sin(\phi - \phi_s), \\ z &= d \cot[\theta(\eta)], \end{aligned} \quad (3)$$

where in ϕ is the parameter describing the helix, ϕ_s is the value of ϕ at Q_0 , and $\eta = k\phi$, k being a parameter related to the helix step by $k = \Delta\eta/2\pi = 1/(2N'' + 1)$.

Let us now denote with ξ and γ the optimal parameter and the phase function, respectively, to get a nonredundant representation along the helix. They can be again determined according to [21]. In particular, ξ is β/W_ξ times the arclength of the projecting point on the spiral wrapping Σ and γ coincides with the phase function ψ relevant to a generatrix, where W_ξ is equal to β/π times the length of the spiral wrapping Σ from pole to pole.

By exploiting the above results, the reduced voltage at any point Q of the helix can be recovered via the OSI expansion [21]:

$$\tilde{V}(\xi) = \sum_{m=m_0-p+1}^{m_0+p} \tilde{V}(\xi_m) \Omega_M(\xi - \xi_m) D_{M''}(\xi - \xi_m), \quad (4)$$

where $2p$ is the number of retained samples $\tilde{V}(\xi_m)$, $m_0 = \text{Int}[(\xi - \xi(\phi_s))/\Delta\xi]$ is the index of the sample nearest (on the left) to Q , and

$$\xi_m = \xi(\phi_s) + m\Delta\xi = \xi(\phi_s) + \frac{2\pi m}{(2M'' + 1)} \quad (5)$$

with $M'' = \text{Int}(\chi M') + 1$ and $M' = \text{Int}(\chi' W_\xi) + 1$. Moreover,

$$\begin{aligned} D_{M''}(\xi) &= \frac{\sin[(2M'' + 1)\xi/2]}{(2M'' + 1)\sin(\xi/2)}, \\ \Omega_M(\xi) &= \frac{T_M[2\cos^2(\xi/2)/\cos^2(\bar{\xi}/2) - 1]}{T_M[2/\cos^2(\bar{\xi}/2) - 1]} \end{aligned} \quad (6)$$

are the Dirichlet and Tschebyscheff sampling functions, respectively, $T_M(\cdot)$ being the Tschebyscheff polynomial of degree $M = M'' - M'$ and $\bar{\xi} = p\Delta\xi$.

Expansion (4) can be properly employed to evaluate the voltage at any point P on the cylinder and, in particular, at those required to carry out the classical NF-FF transformation with cylindrical scanning [12, 13]. Indeed, it allows the evaluation of the “intermediate” samples, that is, the voltages at the intersection points of the helix with the generatrix through P . Once these samples have been determined, the reduced voltage at P can be reconstructed via the following OSI expansion [21]:

$$\tilde{V}(\eta(\vartheta), \varphi) = \sum_{n=n_0-q+1}^{n_0+q} \tilde{V}(\eta_n) \Omega_N(\eta - \eta_n) D_{N''}(\eta - \eta_n), \quad (7)$$

wherein $N = N'' - N'$, $n_0 = \text{Int}[(\eta - \eta_0)/\Delta\eta]$, $2q$ is the number of the retained intermediate samples $\tilde{V}(\eta_n)$, and

$$\eta_n = \eta_n(\varphi) = \eta(\phi_s) + k\varphi + n\Delta\eta = \eta_0 + n\Delta\eta. \quad (8)$$

When the AUT is a quasispherical antenna, it is convenient to consider as surface Σ the smallest sphere of radius a enclosing it. In such a case, $\ell' = 2\pi a$ and $\eta = \vartheta$ so that $W_\eta = \beta a$ and the curves at $\eta = \text{const}$ become radial lines [22]. Moreover,

$$\gamma = \psi = \beta \int_0^r \sqrt{1 - \frac{a^2}{r'^2}} dr' = \beta \sqrt{r^2 - a^2} - \beta a \cos^{-1}\left(\frac{a}{r}\right), \quad (9)$$

and the parameter ξ describing the helix can be expressed in closed form as

$$\xi = \frac{\beta a}{W_\xi} \int_0^\phi \sqrt{k^2 + \sin^2 k\phi'} d\phi', \quad (10)$$

wherein

$$W_\xi = \frac{\beta a}{\pi} \int_0^{(2N''+1)\pi} \sqrt{k^2 + \sin^2 k\phi'} d\phi'. \quad (11)$$

In the case of elongated antennas, an effective modelling is obtained by choosing Σ coincident with the smallest prolate ellipsoid with major and minor semiaxes equal to a and b . Accordingly, the bandwidth W_η , the parameterization η , and the phase function ψ are [7, 8]

$$W_\eta = \left(\frac{4a}{\lambda}\right) E\left(\frac{\pi}{2} \mid \varepsilon^2\right), \quad (12)$$

$$\eta = \frac{\pi}{2} \left[1 + \frac{E(\sin^{-1}u \mid \varepsilon^2)}{E(\pi/2 \mid \varepsilon^2)} \right], \quad (13)$$

$$\gamma = \psi = \beta a \left[v \sqrt{\frac{v^2 - 1}{v^2 - \varepsilon^2}} - E \left(\cos^{-1} \sqrt{\frac{1 - \varepsilon^2}{v^2 - \varepsilon^2}} \mid \varepsilon^2 \right) \right], \quad (14)$$

wherein λ is the wavelength and $u = (r_1 - r_2)/2f$, $v = (r_1 + r_2)/2a$ are the elliptic coordinates, $r_{1,2}$ being the distances from observation point P to the foci of the ellipse C' and $2f$ its focal distance. In the above relations, $\varepsilon = f/a$ is the eccentricity of C' and $E(\cdot \mid \cdot)$ denotes the elliptic integral of second kind.

It is worth noting that, in such a case, the projecting curves are hyperbolas confocal to the ellipse C' . Moreover, the parameter ξ , which is β/W_ξ times the arclength of the projecting point on the spiral wrapping the prolate ellipsoid, and the related bandwidth W_ξ must be numerically evaluated.

3. Aperture Field Representation

It is noted that the rationale of the technique holds for an arbitrary number of disconnected, arbitrarily shaped apertures, as well as for an arbitrarily polarized aperture field. However, in this paper, the approach will be presented in the case of two rectangular-shaped apertures. For each aperture, a separate PSWF expansion is given and the general case of an arbitrarily polarized aperture field will be considered (see Section 4). Furthermore, for the sake of simplicity, when dealing with the unknowns-to-data relation, the attention will be subsequently focused to the two cases of interest for this paper, namely, to tangential aperture field having “vertical” or “horizontal” polarization (in the meaning specified below).

Let us now formally work out the representation. As mentioned, two rectangular apertures, A_1 and A_2 , are considered, both $2a_{ap} \times 2b_{ap}$ sized, with centres at a distance d_a . The radiating system is centred in the $Oxyz$ reference system (see Figure 2). We suppose that the aperture field $\underline{E}_a(x_i, z_i)$ can be either “vertically” polarized, that is, $\underline{E}_a(x_i, z_i) = E_{a_y}(x_i, z_i)\hat{i}_y + E_{a_z}(x_i, z_i)\hat{i}_z$, or “horizontally” polarized, that is, $\underline{E}_a(x_i, z_i) = E_{a_x}(x_i, z_i)\hat{i}_x + E_{a_y}(x_i, z_i)\hat{i}_y$. As well known, the field for $y > 0$ is provided by the knowledge of the projection of the aperture field $\underline{E}_a(x_i, z_i)$ onto the aperture plane xz . Accordingly, in the former case, the field is provided by the knowledge of the function $E_{a_z}(x_i, z_i)$, whereas, in the latter case, by the knowledge of $E_{a_x}(x_i, z_i)$. Therefore, just a representation either for $E_{a_z}(x_i, z_i)$ or $E_{a_x}(x_i, z_i)$ is in order.

Following [14], it is convenient to represent the tangential components of the field on the disconnected aperture $A = A_1 \cup A_2$ by basis functions having support on A and spectrally limited to the visible region of the radiative field. Accordingly, each of the two relevant aperture fields

is represented by means of PSWF expansions, involving different expansion coefficients, that is,

$$E_{a_t}(x_i, z_i) = \begin{cases} \sum_{p=1}^P \sum_{q=1}^Q g_{pq}^{(1)} \Phi_p[c_x, x_i] \Phi_q \left[c_z, z_i - \frac{d_a}{2} \right], & \text{if } (x_i, z_i) \in A_1, \\ \sum_{p=1}^P \sum_{q=1}^Q g_{pq}^{(2)} \Phi_p[c_x, x_i] \Phi_q \left[c_z, z_i + \frac{d_a}{2} \right], & \text{if } (x_i, z_i) \in A_2, \end{cases} \quad t = x, z, \quad (15)$$

where $\Phi_i[c_w, w]$ is the i th, 1D PSWF with “space-bandwidth product” c_w [17, 18], $c_x = a_{ap}u'$, $c_z = b_{ap}v'$, and u' , v' locate the spectral region of interest [14], as $u' \leq \beta$ and $v' \leq \beta$. In (15), $P = \text{Int}[4a_{ap}/\lambda]$, $Q = \text{Int}[4b_{ap}/\lambda]$, and, in our framework, the $g_{pq}^{(1)}$ s and $g_{pq}^{(2)}$ s are the expansion coefficients to be considered as unknowns and to be determined from the knowledge of the voltages delivered by the probe when scanning the measurement curve. Moreover, the 2D PSWFs have separate support over the two apertures A_1 and A_2 and $P \times Q$ represents the number of 2D PSWFs required by each aperture.

4. NF-FF Transformation Technique

In this section, we first derive the link between the unknown expansion coefficients $g_{pq}^{(1)}$ s and $g_{pq}^{(2)}$ s and the measurement voltage V in the case of arbitrarily polarized aperture field. Then, the hypothesis of vertical or horizontal aperture field polarizations will be enforced (Section 4.1). Afterwards, the regularized SVD inversion is described (Section 4.2) and, finally, the radiation process is illustrated (Section 4.3).

4.1. Relevant Unknowns-to-Data Links. Let us begin by observing that the contribution to the radiated electric field at the measurement point (x, y, z) due to the generic aperture element $dx_i dz_i$ located at the point $(x_i, 0, z_i)$ in the aperture plane and corresponding to the aperture field $\underline{E}_a(x_i, z_i) = E_{a_x}(x_i, z_i)\hat{i}_x + E_{a_z}(x_i, z_i)\hat{i}_z$ can be written as [23]

$$\begin{aligned} d\underline{E}^i(x, y, z) &= f(\beta, R) \\ &\times \left\{ -y E_{a_x}(x_i, z_i) \hat{i}_x \right. \\ &\quad + [(z - z_i) E_{a_z}(x_i, z_i) - (x - x_i) E_{a_x}(x_i, z_i)] \hat{i}_y \\ &\quad \left. - y E_{a_z}(x_i, z_i) \hat{i}_z \right\} dx_i dz_i \\ &= dE_x^i \hat{i}_x + dE_y^i \hat{i}_y + dE_z^i \hat{i}_z, \end{aligned} \quad (16)$$

where

$$f(\beta, R) = -\frac{1}{2\pi} \left(\frac{j\beta}{R} + \frac{1}{R^2} \right) \frac{e^{-j\beta R}}{R} \quad (17)$$

and $R = \sqrt{(x - x_i)^2 + y^2 + (z - z_i)^2}$.

Accounting for the probe features, that is, performing the probe compensation, should be in principle carried out by exploiting the plane wave spectrum (PWS) of the radiated field and by taking into account the spectral properties of the probe effective length. However, to unburden the approach, we assume that the probe is located in the far field of the aperture element $dx_i dz_i$ so that the contribution of the latter to V can be calculated as

$$dV^i = h_x(\vartheta_i, \varphi_i) dE_x^i + h_y(\vartheta_i, \varphi_i) dE_y^i + h_z(\vartheta_i, \varphi_i) dE_z^i, \quad (18)$$

where ϑ_i and φ_i are defined in Figure 2 and are such that

$$\begin{aligned} \cos \vartheta_i &= \frac{(z - z_i)}{R}, \\ \sin \varphi_i &= \frac{yx_i}{R_1 d}, \end{aligned} \quad (19)$$

$R_1 = \sqrt{(x - x_i)^2 + y^2}$, d is the radius of the measurement cylinder, and h_x, h_y , and h_z are the x , y , and z components, respectively, of the probe effective length in the $Oxyz$ reference system.

In light of (16) and (18), the voltage V acquired by the probe and due to the whole aperture can be written as

$$\begin{aligned} V(x, y, z) = & - \iint_A f(\beta, R) \{-yE_{ax}(x_i, z_i)h_x(\vartheta_i, \varphi_i) \\ & + [(z - z_i)E_{az}(x_i, z_i) \\ & - (x - x_i)E_{ax}(x_i, z_i)]h_y(\vartheta_i, \varphi_i) \\ & - yE_{az}(x_i, z_i)h_z(\vartheta_i, \varphi_i)\} dx_i dz_i, \end{aligned} \quad (20)$$

where $A = A_1 \cup A_2$ and h_x, h_y , and h_z can be calculated (see Appendix A) according to (A.1) and (A.2).

Equation (20) defines the operator linking the aperture field (and, thus, the coefficients $g_{pq}^{(1)}$ s and $g_{pq}^{(2)}$ s) to the measurement voltage. In the cases of vertical and horizontal polarizations, it specifies as

$$\begin{aligned} V^V(x, y, z) = & - \iint_A f(\beta, R) [(z - z_i)h_y(\vartheta_i, \varphi_i) - yh_z(\vartheta_i, \varphi_i)] \\ & \times E_{az}(x_i, z_i) dx_i dz_i, \end{aligned} \quad (21)$$

$$\begin{aligned} V^H(x, y, z) = & \iint_A f(\beta, R) [yh_x(\vartheta_i, \varphi_i) + (x - x_i)h_y(\vartheta_i, \varphi_i)] \\ & \times E_{ax}(x_i, z_i) dx_i dz_i, \end{aligned} \quad (22)$$

respectively.

The components of the effective length of the probe relevant to the experimental results can be calculated according to [24] (see the Appendix A).

On using the representation (15) and on sampling V^V or V^H at M_P points (x_m, y_m, z_m) of the measurement helix, (21) or (22) can be rewritten as

$$\underline{V} = \underline{T} \underline{g}, \quad (23)$$

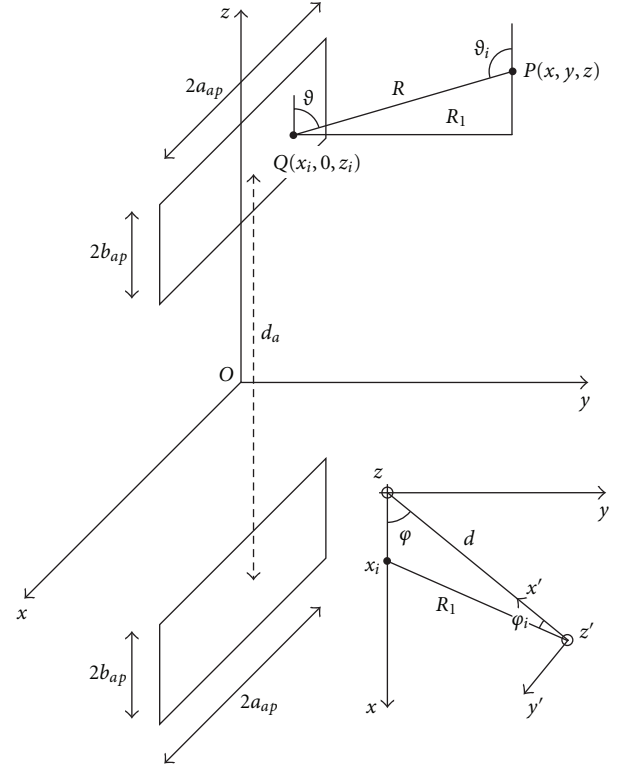


FIGURE 2: Relevant to the geometry of the problem.

where \underline{V} is the $M_P \times 1$ vector containing the M_P voltage samples $V^{V,H}(x_m, y_m, z_m)$, \underline{T} is the block matrix $[\underline{T}_1, \underline{T}_2]$ whose generic element is detailed in Appendix B, and \underline{g} is the $2PQ \times 1$ vector containing the following expansion coefficients:

$$g_h = \begin{cases} g_{pq}^{(1)} & h = (p-1)Q + q, \\ g_{pq}^{(2)} & h = PQ + (p-1)Q + q, \end{cases} \quad (24)$$

$$p = 1, \dots, P, \quad q = 1, \dots, Q.$$

4.2. Regularized SVD Inversion. The characterization of the antenna amounts to the determination of the projection of the aperture field $\underline{E}_a(x_i, z_i)$ onto the aperture plane in terms of \underline{g} . Unfortunately, the inversion of (23) is affected by the ill-conditioning so that a regularized approach should be exploited. A possible solution is herewithin provided by the use of the truncated singular value decomposition (TSVD), even if other regularization strategies are possible [25].

4.3. Radiation. Once the components of the aperture field on the xz plane have been recovered, the φ and ϑ components of the far-field pattern $\underline{E}_\infty(r, \vartheta, \varphi)$ can be determined by resorting to the PWS $\underline{\hat{E}}$ of the radiated field. More in detail,

in the case of vertical polarization, the ϑ component is of interest, which can be determined as

$$E_{\infty\vartheta}(r, \vartheta, \varphi) \propto \frac{v}{\sqrt{1 - (w/\beta)^2}} \hat{E}_z(u, v) \frac{e^{-j\beta r}}{r}, \quad (25)$$

whereas, in the case of horizontal polarization, the φ component of the far field is sought for, which can be determined as

$$E_{\infty\varphi}(r, \vartheta, \varphi) \propto w \hat{E}_x(u, v) \frac{e^{-j\beta r}}{r}. \quad (26)$$

In (25) and (26), $u = -\beta \sin \vartheta \cos \varphi$, $v = \beta \cos \vartheta$, and $w = \beta \sin \vartheta \sin \varphi$.

By exploiting the Fourier transform relationship between the component $\hat{E}_t(u, v)$ homologous to E_{a_t} , $t = x, z$, having determined the expansion coefficients $g_{pq}^{(1)}$ s and $g_{pq}^{(2)}$ s, exploiting the properties of the PSWFs [17, 18], $\hat{E}_t(u, v)$ can be calculated as

$$\hat{E}_t(u, v) = \hat{E}_t^{(1)}(u, v) e^{jv(d_a/2)} + \hat{E}_t^{(2)}(u, v) e^{-jv(d_a/2)}, \quad (27)$$

where

$$\begin{aligned} \hat{E}_t^{(i)}(u, v) = & -\frac{1}{2\pi} \sum_{p=1}^P \sum_{q=1}^Q g_{pq}^{(i)} j^{(p+q)} \\ & \times \sqrt{\frac{a_{ap} b_{ap}}{u' v'}} \sqrt{\lambda_p(c_x) \lambda_q(c_x)} \\ & \times \Phi_p \left[c_x, \frac{a_{ap}}{u'} u \right] \Phi_q \left[c_y, \frac{b_{ap}}{v'} v \right] \end{aligned} \quad (28)$$

and $\lambda_i(c_w)$ is the eigenvalue corresponding to the i th, 1D PSWFs. Obviously, as an alternative to (27) and (28), $\hat{E}_t(u, v)$ can be evaluated by fast routines for the calculation of the Fourier transform provided that they are available.

5. Experimental Results

The approach described in the previous section has been experimentally validated in the anechoic chamber available at the Antenna Characterization Lab of the University of Salerno, which is provided with a NF facility system supplied by MI Technologies. The dimensions of the chamber are $8 \text{ m} \times 5 \text{ m} \times 4 \text{ m}$. Pyramidal absorbers are positioned in order to minimize the reflections. The chamber is equipped with a vertical scanner and a rotating table, so that, by properly matching their movements, the NF data can be acquired at any point on a cylindrical surface surrounding the AUT. The vertical scanner can cover an extension of 240 cm and is characterized by a linear precision of $\pm 0.005 \text{ cm}$. The rotating table, mounted with its rotary axis parallel to the vertical scanner, ensures an angular precision of $\pm 0.09^\circ$. The controller is able to simultaneously drive both the positioners. A vectorial network analyzer Anritsu 37247C provides measurements of both amplitude and phase with a wide dynamic range, high sensitivity, and linearity over



FIGURE 3: Pictorial view of the measurement system.

the range from 40 MHz to 20 GHz. An open-ended MI-6970-WR90 rectangular waveguide, whose end is tapered for minimizing the diffraction effects, is used as probe. A pictorial view of the measurement system is reported in Figure 3.

The measurements, performed at 10 GHz, refer to three test cases: a single horn with vertical polarization, a dual horn with vertical polarization for the case of sum pattern, and a dual horn with horizontal polarization for the two cases of sum and difference patterns.

The first case is considered to show the performance of the method when, at variance with [16], probe compensation is applied. The second case extends the first one to a configuration with two disconnected rectangular apertures. Finally, the third case is introduced to evaluate the performance of the approach in dependence on the polarization and on the radiated beam configuration (sum, difference).

The performance of the approach is benchmarked against the effective techniques in [6–8] based on the sampling representation of the near field, with the aim of showing how the developed approach is capable to reduce the number of required measurements, at the cost of being able to reconstruct the far-field pattern in the only $y > 0$ half space. All the presented results concerning the approaches in [6–8] are probe compensated.

5.1. Single Horn. Let us consider first the case of a single X-band, vertically polarized pyramidal horn antenna with a $0.194 \text{ m} \times 0.144 \text{ m}$ sized aperture. In this case, the domain A consists of only one aperture.

According to the helicoidal sampling strategy described in Section 2 and relevant to the spherical AUT modelling, 1922 NF data have been acquired all around the AUT along a helix lying on a cylinder with radius $d = 0.434 \text{ m}$ and height $h = 2.4 \text{ m}$ (see Figure 1), in order to compare the here proposed approach with the experimental results in [6].

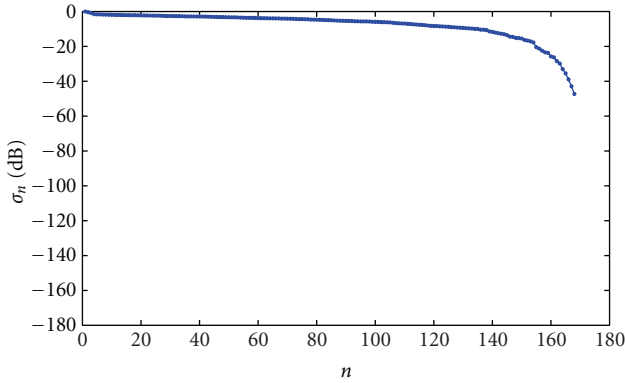
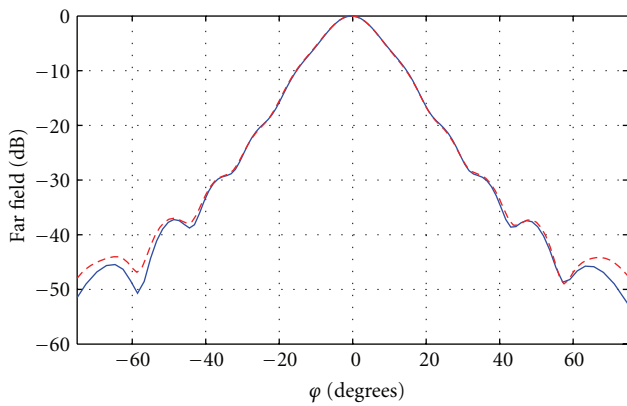


FIGURE 4: Single horn. Singular values.

FIGURE 5: Single horn. φ cut of the ϑ component of the far field. Blue solid line: proposed approach. Red dashed line: approach in [6].

The presented method has been applied to a set of NF data obtained from the original 1922 NF points by first rejecting all those points falling outside an azimuthal angle of 170° in front of the AUT and then by decimating by a factor of two the remaining ones. A resulting set of 453 points has been exploited, and an aperture field expansion involving a number of $P \times Q = 14 \times 12$ PSWFs has been considered.

Figure 4 depicts the behavior of the singular values of the matrix \underline{T} . For this and all the other experimental test cases, the TSVD has been implemented by cutting all the singular values below a threshold set at -40 dB below the maximum one. As it can be seen, only few singular values are dropped and the problem ill-conditioning is not critical for this case.

Figures 5 and 6 show φ and ϑ cuts of the ϑ component of the far field retrieved by the proposed approach and that obtained by the approach in [6, 22]. The agreement between the far field predicted by the approach in [6, 22] and direct far-field measurements has been already reported in [6, 16]. At variance with the results shown in [16], where probe compensation was disregarded, in Figures 5 and 6, probe compensation has been applied for our approach. As can be seen, despite the significant reduction of the number of NF measurement points, the proposed approach still guarantees accurate results, when the interest is focused on the pattern radiated in the front of the AUT, as in the considered case of aperture antennas. On the contrary, the approach in [6, 22],

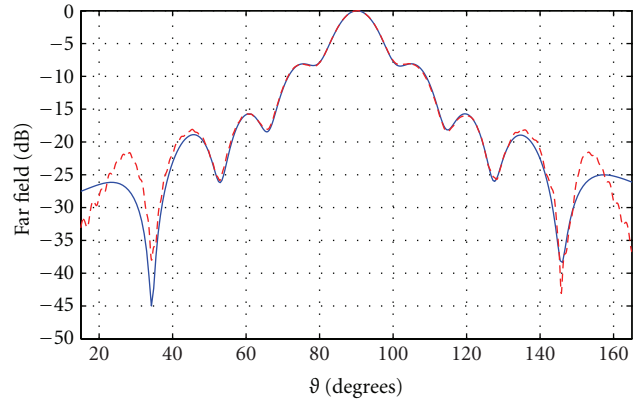
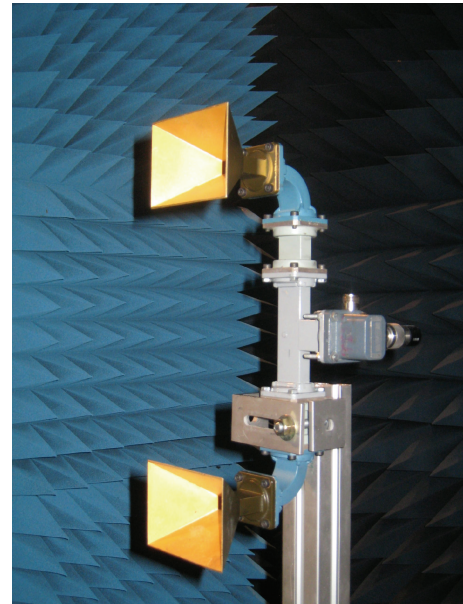
FIGURE 6: Single horn. ϑ cut of the ϑ component of the far field. Blue solid line: proposed approach. Red dashed line: approach in [6].

FIGURE 7: Photo of the vertically polarized dual horn.

even if it requires a greater number of NF data, allows the reconstruction of the complete azimuthal pattern.

5.2. Dual Horn: Vertical Polarization. Experimental results relevant to the characterization of an X-band, dual pyramidal horn antenna with vertical polarization are now illustrated.

Each horn has a $2a_{ap} \times 2b_{ap} = 0.089 \text{ m} \times 0.068 \text{ m}$ sized aperture, and the centre-to-centre distance d_a between the apertures is 0.265 cm (see Figure 7). The NF data have been acquired on a helix wrapping a cylinder with radius $d = 0.196 \text{ m}$ and height $h = 2.40 \text{ m}$. A number of 1946 NF samples has been collected all around the AUT to apply the technique in [7, 8]. As before, the presented approach has been applied to the original set of NF data after having rejected all the points falling outside an azimuthal angle of 170° in front of the AUT and then decimating the remaining points by a factor of 2, thus obtaining 461 near-field samples. The aperture field expansion has comprised a number of

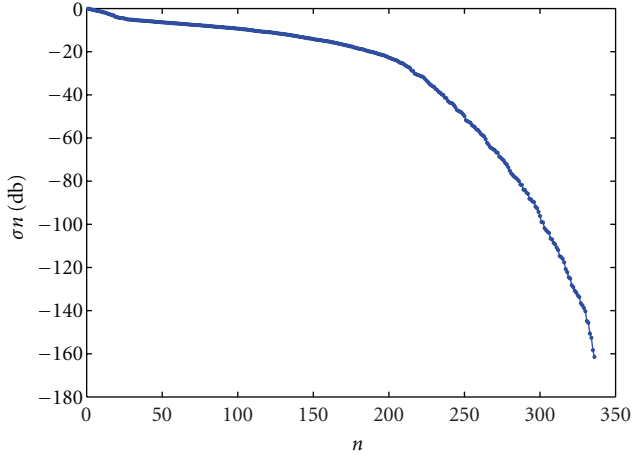


FIGURE 8: Dual horn, vertical polarization. Singular values.

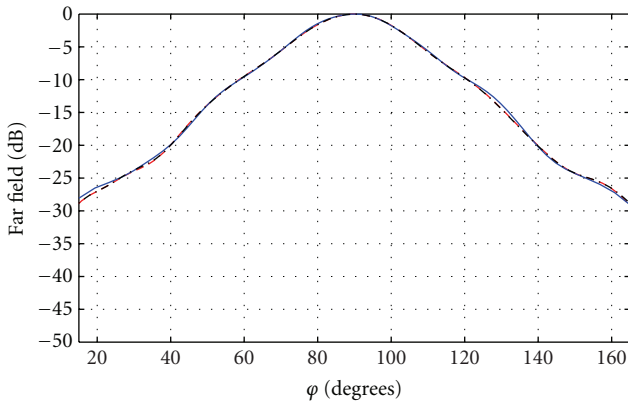


FIGURE 9: Dual horn, vertical polarization. φ cut of the ϑ component of the far field. Blue solid line: proposed approach. Red dashed line: approach in [7, 8]. Black dash-dot line: standard, probe-compensated NF-FF transformation.

$P \times Q = 12 \times 9$ PSWFs for each one of the radiating apertures. Finally, for the sake of comparisons, NF data have been acquired on the classical cylindrical grid to get the far field via the probe-compensated NF-FF transformation [13]. In this case, a number of 6440 NF samples has been required.

Figure 8 displays the behaviour of the singular values of \underline{T} for the considered case. As it can be seen, now many more singular values fall below the -40 dB threshold and so the problem ill-conditioning is more critical as it occurred for the foregoing case. This can be mainly ascribed to the mismatch between the spheroidal modelling of the source employed to determine the field sampling and the planar, disconnected modelling of the source, detailed in Section 3, and used to perform the inversions.

Figures 9 and 10 compare the φ and ϑ cuts of the ϑ component of the far fields obtained by applying the proposed approach with those relevant to the techniques in [7, 8] and [13]. As can be seen, despite the significant reduction in the number of employed NF samples, the presented approach still guarantees accurate results when recovering the radiated field in the only $y > 0$ half space.

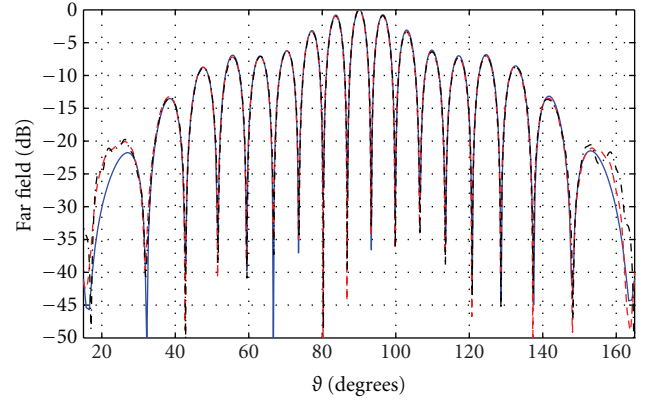


FIGURE 10: Dual horn, vertical polarization. ϑ cut of the ϑ component of the far field. Blue solid line: proposed approach. Red dashed line: approach in [7, 8]. Black dash-dot line: standard, probe-compensated NF-FF transformation.

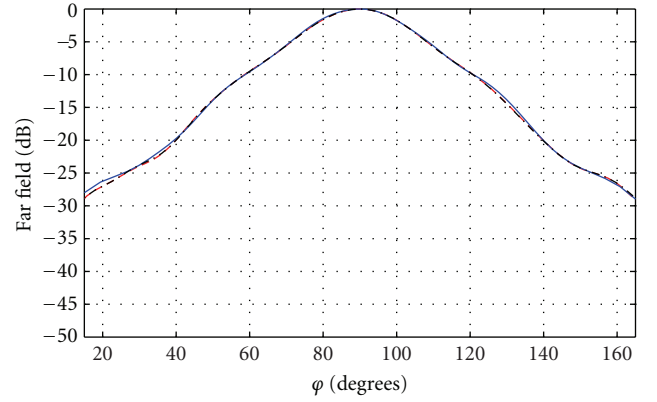


FIGURE 11: Dual horn, vertical polarization. φ cut of the ϑ component of the far field. Blue solid line: proposed approach, when no probe-compensation is applied. Red dashed line: approach in [7, 8]. Black dash-dot line: standard, probe-compensated NF-FF transformation.

On the other side, although requiring a larger number of NF samples, the approach in [7, 8] allows the reconstruction of the full azimuthal pattern, but with a remarkably smaller number of samples as compared to the standard, probe-compensated NF-FF transformation [13].

In order to highlight the need for compensating the receiving features of the probe, in Figures 11 and 12, we show the same results as for Figures 9 and 10, but now when our approach has been applied without any probe compensation. This can be accomplished by setting $h_y = h_z = 1$ in (21). As can be seen, the result worsens, almost entirely for the ϑ cut only. This can be expected since, when the probes rotate around the AUT for a fixed z (and thus move along the φ coordinate), each elementary contribution to the radiated field (see (16)) impinges on the probe itself approximately under the same azimuthal angles so that the elementary contribution to the received voltage (see (18)) experiences approximately the same receiving features of the probe (see Figure 13). On the other side, when the probe moves along the z coordinate for a fixed φ , the elementary field contributions in (16) impinge with different elevation

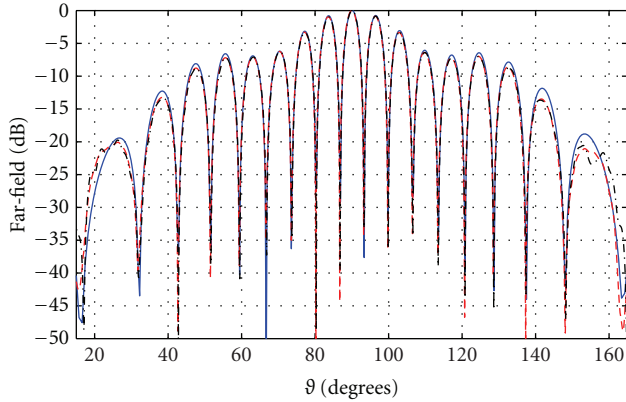


FIGURE 12: Dual horn, vertical polarization. ϑ cut of the ϑ component of the far field. Blue solid line: proposed approach, when no probe compensation is applied. Red dashed line: approach in [7, 8]. Black dash-dot line: standard, probe-compensated NF-FF transformation.

angles so that they experience significantly different receiving features of the probe, which should be then compensated (see Figure 13).

5.3. Dual Horn: Horizontal Polarization. We finally show results concerning the characterization of an X-band, dual pyramidal horn antenna with horizontal polarization.

Each horn has a $2a_{ap} \times 2b_{ap} = 0.068 \text{ m} \times 0.089 \text{ m}$ sized aperture, and the centre-to-centre distance d_a between the apertures is 0.26 cm. The NF data have been acquired again on a helix wrapping a cylinder with radius $d = 0.196 \text{ m}$ and height $h = 2.40 \text{ m}$. A number of 1699 NF samples has been collected all around the AUT for the technique in [7, 8], whereas the presented approach has been applied to such a data set by retaining all the points within an azimuthal angle of 170° in front of the AUT and then decimating them by a factor of 2, obtaining 399 NF samples. A number of $P \times Q = 9 \times 12$ PSWFs for each one of the radiating apertures has been searched for.

The two cases of a sum pattern and of a difference pattern have been dealt with. They have been obtained by setting “in-phase” and “out-of-phase” the aperture fields by properly exploiting a Magic-Tee.

Figures 14 and 15 compare the φ and ϑ cuts, respectively, of the φ component of the far fields obtained by the approach in [7, 8] and by the presented one in the case of sum pattern. The results obtained by the approach in [7, 8] have been already validated for this case in [8] also via direct FF measurements. As it can be seen, again despite the significant reduction in the number of employed NF samples, the presented approach still guarantees accurate results in recovering the radiated field in the only $y > 0$ half space. For reader’s convenience, Figure 16 shows the amplitude and phase of the aperture field for the domain $A = A_1 \cup A_2$ which appears to be “in-phase,” and Figure 17 shows a 2D image of the φ component of the radiated field in the spectral, uv plane.

Finally, Figure 18 shows the good agreement between the ϑ cut of the φ component of the far fields obtained

by the two compared approaches in the case of difference pattern, where the results obtained by the approach in [7, 8] have been already validated in [8] for this case. The φ cut is not shown since it is obviously vanishing. Furthermore, Figure 19 displays the amplitude and phase of the aperture field for the domain $A = A_1 \cup A_2$ which now appears to be “out-of-phase,” whereas Figure 20 shows a 2D image of the φ component of the radiated field in the spectral, uv plane.

6. Conclusions and Future Developments

In this paper, a new NF-FF transformation technique for the characterization of aperture antennas in a cylindrical geometry has been proposed. The approach exploits a fast scanning strategy based on a “nonredundant sampling representation” of the near field and on synchronous movements of probe and AUT. It allows the characterization of aperture antennas, even with disconnected apertures, and conveniently exploits the available a priori information on the AUT shape and size. The technique performs also a proper compensation of the probe effects and exploits a regularized version of the SVD approach.

The experimental analysis performed on single or dual horn antennas, involving different aperture field polarizations and beam configurations (sum, difference), and the comparisons with the effective approach in [6, 8] have highlighted that the proposed technique requires a significantly lower number of NF samples to guarantee an accuracy comparable to that in [6, 8], when the interest is focused on the pattern radiated in the half space in front of the AUT. Of course, the approach in [6, 8], even if in need for a greater number of NF data, allows the reconstruction of the full azimuthal pattern.

Future developments of the presented technique regard extensions to

- (i) different scanning configurations, for example, planar spiral scanning [26];
- (ii) different shapes for the AUT apertures (e.g., circular [27]).

Appendices

A. Probe Compensation Formulas

The components $h_x, h_y,$ and h_z can be related to the Cartesian components $h_{x'}, h_{y'},$ and $h_{z'}$ of the probe effective length in the $Ox'y'z'$ probe reference system as (Figure 2)

$$\begin{aligned} h_x(\vartheta_i, \varphi_i) &= -h_{x'}(\vartheta_i, \varphi_i) \cos \varphi + h_{y'}(\vartheta_i, \varphi_i) \sin \varphi, \\ h_y(\vartheta_i, \varphi_i) &= -h_{x'}(\vartheta_i, \varphi_i) \sin \varphi - h_{y'}(\vartheta_i, \varphi_i) \cos \varphi, \\ h_z(\vartheta_i, \varphi_i) &= h_{z'}(\vartheta_i, \varphi_i), \end{aligned} \quad (\text{A.1})$$

where $\cos \varphi = x/d$, $\sin \varphi = y/d$, and the $Ox'y'z'$ probe reference system is understood to be oriented so that the probe aperture is centered in the $y'z'$ plane, while the x' axis points towards the z axis. The components $h_{x'}, h_{y'},$ and $h_{z'}$,

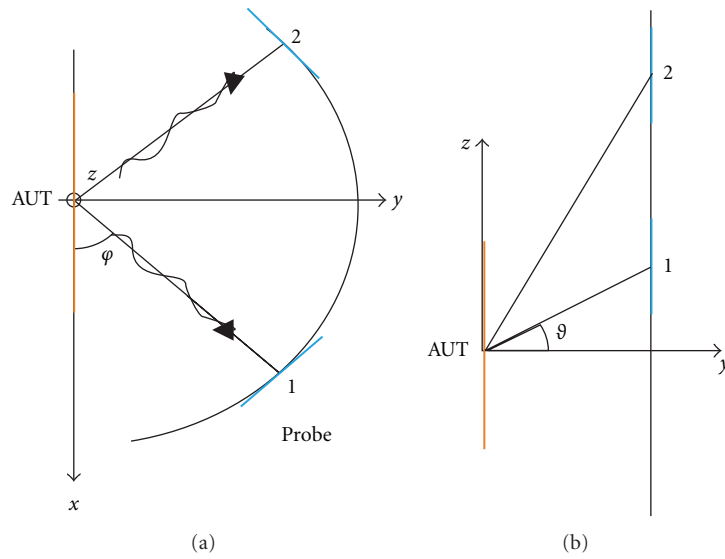


FIGURE 13: Illustrating the need for probe compensation. When the probe rotates around the AUT from position 1 to 2 (a), approximately the same receiving features of the probe are involved. When the probe moves along the z axis from position 1 to 2 (b), different receiving features of the probe become relevant.

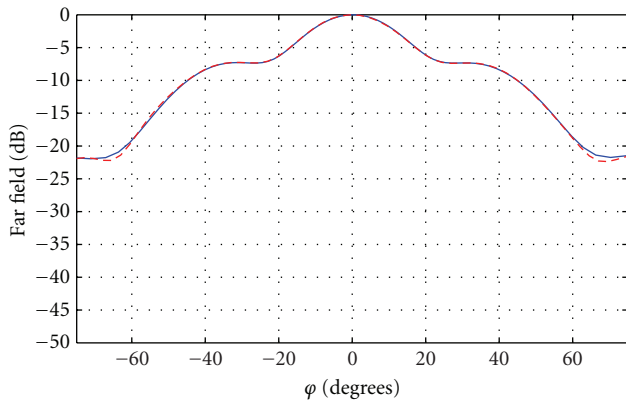


FIGURE 14: Dual horn, horizontal polarization, sum pattern. φ cut of the φ component of the far field. Blue solid line: proposed approach. Red dashed line: approach in [7, 8].

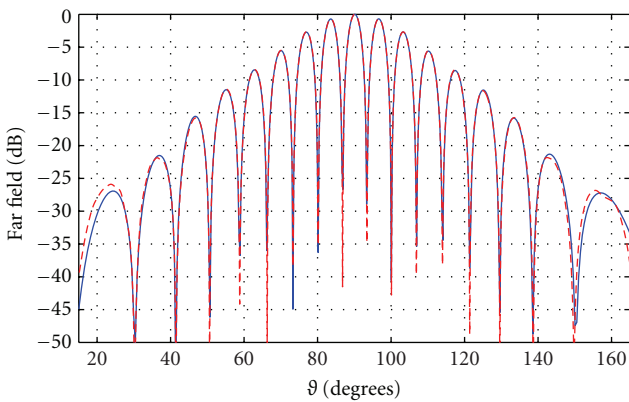


FIGURE 15: Dual horn, horizontal polarization, sum pattern. ϑ cut of the φ component of the far field. Blue solid line: proposed approach. Red dashed line: approach in [7, 8].

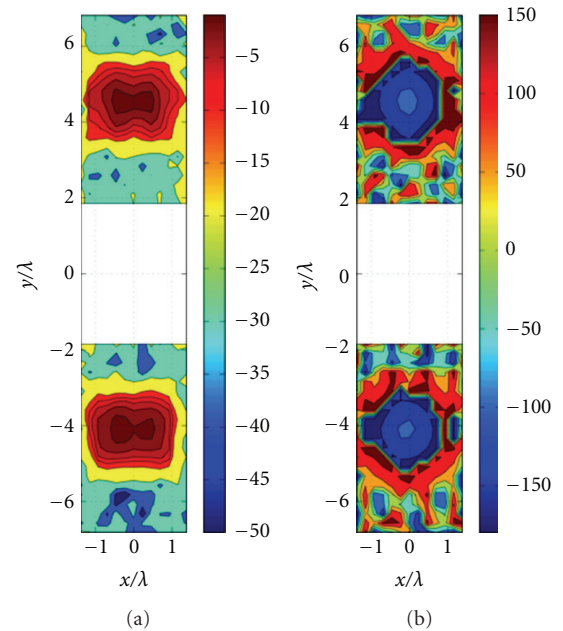


FIGURE 16: Dual horn, horizontal polarization, sum pattern. (a) amplitude of the aperture field distribution. (b) phase of the aperture field distribution.

in turn, can be linked to the ϑ' and φ' components $h_{\vartheta'}$ and $h_{\varphi'}$ as

$$h_{x'}(\vartheta_i, \varphi_i) = h_{\vartheta'}(\vartheta_i, \varphi_i) \cos \vartheta_i \cos \varphi_i - h_{\varphi'}(\vartheta_i, \varphi_i) \sin \varphi_i,$$

$$h_{y'}(\vartheta_i, \varphi_i) = h_{\vartheta'}(\vartheta_i, \varphi_i) \cos \vartheta_i \sin \varphi_i + h_{\varphi'}(\vartheta_i, \varphi_i) \cos \varphi_i,$$

$$h_{z'}(\vartheta_i, \varphi_i) = -h_{\vartheta'}(\vartheta_i, \varphi_i) \sin \vartheta_i.$$

(A.2)

The probe employed in this paper for the measurements is an $a \times b$ sized open-ended rectangular waveguide [24].

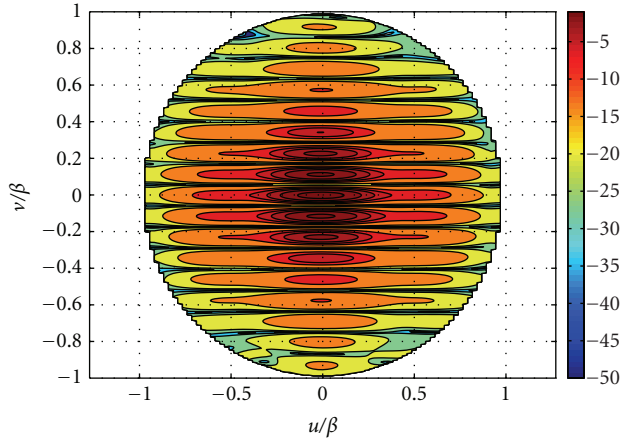


FIGURE 17: Dual horn, horizontal polarization, sum pattern. Amplitude of the φ component of the far field.

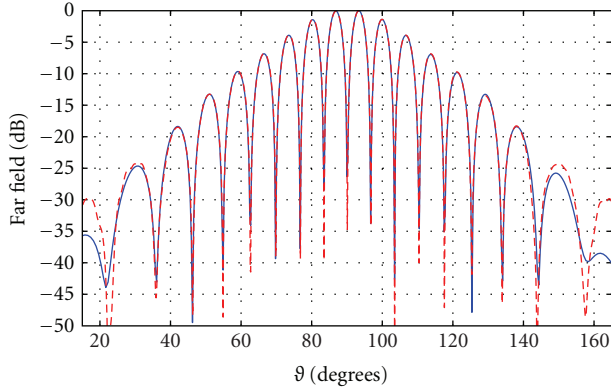


FIGURE 18: Dual horn, horizontal polarization, difference pattern. ϑ cut of the φ component of the far field. Blue solid line: proposed approach. Red dashed line: approach in [7, 8].

The dimensionless components h_{ϑ_S} and h_{φ_S} of the probe effective length in the $Ox_S y_S z_S$ reference system, the same employed in [24], are

$$\begin{aligned}
 h_{\vartheta_S}(\vartheta_S, \varphi_S) &= \left\{ \frac{4}{\pi^2} \left[1 + \left(\frac{k_{TE_{10}}}{\beta} \right) + \Gamma \left(1 - \left(\frac{k_{TE_{10}}}{\beta} \right) \right) \right] + C_0 \right\} \\
 &\quad \times \sin \varphi_S \frac{1 + (k_{TE_{10}}/\beta) \cos \vartheta_S \sin(\beta(b/2) \sin \vartheta_S)}{1 + (k_{TE_{10}}/\beta) \beta(b/2) \sin \vartheta_S}, \\
 h_{\varphi_S}(\vartheta_S, \varphi_S) &= \cos \varphi_S \cos \left(\beta \left(\frac{a}{2} \right) \sin \vartheta_S \right) \\
 &\quad \times \left[\frac{\cos \vartheta_S + (k_{TE_{10}}/\beta) + \Gamma (\cos \vartheta_S - (k_{TE_{10}}/\beta))}{(\pi/2)^2 - (\beta(a/2) \sin \vartheta_S)^2} \right. \\
 &\quad \left. + C_0 \right]
 \end{aligned} \tag{A.3}$$

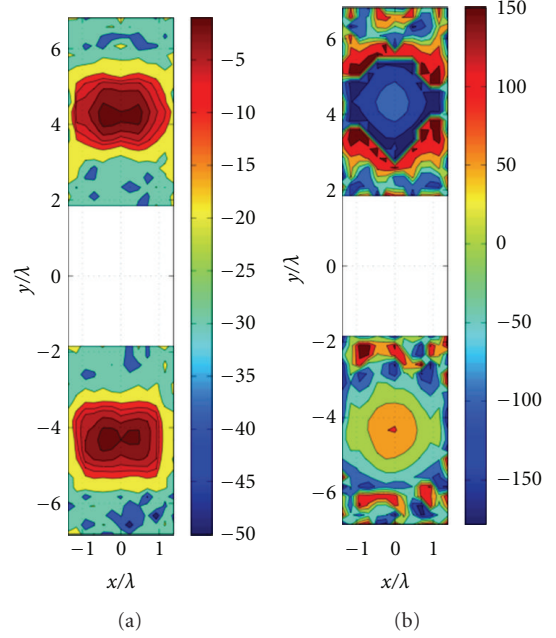


FIGURE 19: Dual horn, horizontal polarization, difference pattern. (a) amplitude of the aperture field distribution. (b) phase of the aperture field distribution.

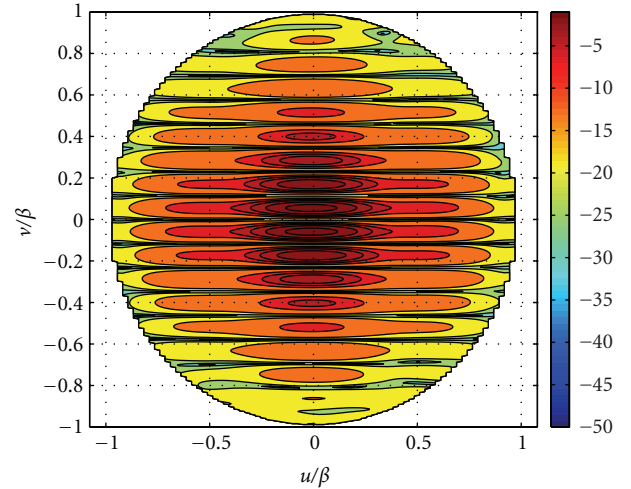


FIGURE 20: Dual horn, horizontal polarization, difference pattern. Amplitude of the φ component of the far field.

where ϑ_S and φ_S are the ϑ and φ coordinates of the corresponding reference system, $k_{TE_{10}}$ is the propagation constant of the TE_{10} propagation mode of the $a \times b$ sized rectangular waveguide, and Γ is the reflection coefficient of the TE_{10} mode from the end of the waveguide, whose value at 10 GHz has been measured in [24] and is approximately equal to $0.0603 + j0.2837$. Moreover, C_0 is a real constant whose value (0.129) has been numerically evaluated according to [24].

During the scanning, the probe is oriented so that the electric field polarization for the TE_{10} mode matches the polarization of the aperture field of interest for the AUT (i.e., vertical or horizontal).

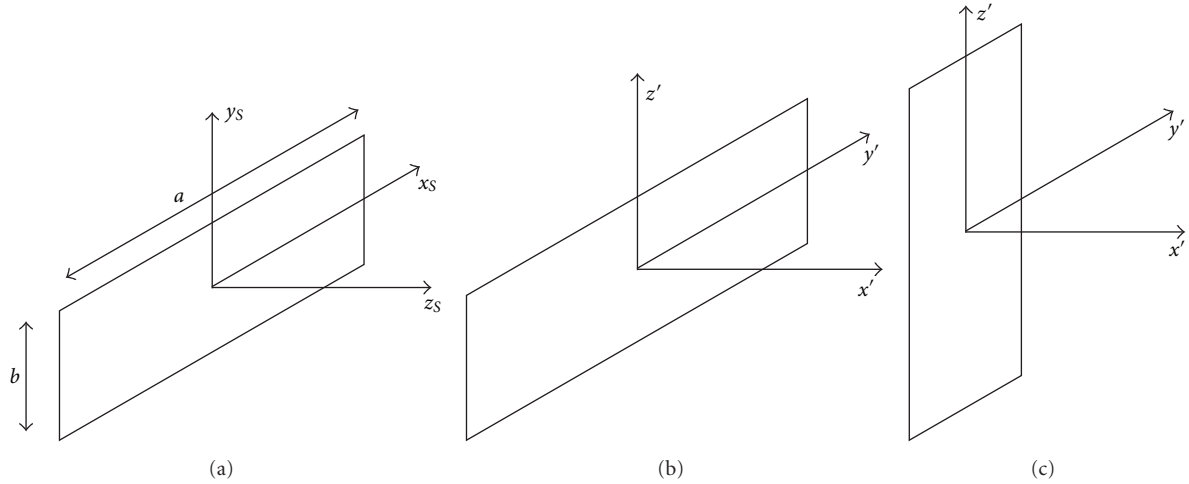


FIGURE 21: Reference systems relevant to the probe compensation. (a) Yaghjian's. (b) vertical polarization. (c) horizontal polarization.

Accordingly, in the case of vertical polarization, $x_s = y'$, $y_s = z'$, and $z_s = x'$ (see Figure 21). Consequently,

$$\tan \varphi_S = \frac{1}{\tan \vartheta_i \sin \varphi_i},$$

$$\cos \vartheta_S = \sin \vartheta_i \cos \varphi_i,$$

$$h_{y'}(\vartheta_i, \varphi_i) = -h_{\vartheta_S}(\vartheta_S, \varphi_S) \cos \varphi_i \sin \varphi_S - h_{\varphi_S}(\vartheta_S, \varphi_S) \frac{\cos \varphi_S}{\sin \vartheta_i},$$

$$h_{\varphi'}(\vartheta_i, \varphi_i) = h_{\vartheta_S}(\vartheta_S, \varphi_S) \frac{\cos \varphi_S}{\sin \vartheta_i} - h_{\varphi_S}(\vartheta_S, \varphi_S) \cos \varphi_i \sin \varphi_S. \quad (\text{A.4})$$

On the other side, in the case of horizontal polarization, $x_s = -z'$, $y_s = y'$, and $z_s = x'$. Thus,

$$\tan \varphi_S = -\tan \vartheta_i \sin \varphi_i,$$

$$\cos \vartheta_S = \sin \vartheta_i \cos \varphi_i,$$

$$h_{y'}(\vartheta_i, \varphi_i) = h_{\vartheta_S}(\vartheta_S, \varphi_S) \cos \varphi_S \cos \varphi_i + h_{\varphi_S}(\vartheta_S, \varphi_S) [\cos \varphi_S \cos \vartheta_i \sin \varphi_i - \sin \varphi_S \sin \vartheta_i],$$

$$h_{\varphi'}(\vartheta_i, \varphi_i) = h_{\vartheta_S}(\vartheta_S, \varphi_S) [\sin \varphi_S \sin \vartheta_i - \cos \varphi_S \cos \vartheta_i \sin \varphi_i] + h_{\varphi_S}(\vartheta_S, \varphi_S) \cos \varphi_S \cos \varphi_i. \quad (\text{A.5})$$

B. The Matrix \underline{T}

The explicit expression of the generic element of the block matrix $\underline{T} = [\underline{T}_1, \underline{T}_2]$ is given by

$$T_{1mh}^V = - \iint_A f(\beta, R_m) [(z_m - z_i)h_y(\vartheta_i, \varphi_i) - y_m h_z(\vartheta_i, \varphi_i)] \times \Phi_p[c_x, x_i] \Phi_q \left[c_z, z_i - \frac{d_a}{2} \right] dx_i dz_i,$$

$$T_{1mh}^H = \iint_A f(\beta, R_m) [y_m h_x(\vartheta_i, \varphi_i) + (x_m - x_i)h_y(\vartheta_i, \varphi_i)] \times \Phi_p[c_x, x_i] \Phi_q \left[c_z, z_i - \frac{d_a}{2} \right] dx_i dz_i,$$

$$T_{2mh}^V = - \iint_A f(\beta, R_m) [(z_m - z_i)h_y(\vartheta_i, \varphi_i) - y_m h_z(\vartheta_i, \varphi_i)] \times \Phi_p[c_x, x_i] \Phi_q \left[c_z, z_i + \frac{d_a}{2} \right] dx_i dz_i,$$

$$T_{2mh}^H = \iint_A f(\beta, R_m) [y_m h_x(\vartheta_i, \varphi_i) + (x_m - x_i)h_y(\vartheta_i, \varphi_i)] \times \Phi_p[c_x, x_i] \Phi_q \left[c_z, z_i + \frac{d_a}{2} \right] dx_i dz_i, \quad (\text{B.1})$$

with $h = (p-1)Q + q$, $p = 1, \dots, P$, $q = 1, \dots, Q$, and $R_m = \sqrt{(x_m - x_i)^2 + y_m^2 + (z_m - z_i)^2}$.

Obviously, the matrices \underline{T}_1 and \underline{T}_2 are constructed by considering only the terms in (B.1) referring to the polarization of interest (i.e., only the terms with the V or H superscripts).

References

- [1] A. D. Yaghjian, "An overview of near-field antenna measurements," *IEEE Transactions on Antennas and Propagation*, vol. AP-34, no. 1, pp. 30–45, 1986.
- [2] "Special Issue on near-field scanning techniques," *IEEE Transactions on Antennas and Propagation*, vol. AP-36, no. 6, pp. 727–901, 1988.
- [3] G. E. Evans, *Antenna Measurement Techniques*, Artech House, Boston, Mass, USA, 1990.
- [4] C. A. Balanis, *Modern Antenna Handbook*, John Wiley & Sons, Hoboken, NJ, USA, 2008.
- [5] O. M. Bucci, C. Gennarelli, G. Riccio, and C. Savarese, "Non-redundant NF-FF transformation with helicoidal scanning," *Journal of Electromagnetic Waves and Applications*, vol. 15, no. 11, pp. 1507–1519, 2001.

- [6] F. D'Agostino, F. Ferrara, C. Gennarelli, R. Guerriero, and M. Migliozzi, "Experimental results validating the near-field to far-field transformation technique with helicoidal scan," *Open Electrical and Electronic Engineering Journal*, vol. 4, pp. 10–15, 2010.
- [7] F. D'Agostino, F. Ferrara, C. Gennarelli, R. Guerriero, and M. Migliozzi, "Near-field—far-field transformation technique with helicoidal scanning for elongated antennas," *Progress in Electromagnetics Research*, vol. 4, pp. 249–261, 2008.
- [8] F. D'Agostino, F. Ferrara, C. Gennarelli, R. Guerriero, and M. Migliozzi, "Laboratory tests assessing the effectiveness of the NF-FF transformation with helicoidal scanning for electrically long antennas," *Progress in Electromagnetics Research*, vol. 98, pp. 375–388, 2009.
- [9] F. D'Agostino, F. Ferrara, J. A. Fordham et al., "An effective near-field-far-field transformation technique for elongated antennas using a fast helicoidal scan," *IEEE Antennas and Propagation Magazine*, vol. 51, no. 4, pp. 134–141, 2009.
- [10] R. G. Yaccarino, L. I. Williams, and Y. Rahmat-Samii, "Linear spiral sampling for the bipolar planar near-field antenna measurement technique," *IEEE Transactions on Antennas and Propagation*, vol. 44, no. 7, pp. 1049–1051, 1996.
- [11] O. M. Bucci, C. Gennarelli, and C. Savarese, "Representation of electromagnetic fields over arbitrary surfaces by a finite and nonredundant number of samples," *IEEE Transactions on Antennas and Propagation*, vol. 46, no. 3, pp. 351–359, 1998.
- [12] W. M. Leach Jr. and D. T. Paris, "Probe compensated near-field measurements on a cylinder," *IEEE Transactions on Antennas and Propagation*, vol. AP-21, no. 4, pp. 435–445, 1973.
- [13] A. D. Yaghjian, "Near-field antenna measurement on a cylindrical surface: a source scattering matrix formulation," Tech. Rep. 696, Government Printing Office, Washington, DC, USA, 1977.
- [14] A. Capozzoli, C. Curcio, G. D'Elia, and A. Liseno, "Phaseless antenna characterization by effective aperture field and data representations," *IEEE Transactions on Antennas and Propagation*, vol. 57, no. 1, pp. 215–230, 2009.
- [15] A. Capozzoli, C. Curcio, G. D'Elia, and A. Liseno, "Singular-value optimization in plane-polar near-field antenna characterization," *IEEE Antennas and Propagation Magazine*, vol. 52, no. 2, pp. 103–112, 2010.
- [16] A. Capozzoli, C. Curcio, G. D'Elia et al., "A SVD-based approach to helicoidal NF-FF transformations," in *Proceedings of the 4th European Conference on Antennas and Propagation (EuCAP '10)*, pp. 1–5, Barcelona, Spain, April 2010.
- [17] B. R. Frieden, "Evaluation, design and extrapolation methods for optical signals, based on use of the prolate functions," in *Progress in Optics*, E. Wolf, Ed., vol. 9, pp. 311–407, North-Holland, Amsterdam, The Netherlands, 1971.
- [18] H. J. Landau and H. O. Pollack, "Prolate spheroidal wave functions, Fourier analysis and uncertainty—III: the dimension of the space of essentially time- and band-limited signals," *Bell System Technical Journal*, vol. 41, pp. 1295–1336, 1962.
- [19] O. M. Bucci, G. D'Elia, F. Soldovieri, and R. Pierri, "An effective strategy in the planar near-field far-field transformation for focussing antennas," in *Proceedings of the 20th ESTEC Antenna Workshop on Millimetre Wave Antenna Technology and Antenna Measurement (ESTEC '97)*, pp. 335–342, Noordwijk, The Netherlands, June 1997.
- [20] O. M. Bucci, G. D'Elia, and M. D. Migliore, "Advanced field interpolation from plane-polar samples: experimental verification," *IEEE Transactions on Antennas and Propagation*, vol. 46, no. 2, pp. 204–210, 1998.
- [21] F. D'Agostino, F. Ferrara, C. Gennarelli, R. Guerriero, and M. Migliozzi, "The unified theory of near-field-far-field transformations with spiral scanings for nonspherical antennas," *Progress In Electromagnetics Research B*, vol. 14, pp. 449–477, 2009.
- [22] F. D'Agostino, C. Gennarelli, G. Riccio, and C. Savarese, "Theoretical foundations of near-field-far-field transformations with spiral scanings," *Progress in Electromagnetics Research*, vol. 61, pp. 193–214, 2006.
- [23] J. W. Goodman, *Introduction to Fourier Optics*, McGraw-Hill, New York, NY, USA, 1996.
- [24] A. D. Yaghjian, "Approximate formulas for the far field and gain of open-ended rectangular waveguide," *IEEE Transactions on Antennas and Propagation*, vol. AP-32, no. 4, pp. 378–384, 1984.
- [25] M. Bertero and P. Boccacci, *Introduction to Inverse Problems in Imaging*, Institute of Physics Publishing, Bristol, UK, 1998.
- [26] F. D'Agostino, F. Ferrara, C. Gennarelli, R. Guerriero, and M. Migliozzi, "An effective NF-FF transformation technique with planar spiral scanning tailored for quasi-planar antennas," *IEEE Transactions on Antennas and Propagation*, vol. 56, no. 9, pp. 2981–2987, 2008.
- [27] D. Slepian, "Prolate spheroidal wave functions, Fourier analysis and uncertainty—IV: extensions to many dimensions; generalized prolate spheroidal functions," *Bell System Technical Journal*, vol. 43, pp. 3009–3057, 1964.

Review Article

Near-Field Antenna Measurements Using Photonic Sensor of Mach-Zehnder Interferometer

Masanobu Hirose, Satoru Kurokawa, Michitaka Ameya, and Koji Komiyama

National Institute of Advanced Industrial Science and Technology, Tsukuba, Ibaraki 305-8568, Japan

Correspondence should be addressed to Masanobu Hirose, masa-hirose@aist.go.jp

Received 15 October 2011; Accepted 19 January 2012

Academic Editor: Amedeo Capozzoli

Copyright © 2012 Masanobu Hirose et al. This is an open access article distributed under the Creative Commons Attribution License, which permits unrestricted use, distribution, and reproduction in any medium, provided the original work is properly cited.

We have been developing a photonic sensor system to measure the electric near-field distribution at a distance shorter than one wavelength from the aperture of an antenna. The photonic sensor is a type of Mach-Zehnder interferometer and consists of an array antenna of 2.4 mm height and 2 mm width on a LiNbO₃ substrate (0.5 mm thickness, 8 mm length, and 3 mm width) supported by a glass pipe. The photonic sensor can be considered to be a receiving infinitesimal dipole antenna that is a tiny metallic part printed on a small dielectric plate at microwave frequency. Those physical and electrical features make the photonic sensor attractive when used as a probe for near-field antenna measurements. We have demonstrated that the system can be applied to planar, spherical, and cylindrical near-field antenna measurements without any probe compensation approximately below 10 GHz. We show the theories and the measurements using the photonic sensor in the three near-field antenna measurement methods.

1. Introduction

The techniques of near-field antenna measurements are the important and prevailing tools for accurate far-field pattern measurements for any kind of antennas [1]. Recently, in the EMC society, the pattern of an antenna used in the SVSWR method [2] is required from 1 GHz up to 6 GHz and it is known that the pattern has significant effects on the validation of test site above 1 GHz and emission measurements [3]. Therefore a compact and easy-to-use equipment for a near-field antenna measurement is desired. The one of the candidates is the near-field antenna measurement system using a photonic sensor [4–6].

A few kinds of electrooptic probes are proposed to detect electric fields or magnetic fields in the air, near antennas or printed boards, and so on. A kind of the probes based on Mach-Zehnder interferometer uses some kinds of antennas on the LiNbO₃ (LN) [7–9]. Another kind of the probes based on polarization modulation uses the crystal bulk [10–13]. Among the probes, we have used the photonic sensor shown below as the one of most promising probes from viewpoints of stability and cost.

The photonic sensor, which detects electric fields by the antenna, consists of a tiny dipole antenna on a LiNbO₃ substrate whose operating principle is a Mach-Zehnder interferometer. The most important characteristic of the sensor is that the sensor can be treated as an infinitesimal dipole antenna working in receiving mode. The merits of the photonic sensor applied to near-field antenna measurements are

- (1) no probe compensation is required below 10 GHz,
- (2) broad band measurements from a few tens MHz to 10 GHz are realized by the single probe,
- (3) the sensor can be treated as the more ideal infinitesimal receiving antenna if the operating frequency becomes the lower,
- (4) the truncation error can be reduced,
- (5) evanescent waves in the immediate vicinity of the aperture can be detected,
- (6) measurement system can be made in small and compact size.

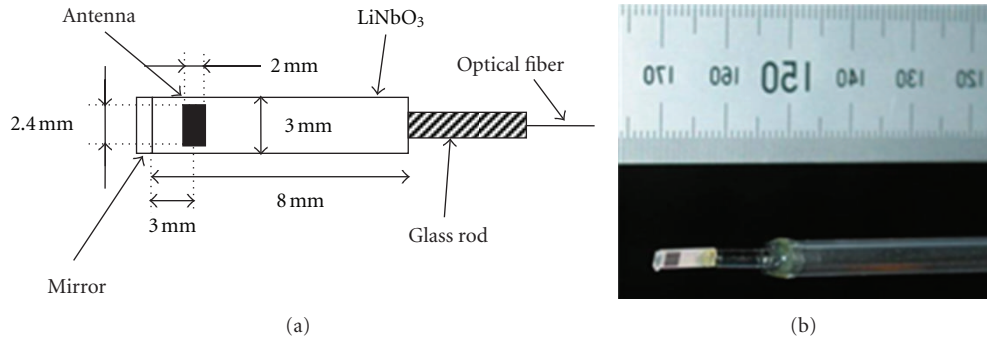


FIGURE 1: Structure of the latest photonic sensor: (a) size and (b) picture.

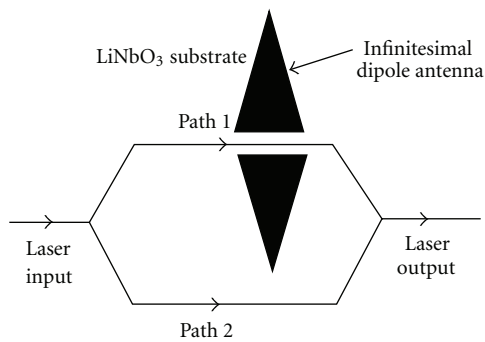


FIGURE 2: Principle of operation.

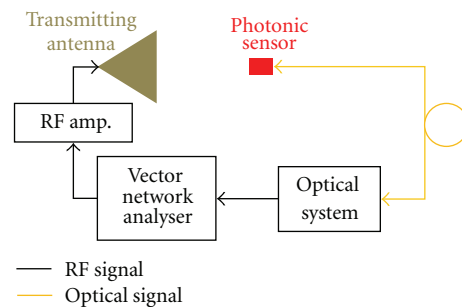


FIGURE 3: Schematic setup for measurements.

Section 2 shows the characteristics of the photonic sensor. Section 3 shows the formulations using the photonic sensor to planar, spherical, and cylindrical near-field antenna measurements and the measurement results for various kinds of antennas are compared with those by various methods. Finally the merits using the photonic sensor are summarized.

2. Photonic Sensor

2.1. Structure and Operating Principle. Our latest photonic sensor is shown in Figure 1 [5, 6]. A small metallic antenna on an LN substrate detects incident electric fields.

The antenna consists of an array of seven short metallic strip dipoles (2.4 mm high, 0.2 mm wide, 0.012 mm gap, and 0.1 mm apart from each element) printed on the LN substrate (0.5 mm thick, 8 mm length, 3 mm width, X-cut, and effective relative permittivity 28) that is connected to a glass rod (called ferrule) to join an optical fiber. The whole of the photonic sensor is supported by a glass pipe that is 5 mm in diameter and 1 mm thick. At the top of the photonic sensor, there is a block of a dielectric optical mirror that reflects laser beams on optical waveguides in the LN substrate.

Figure 2 explains the operating principle of the photonic sensor whose structure is a type of Mach-Zehnder interferometer. The antenna in Figure 2 is a tiny (or infinitesimal)

rhombic dipole antenna that was used as an old type of the photonic sensor. Of course, the principle is entirely the same as that in the latest photonic sensor.

A laser beam along an optical waveguide enters from the left side and splits into two beams at an optical Y-junction. The two beams are combined into one beam at the right-side of an optical Y-junction. Then the output laser beam is travelling along an optical fiber and detected by a photo-detector or to convert an optical signal to a RF signal.

An external electric field excites a voltage at the centre gap of the dipole antenna. When the voltage is applied to one of the optical waveguides (the path 1 in Figure 2), the refractive index of the part of the LN substrate changes depending on the applied voltage due to the Pockels effect. It makes the optical length of the path 1 different from that of the path 2. Since two beams through each path interfere with each other, the amplitude of the combined beam changes depending on the applied voltage. By detecting instantaneously the amplitude of the laser using the photodiode, we can measure the external electric field instantaneously.

The type of the photonic sensor that we use is called a reflection type because the dielectric mirror is placed between the antenna and the right-side of the Y-junction. Owing to this structure, the sensitivity of the sensor is doubled because the laser beam in the path 1 is modulated two times on a lap.

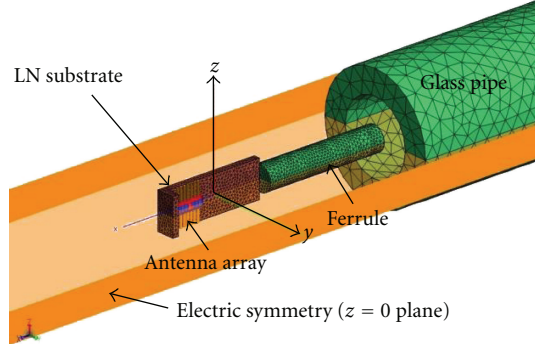
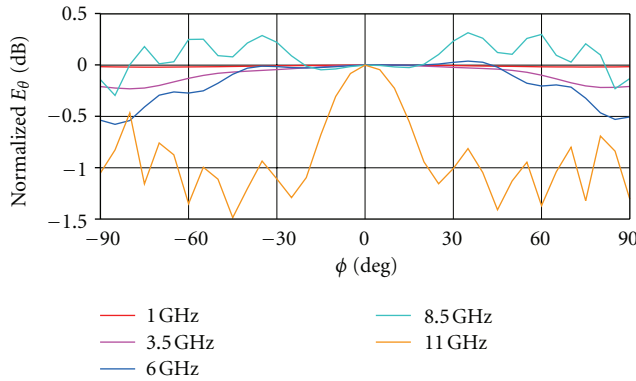


FIGURE 4: Model meshed by FEKO.


 FIGURE 5: Normalized E_θ pattern in the x - y plane.

2.2. Relation between Incident Electric Field and Measured S_{21} .

Figure 3 shows the schematic setup for antenna measurements using the photonic sensor. The photonic sensor can detect the electric field radiated by the transmitting antenna at a small region or effectively a point of space where the sensor is placed because the antenna on the photonic sensor is infinitesimal effectively.

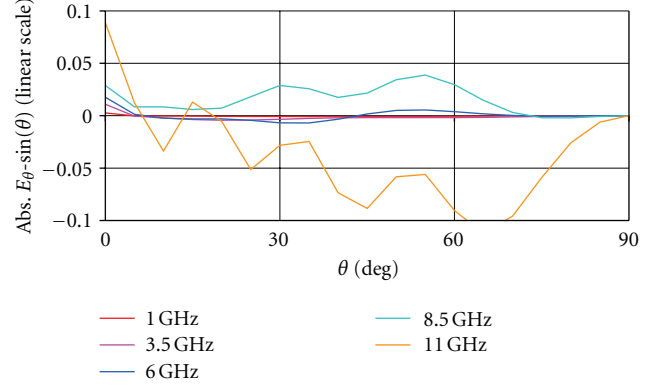
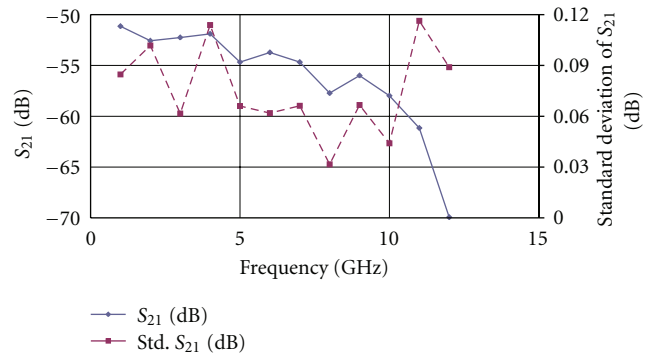
Therefore the S_{21} between the transmitting antenna and the photonic sensor is measured by a vector network analyser (VNA) and expressed as

$$S_{21} = \alpha \hat{\mathbf{p}} \cdot \frac{\mathbf{E}(\mathbf{r})}{a_0}, \quad (1)$$

where α is a constant including the error terms of the system and the reflection coefficient of the transmitting antenna, $\hat{\mathbf{p}}$ is the unit vector parallel to the dipole moment vector of the photonic sensor, $\mathbf{E}(\mathbf{r})$ is the electric field at a position vector \mathbf{r} , and a_0 is the complex amplitude of the incoming wave into the antenna.

From the plane-wave scattering-matrix theory of antennas [14], we have proved (1) clearly in [4]. More intuitively, the same equation can be derived from the concept of the open voltage of the antenna.

If the antenna on the photonic sensor is at transmitting mode, the current \mathbf{J}_p on the antenna is considered to be concentrated at a point effectively because the antenna is


 FIGURE 6: Difference between normalized E_θ and $\sin \theta$ in the z - x plane. Linear scale.

 FIGURE 7: Frequency characteristics and the standard deviation of S_{21} of the present antenna measurement system using the photonic sensor.

effectively infinitesimal. On the assumption, the open voltage V_{open} induced on the antenna is approximated as [15]

$$\begin{aligned} -V_{\text{open}} I_{\text{in}} &= \int \mathbf{E}(\mathbf{r} + \mathbf{r}') \cdot \mathbf{J}_p(\mathbf{r}') e^{j\mathbf{k} \cdot \mathbf{r}'} d\mathbf{r}' \\ &\cong \mathbf{E}(\mathbf{r}) \cdot \int \mathbf{J}_p(\mathbf{r}') e^{j\mathbf{k} \cdot \mathbf{r}'} d\mathbf{r}' \\ &= \mathbf{E}(\mathbf{r}) \cdot (\alpha \hat{\mathbf{p}}), \end{aligned} \quad (2)$$

where I_{in} is the input current of the antenna and \mathbf{r}' is the position vector whose origin is the centre of the antenna. Therefore we obtain the same equation as (1) intuitively.

From the above discussion, it is important to determine the maximum frequency where the photonic sensor is treated as an infinitesimal antenna. For the purpose, we have calculated the antenna pattern using the electromagnetic simulator (FEKO [16]).

Figure 4 shows the model after meshing and the electric symmetry at $z = 0$ plane. The relative dielectric constants of the LN substrate, the ferrule, and the glass pipe are assumed to be 28, 4, and 4, respectively. The corresponding mesh sizes are 0.3 mm, 0.3 mm, and 1.2 mm respectively. The excited antenna is the centre in the array of seven elements.

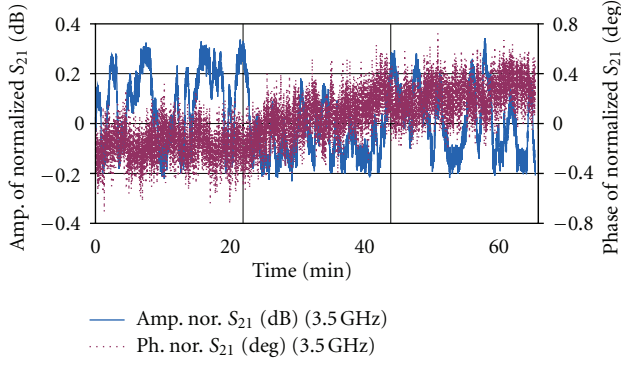


FIGURE 8: Long-term stability of the amplitude and phase of S_{21} normalized by the average value at 3.5 GHz (worst case).

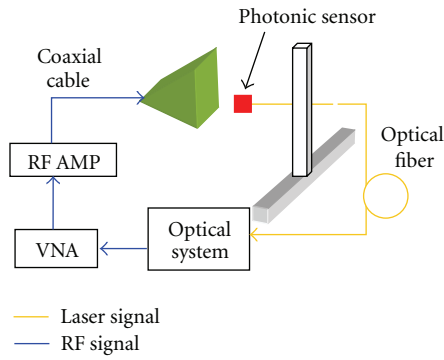


FIGURE 9: Measurement setup using planar scanning.

Figure 5 shows the normalized E_{θ} pattern in the x - y plane. Figure 6 shows the difference between the normalized E_{θ} and $\sin \theta$ in the z - x plane. If the antenna is an infinitesimal antenna, the patterns in the x - y plane and the z - x plane should be isotropic and $\sin \theta$, respectively. Therefore the normalized E_{θ} pattern should be 0 dB in Figure 5 and the difference should be zero in Figure 6 if the antenna is infinitesimal. From Figures 5 and 6, we can consider the photonic sensor as infinitesimal below 8 GHz approximately. The deviation from the infinitesimal dipole is mainly due to the glass pipe to support the sensor. Then if the glass pipe is replaced to a styrene foam, the maximum frequency (for the old sensor) is over 10 GHz from the calculation by FEKO.

2.3. Sensitivity and Stability of System. The sensitivity of the photonic sensor is so low that an RF amplifier must be used in antenna measurements because the power of a conventional VNA is at most 10 dBm. The minimum sensitivity of the sensor is approximately 0.5 V/m at 2.45 GHz. Therefore, to obtain the SNR of S_{21} larger than 40 dB at peak level, the input power greater than 30 dBm or 1 W is required for a standard horn antenna whose gain is 17 dBi at 2.45 GHz.

The frequency characteristics of the system including every characteristics of the antenna (ETS-Lindgren 3115), the coaxial cables (about 10 m), the optical fiber (50 m), and the RF amplifier are shown in Figure 7. The standard deviation is calculated in the time interval of 3 minutes. The

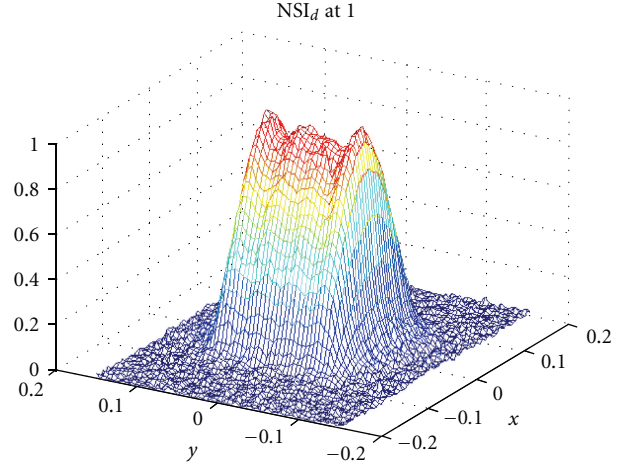


FIGURE 10: The amplitude of S_{21} at 10 mm apart from the aperture of the standard horn antenna measured by the old type of the photonic sensor.

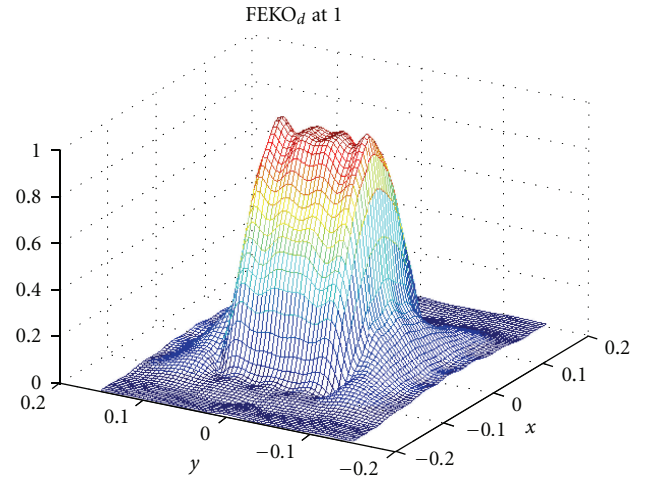


FIGURE 11: The amplitude of E_y at 10 mm apart from the aperture of the standard horn antenna calculated by FEKO.

conditions of each component of the system are described below: the gain of the RF amplifier (HP8348A) is about 35 dB, the cable loss is less than 5 dB at 2.45 GHz, the output power and the IF of the VNA (Agilent E8363C) are set to be 0 dBm and 100 Hz, respectively, the distance between the aperture of the antenna and the photonic sensor is 63 mm. Since the sensor is set in right front of the centre of the antenna aperture, the measured level is almost at maximum.

The measured S_{21} becomes worse above 11 GHz because of the characteristic of the inner RF amplifier of the optical controller (Seiko Giken OEFS-S1). We have verified that the photonic sensor itself can be used up to 18 GHz using another optical system.

The long-term (1 hour) stability at 3.5 GHz (worst case) is shown in Figure 8 because the measuring time of a few hours is a typical in the near-field measurement using the photonic sensor. The standard deviation of the amplitude

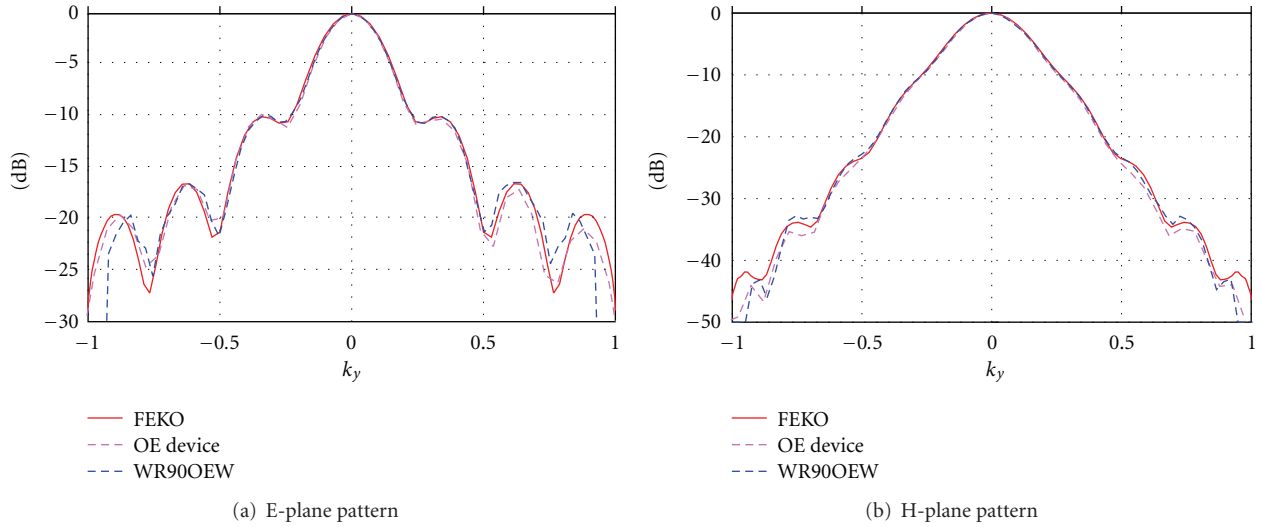


FIGURE 12: Normalized patterns of the standard horn antenna obtained by the old photonic sensor (OE device), the WR90 OEW probe, and FEKO. (a) E-plane pattern. (b) H-plane pattern.

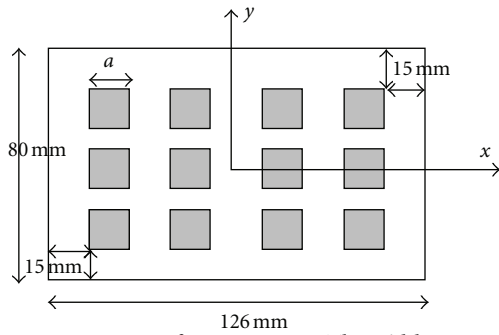


FIGURE 13: 3×4 array of square MSAs. The width $a = 11$ mm for each antenna.

and phase of S_{21} is 0.14 dB and 0.23 degrees. In Figure 8, the amplitude changes about 0.4 dB in a few minutes.

Those abrupt changes probably are due to the stability of the photonic sensor and the optical controller. However, the amplitude is constant on average. The phase on average increases linearly about 0.4 degrees in 1 hour. Because the instability can be considered as a kind of noise, the effect of the instability on the far-field pattern can be calculated by [17, 18] for planar near-field measurements and [19] for cylindrical near-field measurements.

After all, the photonic sensor can be used as an infinitesimal antenna up to approximately 8 GHz and measure an incident electric field over 0.5 V/m at 0 dB of SNR deduced from Figure 8.

To increase the sensitivity about ten times, we have a plan to insert an optical amplifier with low noise figure between the sensor and the photodiode to increase the modulated laser beam.

3. Near-Field Measurements

Using the photonic sensor system, we have measured various kinds of antennas in planar, spherical, and cylindrical

scanning techniques successfully. In all scanning techniques, we assume the photonic sensor to be infinitesimal. Therefore no probe compensations are used in the formulations of the scanning techniques.

3.1. Planar Near-Field Measurements. A standard horn antenna (Mode 12-8.2 manufactured by Scientific Atlanta). The aperture size is 194 mm (H plane) \times 144 mm (H plane). The antenna was measured using the planar scanner (Model 200 V-3x3 manufactured by NSI) as shown in Figure 9.

The photonic sensor used was an old type and the antenna shape was the same as that in Figure 2. However the sensitivity is almost the same as the present one because the base size of the rhombic antenna (1.5 mm) is comparable to the present size (1.4 mm = 0.2 mm \times 7) and the old sensor was also a reflection type [20].

Figure 10 shows the amplitude of the measured S_{21} at the 10 mm plane apart from the aperture using the old type of the photonic sensor. In the following, the distance between the photonic sensor and the antenna aperture is defined as that between the centre of the array or the antenna on the sensor and the aperture. The amplitude is normalized relative the maximum. The antenna polarization of the sensor is along in the y -axis. The frequency is 8 GHz and the scan area is ± 200 mm (the x axis or H plane) \times ± 150 mm (the y -axis or E plane) with 5 mm steps.

Figure 11 shows E_y component of the electric field at 10 mm apart from the aperture calculated by FEKO. The meshing size is approximately 1/9 wavelengths. The amplitude is normalized relative to the maximum and the scan area is the same as the one of the measurement in Figure 10.

Comparing Figures 10 and 11, we can conclude that the photonic sensor can be considered to be infinitesimal at 8 GHz. This is compatible with the conclusion deduced from Figures 5 and 6.

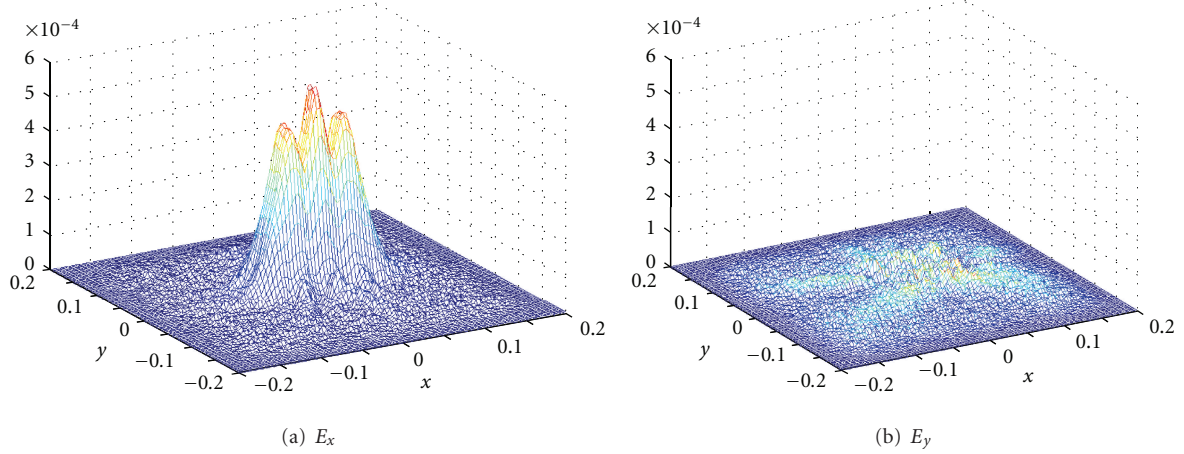


FIGURE 14: The amplitudes of the measured S_{21} corresponding to (a) E_x and (b) E_y at 10 mm apart from the antenna aperture using the old photonic sensor.

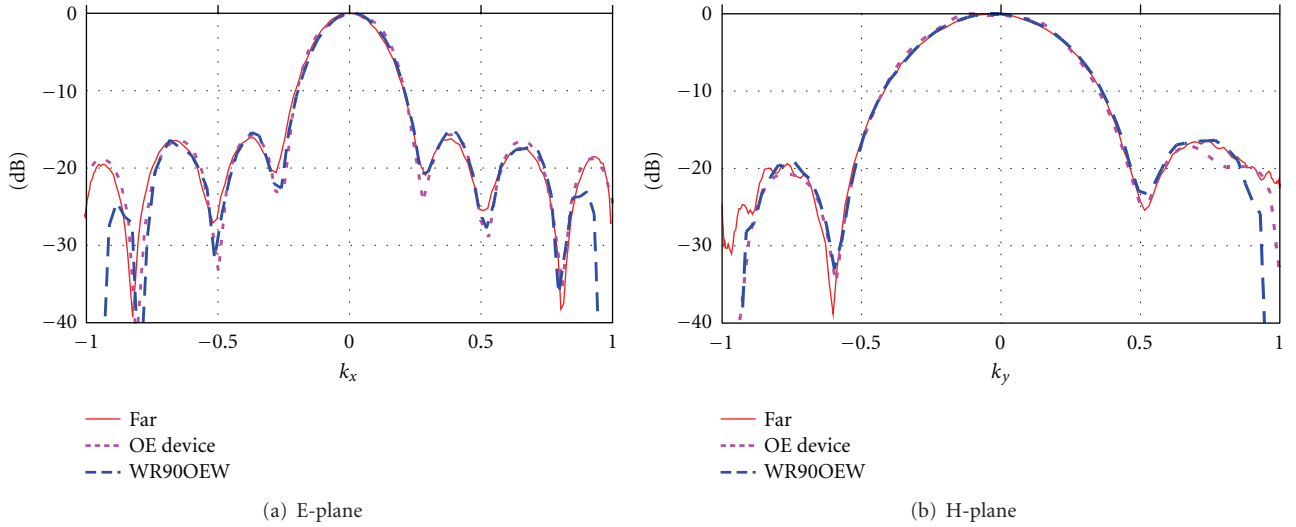


FIGURE 15: Normalized patterns of the array of the MSAs obtained by the old photonic sensor (OE device), the OEW probe (WR90OEW), and far-field measurement (Far). (a) E-plane pattern. (b) H-plane pattern.

From (1), an antenna pattern $D(\mathbf{K})$ is simply obtained by the Fourier transform of the measured S_{21} s corresponding to the E_x and E_y components as

$$S_{21x}\mathbf{x} + S_{21y}\mathbf{y} = \iint \mathbf{F}(\mathbf{K})e^{-j\mathbf{k}\cdot\mathbf{r}}d\mathbf{K}, \quad (3)$$

$$D(\mathbf{K}) = \alpha_p |\mathbf{k} \times \mathbf{F}(\mathbf{K})|^2,$$

where S_{21x} , S_{21y} are the measured S_{21} s corresponding to the E_x and the E_y respectively. α_p is a constant, \mathbf{x} and \mathbf{y} are unit vectors for each directions, \mathbf{k} is the wavenumber vector, and \mathbf{K} is its projection vector on the x - y plane.

The E-plane and the H-plane patterns obtained by the near-field to far-field transformations without probe compensation are shown in Figure 12. For the references, the patterns calculated by FEKO and the patterns obtained by the

conventional open-ended waveguide probe (OEW) are also shown in the same figure. The near-field data measured by the OEW was measured at 110 mm apart from the aperture in the scan area of $\pm 326 \text{ mm} \times \pm 326 \text{ mm}$ (18 mm steps). The probe compensation was done using the pattern of the OEW (WR 90). The patterns by the three methods agree well each other.

As another type of antenna, we have measured an array (3×4) of microstrip antennas (MSA) shown in Figure 13 [4, 21]. Each square MSA is coupled electromagnetically through thin slotted apertures to the feeding microstrip lines at the back of the antenna. The polarization of the array is along the x axis.

Figure 14 shows the amplitudes of the measured S_{21} for the E_x and the E_y components of the array at 10 mm apart from the antenna plane. The frequency is 9.41 GHz. That

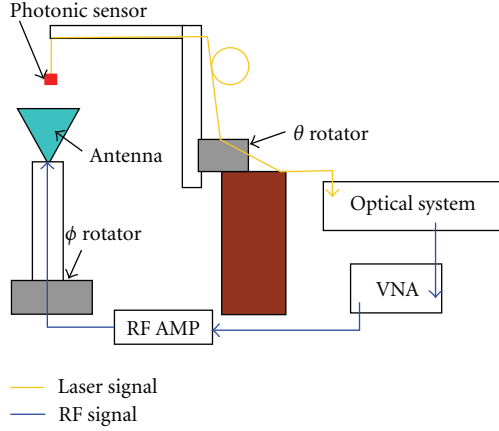


FIGURE 16: Measurement setup for spherical near-field scanning.

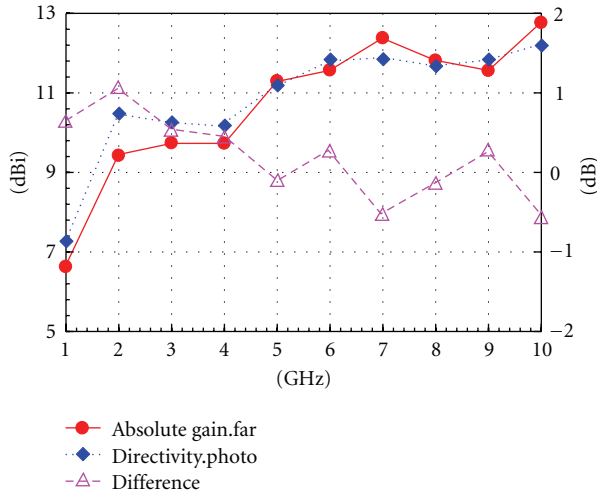


FIGURE 17: Absolute boresight gains (dBi) obtained by the far-field three antenna method (far) and the proposed method using the photonic sensor (photo).

means that the polarizations of the photonic sensor are along the x axis and y axis respectively. The scanned area is $\pm 200 \text{ mm} \times \pm 200 \text{ mm}$ and the sampling interval is 4 mm.

The peaks of E_x is at the centres of the spaces of the antennas along the x -axis. This is because the radiation by the MSA comes from the radiation edge of the antenna. This is different from the cosine tapered electric-field distribution of the horn antenna in Figure 10.

Figure 15 compares the patterns measured by the photonic sensor (OE device), the conventional far-field method (Far), and the WR90 OEW probe. The OEW measurement done in the scan is of $67.2 \text{ cm} \times 67.2 \text{ cm}$, at the distance of 110 mm between the aperture of the OEW and that of the antenna plan. We found that the patterns by the three measurement methods agree well with each other.

From the results, we conclude that the old photonic sensor can be considered to be an infinitesimal receiving antenna below approximately 10 GHz. This is not contradicting with Figures 5 and 6 because the photonic sensor (old) used in

the above measurements was supported by a styrene foam block instead of the glass pipe that is used for the latest photonic sensor. The effect of the styrene foam on the pattern of the old photonic was calculated by FEKO and proved to be negligible even at 10 GHz.

3.2. Spherical Near-Field Measurements. Absolute gain measurements using the photonic sensor are easily realized in the spherical near-field measurements [22]. The measurements require an antenna with unknown gain, unknown pattern, however almost 100% efficiency. It is easy to realize an antenna with almost 100% efficiency if the antenna is composed by all metallic parts such as a standard horn antenna [23]. Since the efficiency of 98% equals to loss less than 0.1 dB, the assumption of at almost 100% means the error less than 0.1 dB, which is acceptable in many measurements.

Measurement setup is shown in Figure 16. The system was designed by ourselves. All parts irradiated by the antenna under measurement are covered by electromagnetic absorbers. The polarization of the photonic sensor can be adjusted to the theta or phi direction of the measurement coordinate system.

From (1), the measured S_{21} s corresponding to the E_θ and E_ϕ components are represented as

$$S_{21\theta} = \alpha' \sum_{s=1}^2 \sum_{n=1}^N \sum_{m=-n}^n T_{smn} \vec{F}_{smn}^{(3)}(R, \theta, \phi) \cdot \hat{\theta}, \quad (4)$$

$$S_{21\phi} = \alpha' \sum_{s=1}^2 \sum_{n=1}^N \sum_{m=-n}^n T_{smn} \vec{F}_{smn}^{(3)}(R, \theta, \phi) \cdot \hat{\phi},$$

where $\hat{\theta}$, $\hat{\phi}$ are unit vectors. α' is equal to $\alpha k \sqrt{Z_{\text{free}}}$, where Z_{free} is the free space impedance. T_{smn} is the coefficient for the spherical wave function, $\vec{F}_{smn}^{(3)}(R, \theta, \phi)$ [24], and R is the distance between the photonic sensor and the centre of the measurement coordinate system. For our system, R is typically 60 cm approximately.

$\alpha' T_{smn}$ is determined by the numerical integration as

$$\alpha' T_{smn} = (-1)^m \{R_{sn}^{(3)}(kR)\}^{-2} \times \int_{\phi=0}^{2\pi} \int_{\theta=0}^{\pi} \{S_{21\theta} \hat{\theta} + S_{21\phi} \hat{\phi}\} \cdot \vec{F}_{s,-m,n}^{(3)}(R, \theta, \phi) \times \sin \theta d\theta d\phi, \quad (5)$$

where $R_{sn}^{(3)}(kR)$ is the radial function [24].

On the other hand, the gain of the antenna is given as

$$G(\theta, \phi) = \frac{|\sum_{smn} \alpha' T_{smn} \vec{K}_{smn}(\theta, \phi)|^2}{1 - |\Gamma|^2} \frac{1}{|\alpha'|^2}, \quad (6)$$

where Γ is the reflection coefficient of the antenna and $\vec{K}_{smn}(\theta, \phi)$ is the far-field pattern function [24]. Assuming the antenna to be 100% efficiency, the integration of the gain on all solid angles must be 4π . Therefore α' is determined as

$$|\alpha'|^2 = \frac{\int |\sum_{smn} \alpha' T_{smn} \vec{K}_{smn}(\theta, \phi)|^2 d\Omega}{4\pi(1 - |\Gamma|^2)}. \quad (7)$$

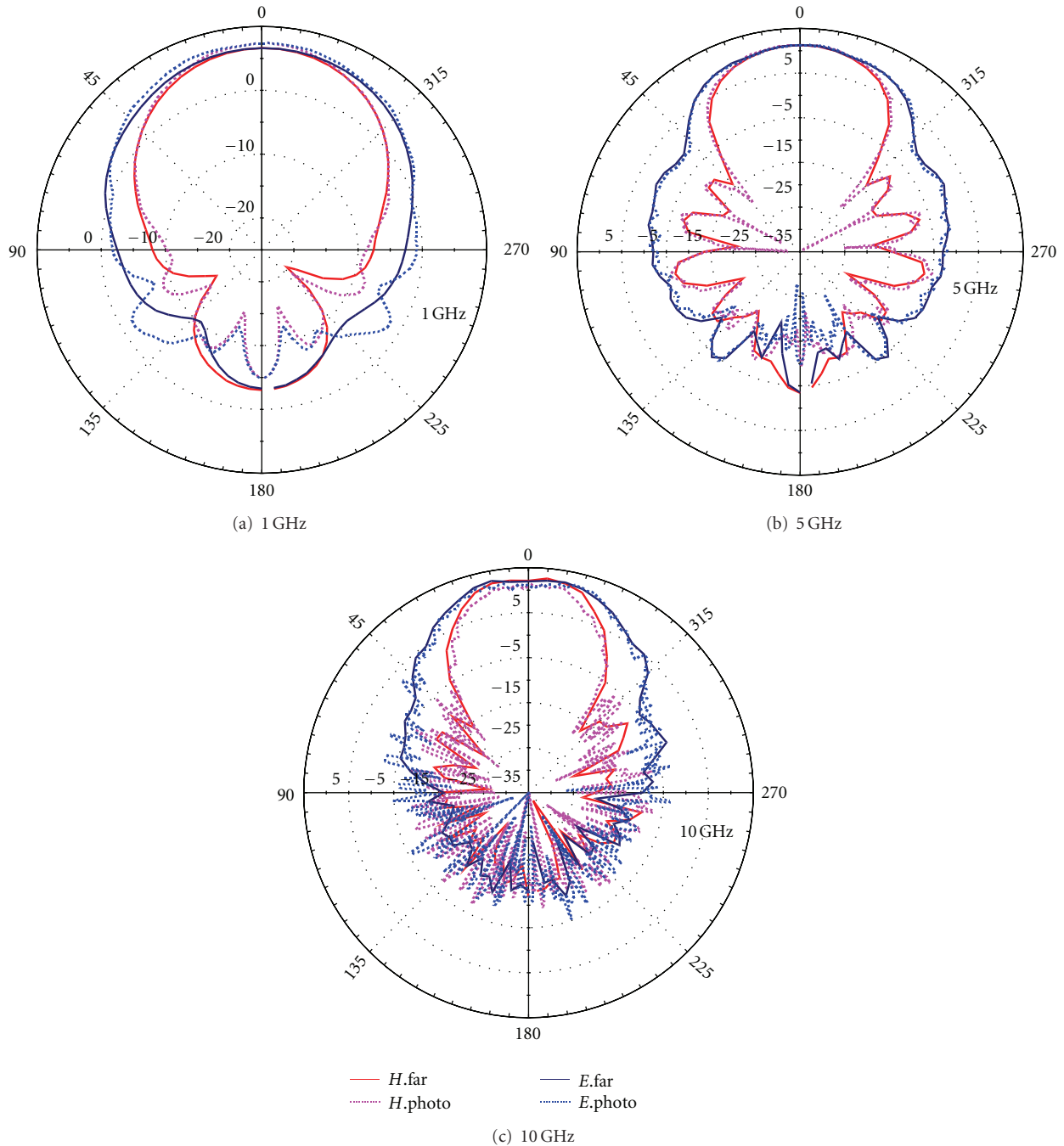


FIGURE 18: Absolute gain patterns in the E and H planes, obtained by the far-field method (far), and the proposed method using the photonic sensor (photo).

Inserting $|\alpha'|^2$ in the denominator of (6), the absolute gain pattern is finally obtained.

To demonstrate the validity of the proposed method, a double-ridged waveguide horn antenna (Model 3115 manufactured by EMCO) was used because the antenna efficiency can be assumed to be 100%. The absolute boresight gain obtained by the proposed method is shown in Figure 17. For comparison, the absolute gain by the far-field three antenna method is also shown. The both absolute gains agree with

each other within 1 dB below 10 GHz. The error of the method comes from the pattern error: the error below 2 GHz is due to the scattering around equipment as in Figure 18(a); the error above 9 GHz is due to the noise as in Figure 18(c). If those factors can be reduced, the error of the method will be reduced to about 0.3 dB or less in our experiences.

In Figure 18, the patterns of the absolute gains by both methods in the E plane and the H plane are shown at 1 GHz, 5 GHz, and 10 GHz. They agree well with each other.

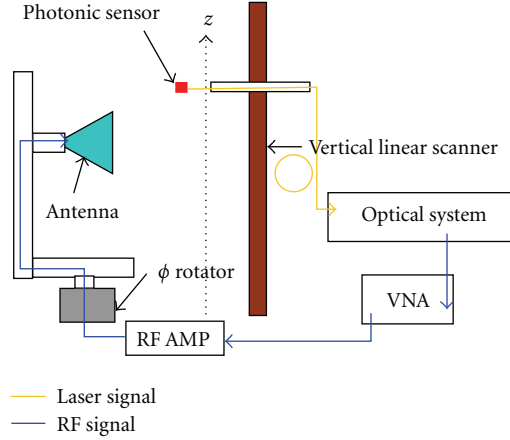


FIGURE 19: Measurement setup for cylindrical near-field scanning.

From the results, the photonic sensor can be considered to be an infinitesimal receiving antenna below 10 GHz in spherical near-field measurements as well as planar near-field measurements.

3.3. Cylindrical Near-Field Measurements. Figure 19 shows a cylindrical near-field measurement system using the photonic sensor. Because the polarizations of the sensor are set to be parallel to E_ϕ and E_z , the measured S_{21} s are proportional to each component and expressed as [25]

$$S_{21z}(R, \phi, z) = \alpha_c \sum_{n=-\infty}^{\infty} e^{jn\phi} \int_{-\infty}^{+\infty} b_n(h) \frac{\Lambda^2}{k} H_n^{(2)}(\Lambda R) e^{-jh z} dh, \quad (8)$$

$$\begin{aligned} S_{21\phi}(R, \phi, z) &= \alpha_c \sum_{n=-\infty}^{\infty} e^{jn\phi} \\ &\times \int_{-\infty}^{+\infty} \left[b_n(h) \frac{nh}{kR} H_n^{(2)}(\Lambda R) - a_n(h) \frac{\partial H_n^{(2)}(\Lambda R)}{\partial R} \right] \\ &\times e^{-jh z} dh, \end{aligned} \quad (9)$$

where α_c is a constant, (R, ϕ, z) is the position of the sensor, $H_n^{(2)}$ is the Hankel function of the second kind, and $\Lambda = \sqrt{k^2 - h^2}$. The coefficients $a_n(h)$ and $b_n(h)$ are determined by the Fourier transform.

Since the normalized electric far-field is given as

$$\begin{aligned} \mathbf{E}(\theta, \phi) &= -2k \sin \theta \sum_{n=-\infty}^{\infty} j^n e^{jn\phi} \left[\hat{\phi} a_n(k \cos \theta) + \hat{\theta} j b_n(k \cos \theta) \right], \end{aligned} \quad (10)$$

the absolute gain pattern is obtained by

$$G(\theta, \phi) = \frac{16\pi Z_0 k^2}{Z_{\text{free}} (1 - |\Gamma|^2)} |\mathbf{E}(\theta, \phi)|^2, \quad (11)$$

where Z_0 and Γ are the characteristics impedance of the cable and the reflection coefficient of the antenna, respectively.

To verify the equations from (8) up to (11), a standard horn antenna (MI 12-1.7 manufactured by MI Technologies) at 1.7 GHz was measured by a cylindrical scanner (Model 300 V-8x8 manufactured by NSI). The E plane of the antenna is along the ϕ axis and the H plane is parallel to the z axis. Figure 20 shows the absolute gain patterns of the horn antenna obtained by the conventional WR430 OEW probe, FEKO, and the photonic sensor. Since the photonic sensor system (at present) cannot measure the absolute gain, the relative patterns whose maximum is set to the maximum of the patterns by the OEW probe are shown. The results by the three methods agree with each other. The differences between FEKO and the measurements probably come from the electromagnetic absorber around the horn antenna that was used only for the measurements.

Figure 21 shows the relative phase patterns of E_ϕ obtained by FEKO, the photonic sensor, and the OEW probe. E_ϕ is the principal component in the setting of the antenna. To calculate each phase, the origin of each coordinate system is set to the centre of the antenna aperture and each phase at $(\phi, k_z) = (0, 0)$ is set to that of FEKO. Those by FEKO and the sensor agree well with each other. Slight difference in the OEW probe may be error in the characterization of the OEW probe or the setting of the antenna in the measurement.

The measurement conditions for the OEW probe are determined to satisfy the criteria [1] where the distance between the aperture of the antenna and that of the OEW probe is 50 cm, $R = 0.96$ m, $\phi = -157.5$ degrees To $+157.5$ degrees, $\Delta\phi = 3.75$ degrees, $z = -1.188$ m to $+1.188$ m, $\Delta z = 0.066$ m. The measurement by the photonic sensor was done on the conditions where the distance between the aperture and the sensor is 6.5 cm, $R = 0.5$ m, $\phi = -152$ degrees To $+152$ degrees, $\Delta\phi = 4$ degrees, $z = -1.08$ m to $+1.08$ m, $\Delta z = 0.036$ m. The model calculated by FEKO has the parameters where the aperture and the height of the horn is 367 mm \times 273 mm \times 265 mm, the waveguide size and the length are 109.2 mm \times 54.6 mm \times 150 mm, the meshing size is 10 mm.

4. Summary

We have demonstrated the utilities of the photonic sensor applied to planar, spherical, and cylindrical near-field antenna measurements. The photonic sensor consists of the array antenna with 2.4 mm height and 2 mm width on LiNbO_3 substrate and operates in the principle of the Mach-Zehnder interferometer. Due to the physical smallness, the photonic sensor can be considered to be an infinitesimal receiving antenna below 10 GHz. Therefore no probe compensation is required for any kinds of near-field measurements.

As for the sensitivity, the overall minimum sensitivity of the present photonic sensor system is 0.5 V/m approximately. This means that the system can be used to measure an antenna whose gain is over 10 dB, at about 50 mm apart from the aperture of the antenna, using a vector network analyzer in SNR over 30 dB with an RF amplifier of about 30 dB gain.

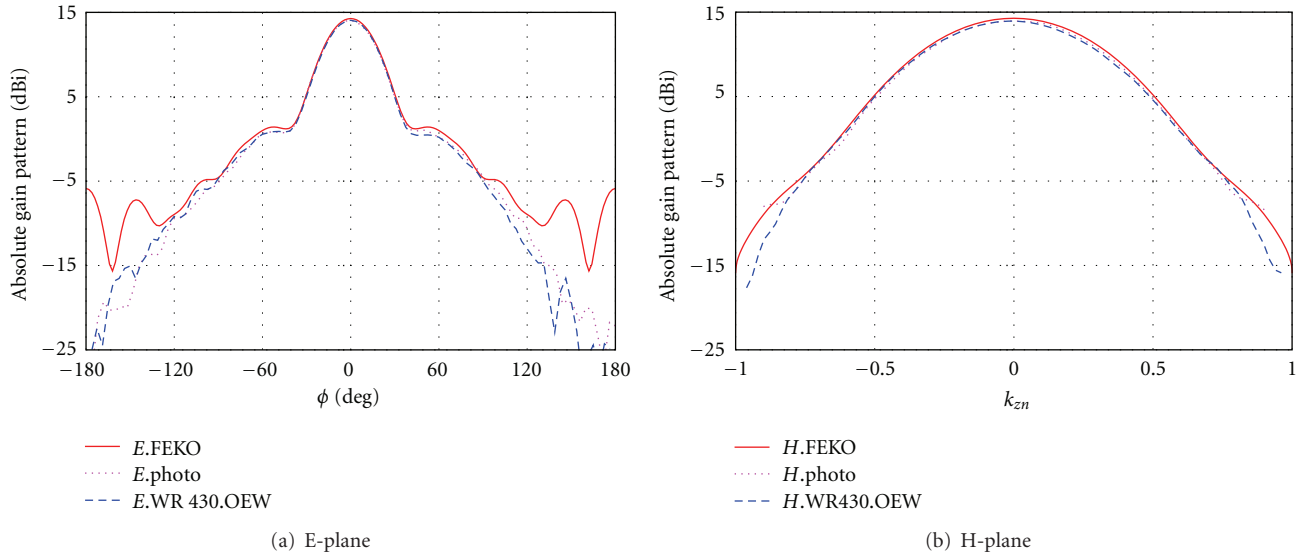


FIGURE 20: Absolute gain patterns of the standard horn antenna obtained by the OEW (WR430) probe, FEKO, and the relative pattern of the photonic sensor at 1.7 GHz. (a) E-plane. (b) H-plane.

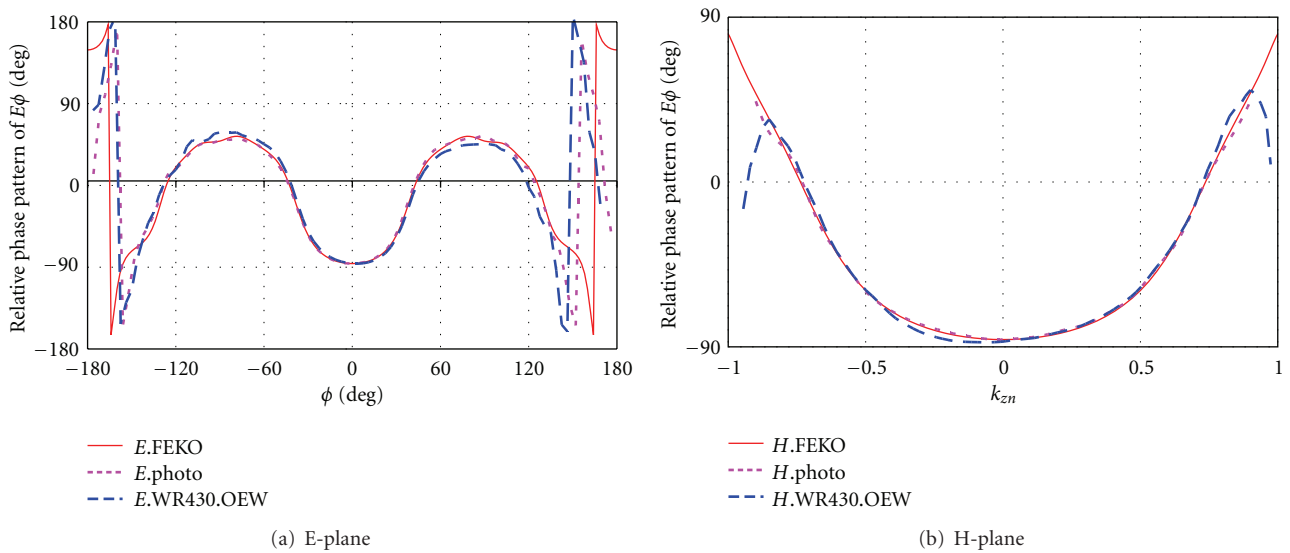


FIGURE 21: Relative phase patterns of E_ϕ (principal component) of the standard horn antenna obtained by the OEW (WR430) probe, FEKO, and the photonic sensor at 1.7 GHz. (a) E-plane. (b) H-plane.

To summarise, the merits of the photonic sensor applied to near-field antenna measurements are

- (1) no probe compensation is required below 10 GHz,
- (2) broad band measurements from a few tens MHz to 10 GHz are realized by the single probe,
- (3) the sensor can be treated as the more ideal infinitesimal receiving antenna if the operating frequency becomes the lower,
- (4) the truncation error can be reduced,
- (5) evanescent waves in the immediate vicinity of the aperture can be detected,

- (6) measurement system can be made in small and compact size.

We are continuously developing a new optical system that will have the overall minimum sensitivity of 1 mV/m and need no RF amplifier. The system combined with a VNA will realize antenna measurements calibrated by various kinds of calibration methods.

References

- [1] A. D. Yaghjian, "An overview of near-field antenna measurements," *IEEE Transactions on Antennas and Propagation*, vol. 34, no. 1, pp. 30–45, 1986.

- [2] CISPR 16-1-4, "Specification for radio disturbance and immunity measuring apparatus and methods—part 1-4: radio disturbance and immunity measuring apparatus—ancillary equipment—radiated disturbances," *International Electrotechnical Commission IEC, Edition 1.1*, 2004-2005.
- [3] S. Battermann and H. Garbe, "Influence of the receiving antenna pattern on the Site-VSWR validation procedure above 1 GHz," in *Proceedings of the IEEE International Symposium on EMC*, pp. 1-5, August 2008.
- [4] M. Hirose, T. Ishizone, and K. Komiyama, "Antenna pattern measurements using photonic sensor for planar near-field measurement at X band," *IEICE Transactions on Communications*, vol. 87, no. 3, pp. 727-734, 2004.
- [5] M. Hirose, S. Kurokawa, and K. Komiyama, "Compact spherical near-filed measurement system for UWB antennas," in *Proceedings of the IEEE International Symposium on Antennas and Propagation (ISAP '05)*, vol. 4, pp. 692-695, July 2005.
- [6] A. Capozzoli, C. Curcio, G. D'Elia et al., "Photonic probes and advanced (also phaseless) near-field far-field techniques," *IEEE Antennas and Propagation Magazine*, vol. 52, no. 5, pp. 232-241, 2010.
- [7] M. Schwerdt, J. Berger, B. Schüppert, and K. Petermann, "Integrated optical E-Field sensors with a balanced detection scheme," *IEEE Transactions on Electromagnetic Compatibility*, vol. 39, no. 4, pp. 386-390, 1997.
- [8] K. Tajima, R. Kobayashi, N. Kuwabara, and M. Tokuda, "Improving design method for sensitivity and frequency response of e-field sensor using a mach-zehnder interferometer," *IEICE Transactions on Electronics*, vol. 83, no. 3, pp. 347-354, 2000.
- [9] T. Ichikawa, "Fabrication and characterization of a retroreflective type of practical LiNbO₃ voltage sensor operating in the range of 6 Hz to 2 GHz," *IEICE Transactions on Electronics*, vol. 83, no. 3, pp. 355-359, 2000.
- [10] A. I. Sasaki and T. Nagatsuma, "Electric-field scanning system using electro-optic sensor," *IEICE Transactions on Electronics*, vol. 86, no. 7, pp. 1345-1351, 2003.
- [11] E. Suzuki, S. Arakawa, H. Ota, K. I. Arai, and R. Sato, "Optical magnetic field probe with a loop antenna element doubly loaded with LiNbO₃ crystals," *IEICE Transactions on Electronics*, vol. 87, no. 11, pp. 1989-1996, 2004.
- [12] H. Togo, N. Kukutsu, N. Shimizu, and T. Nagatsuma, "Sensitivity-stabilized fiber-mounted electrooptic probe for electric field mapping," *Journal of Lightwave Technology*, vol. 26, no. 15, pp. 2700-2705, 2008.
- [13] D.-J. Lee, N.-W. Kang, J.-H. Choi, J. Kim, and J. F. Whitaker, "Recent advances in the design of electro-optic sensors for minimally destructive microwave field probing," *Sensors*, vol. 11, no. 1, pp. 806-824, 2011.
- [14] D. M. Kern, *Plane-Wave Scattering-Matrix Theory of Antennas and Antenna-Antenna Interactions*, chapter 2, National Bureau of Standards Monographs, 1981.
- [15] R. E. Collin, *Antennas and Radiowave Propagation*, chapter 5, McGraw-Hill, 1985.
- [16] <http://www.feko.info/>.
- [17] A. C. Newell and C. F. Stubenrauch, "Effect of random errors in planar near-field measurement," *IEEE Transactions on Antennas and Propagation*, vol. 36, no. 6, pp. 769-773, 1988.
- [18] J. B. Hoffman and K. R. Grimm, "Far-field uncertainty due to random near-field measurement error," *IEEE Transactions on Antennas and Propagation*, vol. 36, no. 6, pp. 774-780, 1988.
- [19] J. Romeu, L. Jofre, and A. Cardama, "Far-field errors due to random noise in cylindrical near-field measurements," *IEEE Transactions on Antennas and Propagation*, vol. 40, no. 1, pp. 79-84, 1992.
- [20] M. Hirose, K. Komiyama, J. Ichijo, and S. Torihara, "Pattern measurement of X-band standard gain horn antenna using photonic sensor and planar near field scanning technique," in *Proceedings of the Antenna Measurement Techniques Association Symposium (AMTA '02)*, pp. 284-288, 2002.
- [21] M. Hirose, T. Ishizone, J. Ichijoh, S. Torihata, and K. Komiyama, "Planar near-field measurements of microstrip array antenna using photonic sensor at X band," in *Proceedings of the IEEE International Symposium on Antennas and Propagation (ISAP '03)*, vol. 4, pp. 67-70, 2003.
- [22] M. Hirose, S. Kurokawa, and K. Komiyama, "A probe calibration method to measure absolute gain by spherical near-field measurement system using photonic sensor," in *Proceedings of the IEEE International Symposium on Antennas and Propagation (ISAP '05)*, vol. 1, pp. 277-280, Seoul, Korea, October 2005.
- [23] M. Kanda and S. F. Kawalko, "Near-zone gain of 500 MHz to 2.6 GHz rectangular standard pyramidal horns," *IEEE Transactions on Electromagnetic Compatibility*, vol. 41, no. 2, pp. 85-92, 1999.
- [24] J. E. Hansen, Ed., *Spherical Near-Field Antenna Measurements*, vol. 26 of *IEE Electromagnetic Waves Series*, Peter Peregrinus, London, UK, 1998.
- [25] O. M. Bucci and C. Gennarelli, "Use of sampling expansions in near-field-far-field transformation: the cylindrical case," *IEEE Transactions on Antennas and Propagation*, vol. 36, no. 6, pp. 830-835, 1988.

Research Article

A Microwave Holographic Procedure for Large Symmetric Reflector Antennas Using a Fresnel-Zone Field Data Processing

Giuseppe Mazarella,¹ Giorgio Montisci,¹ and Giampaolo Serra²

¹Dipartimento di Ingegneria Elettrica ed Elettronica, Università di Cagliari, Piazza D'Armi, 09123 Cagliari, Italy

²Osservatorio Astronomico di Cagliari, Istituto Nazionale di Astrofisica, Loc. Poggio dei Pini, 09012 Capoterra, Italy

Correspondence should be addressed to Giorgio Montisci, giorgiom@diee.unica.it

Received 28 September 2011; Accepted 19 December 2011

Academic Editor: Claudio Gennarelli

Copyright © 2012 Giuseppe Mazarella et al. This is an open access article distributed under the Creative Commons Attribution License, which permits unrestricted use, distribution, and reproduction in any medium, provided the original work is properly cited.

In this paper we propose a new holographic procedure for the diagnostic of large reflector antennas, based on the direct use of the Fresnel-field pattern. The relation leading from the Fresnel field to the current on the reflector surface is formulated in the least-squares sense as a discrete data inverse problem and then regularized by using a singular value decomposition approach. A detailed theoretical analysis of the problem and full assessment of the presented technique are provided. Simulations are carried out by using the radiative near-field pattern generated with a commercial software. Results show good accuracy and robustness to noise for the retrieval of the panel-to-panel misalignment of a reflector antenna.

1. Introduction

The surface diagnostic of large reflector antennas, such as radio telescopes, is a key step in order to preserve their performance at all operating frequencies. The main reflector of a radio telescope is usually composed by a set of panels, which must be aligned to an ideal surface profile, with as the greater accuracy as possible.

The surface profile accuracy is mainly limited by two factors:

- (i) the mechanical fabrication tolerance of the panels;
- (ii) the alignment of the panels, which can be strongly modified by surface heating and gravitational load.

Therefore, in order to achieve the required antenna efficiency even at high operating frequencies, the primary reflector surface must be periodically checked. This means that the misalignments of the panels must be detected by using an effective and accurate diagnostic procedure and adjusted when it is possible.

Among the different measurement methods available in the open literature [1–7], we focus our attention on the

microwave holography, an inverse method for the reflector surface profile reconstruction. This technique obtains the current induced on the reflector surface, and then the information about the surface misalignments, by the inversion of the antenna field pattern.

The measurement of the radiation pattern of large reflector antennas can be performed by pointing the antenna towards a radio source and changing the antenna azimuth and elevation along the points of a suitable grid. Nikolic et al. [8] use a cosmic radio source in order to perform measurements at different elevation angles and to check the reflector surface at high frequencies by using the radio astronomical receivers. In this case the signal-to-noise ratio (SNR) is enough to recover large-scale deformations, but not sufficient to retrieve the panel-to-panel misalignments with the same accuracy. Therefore, the signals of geostationary satellites [9] in the X and Ku band are commonly used as sources, since they provide a higher SNR than the cosmic sources.

If a source with the required SNR and operating frequency is not available in far field, a terrestrial transmitter in the radiative near field (known as Fresnel zone field) of the

antenna under test (AUT) can be used for the holographic measurements [10]. In these cases, the reduced distance between the AUT and the transmitter allows a higher SNR than that achievable with far field measurements. Moreover, the operating frequency of the transmitter can be suitably chosen in order to arrange the measuring distance based on the morphology of the site around the AUT and/or to improve the accuracy of the deformation map.

The subject of this paper is microwave holography from Fresnel-field data. In Section 2 we will describe the issues related to this topic. In Sections 3 and 4 mathematical details of the procedure proposed in this paper have been discussed. Then, in Section 5, a number of surface deformations of arbitrary amount and position have been considered on a test axis symmetric parabolic reflector. These deformations have been recovered with good accuracy and the robustness to noise has been extensively checked.

A commercial software for the analysis of reflector antennas (GRASP 9 by TICRA) has been used to generate the Fresnel-field data of a parabolic reflector with a surface made up of a set of adjustable panels. The geometry of the reflector under test has been chosen equal to the 64 m primary reflector of the Sardinia Radio Telescope (SRT), a radio telescope with active surface, which will be soon inaugurated in Italy. The operating frequency has been selected at 22 GHz based on the required surface accuracy.

2. Holography from Fresnel Pattern

The performance of large reflector antennas depends on the ability to keep the maximum surface accuracy even at high operating frequencies. Indeed, in order to achieve a high antenna aperture efficiency η , the surface deformation must be small compared to the free space wavelength λ , as shown in the Ruze formula [11]:

$$\frac{\eta}{\eta_0} = \exp \left[- \left(\frac{4\pi\varepsilon}{\lambda} \right)^2 \right], \quad (1)$$

wherein η_0 is the aperture efficiency of an ideal reflector and ε is the RMS value of the deformation error on the actual reflector surface. For example, from (1), we derive that a surface efficiency of 67% can be achieved if the RMS error is less than $\lambda/20$, that is, 680 μm at 22 GHz and 130 μm at 115 GHz.

Therefore, in order to obtain a high efficiency at operating frequencies in the K band and over, the accuracy in the evaluation of the reflector surface must be of the order of a few hundred microns. As a consequence, in the holographic diagnostic procedure, the measurement frequency must be set in the K band or over, and a high SNR is needed to achieve the required reconstruction accuracy.

Microwave holography from Fresnel-field data provides a high SNR and flexibility in the choice of the measurement frequency. Nevertheless, the closeness between the terrestrial transmitter and the AUT limits the measurement elevation angles (usually below 10 degrees).

From the point of view of the data analysis, a critical aspect of this holographic method is that only a limited

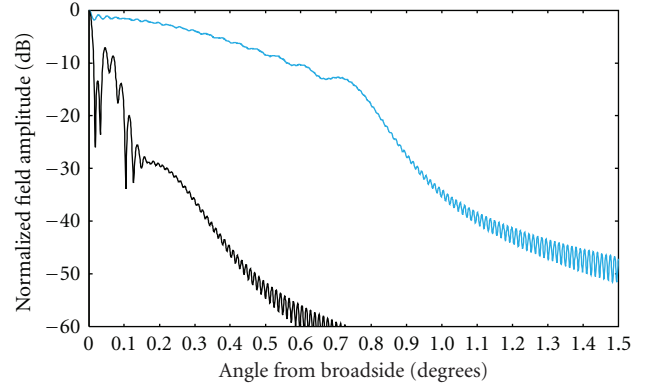


FIGURE 1: Comparison between simulated Near-Field pattern at the distance of 2160 m (blue line), and Near-Field pattern, at the distance of 2160 m, with an axial displacement of the feed $\Delta f = 301$ mm (black line).

amount of information on the antenna field is available to calculate the current induced on the reflector surface. In addition, a smooth Green's function and a limited integration domain complicate the computation of the surface current and ask for a regularized solution to an ill-conditioned inverse problem [12].

Recently, a holographic method for large reflector antennas, based on the use of Fresnel-field data, has been proposed by Baars et al. [10]. They apply a Fourier transform inversion [3] on data which have been suitably phase-distorted. In practice, this implies a refocusing of the parabolic reflector by means of an axial displacement of the feed. This displacement must be properly evaluated in order to minimize the rapid phase variation on the aperture plane, before the Fourier transform is applied.

The main consequence of this technique is the modification of the dynamic range of the measured field. As a matter of fact, the large longitudinal displacement of the feed (of the order of tens of wavelengths) defocuses significantly the far field while, at the same time, narrowing the Fresnel-field.

In Figure 1, we show the field calculated in the Fresnel zone, with and without an axial displacement of the feed Δf . The value $\Delta f = 301$ mm (used in Figure 1) has been calculated by applying the algorithm proposed by Baars et al. [10] to SRT at 22 GHz.

The approach of [10] provides a good approximation of the relationship between the Fresnel-field pattern and the aperture field, but the residual phase variation does not allow to make a rigorous inversion of this electromagnetic problem. Moreover, each AUT allows only a limited back-and-forth shift of the feed along the reflector axis, which is set by its design and operative constraints. As a consequence, the axial displacement Δf , which minimizes the phase variation on the aperture plane, cannot be implemented for all AUTs.

In this paper we propose a microwave holographic technique, applied to axis symmetric reflectors, based on the direct use of the Fresnel zone field data. These data are not used to obtain the far field pattern by means of a NF-FF transformation, as in [13], but they are directly used

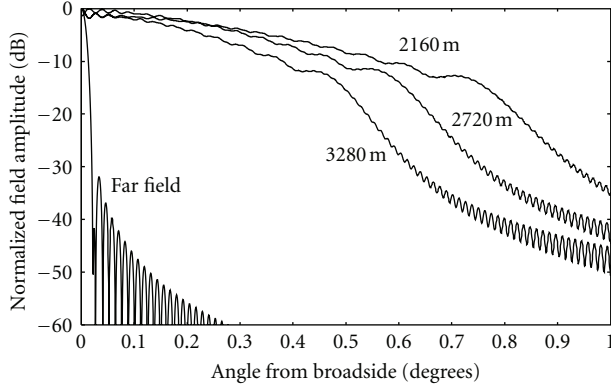


FIGURE 2: Simulated amplitude pattern at 22 GHz of Sardinia Radio Telescope (64 m diameter parabolic reflector) for different distances.

by the procedure, without any correction, as in [10]. The relation between the Fresnel zone field and the current on the parabolic reflector surface is formulated in the least-squares sense as a discrete data inverse problem and then regularized by using a singular value decomposition (SVD) approach. This procedure is based on the exact relationship between the field in the Fresnel zone and the current induced on the reflector surface, and it requires neither a paraxial approximation, as in the case of microwave holography from far field data [3], nor the axial displacement of the feed [10].

Nevertheless, the use of the Fresnel pattern for microwave holographic diagnostic needs some important clarifications, as pointed out in the following discussion.

A typical sampling window in the far field of the AUT includes the main lobe and the few first side lobes. Therefore, its dimension is determined by the required surface resolution [4, 6]. On the other hand, the dynamic range of the Fresnel pattern depends on the distance of the observation window and is always much smaller than the far field one (Figure 2). As a consequence, attention must be paid to the choice of the sampling window, which has to provide enough information to extract the reflector surface current. Actually, holography from near-field data requires a larger sampling window than holography from far field pattern to collect the same amount of information. Therefore, a larger number of samples must be measured. This improves the spatial resolution, but obviously increases the measurement time.

3. Problem Framework

The relationship between the field in the Fresnel zone [14] $\underline{E}(r, \theta, \phi)$ and the current $\underline{J}(\underline{r}')$ on the reflector surface is

$$\underline{E}(r, \theta, \phi) = -j\beta\xi \frac{e^{-j\beta r}}{4\pi r} \underline{E}(r, \theta, \phi), \quad (2)$$

$$\underline{E}(r, \theta, \phi) = \left[\underline{I} - \underline{i}_r \underline{i}_r \right] \cdot \iint_S \underline{J}(\underline{r}') e^{j\beta \underline{i}_r \cdot \underline{r}' - j\beta(1/2r)[(r')^2 - (\underline{i}_r \cdot \underline{r}')^2]} ds, \quad (3)$$

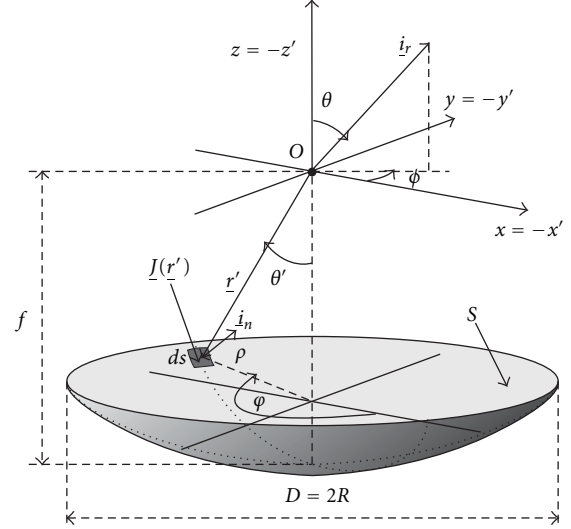


FIGURE 3: Reflector Geometry.

wherein r is the distance of the measurement points, which is chosen constant for all the samples of the measurement window, $\beta = 2\pi/\lambda$, λ being the free-space wavelength, $\xi = 120\pi$ is the free-space impedance, \underline{I} is the identity matrix, \underline{i}_r is the unit vector that points toward the direction (θ, ϕ) , S is the surface of the parabolic reflector (with diameter D and focal length f), and \underline{r}' is the vector that points on the reflector surface element ds (see Figure 3).

The polarization of radio astronomical feeds is almost perfectly pure. Therefore for sake of simplicity, we assume that the reflector antenna is illuminated by a feed, located at the focal point (O in Figure 1), with an ideal linear polarization. Since the reflector is axis symmetric, we choose the x -axis along the E -plane of the feed.

The current induced on the reflector surface $\underline{J}_t(\underline{r}')$ is our unknown. However, we can take advantage of the polarization purity of the feed to reformulate, and solve, the problem as a scalar one. We assume that the current direction \underline{i}_j can be computed as the direction of the physical optics (PO) currents.

The direction of the incident magnetic field generated by the feed is

$$\underline{i}_H = \frac{-\sin^2\theta' (\sin(2\phi)/2) \underline{i}_x + (\mathfrak{N}) \underline{i}_y - (\sin(2\theta')/2) \sin\phi \underline{i}_z}{\left| -\sin^2\theta' (\sin(2\phi)/2) \underline{i}_x + (\mathfrak{N}) \underline{i}_y - (\sin(2\theta')/2) \sin\phi \underline{i}_z \right|}, \quad (4)$$

where \mathfrak{N} denotes $1 - \sin^2\theta' \sin\phi$, wherein $\theta'(\rho) = 2 \arctan[\rho/(2f)]$ is the angle measured from the feed bore-sight and (ρ, ϕ) are the aperture coordinates ($z' = -z$, $x' = x = \rho \sin\phi$, $y' = -y = \rho \cos\phi$) (see Figure 3).

Then, letting \underline{i}_n the normal to the reflector surface, we assume

$$\underline{i}_j = \frac{\underline{i}_n \times \underline{i}_H}{\left| \underline{i}_n \times \underline{i}_H \right|}, \quad (5)$$

so that the current amplitude $J(\underline{r}')$, defined as $\underline{J}_t(\underline{r}') = J(\underline{r}') \underline{i}_j$, becomes the unknown of the problem.

The integral (3) can be written in terms of the aperture coordinates (ρ, φ) by using the surface Jacobian transformation [14]:

$$\begin{aligned} \underline{E}(r, \theta, \phi) &= [\underline{I} - \underline{i}_r \underline{i}_r] \cdot \iint_{S'} J(\rho, \varphi) \underline{i}_j e^{j\beta \underline{i}_r \cdot \underline{r}' - j\beta(1/2r)[(r')^2 - (\underline{i}_r \cdot \underline{r}')^2]} B \rho d\rho d\varphi, \end{aligned} \quad (6)$$

wherein the Jacobian B is given by

$$B = \left[\left(\frac{\partial g(x', y')}{\partial x'} \right)^2 + \left(\frac{\partial g(x', y')}{\partial y'} \right)^2 + 1 \right]^{1/2} \quad (7)$$

and $g(x', y') = z'$ is the function describing the surface of the parabolic reflector.

The new integration domain S' in (6) is the projection of the reflector surface S on the aperture plane and therefore is defined in the following range: $\rho \in [R_b, R]$, $\varphi \in [0, 2\pi]$, where R_b and R are, respectively, the blocking and external radii of the reflector.

Let us now define an equivalent current $\tilde{J}(\rho, \varphi) = BJ(\rho, \varphi)$ and replace \underline{i}_r and \underline{r}' by their spherical components. Equation (6) becomes

$$\begin{aligned} \underline{E}(r, \theta, \phi) &= [\underline{I} - \underline{i}_r \underline{i}_r] \\ &\cdot \int_{R_b}^R \int_0^{2\pi} \underline{i}_j \tilde{J}(\rho, \varphi) G(r, \theta, \phi, \rho, \varphi) \rho d\rho d\varphi, \end{aligned} \quad (8)$$

where

$$\begin{aligned} G(r, \theta, \phi, \rho, \varphi) &= \exp[j\beta(\alpha\rho^2 - 2\eta z'^2)] \\ &\cdot \exp\{j\beta[z' \cos\theta + (\rho \sin\theta + \rho z' \gamma) \cos(\phi - \varphi)]\} \\ &\cdot \exp\{j\beta[\eta\rho^2 \cos 2(\phi - \varphi)]\}, \end{aligned} \quad (9)$$

$$\alpha(r, \theta) = \frac{\sin^2\theta - 2}{4r},$$

$$\eta(r, \theta) = \frac{\sin^2\theta}{4r},$$

$$\gamma(r, \theta) = \frac{\sin 2\theta}{2r},$$

and $z'(\rho) = [\rho^2/(4f)] - f$ is the reflector nominal profile.

Now, since our attention is aimed at the reflector profile, that is, at a scalar quantity, only one component of the induced current is sufficient to obtain the required information on the reflector surface. As a consequence, only one component of the Fresnel field can be considered, and we choose the field copolar component

$$\begin{aligned} F_c(r, \theta, \phi) &= \underline{i}_c \cdot [\underline{I} - \underline{i}_r \underline{i}_r] \\ &\cdot \int_{R_b}^R \int_0^{2\pi} \underline{i}_j \tilde{J}(\rho, \varphi) G(r, \theta, \phi, \rho, \varphi) \rho d\rho d\varphi, \end{aligned} \quad (10)$$

because it allows for the best SNR on the data. In (10) the vector

$$\begin{aligned} \underline{i}_c &= \cos\phi \underline{i}_\theta - \sin\phi \underline{i}_\varphi \\ &= [1 - \cos^2\phi(1 - \cos\theta)] \underline{i}_x \\ &\quad - (1 - \cos\theta) \sin\phi \cos\phi \underline{i}_y - \sin\theta \cos\phi \underline{i}_z, \end{aligned} \quad (11)$$

is the field copolar component direction (Ludwig's third definition [15]), assuming that the radiated electric field is predominantly x -polarized. Note that, for large and focusing reflectors, as radio astronomical ones, we can assume $\theta \ll 1$ ($\cos\theta \cong 1$ and $\sin\theta \cong 0$) and find an approximate expression for (11)

$$\underline{i}_c \cong \underline{i}_x. \quad (12)$$

It is worth noting that no paraxial approximation has been made in the phase terms of (10). As a matter of fact, we used $\theta \ll 1$, to approximate only the amplitude and direction of the copolar field component, as apparent from (12).

Equation (10) is a (two-dimensional) linear Fredholm integral equation of the first kind [12], where $\tilde{J}(\rho, \varphi)$ is the unknown and $F_c(\theta, \phi)$ the known term. Its inversion is a severely ill-posed problem because of its very smooth kernel and the limited integration domain S' [12]. It follows that (10) cannot be simply inverted, but it is necessary to apply a regularization procedure, which generally needs also a different solution definition, in view of the fact that the measured data $F_c(\theta, \phi)$ will include an unavoidable noise. Therefore, the problem must be analyzed as a discrete data inverse problem [16, 17].

Let (θ_p, ϕ_p) be the set of field measurement points (with $p = 1, \dots, M$) and L_p the functional which supplies $F_c(\theta_p, \phi_p)$. If f_p are the measured values, then

$$f_p = L_p[\tilde{J}] + n_p = f_p^t + n_p, \quad (13)$$

where f_p^t is the field's "ideal" value (i.e., without noise) and n_p is the noise on the p th measure. In order to solve (13), the unknown current must be discretized too, by choosing a suitable set of basis functions $I_q(\rho, \varphi)$, $q = 1, \dots, N$. Therefore, the unknown current can be expressed as $\tilde{J} = \sum_{q=1}^N J_q I_q(\rho, \varphi)$, and (13) can be rewritten as

$$f_p = \sum_{q=1}^N J_q L_p[I_q(\rho, \varphi)] + n_p. \quad (14)$$

If the functional L_p is not directly invertible, as in (10), the problem must be formulated in the least-squares sense. Defining the numerical vector $\underline{f} \in \mathbb{C}^{M \times 1}$, having components f_p , and the matrix \underline{L} associated with the functional L_p , we must seek for a solution \tilde{J}_{LS} (having components J_q) that minimizes the residual 2-norm

$$\min_{\tilde{J} \in \mathbb{C}^{N \times 1}} \|\underline{L} \cdot \tilde{J} - \underline{f}\|_2. \quad (15)$$

This solution is usually termed “least-squares solution” or “pseudosolution” [12] and depends linearly on the data \underline{f} , so that we can write

$$\underline{\tilde{f}}^{LS} = \underline{L}^\dagger \cdot \underline{f}, \quad (16)$$

wherein \underline{L}^\dagger is the so-called generalized inverse (or Moore-Penrose inverse) of the matrix \underline{L} [12]. The main point is that, even though this discrete data problem is well posed, it turns out to be heavily ill conditioned [12], because (10) is ill-posed. Therefore, it needs to be solved through a suitable regularization procedure [18].

4. Solution Approach

In Section 4.1 we describe the main steps that lead from the acquisition of the Fresnel-field data to the final map of the reflector surface. These steps will be discussed in detail in Section 4.2.

4.1. A Brief Overview of the Algorithm. The holographic procedure presented in this paper can be applied to reflector antennas whose external boundary is a circumference located on a plane orthogonal to the reflector axis. This assumption is mandatory for the examples presented in this paper. In fact, in order to reduce the computational load, we represent both the field and the current induced on the reflector surface as a truncated Fourier series. As a consequence, our procedure requires the following steps.

- (i) The measurement points must be located on concentric circles (antenna framework), while typical measured data are available in azimuth-elevation coordinates. Therefore, the first operative step is a data transformation from the terrestrial framework (a regular lattice in azimuth elevation) to the antenna framework. This has been done using an interpolation with band-limited self-truncating functions [19].
- (ii) Exploiting the representation of the field and the induced current as Fourier harmonics, we express the relation between the field and the current through a number of decoupled integral equations, one for each harmonic.
- (iii) Each integral equation is transformed into a linear system. In order to do that: (a) the coefficients of the Fourier harmonics are expressed in terms of a set of piecewise-constant basis functions with respect to the radial coordinate; (b) the integral equation is sampled at the measurement points.
- (iv) Each linear system is solved in the least-squares sense, by using a regularization procedure based on the singular value decomposition. The known term is the harmonic of the field sampled at the measurement points, and the unknown is the harmonic of the current discretized over the reflector surface, with respect to the radial coordinate.

- (v) After solving the linear systems, we obtain the Fourier harmonics of the induced current, and the truncated Fourier series gives the total induced current on the reflector surface.
- (vi) Finally, the phase of the current induced on the displaced surface is compared to the phase of the current induced on the reference surface profile, after a suitable unwrapping procedure.

4.2. Description of the Holographic Procedure. The unknown current $\tilde{J}(\rho, \varphi)$ on the reflector surface is retrieved by using a formulation like (16). Therefore, $\tilde{J}(\rho, \varphi)$ is discretized according to the required *graphical* resolution, and the least-squares solution is regularized by using the SVD.

The SVD approach applied to the calculation of a large linear system, as that deriving from the application of (16) to a large reflector antenna, is computationally heavy. However, this problem can be overcome by using the axial symmetry of a lot of radio telescopes. In fact, this feature allows to better represent both the surface current and the radiation pattern as Fourier series. Obviously, for numerical computation, it is necessary to truncate the series to a finite number of terms with suitable upper limits. These limits can be determined by exploiting the fact that the radiation pattern is a quasi-band-limited function [20]. This property suggests that the number of the retained series terms can be obtained by the spatial bandwidth of the scattered field, as widely discussed in [20]. For a large scattering system, the effective bandwidth of the scattered field, measured on a circular domain, can be identified as

$$w = \frac{2P + 1}{2 \sin \theta_{\max}} = \chi \beta R, \quad (17)$$

wherein R is the radius of the sphere which includes the scatterer (we assume it equal to the radius of the reflector); χ is an excess bandwidth factor and has to be set slightly larger than unity to ensure a negligible representation error [19, 20]; θ_{\max} is the maximum value of the θ angle of the measured circular domain (see Figure 3), $2P + 1$ is the number of the Fourier harmonics. Solving (17) with respect to P , it follows that the higher harmonic P is given by

$$P \cong \chi \beta R \sin \theta_{\max}. \quad (18)$$

Therefore, letting $C_i(\rho)$ the i th harmonic of the current and $t_i(\theta)$ the i th harmonic of the field, the truncated Fourier series representation for the current and the radiation pattern is

$$\tilde{J}(\rho, \varphi) = \sum_{i=-P}^P C_i(\rho) \exp[j(i\varphi)], \quad (19)$$

$$F_c(\theta, \phi) = \sum_{i=-P}^P t_i(\theta) \exp[j(i\phi)], \quad (20)$$

wherein each harmonic $t_i(\theta)$ can be calculated as

$$2\pi t_i(\theta) = \int_0^{2\pi} F_c(\theta, \phi) \exp[-j(i\phi)] d\phi. \quad (21)$$

Now, carrying out the scalar products in (10), substituting the expressions (19) and (21) in (10) and using the approximated expression (12), after calculating the integrals with respect to the variables φ and ϕ , we get a set of $2P + 1$ one-dimensional integral equations, one for each harmonic

$$\begin{aligned} t_i(\theta) \cong & \pi \int_{R_b}^R \left[4 \cos\left(\frac{\theta'}{2}\right) - 2 \sin\theta' \sin\left(\frac{\theta'}{2}\right) \right] Q_i(\rho, \theta) C_i(\rho) \rho d\rho \\ & + \frac{\pi}{4} \int_{R_b}^R \sin\theta' \sin\left(\frac{\theta'}{2}\right) Q_i(\rho, \theta) C_{i-2}(\rho) \rho d\rho \\ & + \frac{\pi}{4} \int_{R_b}^R \sin\theta' \sin\left(\frac{\theta'}{2}\right) Q_i(\rho, \theta) C_{i+2}(\rho) \rho d\rho \end{aligned} \quad (22)$$

with $\theta'(\rho) = 2 \arctan[\rho/(2f)]$ and

$$\begin{aligned} Q_i(\rho, \theta) = & \exp\left[j\beta(\alpha\rho^2 - 2\eta z'^2 + z' \cos\theta) \right] \\ & \cdot \sum_{k=-\infty}^{\infty} j^{i-k} J_{i-2k}(\beta\rho \sin\theta + \beta\rho z' \gamma) J_k(\beta\eta\rho^2), \end{aligned} \quad (23)$$

wherein J_i is the Bessel function of the first kind.

Based on the same consideration carried on in [18] we can neglect the coupling between the i th harmonic of the field $t_i(\theta)$ and the $(i - 2)$ th and $(i + 2)$ th harmonics of the current (C_{i-2} and C_{i+2}). Therefore, we are left with a new set of $2P + 1$ decoupled equations

$$\begin{aligned} t_i(\theta) \cong & 4\pi \int_{R_b}^R \cos\left(\frac{\theta'(\rho)}{2}\right) Q_i(\rho, \theta) C_i(\rho) \rho d\rho, \\ & i \in [-P, P]. \end{aligned} \quad (24)$$

Each Fredholm equation (24) can be transformed into a linear system by representing the coefficient of the i th Fourier harmonic $C_i(\rho)$ in terms of a set of piecewise-constant basis functions $\{I_q(\rho)\}$, $q = 1, \dots, N$. Therefore, we divide the integration domain of (24) into N subdomains such that

$$\Delta\rho = \frac{R - R_b}{N}. \quad (25)$$

Then, we sample both sides of (24) at the measurement points.

This is not a direct task, since $F_c(\theta, \phi)$ (and then $t_i(\theta)$) requires the measurement points to be located on concentric circles (antenna framework), while typical measured data are available in azimuth-elevation coordinates (Θ_h, Φ_k) (terrestrial framework). Therefore, a data transformation is required and can be performed in two steps.

- (i) The measured data are transformed from the terrestrial framework (a regular lattice in azimuth-elevation) to the antenna framework, which can be considered a regular lattice in (u, v) for small θ angles (wherein $u = \sin\theta \cos\phi$, $v = \sin\theta \sin\phi$);
- (ii) The new data in the antenna framework are interpolated in a set of points placed on concentric circles

with equispaced values $\theta_p = p\Delta\theta$, with $p = 1, \dots, M$ and $\Delta\theta = \theta_{\max}/M$. This interpolation is performed by using band-limited self-truncating functions [19], and, for each value of θ_p , the number of interpolating points with respect to the ϕ coordinate, n_ϕ , is determined by the constraint on the limited spatial band of the reflector field [20], that is, $n_\phi(\theta_p) = \chi\beta R \sin\theta_p$. Therefore, the spacing between the field samples along each circle θ_p is $\Delta\phi_p = 2\pi/[2n_\phi(\theta_p) + 1]$.

The number of unknowns involved in the least-squares problems is determined by the choice of N , as apparent from (25). Nevertheless, for each harmonic we have a different linear system, with different matrix and data vector. More precisely, a given circular ring, at a distance R_0 from the reflector axis (i.e., all the reflector points having radial coordinate $\rho \cong R_0$), produces, in the measurements region, only field harmonics up to $P(R_0) = \hat{P}(R_0) = \chi\beta R_0 \sin\theta_{\max}$ (see (18)). Therefore, its current must be retrieved by using only the harmonics in the range $[-\hat{P}(R_0), \hat{P}(R_0)]$. As a consequence, for the i th harmonic, only $\tilde{N}_i \leq N$ unknowns are involved in the i th linear system.

Furthermore, for each measurement point θ_p , the limited spatial bandwidth of the scattered field is $(2P+1)/(2 \sin\theta_p) = \chi\beta R$ (see (17)). This means that the maximum index of the Fourier harmonics $P(\theta_p)$ is given by $P(\theta_p) = \chi\beta R \sin\theta_p$. As a consequence, the number of equations $\tilde{M}_i \leq M$ of the i th linear system is a decreasing function of i .

Then, we represent each harmonic $C_i(\rho)$ in terms of the set $\{I_q(\rho)\}$

$$C_i(\rho) = \sum_{q=N-\tilde{N}_i+1}^N A_q^{(i)} I_q(\rho), \quad (26)$$

and let $\underline{A}^{(i)}$ be the vector with components $A_q^{(i)}$ and $\underline{T}^{(i)}$ the vector with components $t_i(\theta_p)$, with $p = M - \tilde{M}_i + 1, \dots, M$.

Since the solution of each i th linear system can be found in the same way and independently from the others, we need a solution technique for the general form of such systems

$$\underline{\underline{L}} \cdot \underline{A} = \underline{T}, \quad (27)$$

wherein $\underline{\underline{L}} \in C^{\tilde{M} \times \tilde{N}}$, $\underline{A} \in C^{\tilde{N} \times 1}$, $\underline{T} \in C^{\tilde{M} \times 1}$.

Equation (27) can be solved in the least-squares sense [12], by using a regularization procedure based on the SVD of the matrix $\underline{\underline{L}}$. In [18] the same method has been applied by the authors to the reflector surface retrieval problem, but using far field instead of Fresnel-field data. Therefore, the reader is referred to Section 4 of [18] for the details of this SVD regularization procedure.

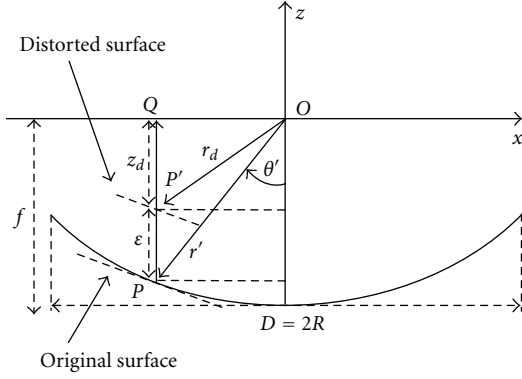


FIGURE 4: Description of surface deformation.

Once the least-squares solution $\underline{A}_{LS}^{(i)}$ has been computed, we can find the currents on the reflector as the sum of Fourier harmonics:

$$\begin{aligned} J_{LS}(\rho, \varphi) &= \sum_{i=-P}^P C_i(\rho) \exp[j(i\varphi)] \\ &= \sum_{i=-P}^P \sum_{q=N-\tilde{N}_i+1}^N A_q^{(i)} I_q(\rho) \exp[j(i\varphi)], \end{aligned} \quad (28)$$

where the discretization of radial coordinate ρ depends on the sampling points of the $J_{LS}(\rho, \varphi)$ according to (25), whereas the angular coordinate φ is suitably discretized according to the required graphical resolution.

The currents induced on the reflector surface (28) are related to the surface profile, and the comparison between the calculated profile and the nominal profile allows us to find the deformations of the reflector surface. In order to extract the surface profile information from (28), we assume that the phase center of the feed is placed at the focal point and that the surface error is described by the function $\varepsilon(x, y)$ in the z direction, as shown in Figure 4. After simple geometrical considerations, the surface deformation is obtained by

$$\varepsilon(x, y) = \frac{\lambda}{2\pi(1 + \cos \theta')} \Delta\delta, \quad (29)$$

wherein $\Delta\delta = \text{phase}(J_{\text{ref}}) - \text{phase}(J^{LS})$ is the difference between the phase of the reference current (induced on a reflector surface without deformations) and the phase of the recovered current. Both phases have been unwrapped by using the 2D procedure described in [21].

It is worth noting that the choice of a deformation in the z direction has been made for compatibility with the deformations produced by the commercial software used to test our procedure (GRASP 9). Of course, the results can be easily extended to the case of a deformation in the direction normal to the surface profile with similar geometrical considerations. In any case, this choice depends only on the construction details of the active surface.

5. Results and Discussion

In order to assess the proposed technique, many different tests have been performed on a reflector with the same geometrical configuration of the SRT primary reflector. The reflector diameter is 64 m, the blockage region diameter is 8 m; and the focal length-diameter ratio is 0.33. For the sake of simplicity, in our tests, we consider an ideal Gaussian feed, linearly polarized, with an aperture taper of -12 dB. Moreover, we suppose to neglect the diffraction effects due to the subreflector and the quadripod.

The reflector field in the Fresnel region has been simulated with GRASP, at the operating frequency of 22 GHz, on a suitable grid in the terrestrial framework, and then interpolated in the antenna framework using the self-truncating functions. The reflector model, created with GRASP, subdivides the reflector surface in a number of panels (Figures 5 and 8), whose dimensions and possible displacements with respect to the ideal profile can be assigned arbitrarily. In our case the number and the location of the panels have been chosen the same as SRT, that is, 1008 individual panels (with area in the range $[2.4 \text{ m}^2 - 5.3 \text{ m}^2]$), divided in 14 concentric circles (Figure 8).

In the GRASP modelling, each panel has up to four control points (P_1, P_2, P_3 , and P_4), that is, the position of the panel vertexes (Figure 5). For the sake of simplicity, we impose the panel misalignment by modifying only the z coordinate of each control point of the same amount ε for all the control points.

First of all, the phase of J_{ref} (i.e., the surface current in the reference case) is evaluated starting from the reference field, that is, the Fresnel pattern generated by the nominal reflector, without any surface deformation. Then, a Fresnel pattern is generated starting from a surface profile with a test deformation obtained with a panel displacement in the z direction. Finally, we get the estimation of this surface deformation by applying the solution approach described in Section 4 to retrieve both J_{ref} and J_{LS} and by using (29).

In Section 5.1 of this section we will discuss the issues related to the sampling of the field in the Fresnel region. In Section 5.2 we will apply our procedure to the reconstruction of the surface profile of the parabolic reflector under test.

5.1. The Choice of the Sampling Window. The inversion of the antenna field pattern requires that the measurement window provides enough information to derive the reflector surface current. This task is implicit in the holographic procedure from far field data, since far field pattern has a high dynamic range (Figure 2). Nevertheless, due to the reduced dynamic range of the near-field pattern, microwave holography from Fresnel data requires an accurate evaluation of the dimension of the sampling window, which must be large enough to contain the information needed to provide the reflector surface current with good accuracy. We evaluate the amount of information contained in the observation window by using the percentage of radiated power inside this window.

In order to quantify this problem we have created, by using the commercial software GRASP, the model of the prime reflector of SRT, including 1008 panels. We have

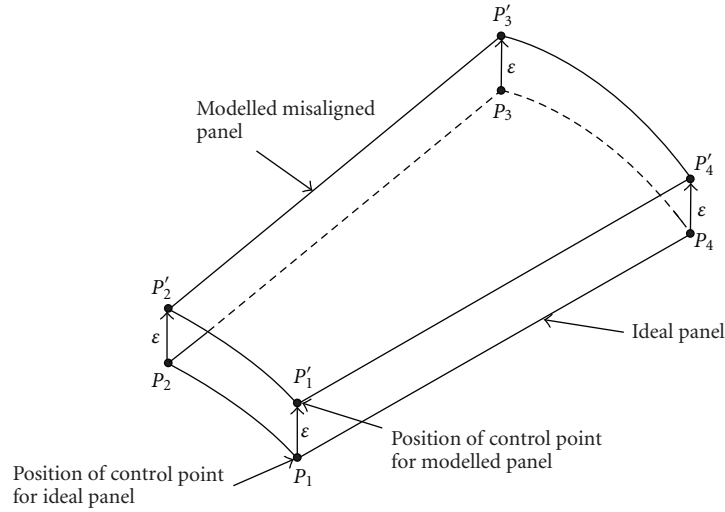


FIGURE 5: GRASP CAD modelization of a panel.

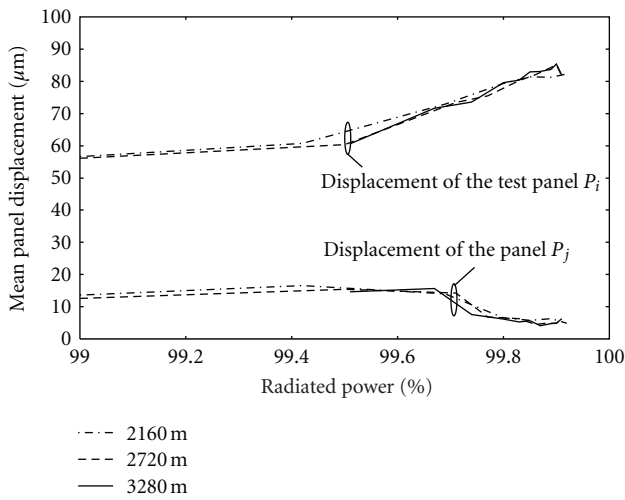
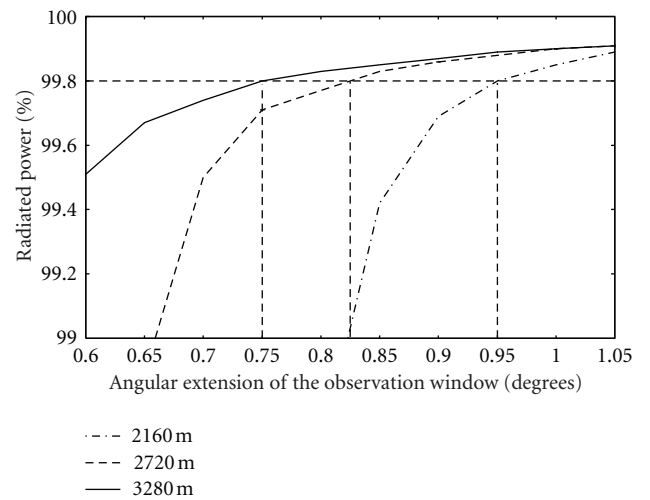
FIGURE 6: Deformation of $100\mu\text{m}$ of the panel under test P_i . P_j (with $j \neq i$) is the panel with the highest mean deformation.

FIGURE 7: Power radiated by a parabolic reflector with the same geometry of SRT, as a function of the angular extension of the observation window.

imposed a displacement of $100\mu\text{m}$ of a single panel P_i identified by the following coordinates $\rho \in [26.24455\text{ m}, 28.03525\text{ m}]$, $\varphi \in [26.25^\circ, 30^\circ]$, whereas all the other panels are aligned to the ideal parabolic profile. Then, the proposed diagnostic procedure has been applied to the reconstruction of this surface profile.

The accuracy of the surface recovering technique has been evaluated by the comparison between the recovered deformation of the test panel P_i , which should be as near to $100\mu\text{m}$ as possible, and the recovered deformation of the rest of the reflector, which should be negligible if the diagnostic procedure works well.

Therefore, we let P_j (with $j \neq i$) be the panel with the highest mean deformation among all the other panels of the reflector surface different from P_i . It is evident that the lower

the deformation of P_j , the lower the error in the recovered deformation of the panels different from P_i .

In Figure 6 we give a quantitative estimation of the accuracy of the technique for different percentage of the radiated power inside the observation window. We compare the deformation of the test panel P_i and the deformation of the panel P_j . As apparent from this figure, the recovered displacement on the reflector panels depends only on the percentage of radiated power, independently of the distance of the terrestrial source, and good results are achieved when the power radiated inside the observation window is more than 99.8%.

In Figure 7 the percentage of the radiated power as a function of the extension of the observation window is shown for different measuring distances. The test distances,

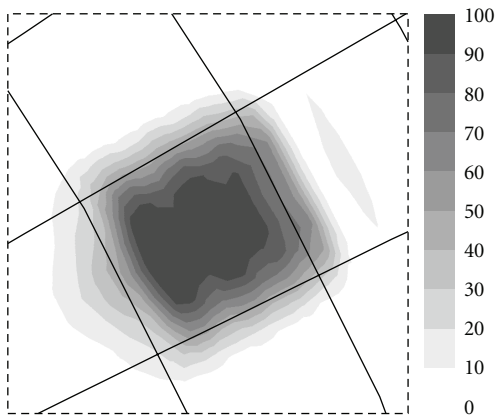
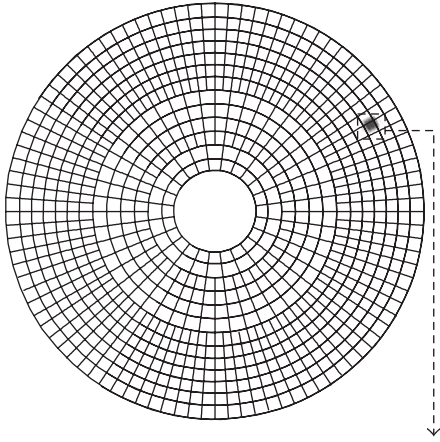


FIGURE 8: Gray scale map of the retrieved reflector surface for a deformation of $100\ \mu\text{m}$ of the panel under test. The gray scale bar is in unit of μm .

2160 m, 2720 m, and 3280 m, are all within the Fresnel zone. The angular extension of the sampling window, required to guarantee 99.8% of radiated power, can be calculated by using the curves in Figure 7.

5.2. Validation of the Holographic Procedure. The field data used to validate the holographic method proposed in this paper have been calculated by using the software GRASP 9 by TICRA, at a distance equal to 2160 m. This choice would allow us to mount a radio transmitter over a tower placed on a nearby hill at 2160 m from the SRT. In this way, we could perform measurements at an elevation angle of about 8 degrees. We will not give any other details of a possible measurement scenario because this is not the aim of the present work.

Once the distance of the transmitter has been selected, both the frequency and the observation window are chosen according to Section 5.1.

Therefore, at 2160 m, with an operating frequency of 22 GHz, the angular extension of the sampling window,

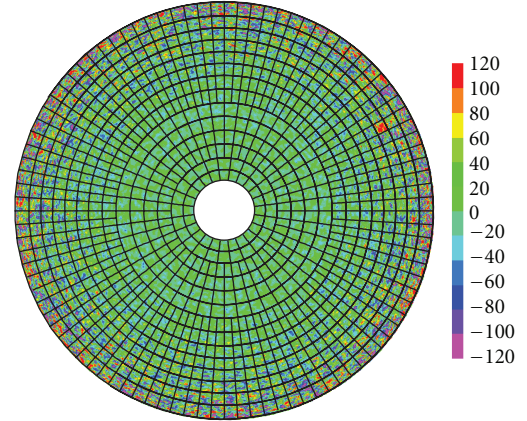


FIGURE 9: Map of the retrieved reflector surface for a deformation of $100\ \mu\text{m}$ of the panel under test. SNR = 40 dB. The color bar is in unit of μm .

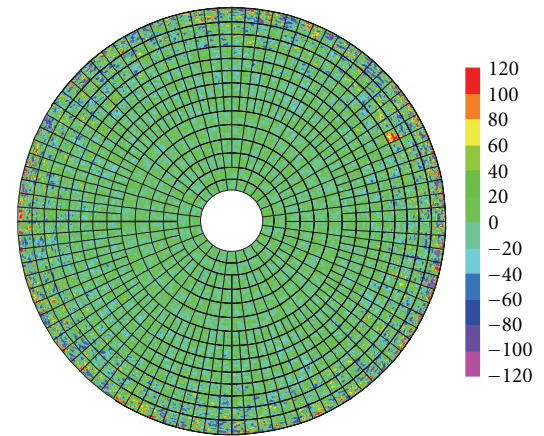


FIGURE 10: Map of the retrieved reflector surface for a deformation of $100\ \mu\text{m}$ of the panel under test. SNR = 44 dB. The color bar is in unit of μm .

corresponding to 99.8% of radiated power, is $\theta_{\max} = 0.95$ degrees (Figure 7). Then $u_{\max} = v_{\max} = \sin(\theta_{\max}) = 0.016581$ are the boundaries of the lattice in the antenna framework (coordinates u, v). According to the sampling theorem the number of sampling points in the antenna framework is $(N_s)^2$ with [3]:

$$N_s = \text{int} \left[2u_{\max} \frac{D}{\lambda} \chi \right] + 1, \quad (30)$$

wherein D is the parabolic reflector diameter, λ is the free space wavelength, and $\chi > 1$ is an excess bandwidth factor, also called oversampling factor.

For the SRT geometry ($D = 64$ m), with $\chi = 1.203$, (30) provides $N_s = 188$.

As a consistency test, we have first recovered a displacement of $100\ \mu\text{m}$ of the panel under test P_i by inversion of noise-free field data. This test has been fully successful, and in Figure 8 we show the greyscale map of the reflector with the recovered deformation.

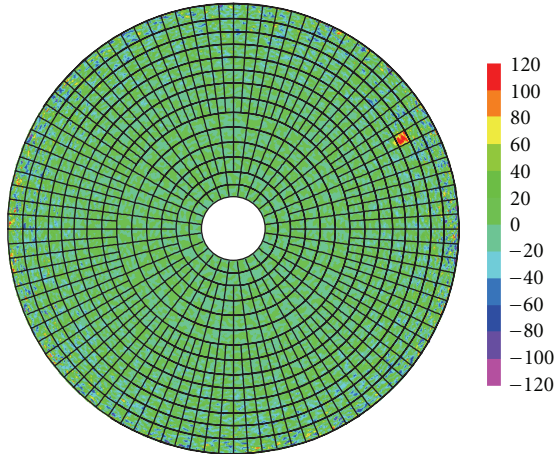


FIGURE 11: Map of the retrieved reflector surface for a deformation of $100 \mu\text{m}$ of the panel under test. SNR = 48 dB. The color bar is in unit of μm .

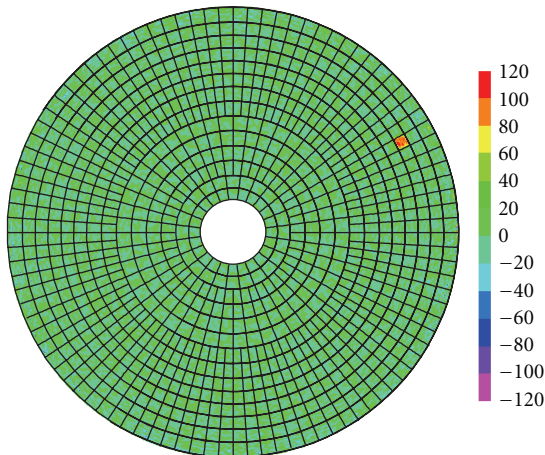


FIGURE 12: Map of the retrieved reflector surface for a deformation of $100 \mu\text{m}$ of the panel under test. SNR = 56 dB. The color bar is in unit of μm .

The approach proposed in this paper has been then extensively checked in the realistic case of noisy field data, obtained by adding a zero-mean complex Gaussian noise to the noise-free data provided with GRASP. Therefore, the noisy samples on the terrestrial framework are given by:

$$F_C(\Theta_h, \Phi_k) = F_C^T(\Theta_h, \Phi_k) + n_R(\Theta_h, \Phi_k) + jn_I(\Theta_h, \Phi_k), \quad (31)$$

wherein F_C^T is the field's "ideal" value and n_R and n_I are independent Gaussian distributions with mean zero and standard deviation $\sigma = \max_{p,k} \{|F_C^T|\} / \text{SNR}$. This definition of σ implies that the SNR is calculated with respect to the maximum of the field pattern.

In Figures 9–12, a displacement of $100 \mu\text{m}$ of the panel under test P_i has been retrieved for different values of the

TABLE 1: Recovered deformations on the reflector surface for varying values of the SNR.

SNR [dB]	Mean in P_i [μm]	Mean in P_j [μm]	RMS [μm]	Figure
38	50	70	55.4	—
40	90	43	44.6	Figure 9
42	70	40	34.9	—
44	70	35	27.8	Figure 10
46	74	23	22.1	—
48	84	18	17.7	Figure 11
50	82	13	14.3	—
56	79	8	7.5	Figure 12
62	80	8	4.5	—
∞	80	5	2.8	Figure 8

SNR. In Table 1, the accuracy of the procedure has been tested by

- (i) the comparison between the recovered deformation of P_i and that of P_j , which is the panel with the highest deformation among all the panels of the reflector surface different from P_i ;
- (ii) the evaluation of the rms value (RMS in Table 1), over all the reflector panels.

As apparent in Table 1 and Figures 9, 10, 11, and 12, a beam peak voltage SNR in the range 40–44 dB is enough to achieve an accuracy of $100 \mu\text{m}$.

6. Conclusion

The surface profile diagnostic of large reflector antennas has been addressed with a new microwave holographic technique, based on the direct use of Fresnel-field data. The proposed procedure provides the inversion of the Field data by using a SVD regularization technique. A thorough analysis, based on data computed using the well-assessed GRASP commercial software, has shown the accuracy of this holographic technique. The high *flexibility* of the procedure (e.g., in the choice of the operating frequency and measuring distance) and the stronger signal achievable with a terrestrial transmitter, make this procedure very promising to retrieve the panels misalignments of large reflector antennas and radio telescopes.

Acknowledgment

The authors would like to thank G. A. Casula and P. Bolli for helpful discussion and suggestions.

References

- [1] M. J. Kesteven, B. F. Parsons, and D. E. Yabsley, "Antenna reflector metrology: the Australia telescope experience," *IEEE Transactions on Antennas and Propagation*, vol. 36, no. 10, pp. 1481–1484, 1988.

- [2] R. Subrahmanyam, "Photogrammetric measurement of the gravity deformation in a Cassegrain antenna," *IEEE Transactions on Antennas and Propagation*, vol. 53, no. 8, pp. 2590–2596, 2005.
- [3] Y. Rahmat-Samii, "Surface diagnosis of large reflector antennas using microwave holographic metrology," *Radio Science*, vol. 19, no. 5, pp. 1205–1217, 1984.
- [4] P. F. Scott and M. Ryle, "A rapid method for measuring the figure of a radio telescope reflector," *Monthly Notices of the Royal Astronomical Society*, vol. 178, pp. 539–545, 1977.
- [5] J. C. Bennet, A. P. Anderson, P. A. McInnes, and A. J. T. Whitaker, "Microwave holographic metrology of large reflector antennas," *IEEE Transactions on Antennas and Propagation*, vol. 24, pp. 295–303, 1976.
- [6] Y. Rahmat-Samii, "Microwave holography of large reflector antennas—simulation algorithms," *IEEE Transactions on Antennas and Propagation*, vol. 33, pp. 1194–1203, 1985.
- [7] G. Mazzarella, G. Montisci, N. Schirru, and G. Serra, "A Backus-Gilbert approach to the reflector surface reconstruction," in *Proceedings of the IEEE Antennas and Propagation Society International Symposium (APS '06)*, pp. 1053–1056, July 2006.
- [8] B. Nikolic, R. M. Prestage, D. S. Baiser, C. J. Chandler, and R. E. Hills, "Out-of-focus holography at the Green Bank Telescope," *Astronomy and Astrophysics*, vol. 465, no. 2, pp. 685–693, 2007.
- [9] D. J. Rochblatt and Y. Rahmat-Samii, "Effects of measurement errors on microwave antenna holography," *IEEE Transactions on Antennas and Propagation*, vol. 39, no. 7, pp. 933–942, 1991.
- [10] J. W. M. Baars, R. Lucas, J. G. Mangum, and J. A. Lopez-Perez, "Near-field radio holography of large reflector antennas," *IEEE Antennas and Propagation Magazine*, vol. 49, no. 5, pp. 24–31, 2007.
- [11] J. Ruze, "Antenna tolerance theory—a review," *Proceedings of the IEEE*, vol. 54, no. 4, pp. 633–640, 1966.
- [12] C. Hansen, *Rank-Deficient and Discrete Ill-Posed Problems*, SIAM, New York, NY, USA, 1998.
- [13] Y. Rahmat-Samii and J. Lemanczyk, "Application of spherical near-field measurements to microwave holographic diagnosis of antennas," *IEEE Transactions on Antennas and Propagation*, vol. 36, no. 6, pp. 869–878, 1988.
- [14] C. A. Balanis, *Antenna Theory, Analysis and Design*, John Wiley & Sons, New York, NY, USA, 1997.
- [15] A. C. Ludwig, "The definition of cross-polarization," *IEEE Transactions on Antennas and Propagation*, vol. 21, pp. 116–119, 1973.
- [16] M. Bertero, C. de Mol, and E. R. Pike, "Linear inverse problems with discrete data. I. General formulation and singular system analysis," *Inverse Problems*, vol. 1, no. 4, article 004, pp. 301–330, 1985.
- [17] M. Bertero, C. de Mol, and E. R. Pike, "Linear inverse problems with discrete data: II. Stability and regularisation," *Inverse Problems*, vol. 4, no. 3, article 004, pp. 573–594, 1988.
- [18] P. Bolli, G. Mazzarella, G. Montisci, and G. Serra, "An alternative solution for the reflector surface retrieval problem," *Progress in Electromagnetics Research*, vol. 82, pp. 167–188, 2008.
- [19] O. M. Bucci and G. di Massa, "Truncation error in the application of sampling series to electromagnetic problems," *IEEE Transactions on Antennas and Propagation*, vol. 36, no. 7, pp. 941–949, 1988.
- [20] O. M. Bucci and G. Franceschetti, "On the spatial bandwidth of scattered fields," *IEEE Transactions on Antennas and Propagation*, vol. 35, no. 12, pp. 1445–1455, 1987.
- [21] D. C. Ghiglia and M. D. Pritt, *Two Dimensional Phase Unwrapping: Theory, Algorithms and Software*, John Wiley & Sons, New York, NY, USA, 1998.

Review Article

Application of Nonredundant Sampling Representations of Electromagnetic Fields to NF-FF Transformation Techniques

Ovidio M. Bucci¹ and Claudio Gennarelli²

¹*Dipartimento di Ingegneria Biomedica, Elettronica e delle Telecomunicazioni, University of Naples Federico II, Via Claudio 21, 80125 Napoli, Italy*

²*Dipartimento di Ingegneria Elettronica ed Ingegneria Informatica, University of Salerno, via Ponte Don Melillo, 84084 Fisciano, Italy*

Correspondence should be addressed to Claudio Gennarelli, gennar@diie.unisa.it

Received 31 August 2011; Accepted 23 December 2011

Academic Editor: Daniël Janse van Rensburg

Copyright © 2012 O. M. Bucci and C. Gennarelli. This is an open access article distributed under the Creative Commons Attribution License, which permits unrestricted use, distribution, and reproduction in any medium, provided the original work is properly cited.

An overview of the application of the band-limitation properties and nonredundant sampling representations of electromagnetic fields to NF-FF transformations is presented. The progresses achieved by applying them to data acquired on conventional NF scanning surfaces are discussed, outlining the remarkable reduction in the number of needed NF samples and measurement time. An optimal sampling interpolation expansion for reconstructing the probe response on a rotational scanning surface from a non-redundant number of its samples is also discussed. A unified theory of the NF-FF transformations with spiral scannings, which allow a remarkable reduction of the measurement time, is then reviewed by describing a sampling representation of the voltage on a quite arbitrary rotational surface from its nonredundant samples collected on a proper spiral wrapping it. Some numerical and experimental results assessing the effectiveness of the considered NF-FF transformations are shown too.

1. Introduction

Sampling representations play a significant role in many topics of applied electromagnetism, such as antenna analysis, synthesis and diagnostics, antenna near-field (NF) and far-field (FF) measurements, microwave nondestructive testing and imaging, and so forth. They are usually more convenient and efficient than the representations of electromagnetic (EM) fields based on modal or asymptotic expansions. This is due to the fact that the expansion coefficients are the field values at the sampling points (i.e., the available measured or computed quantities), and the basis functions are simple and universal. Accordingly, they can be employed to represent in an efficient and accurate way the radiated (or scattered) EM field on substantially arbitrary surfaces. The possibility and effectiveness of the sampling representations rely on the quasi-band-limitedness property of the field radiated (or scattered) by arbitrary (non super directive) sources. As a matter of fact, it is shown in [1] that the fields radiated

by sources enclosed in a sphere of radius a and observed on an analytical curve C external to it can be very well approximated by spatially band-limited functions. For large sources, the bandwidth is practically equal to βa (β being the wave number), provided that the phase propagation factor is extracted from the field expression, that a normalized arc length is used to parameterize C and that C is some wavelength far from the source. Since a regular surface \mathcal{M} can be described by two families of coordinate curves, the extension to this last case is straightforward. This property implies that the field over any regular surface surrounding the source can be accurately represented by a standard cardinal series (CS).

This possibility has been first successfully applied to the NF-FF transformation with cylindrical scanning [2]. Unlike the standard approaches [3, 4], the number of samples on each ring decreases as we move from the central rings to the peripheral ones, and the linear spacing between the rings also grows when the radius of the scanning cylinder increases.

Accordingly, it can become significantly greater than half-wavelength, then commonly accepted in literature as the maximum possible sampling interval. However, the use of the CS, while completely satisfactory from the accuracy point of view, has the drawback that all samples (or, at least, all the relevant ones) must be considered in evaluating the field at a given point, otherwise a relatively large truncation error is introduced, due to the slow decay of the sampling functions (It must be noted that this slow decay becomes beneficial when we want *extrapolate* the measured data, f. i., to reduce the error due to the unavoidable truncation of the measurement zone [5]). Such a slow decay leads to a further difficulty related to the fact that in practice we deal with inaccurate data. Provided that we are well above the noise level, the measured results are usually affected by an approximately constant *relative* error, so that the *absolute* error corresponding to the highest field values can be relatively large. This error is spread out by the sampling functions without a severe attenuation, and this can induce significant relative error in the zones where the field level is low.

The above difficulties have been overcome by resorting to optimal sampling interpolations (OSIs) of central type [6, 7], in which only relatively few samples in the neighbourhood of the output point are used in the reconstruction. These algorithms minimize the truncation error for a given number of retained samples and are more stable than the CS expansions with respect to random errors affecting the data. By taking advantage of the aforementioned band-limitation property, effective NF-FF transformations with plane-polar [8] and bipolar scanning [9–12] have been developed. They make use of efficient OSI expansions to reconstruct the NF data needed by the classical plane-rectangular NF-FF transformation from the knowledge of the acquired ones. Although a significant reduction on the number of required samples is obtained in such a way, their number increases indefinitely when the cylinder height or the radius of the scanning zone approach infinity. This shortcoming is a typical companion of unbounded observation surfaces, such as the cylinder and the plane. On the other hand, for a spherical scanning geometry, the number of needed samples is finite, independent of the sphere size, and essentially coincident with the number of degrees of freedom of the field [13], that is, the number of independent parameters necessary to represent it with a given precision. As the knowledge of the field on a sphere encircling the source uniquely determines the field at its exterior, this clearly shows that above representations are *redundant*.

Apart from above drawback, the hypothesis that the antenna is contained in a sphere is not always the most natural one. If the source geometry departs significantly from the spherical one, this choice leads again to redundancy (see Section 2) and does not make it possible to consider observation domains close to the source.

Note that the redundancy of the representation, which in direct type problems affects the efficiency but not the stability of the algorithms, becomes of crucial importance in inverse problems (antenna synthesis, inverse scattering, phase retrieval, image restoration, etc.) where, due to ill-posedness, it is not possible to recover a number of inde-

pendent parameters greater than the number of degrees of freedom [14].

Nonredundant sampling representations of the EM fields radiated or scattered by sources enclosed in a convex domain \mathcal{D} of finite size, bounded by a surface Σ with rotational symmetry, and observed on a regular surface \mathcal{M} external to \mathcal{D} and having the same symmetry have been developed in [15], by properly generalizing the approach introduced in [1]. Now, the number of required samples is finite also for an unbounded observation domain, independent of its shape and size, and essentially coincident with the number of degrees of freedom of the field. This is obtained by a proper choice of the phase factor to extract from the field and of the parameterizations adopted to describe \mathcal{M} . Of course, OSI expansions can be exploited for minimizing the truncation error, allowing effective sampling representations also on subdomains of \mathcal{M} . Moreover, since, as shown in [16], the output of a nondirective probe (the voltage, say) has the same effective spatial bandwidth of the field radiated by the source, the nonredundant sampling representations can be directly applied to it. This allows to accurately reconstruct the NF data required to carry out the corresponding NF-FF transformation, starting from a nonredundant set of measurements. In this way, effective NF-FF transformations requiring a minimum number of measurements have been developed, for various source shapes, in plane-polar [16–18], bipolar [19], planar wide mesh [20], cylindrical [21–23], and spherical [24, 25] scanning geometries. It must be stressed that the reduction in the number of the NF samples to be acquired reflects in a decrease of the measurement time, which is a very important issue, since nowadays such a time is much larger than that needed to carry out the NF-FF transformation.

For drastically reducing the acquisition time, the use of the modulated scattering technique, employing arrays of scattering probes, which allows a very fast electronic scanning, has been proposed since 1988 [26]. However, apart from measurement precision issues, antenna testing facilities based on such a technique are not very flexible. Anyway, exploitation of nonredundant sampling theory could allow to reduce the number of required probes. Moreover, scanning schemes for reducing the NF data acquisition time in the spherical near-field measurements of electrically large antennas have been recently proposed and experimentally validated in [27–29].

Another way to reduce the measurement time is the use of *spiral* scanning techniques. They have been implemented, as suggested by Yaccarino et al. in [30], by means of continuous and synchronized movements of the positioning systems of the probe and antenna under test (AUT). Accurate, stable and efficient NF-FF transformations with helicoidal, planar and spherical spiral scanning have been developed in the last decade [31–41]. They rely on nonredundant sampling representations to reconstruct the NF data needed by the classical NF-FF transformation corresponding to the adopted scanning surface, by interpolating, via appropriate OSI formulas, the nonredundant samples collected on the spiral. The AUT has been assumed enclosed in the smallest sphere able to contain it in [31–34], whereas more effective AUT

modellings, that allow a further reduction of required NF samples when dealing with antennas having one or two predominant dimensions, have been adopted in [35–41]. A unified theory for spiral scanning and nonspherical antennas is reported in [41].

However, when dealing with aperture antennas, such an additional a priori information available on the AUT can be conveniently exploited to provide the aperture field with an effective representation, suitably accounting for its shape and size as well as for its radiating features, thus further reducing the number of required samples [42–44].

As a final remark, note that sampling representations have been also employed to develop NF-FF transformation techniques from phaseless NF data in the plane-polar [45], bipolar [46, 47], or cylindrical [48] scanning geometries.

In this paper we provide an overview of the application of the nonredundant sampling representations to NF-FF transformations, with particular emphasis on spiral scanning. The paper is organized as follows. The theoretical results concerning the nonredundant sampling representation of EM fields are summarized in Section 2, highlighting the role of the optimal parameterization and phase factor. The ellipsoidal (oblate and prolate) modelling of the source, suitable for quasiplanar and elongated antennas, is explicitly reported. In Section 3, a two-dimensional OSI expansion for reconstructing the probe voltage on an arbitrary rotational scanning surface from its nonredundant samples is presented, and representative numerical and experimental results relevant to the cylindrical scanning case are reported. The unified theory of the NF-FF transformations with spiral scanning, for antennas with two dimensions very different from the third one [41], is described in Section 4, by presenting a sampling representation of the probe voltage on a quite arbitrary rotational surface from its nonredundant samples collected on a proper spiral wrapping the surface. Application of this theory to helicoidal scanning and elongated antennas is also reported in the same Section, and experimental results validating the related NF-FF transformation are shown. At last, conclusions are summarized in Section 5.

2. Nonredundant Sampling Representations of Electromagnetic Fields

Let us consider the field radiated by a nonsuperdirective source S , enclosed in a convex domain \mathcal{D} of finite size, bounded by a surface Σ with rotational symmetry, and observed on a regular surface \mathcal{M} , external to \mathcal{D} and with the same symmetry. Since \mathcal{M} can be described by two families of coordinate curves, namely meridian curves and azimuthal circumferences, in the following we deal with the field representation over a regular curve C described by a regular parameterization $\underline{r} = \underline{r}(\xi)$. As shown in [1, 15], the “band-limitation” error, which occurs when the “reduced electric field”

$\gamma(\xi)$, being a regular function of ξ , is approximated by a spatially band-limited function, becomes negligible as the bandwidth exceeds the critical value

$$W_\xi = \max_\xi [w(\xi)] = \max_\xi \left[\max_{\underline{r}'} \left| \frac{d\gamma(\xi)}{d\xi} - \beta \frac{\partial R(\xi, \underline{r}')}{\partial \xi} \right| \right]. \quad (2)$$

In (2), \underline{r}' denotes the source point and $R = |\underline{r}(\xi) - \underline{r}'|$. In fact, for large sources and observation curves, some wavelengths far from \mathcal{D} , such an error exhibits a step-like behaviour, decreasing more than exponentially as the bandwidth exceeds W_ξ [1, 15]. Accordingly, it can be effectively controlled by choosing a bandwidth slightly larger than W_ξ . And so, $\underline{E}(\xi)$ can be represented on C by a CS in ξ , with a sampling rate slightly larger than W_ξ/π . To obtain a nonredundant representation, that is, to minimize the number of required samples, it is shown in [15] that two conditions must be satisfied; namely,

- (1) γ must be chosen in such a way that its derivative is equal to the mean between the maximum and minimum values of $\beta \partial R/\partial \xi$ when \underline{r}' varies in \mathcal{D} ;
- (2) the parameter ξ must be such that the local bandwidth $w(\xi)$ is constant with ξ .

Condition (2) arises from the fact that if $w(\xi)$ is variable with ξ , the sample spacing becomes unnecessary small in the zones wherein $w(\xi)$ is smaller than its maximum value W_ξ .

According to the above conditions, by denoting with s , the curvilinear abscissa along the curve C and assuming $\gamma(0) = 0$ and $\xi(0) = 0$, it results in [15]:

$$\begin{aligned} \gamma &= \gamma(\xi) = \frac{\beta}{2} \int_0^{s(\xi)} \left[\max_{\underline{r}'} \frac{\partial R}{\partial s} + \min_{\underline{r}'} \frac{\partial R}{\partial s} \right] ds \\ &= \frac{\beta}{2} \int_0^s \left[\max_{\underline{r}'} \hat{R} \cdot \hat{t} + \min_{\underline{r}'} \hat{R} \cdot \hat{t} \right] ds, \end{aligned} \quad (3)$$

$$\begin{aligned} \xi &= \frac{\beta}{2W_\xi} \int_0^s \left[\max_{\underline{r}'} \frac{\partial R}{\partial s} - \min_{\underline{r}'} \frac{\partial R}{\partial s} \right] ds \\ &= \frac{\beta}{2W_\xi} \int_0^s \left[\max_{\underline{r}'} \hat{R} \cdot \hat{t} - \min_{\underline{r}'} \hat{R} \cdot \hat{t} \right] ds, \end{aligned} \quad (4)$$

where \hat{t} is the unit vector tangent to C at the observation point P , \hat{R} is the unit vector pointing from the source point to P , and (\cdot) denotes the inner product. According to (4), a change of W_ξ is reflected in a simple change of scale for ξ .

When C is a meridian curve (see Figure 1) and \hat{t} is external to the cone of vertex P tangent to Σ , the extreme values of $\hat{R} \cdot \hat{t}$ occur at the two tangency points $P_{1,2}$ on C' (intersection curve between the meridian plane and Σ). By taking into account that [15]

$$\frac{\partial R}{\partial s} \Big|_{s'_{1,2}} = \frac{dR_{1,2}}{ds} \pm \frac{ds'_{1,2}}{ds}, \quad (5)$$

$$\underline{E}(\xi) = \underline{E}(\xi) e^{j\gamma(\xi)}, \quad (1)$$

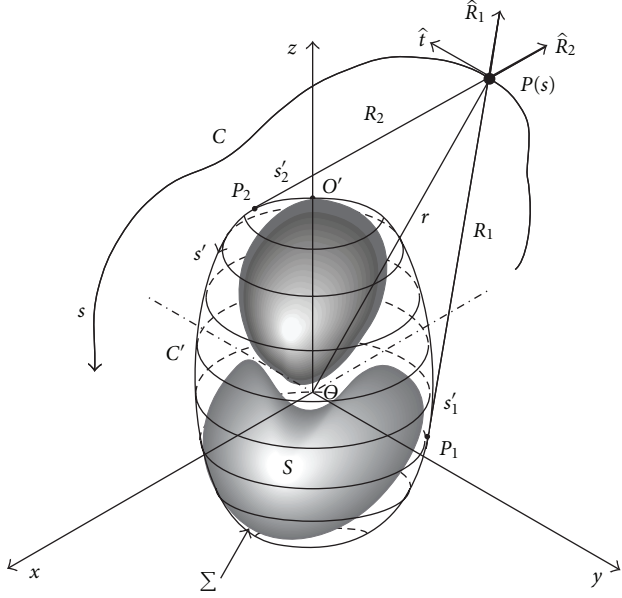


FIGURE 1: Relevant to a meridian observation curve.

where $s'_{1,2}$ are the arc length coordinates of $P_{1,2}$ and $R_{1,2}$ the distances from P to $P_{1,2}$ (see Figure 1), and choosing $W_\xi = \beta \ell' / 2\pi$ (ℓ' being the length of C'), we have

$$\gamma = \frac{\beta}{2} [R_1 + R_2 + s'_1 - s'_2], \quad (6)$$

$$\xi = \frac{\pi}{\ell'} [R_1 - R_2 + s'_1 + s'_2]. \quad (7)$$

It is useful to note that, according to (7), the angular-like parameter ξ covers a 2π range when P encircles the source once. Moreover, the number of samples at Nyquist spacing ($\Delta\xi = \pi/W_\xi$) on a closed meridian curve C is always finite (also when this last is unbounded) and equal to $N_\xi = 2\pi/\Delta\xi = 2\ell'/\lambda$, λ being the wavelength.

When C is an azimuthal circumference of radius ρ , the extreme values of $\hat{R} \cdot \hat{t}$ are opposite and constant along it. It follows from (3) and (4) that γ is constant, and any parameter proportional to the arc length is optimal. Accordingly, it is convenient to use the azimuthal angle φ as parameter and to choose for γ the value relevant to any meridian curve passing through the observation point on C . The corresponding bandwidth is [15]

$$\begin{aligned} W_\varphi &= \frac{\beta}{2} \max_{z'} (R^+ - R^-) \\ &= \frac{\beta}{2} \max_{z'} \left(\sqrt{(z - z')^2 + (\rho + \rho'(z'))^2} \right. \\ &\quad \left. - \sqrt{(z - z')^2 + (\rho - \rho'(z'))^2} \right), \end{aligned} \quad (8)$$

wherein $\rho'(z')$ is the equation of Σ in cylindrical coordinates, and R^+ , R^- are the maximum and minimum distance, respectively, from each circumference describing the surface Σ to the observation point P . It can be easily shown that the

maximum is attained on that zone of the surface Σ lying on the same side of the observation circumference with respect to its maximum transverse circle. When the observation circle moves toward infinity, it results in $R^+ = R^- + 2\rho' \sin \vartheta$, and, accordingly, we have

$$W_\varphi = \beta \rho'_{\max} \sin \vartheta, \quad (9)$$

ρ'_{\max} being the maximum transverse radius of Σ and ϑ the polar angle of the circle points. It can be shown [15] that the number of field samples on any closed observation surface (also unbounded) surrounding the source is

$$N_0 \cong \frac{\text{area of } \Sigma}{(\lambda/2)^2}. \quad (10)$$

Taking into account that the two tangential components of the electric field over any surface enclosing the source uniquely determine the field outside it, we realize that the number of degrees of freedom of the field radiated by an arbitrary source within \mathcal{D} is practically equal to $2N_0$, as a number of samples slightly larger than N_0 ensures a negligible representation error.

According to (10), \mathcal{D} must fit the antenna geometry, as much as possible, in order to minimize the overall number of samples.

As representative examples, we report in the following the results relative to ellipsoidal geometries. A prolate ellipsoid, having major and minor semiaxes equal to a and b (Figure 2), is an effective modelling for elongated antennas, whereas an appropriate modelling for quasiplanar ones is obtained by choosing Σ coincident with an oblate ellipsoid. These models are quite general and contain the spherical and planar ones as particular cases. For both types of ellipsoids, it can be shown [15] that in any meridian plane the curves $\gamma = \text{const}$ and $\xi = \text{const}$ are ellipses and hyperbolas confocal to C' . Accordingly, ξ and γ are functions only of the elliptic coordinates $u = (r_1 - r_2)/2f$ and $v = (r_1 + r_2)/2a$, where $2f$ is the focal distance of the ellipse C' and $r_{1,2}$ the distances from observation point P on the meridian curve to the foci (Figure 2).

By straightforward but lengthy computations, from (6) and (7), it results in [15]

$$\gamma = \beta a \left[v \sqrt{\frac{v^2 - 1}{v^2 - \varepsilon^2}} - E \left(\cos^{-1} \sqrt{\frac{1 - \varepsilon^2}{v^2 - \varepsilon^2}} \mid \varepsilon^2 \right) \right], \quad (11)$$

$$\xi = \frac{\pi}{2} \begin{cases} \frac{E(\sin^{-1} u \mid \varepsilon^2)}{E(\pi/2 \mid \varepsilon^2)} + 1 & \text{prolate ellipsoid,} \\ \frac{E(\sin^{-1} u \mid \varepsilon^2)}{E(\pi/2 \mid \varepsilon^2)} & \text{oblate ellipsoid,} \end{cases} \quad (12)$$

where $\varepsilon = f/a$ is the eccentricity of C' , and $E(\cdot \mid \cdot)$ denotes the elliptic integral of second kind.

Relation (12) is valid when the angle ϑ lies in the range $[0, \pi/2]$. The case in which ϑ belongs to $[\pi/2, \pi]$ can be easily handled by determining the value ξ' corresponding to the point specified by the angle $\pi - \vartheta$ and then putting $\xi = \pi - \xi'$.

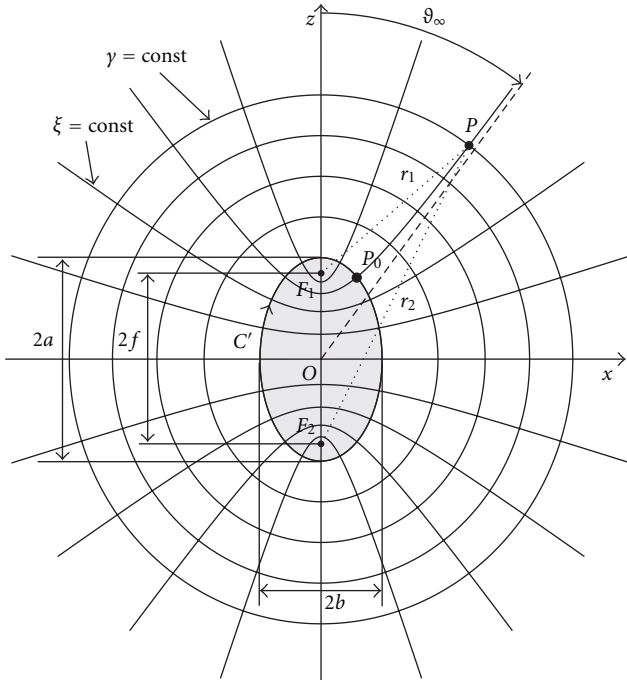


FIGURE 2: Ellipsoidal source modelling: prolate case.

With reference to an azimuthal circumference, it can be shown [15] that the same value of W_φ corresponds to all transverse circles on the hyperboloid of rotation fixed by ξ . Accordingly, moving the circle to infinity and taking (9) into account, we get the following:

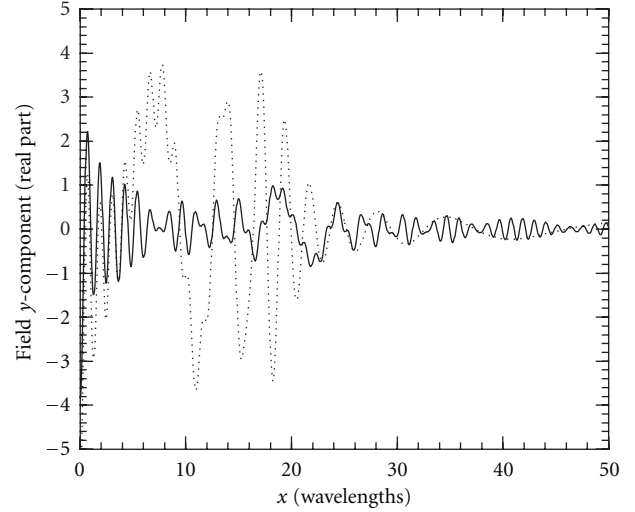
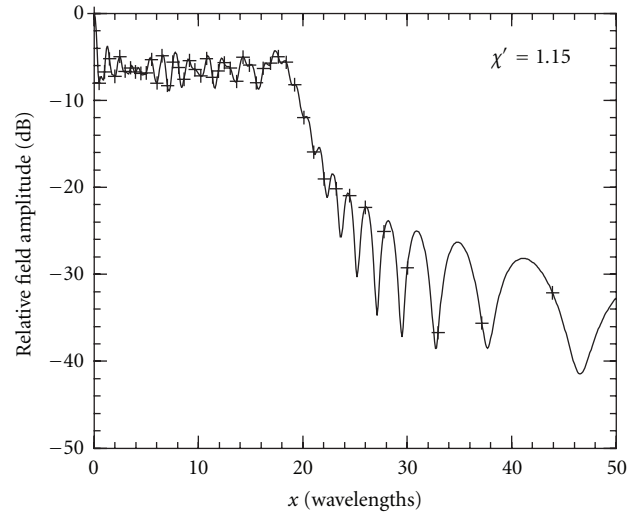
$$W_\varphi(\xi) = \begin{cases} \beta b \sin \vartheta_\infty(\xi) & \text{prolate ellipsoid,} \\ \beta a \sin \vartheta_\infty(\xi) & \text{oblate ellipsoid,} \end{cases} \quad (13)$$

wherein ϑ_∞ is the polar angle of the asymptote to the hyperbola through P (Figure 2) and is given by

$$\vartheta_\infty = \begin{cases} \sin^{-1} u + \frac{\pi}{2} & \text{prolate ellipsoid,} \\ \sin^{-1} u & \text{oblate ellipsoid.} \end{cases} \quad (14)$$

In order to show the effect of multiplying the field by the factor $e^{j\gamma(\xi)}$, the real part of the electric field and of the reduced electric field y -component radiated by an antenna along a line are reported in Figure 3. The considered antenna is a uniform planar circular array with radius equal to 20λ , lying in the plane $z = 0$. Its elements, radially and azimuthally spaced of 0.8λ , are elementary Huygens sources linearly polarized along the y axis. Accordingly, an oblate ellipsoidal modelling with $2a = 40\lambda$ and $2b = 5\lambda$ has been used. The straight line is the x -directed line at $y = 0$, lying on a plane at distance $d = 12\lambda$ from the antenna. As can be seen, as x increases, the spatial variations of the real part of the reduced field become increasingly slower than those of the electric field, since the local bandwidth has been minimized by choosing the optimal phase function. Quite analogous results are obtained for the imaginary parts.

To highlight the role of the optimal parameter ξ , the amplitude of the electric field y -component along the same


 FIGURE 3: Real part of the NF y -component on the line $y = 0$, $z = 12\lambda$. Solid line: field. Dashed line: reduced field.

 FIGURE 4: Amplitude of the NF y -component on the line $y = 0$, $z = 12\lambda$ as function of x . The samples distribution (crosses) when adopting a uniform sampling in ξ is also shown.

line is plotted as function of x and ξ in Figures 4 and 5. As can be seen, when using ξ , the spatial variations are made uniform, by reducing the scale when these variations slow down. Thus, a uniform sampling in ξ gives rise to a denser samples distribution where $w(\xi)$ is greater and to a sparser one in the zones characterized by smaller values of $w(\xi)$ (see Figure 4).

3. Representation of the Probe Voltage on a Scanning Surface

Let us consider an AUT enclosed in a convex domain bounded by a rotational surface Σ and a nondirective probe scanning an arbitrary surface obtained by rotating a meridian curve always external to the cone of vertex at

the observation point P and tangent to Σ . Since the voltage V measured by such a kind of probe has essentially the same effective spatial bandwidth of the AUT field [16], the nonredundant sampling representations of EM fields can be applied to it.

As a consequence, the reduced voltage $\tilde{V}(\xi) = V(\xi)e^{j\gamma(\xi)}$ at $P(\xi(\vartheta), \varphi)$ on the meridian curve fixed by φ can be evaluated via the OSI expansion

$$\tilde{V}(\xi(\vartheta), \varphi) = \sum_{m=m_0-q+1}^{m_0+q} \tilde{V}(\xi_m, \varphi) \Omega_M(\xi - \xi_m) D_{M''}(\xi - \xi_m), \quad (15)$$

where $m_0 = \text{Int}[\xi/\Delta\xi]$ is the index of sample nearest (on the left) to P , $2q$ is the number of the retained intermediate samples $\tilde{V}(\xi_m, \varphi)$, that is, the reduced voltages at the intersection points between the sampling parallels and the considered meridian curve, and

$$\xi_m = m\Delta\xi = \frac{2\pi m}{(2M'' + 1)}, \quad (16)$$

$$M'' = \text{Int}(\chi M') + 1, \quad M' = \text{Int}(\chi' W_\xi) + 1, \quad (17)$$

χ' being a factor, slightly larger than one, controlling the band-limitation error, χ an analogous one controlling the truncation error [7, 15], and $\text{Int}(x)$ denoting the integer part of x . Moreover,

$$D_{M''}(\xi) = \frac{\sin[(2M'' + 1)\xi/2]}{(2M'' + 1)\sin(\xi/2)}, \quad (18)$$

$$\Omega_M(\xi) = \frac{T_M[2\cos^2(\xi/2)/\cos^2(\bar{\xi}/2) - 1]}{T_M[2/\cos^2(\bar{\xi}/2) - 1]},$$

are the Dirichlet and Tschebyscheff Sampling functions, respectively, $T_M(\cdot)$ being the Tschebyscheff polynomial of degree $M = M'' - M'$ and $\bar{\xi} = q\Delta\xi$.

The intermediate samples $\tilde{V}(\xi_m, \varphi)$ can be evaluated via the OSI formula

$$\tilde{V}(\xi_m, \varphi) = \sum_{n=n_0-p+1}^{n_0+p} \tilde{V}(\xi_m, \varphi_{n,m}) \Omega_{N_m}(\varphi - \varphi_{n,m}) D_{N'_m}(\varphi - \varphi_{n,m}), \quad (19)$$

where $\tilde{V}(\xi_m, \varphi_{n,m})$ are the reduced samples on the parallel fixed by ξ_m , $2p$ is the retained samples number, $n_0 = \text{Int}(\varphi/\Delta\varphi_m)$, and

$$\varphi_{n,m} = n\Delta\varphi_m = \frac{2\pi n}{2N'_m + 1},$$

$$N'_m = \text{Int}(\chi N'_m) + 1,$$

$$N'_m = \text{Int}[\chi^* W_\varphi(\xi_m)] + 1, \quad (20)$$

$$N_m = N'_m - N'_m,$$

$$\chi^* = 1 + (\chi' - 1) [\sin \vartheta(\xi_m)]^{-2/3}.$$

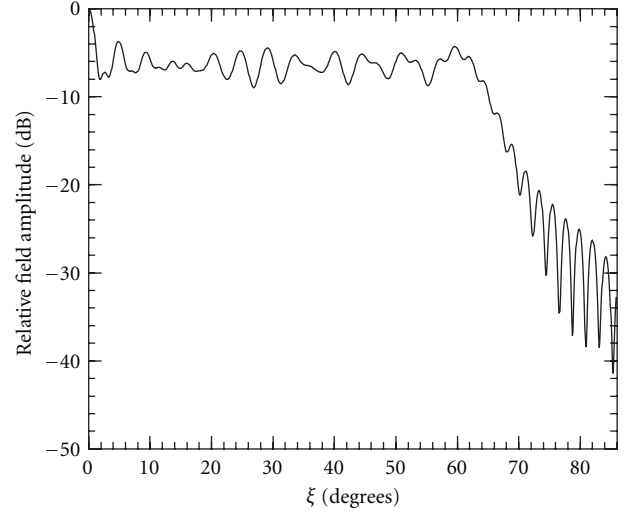


FIGURE 5: Amplitude of the NF γ -component on the line $y = 0$, $z = 12\lambda$ as function of the optimal parameter ξ .

The variation of χ^* with ξ is required to ensure a band-limitation error constant with respect to ξ [1].

As mentioned in the Introduction, above representations have been applied to a large variety of source and scanning geometries, showing that they are indeed robust against noise and that with $\chi' = \chi \approx 1.2$ and $p = 6-7$ we get absolute relative errors of the order of -60 dB and a mean square one about 10 dB lower.

As an example of these performances, we report in the following some numerical and experimental results relative to the cylindrical scanning geometry. Experimental results relative to the plane-polar geometry can be found in [16].

We consider an elongated AUT and a scanning cylinder of radius d . An effective modelling for such an antenna is obtained by choosing the surface Σ enclosing it coincident with the smallest prolate ellipsoid having major and minor semiaxes equal to a and b (see Figure 6). By properly employing the OSI expansions (Note that, to have an equal amount of truncation error at both the cylinder ends, the distribution of rings must be symmetrical with respect to $z = 0$. Therefore, their position is fixed according to the sampling law $\xi_m = m\Delta\xi + \Delta\xi/4$, instead of (16). Moreover, in (15), $m_0 = \text{Int}[(\xi - \Delta\xi/4)/\Delta\xi]$ (15) and (19), it is so possible to recover the probe and rotated probe voltages V and V' at the points needed to carry out the classical NF-FF transformation with cylindrical scanning [3].

The effectiveness and robustness of the so-developed nonredundant cylindrical NF-FF transformation have been assessed by many numerical tests. The reported simulations refer to a uniform planar array of $\lambda/2$ -spaced elementary Huygens sources, polarized along the z axis, and covering an elliptical zone in the plane $y = 0$, with major and minor semiaxes equal to 25λ and 6λ . Accordingly, a prolate ellipsoidal modelling with $2a = 50\lambda$ and $2b = 12\lambda$ has been used. The radius d of the scanning cylinder is equal to 12λ , and its height h is 160λ . The working frequency is 10 GHz, and an open-ended WR-90 rectangular waveguide is chosen

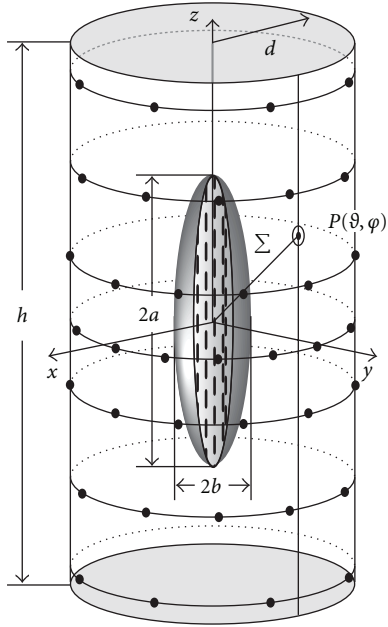
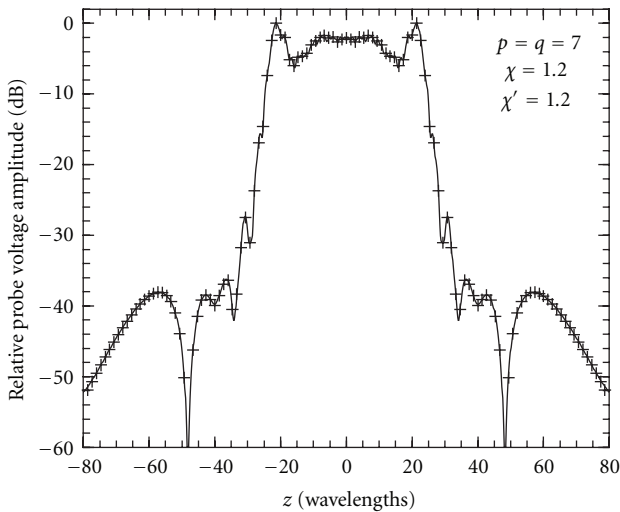
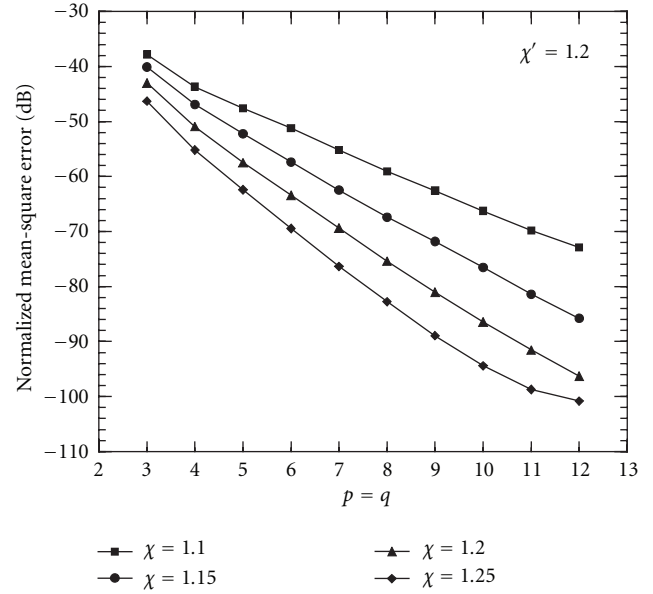


FIGURE 6: Cylindrical scanning: the prolate ellipsoidal modelling.


 FIGURE 7: Amplitude of the probe output voltage V on the generatrix at $\varphi = 90^\circ$. Solid line: exact. Crosses: interpolated.

as probe. Figure 7 shows a representative reconstruction example of the amplitude of the voltage V (the most significant one) over the cylinder generatrix at $\varphi = 90^\circ$. As can be seen, there is an excellent agreement between the exact voltage and the reconstructed one. The accuracy in the NF interpolation is confirmed also by the maximum and mean-square error values. They are obtained by comparing the interpolated values of V with those directly evaluated on a close grid in the central zone of the scanning cylinder, so that the existence of the guard samples is assured. Figure 8 shows the mean-square error, normalized to the voltage maximum value over the cylinder, for $p = q$ ranging from 3 to 12, $\chi' = 1.20$, and $\chi = 1.10, 1.15, 1.20$, and 1.25. As


 FIGURE 8: Mean-square reconstruction error of the probe voltage V .

expected, it decreases up to very low values on increasing the oversampling factor and/or the retained samples number. The algorithm stability has been investigated by adding random errors to the exact samples. These errors simulate a background noise (bounded to Δa dB in amplitude and with arbitrary phase) and an uncertainty on the data of $\pm \Delta a_r$ dB in amplitude and $\pm \Delta \alpha$ degrees in phase. As shown in Figure 9, the algorithm is stable. The algorithm has been applied to recover the NF data needed for the classical probe compensated NF-FF transformation [3]. The reconstruction of the antenna FF pattern in the E-plane is reported in Figure 10. As can be seen, the exact and recovered fields are practically indistinguishable. It can be interesting to compare the number of the used NF samples (13 566) with that (40 960) required by the classical NF-FF transformation [3].

The nonredundant NF-FF transformation with cylindrical scanning has been experimentally validated using the facilities available at the antenna characterization laboratory of the University of Salerno, where an advanced cylindrical NF measurement facility supplied by MI Technologies is available, and at the anechoic chamber of the University of Naples Parthenope, provided with a FF measurement range. The AUT, located in the plane $x = 0$, is a very simple H-plane monopulse antenna, operating at 10 GHz in the difference mode. It has been realized by using two pyramidal horns (8.9×6.8 cm) of Lectronic Research Labs at a distance of 26 cm (between centers) and a hybrid Tee. The AUT has been modelled as enclosed in a prolate ellipsoid with major and minor semi-axes equal to 27 cm and 5 cm. The probe voltages have been acquired on a cylinder with $d = 16.6$ cm and $h = 240$ cm. To assess the effectiveness of the sampling representation, the amplitude and phase (in the range $[-20$ cm, 120 cm]), to improve its readability) of the reconstructed probe voltage relevant to the generatrix at $\varphi = 0^\circ$

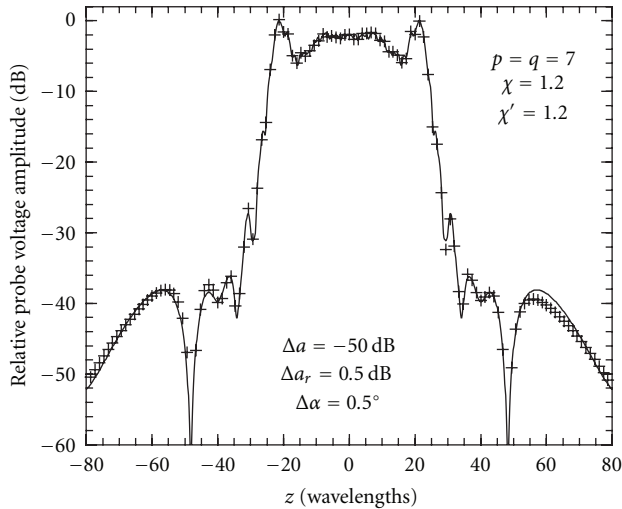


FIGURE 9: Amplitude of the probe output voltage V on the generatrix at $\varphi = 90^\circ$. Solid line: exact. Crosses: reconstructed from error affected data.

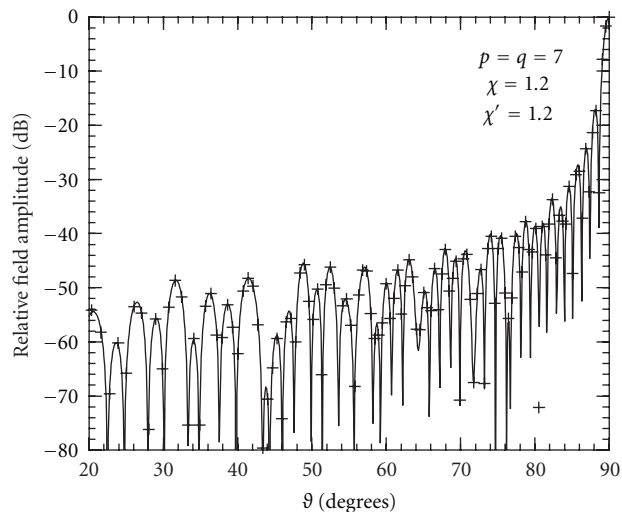


FIGURE 10: Far-field pattern in the E-plane. Solid line: exact field. Crosses: reconstructed from nonredundant cylindrical NF data.

are compared in Figures 11 and 12, respectively, with those directly measured on the same generatrix. As can be seen, the reconstruction is everywhere very good, save for the peripheral zone (below about -60 dB). The reconstructed voltage exhibits a smoother behaviour as compared to the measured one. This is due to the low pass filtering properties of the interpolation functions, which cut away the noise outside the AUT spatial bandwidth. All the reported reconstructions have been obtained by using $\chi' = 1.35$, $\chi = 1.20$, and $p = q = 8$. The comparison between the H-plane FF pattern reconstructed from the acquired nonredundant cylindrical NF data and that obtained directly from the data measured on the classical cylindrical grid (see Figure 13) assesses the overall effectiveness of the NF-FF transformation technique. In both cases, the software package MI-3000 has been used to get the FF reconstructions.

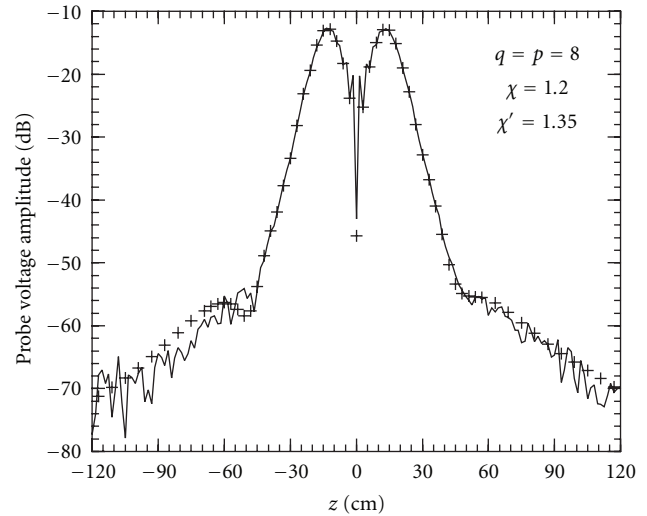


FIGURE 11: Amplitude of the probe output voltage V on the generatrix at $\varphi = 0^\circ$. Solid line: measured. Crosses: interpolated.

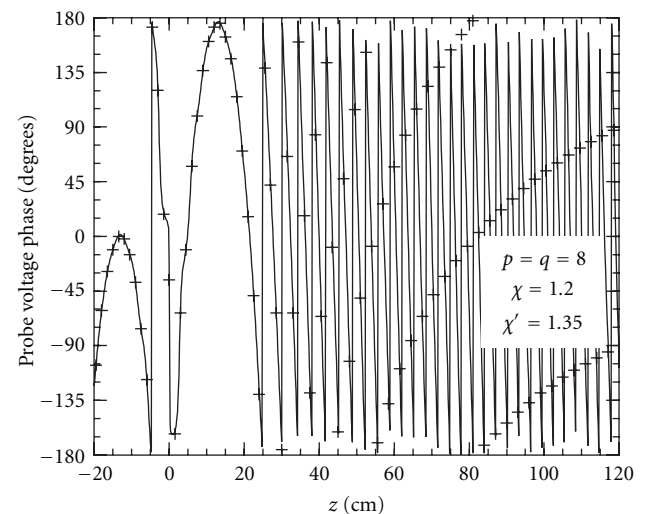


FIGURE 12: Phase of the probe output voltage V on the generatrix at $\varphi = 0^\circ$. Solid line: measured. Crosses: interpolated.

The accuracy of the FF reconstruction process is further confirmed by comparing (see Figure 14) the H-plane pattern obtained from the nonredundant measurements with that directly measured in the FF region at the anechoic chamber of the University of Naples Parthenope. As can be seen, although the measurements have been carried out with quite different techniques and environmental conditions, a very good agreement results, save for small discrepancies in the far-out side lobes region, due to the truncation of the scanning zone. It must be stressed that the described technique allows a significant reduction of the number of measurements, without losing the accuracy of the classical approach. As a matter of fact, the number of samples needed by the described NF-FF transformation with cylindrical scan is 1 895 against that (5 760) required by MI-3000 package to cover the same scanning zone.

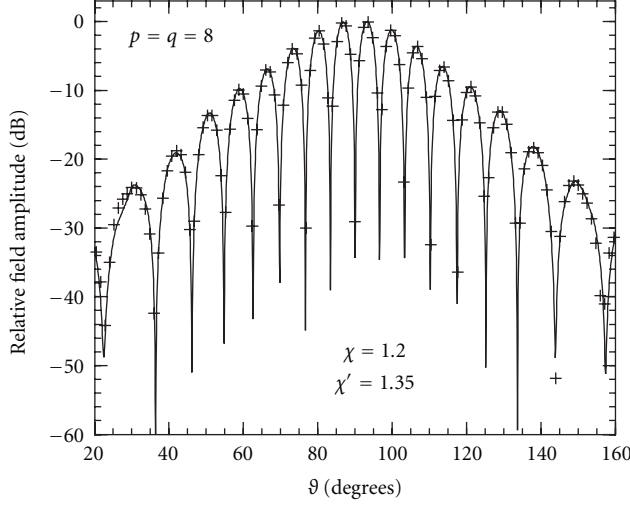


FIGURE 13: H-plane pattern. Solid line: obtained from NF data measured on the classical cylindrical grid. Crosses: reconstructed from NF data acquired via the nonredundant cylindrical scanning.

4. Voltage Reconstruction from Nonredundant Samples along a Spiral

As emphasized in the Introduction, the adoption of a spiral scanning can improve the performance of NF-FF measurement techniques by significantly reducing the measurement time. Accordingly, in this Section, we report the main results concerning the reconstruction of the probe voltage on a quite arbitrary rotational surface \mathcal{M} (with the same rotational symmetry of the surface Σ bounding the source) from the knowledge of a nonredundant number of its samples lying on a spiral wrapping the surface [34, 41].

In order to get such a sampling representation of the voltage, it is necessary [34]

- (i) to choose the pitch of the spiral coincident with the sample spacing needed for the interpolation along a meridian curve,
- (ii) to develop a nonredundant sampling representation of the voltage on the spiral, based on the theoretical results in [15].

As the sample spacing is uniform in the ξ variable associated to Σ (see formula (7)), condition (i) implies that the spiral equation is

$$\xi = k\phi, \quad (21)$$

where ϕ is the angular parameter describing the spiral.

Such a spiral can be viewed as intersection of the surface \mathcal{M} with the line $\xi = \text{const}$ in the meridian plane, emanating from a point which moves on a spiral that wraps, with a constant pitch, the surface Σ enclosing the AUT. As the variable ξ varies in the range $[-\pi, \pi]$, the aforementioned condition on the spiral pitch implies that the constant k must be such that the interval $\Delta\xi = 2\pi k$ between two consecutive intersections of the spiral with the meridian curve is equal

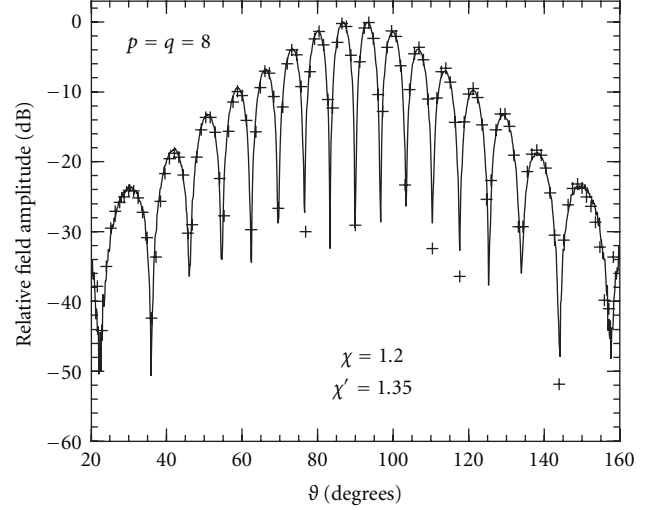


FIGURE 14: H-plane pattern. Solid line: direct FF measurements. Crosses: reconstructed from NF data acquired via the nonredundant cylindrical scanning.

to $2\pi/(2M'' + 1)$, with $M'' = \text{Int}(\chi M') + 1$, and $M' = \text{Int}(\chi' W_\xi) + 1$. It follows that $k = 1/(2M'' + 1)$.

The determination of optimal phase factor ψ and parameter η to get a nonredundant representation of the voltage along the spiral is a more difficult task, as the influence of the source geometry is more involved. In the case of a spherical source, the result can be obtained [34] by observing that the extreme values of $\hat{R} \cdot \hat{t}$ in (3) and (4) are determined by considering the intersection of the plane defined by \hat{t} and the unit vector \hat{r} with the cone having the vertex at the generic point Q on the spiral and the generatrices coincident with the tangents to the sphere modelling the AUT. Denoting by $\hat{R}_{1,2}$ the related unit vectors and by ε the angle between \hat{r} and \hat{t} (Figure 15), we get [34] the following

$$\frac{(\hat{R}_1 + \hat{R}_2)}{2} = \hat{r} \sin \delta = \hat{r} \sqrt{1 - \frac{a^2}{r^2}}, \quad (22)$$

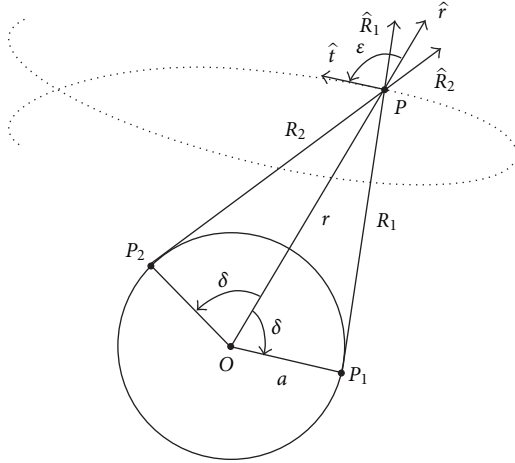
$$\frac{(\hat{R}_1 - \hat{R}_2) \cdot \hat{t}}{2} = \cos \delta \sin \varepsilon = \left(\frac{a}{r}\right) \sin \varepsilon. \quad (23)$$

By substituting (22) in (3), and taking into account that $d\mathbf{r} = \hat{r} \cdot \hat{t} ds$, it results in the following:

$$\begin{aligned} \psi &= \beta \int_0^r \sqrt{1 - \frac{a^2}{r^2}} dr \\ &= \beta \sqrt{r^2 - a^2} - \beta a \cos^{-1} \left(\frac{a}{r} \right). \end{aligned} \quad (24)$$

On the other hand [34],

$$\begin{aligned} ds &= \sqrt{r^2 \sin^2 \theta + k^2 r^2 + k^2 \dot{r}^2} d\phi, \\ \sin \varepsilon &= \sqrt{1 - (\hat{r} \cdot \hat{t})^2}, \end{aligned} \quad (25)$$

FIGURE 15: Geometry of the problem in the plane \hat{t}, \hat{r} .

wherein $\dot{r} = dr/d\vartheta$ and, being in such a case ξ equal to the polar angle ϑ ,

$$\begin{aligned} \hat{r} \cdot \hat{t} &= \frac{dr}{ds} = \frac{dr}{d\phi} \frac{d\phi}{ds} \\ &= \left[\frac{dr}{d\vartheta} \frac{d\vartheta}{d\phi} \right] \frac{d\phi}{ds} \\ &= k\dot{r} \frac{d\phi}{ds} = \frac{k\dot{r}}{\sqrt{r^2 \sin^2 \vartheta + k^2 r^2 + k^2 \dot{r}^2}}. \end{aligned} \quad (26)$$

By substituting relations (23) and (25) in (4), it results:

$$\eta = \frac{\beta a}{W_\eta} \int_0^\phi \sqrt{k^2 + \sin^2 k\phi} d\phi. \quad (27)$$

It is worth noting that the expression (24) of the phase function ψ relevant to the sampling representation along the spiral coincides with that γ relevant to the representation on a meridian curve [15].

According to (27), the parameter η is β/W_η times the arc-length along the spiral which wraps the sphere modelling the AUT. Since such a spiral is a closed curve, it is convenient to choose the bandwidth W_η such that η covers a 2π range when the whole projecting curve on the sphere is described. As a consequence,

$$W_\eta = \frac{\beta a}{\pi} \int_0^{(2M''+1)\pi} \sqrt{k^2 + \sin^2 k\phi} d\phi, \quad (28)$$

namely, the bandwidth W_η is β/π times the length of the spiral that wraps from pole to pole the sphere modelling the AUT.

Let us now turn to the case of nonspherical modelling of the source. By following a heuristic reasoning, one can determine [41] the phase factor ψ and parameterization η also in this case. In particular, by generalizing the corresponding relations for the case of spherical modelling (see (24), (27), and (28)), ψ coincides with the phase function γ relevant to a meridian curve, η is β/W_η times the arc length of the projecting point that lies on the spiral wrapping the surface

Σ , and the bandwidth W_η is β/π times the length of the spiral wrapping Σ from pole to pole. Namely, the spiral, ψ and η are such that they coincide with those relevant to the spherical modelling when the surface Σ leads to a sphere.

According to the above results, the OSI formula for reconstructing the reduced voltage at any point Q of the spiral is [34, 41]

$$\tilde{V}(\eta) = \sum_{n=n_0-p+1}^{n_0+p} \tilde{V}(\eta_n) \Omega_N(\eta - \eta_n) D_{N''}(\eta - \eta_n), \quad (29)$$

where $n_0 = \text{Int}(\eta/\Delta\eta)$ is the index of the sample nearest (on the left) to the point Q , $2p$ the number of retained samples $\tilde{V}(\eta_n)$, and

$$\eta_n = n\Delta\eta = 2\pi n / (2N'' + 1), \quad (30)$$

with $N'' = \text{Int}(\chi N') + 1$ and $N' = \text{Int}(\chi' W_\eta) + 1$.

It must be stressed that, when interpolating the voltage in the neighbourhood of the poles ($\vartheta = 0$ and $\vartheta = \pi$), the enlargement bandwidth factor χ' must be properly increased to avoid a significant growth of the band-limitation error. This is due to the fact that small variations of η correspond to very large changes of ϕ in these zones.

The OSI expansion (29) can be employed to evaluate the reduced voltage values at the intersection points between the spiral and the meridian curve passing through the observation point P . Once these intermediate samples have been determined, the reduced voltage at P can be reconstructed via the following OSI formula:

$$\tilde{V}(\xi(\vartheta), \varphi) = \sum_{m=m_0-q+1}^{m_0+q} \tilde{V}(\xi_m) \Omega_M(\xi - \xi_m) D_{M''}(\xi - \xi_m), \quad (31)$$

wherein $m_0 = \text{Int}[(\xi - \xi_0)/\Delta\xi]$ is the index of sample nearest (on the left) to P , $\tilde{V}(\xi_m)$ are the intermediate samples,

$$\xi_m = \xi_m(\varphi) = k\varphi + m\Delta\xi = \xi_0 + m\Delta\xi, \quad (32)$$

and the other symbols have the same meanings as in (15).

In order to illustrate above results and for its practical relevance, let us consider the case of an elongated AUT whose NF is probed on a proper helix lying on a cylinder of radius d (Figure 16). For such a kind of antenna, a flexible modelling, which can be a convenient alternative to the prolate ellipsoidal one, is the rounded cylinder modelling. It is obtained by choosing Σ coincident with a cylinder of height h' ended in two half-spheres of radius a' (Figure 16). By taking into account that in the helicoidal scanning case $r(\vartheta) = d/\sin \vartheta$ and imposing the passage of the helix through a fixed point Q_0 of the generatrix at $\varphi = 0$, the helix equations read

$$\begin{aligned} x &= d \cos(\phi - \phi_s), \\ y &= d \sin(\phi - \phi_s), \\ z &= d \cot[\vartheta(\xi)], \end{aligned} \quad (33)$$

wherein ϕ_s is the value of ϕ at Q_0 .

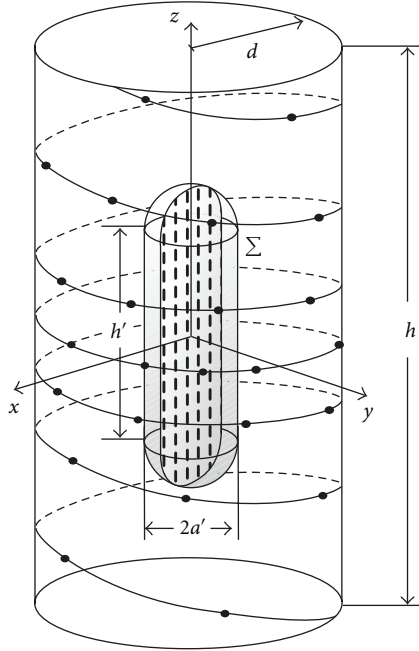


FIGURE 16: Helicoidal scanning: the rounded cylinder modelling.

It can be easily verified (see Figure 17) that, for the considered source modelling, the parameters involved in the expressions (6) and (7) of the phase factor and optimal parameter relevant to the nonredundant representation along a generatrix are [22, 36]

$$\begin{aligned} \ell' &= 2(h' + \pi a'), \\ R_{1,2} &= \sqrt{\left(z \mp \frac{h'}{2}\right)^2 + d^2 - a'^2}, \\ s'_1 &= a' \sin^{-1} \left(\frac{a'd + R_1 \left(\left(\frac{h'}{2}\right) - z \right)}{R_1^2 + a'^2} \right), \\ s'_2 &= h' + a' \left[\pi - \sin^{-1} \left(\frac{a'd + R_2 \left(\left(\frac{h'}{2}\right) + z \right)}{R_2^2 + a'^2} \right) \right]. \end{aligned} \quad (34)$$

The reduced voltage at P can be again reconstructed by means of (31), wherein the intermediate samples are still determined via (29), but, having imposed in such a case the passage of the helix through the point Q_0 , the expressions of ξ_m , η_n , and n_0 become $\xi_m = \xi_m(\varphi) = \xi(\phi_s) + k\varphi + m\Delta\xi = \xi_0 + m\Delta\xi$, $n_0 = \text{Int}[(\eta - \eta_0)/\Delta\eta]$, and $\eta_n = \eta(\phi_s) + n\Delta\eta = \eta_0 + 2\pi n/(2N'' + 1)$.

By properly employing the OSI expansions (29) and (31), it is so possible to recover the probe and rotated probe voltages V and V' at the points needed to perform the classical NF-FF transformation with cylindrical scanning [3], thus getting a nonredundant NF-FF transformation with helicoidal scanning.

Such a NF-FF transformation has been numerically assessed in [36], obtaining results quite similar (in terms of accuracy and data reduction) to those reported in

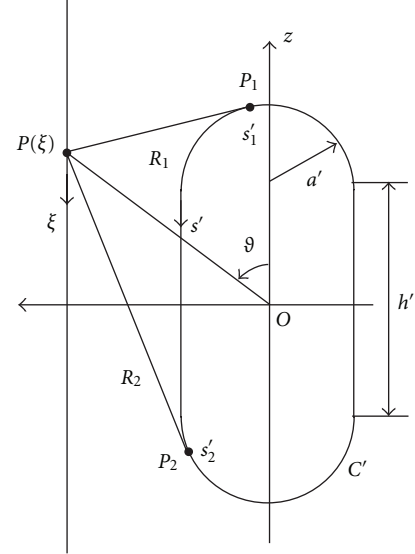
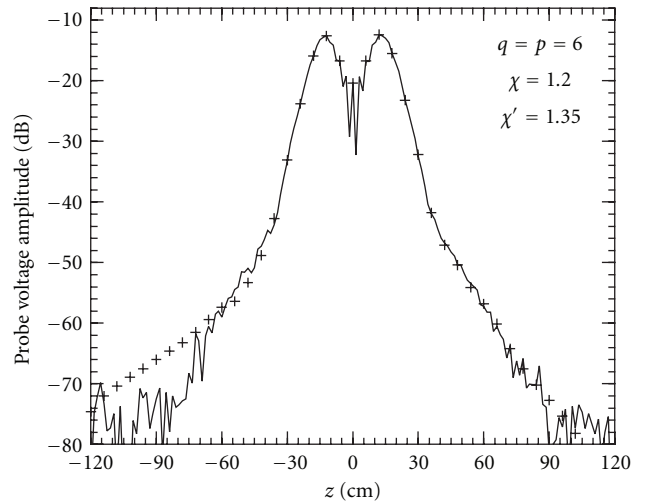


FIGURE 17: Relevant to a cylinder generatrix.


 FIGURE 18: Amplitude of the probe output voltage V on the generatrix at $\varphi = 0^\circ$. Solid line: measured. Crosses: interpolated.

the previous section with reference to the nonredundant cylindrical NF-FF transformation.

Some experimental results performed at the antenna characterization laboratory of the University of Salerno and assessing the validity of the technique are reported in the following. The dimensions of the cylinder wrapped by the helix, the probe, the working frequency, and the AUT are the same as in Section 3. In such a case, the AUT operates in the sum mode and is modelled by a rounded cylinder with $h' = 35$ cm and $a' = 3.4$ cm. In Figures 18 and 19, the amplitude and phase of the reconstructed probe voltage relevant to the generatrix at $\varphi = 0^\circ$ are compared with those directly measured on the same generatrix. The same comments already done with reference to Figures 11 and 12 hold. The overall effectiveness of the described NF-FF transformation is assessed by comparing (Figures 20 and 21) the

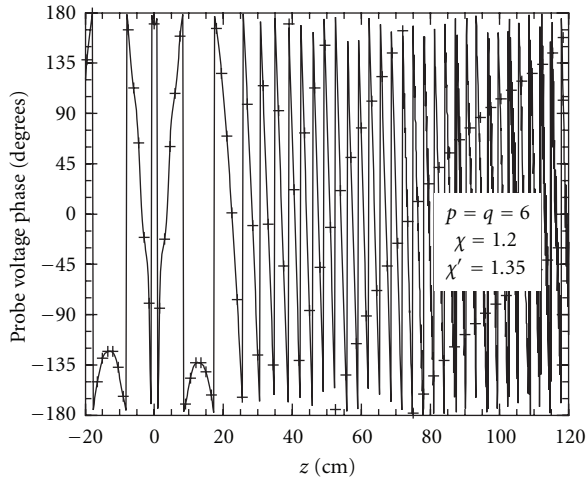


FIGURE 19: Phase of the probe output voltage V on the generatrix at $\varphi = 0^\circ$. Solid line: measured. Crosses: interpolated.

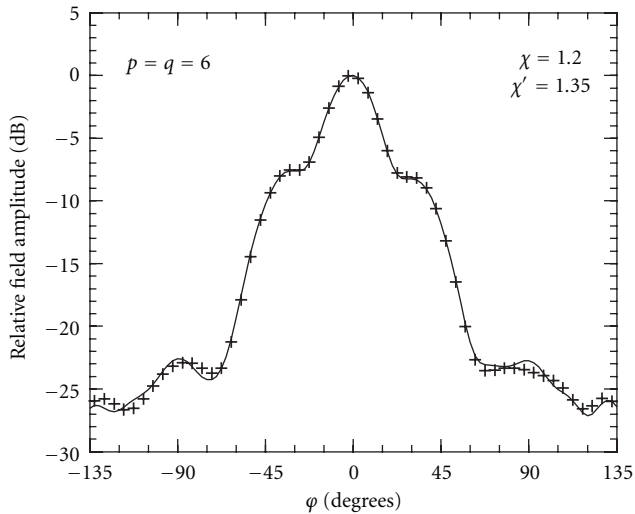


FIGURE 20: E-plane pattern. Solid line: reference. Crosses: reconstructed from NF data acquired via the helicoidal scanning.

FF patterns in the principal planes E and H reconstructed from the acquired NF data with those (references) obtained by using the software package MI-3000 from the data directly measured on the classical cylindrical grid. The same software has been used to get the FF reconstruction from the helicoidal NF data. To this end, the described OSI algorithm has been used for recovering the required cylindrical NF data. Moreover, the H-plane pattern obtained from the helicoidal measurements is compared in Figure 22 with that directly measured in the FF zone. As can be seen, in all the cases, there is a very good agreement, thus confirming the effectiveness of the technique.

It is interesting to compare the number of samples (948) needed by such a NF-FF transformation with helicoidal scan with that (5760) required by the traditional NF cylindrical scanning to cover the same measurement zone. As shown, the described technique allows a significant reduction of the

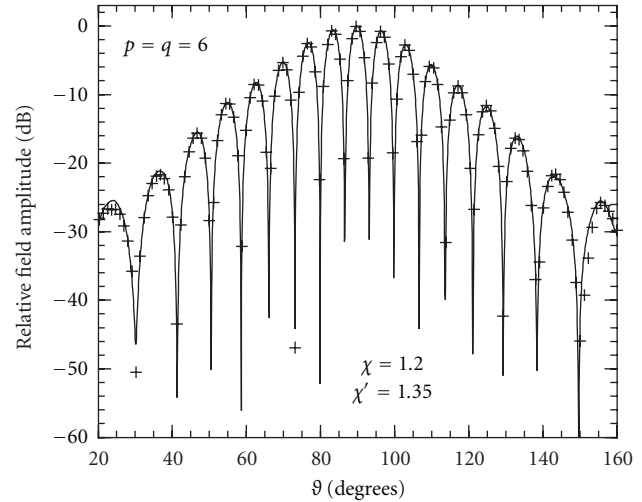


FIGURE 21: H-plane pattern. Solid line: reference. Crosses: reconstructed from NF data acquired via the helicoidal scanning.

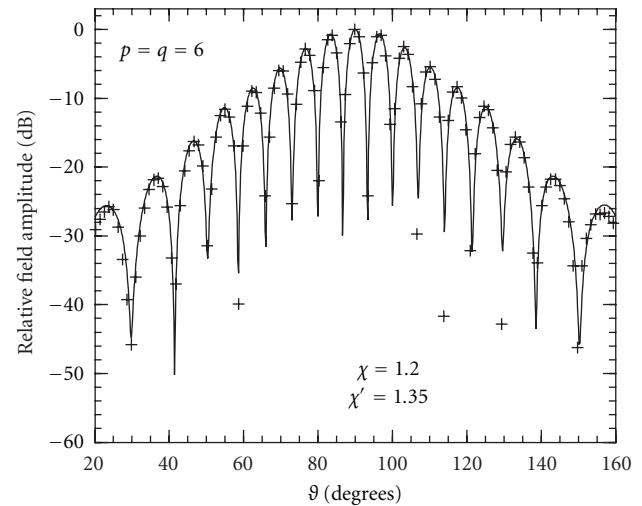


FIGURE 22: H-plane pattern. Solid line: direct FF measurements. Crosses: reconstructed from NF data acquired via the helicoidal scanning.

number of measurements, without losing the accuracy of the classical approach.

5. Conclusions

In this paper, we have presented an overview of the application of the band-limitation properties and nonredundant sampling representations of EM fields to NF-FF transformation techniques, outlining the remarkable reduction in the number of needed NF samples and measurement time so achievable in all conventional scanings. Then, the unified theory of the NF-FF transformations with spiral scanings has been reviewed highlighting that these transformations allow a further substantial reduction of the measurement time. In both cases, proper OSI formulas to efficiently

reconstruct the NF data needed by the classical NF-FF transformation corresponding to the adopted scanning surface from the acquired nonredundant samples are reported. At last numerical, as well as, experimental results assessing the effectiveness of the considered NF-FF transformations are shown.

References

- [1] O. M. Bucci and G. Franceschetti, "On the spatial bandwidth of scattered fields," *IEEE Transactions on Antennas and Propagation*, vol. 35, no. 12, pp. 1445–1455, 1987.
- [2] O. M. Bucci and Gennarelli, "Use of sampling expansions in near-field-far-field transformation: the cylindrical case," *IEEE Transactions on Antennas and Propagation*, vol. 36, no. 6, pp. 830–835, 1988.
- [3] W. M. Leach Jr. and D. T. Paris, "Probe compensated near-field measurements on a cylinder," *IEEE Transactions on Antennas and Propagation*, vol. 21, no. 4, pp. 435–445, 1973.
- [4] A. D. Yaghjian, "Near-field antenna measurement on a cylindrical surface: a source scattering matrix formulation," NBS Technical Note 696, U.S. Government Printing Office, Washington, DC, USA, 1977.
- [5] O. M. Bucci, G. D'Elia, and M. D. Migliore, "A new strategy to reduce the truncation error in near-field/far-field transformations," *Radio Science*, vol. 35, no. 1, pp. 3–17, 2000.
- [6] O. M. Bucci and G. Di Massa, "Truncation error in the application of sampling series to electromagnetic problems," *IEEE Transactions on Antennas and Propagation*, vol. 36, no. 7, pp. 941–949, 1988.
- [7] O. M. Bucci, C. Gennarelli, and C. Savarese, "Optimal interpolation of radiated fields over a sphere," *IEEE Transactions on Antennas and Propagation*, vol. 39, no. 11, pp. 1633–1643, 1991.
- [8] O. M. Bucci, C. Gennarelli, and C. Savarese, "Fast and accurate near-field-far-field transformation by sampling interpolation of plane-polar measurements," *IEEE Transactions on Antennas and Propagation*, vol. 39, no. 1, pp. 48–55, 1991.
- [9] L. I. Williams, Y. Rahmat-Samii, and R. G. Yaccarino, "The bipolar planar near-field measurement technique, part I: implementation and measurement comparisons," *IEEE Transactions on Antennas and Propagation*, vol. 42, no. 2, pp. 184–195, 1994.
- [10] R. G. Yaccarino, Y. Rahmat-Samii, and L. I. Williams, "The bipolar planar near-field measurement technique, part II: near-field to far-field transformation and holographic imaging methods," *IEEE Transactions on Antennas and Propagation*, vol. 42, no. 2, pp. 196–204, 1994.
- [11] Y. Rahmat-Samii, L. I. Williams, and R. G. Yaccarino, "The UCLA bi-polar planar-near-field antenna-measurement and diagnostics range," *IEEE Antennas and Propagation Magazine*, vol. 37, no. 6, pp. 16–35, 1995.
- [12] T. Brockett and Y. Rahmat-Samii, "A novel portable bipolar near-field measurement system for millimeter-wave antennas: construction, development, and verification," *IEEE Antennas and Propagation Magazine*, vol. 50, no. 5, pp. 121–130, 2008.
- [13] O. M. Bucci and G. Franceschetti, "On the degrees of freedom of scattered fields," *IEEE Transactions on Antennas and Propagation*, vol. 37, no. 7, pp. 918–926, 1989.
- [14] O. M. Bucci and T. Isernia, "Electromagnetic inverse scattering: retrievable information and measurement strategies," *Radio Science*, vol. 32, no. 6, pp. 2123–2137, 1997.
- [15] O. M. Bucci, C. Gennarelli, and C. Savarese, "Representation of electromagnetic fields over arbitrary surfaces by a finite and nonredundant number of samples," *IEEE Transactions on Antennas and Propagation*, vol. 46, no. 3, pp. 351–359, 1998.
- [16] O. M. Bucci, G. D'Elia, and M. D. Migliore, "Advanced field interpolation from plane-polar samples: experimental verification," *IEEE Transactions on Antennas and Propagation*, vol. 46, no. 2, pp. 204–210, 1998.
- [17] O. M. Bucci, C. Gennarelli, G. Riccio, and C. Savarese, "Near-field-far-field transformation from nonredundant plane-polar data: effective modellings of the source," *IEE Proceedings—Microwaves, Antennas and Propagation*, vol. 145, no. 1, pp. 33–38, 1998.
- [18] O. M. Bucci, F. D'Agostino, C. Gennarelli, G. Riccio, and C. Savarese, "NF-FF transformation with plane-polar scanning: ellipsoidal modelling of the antenna," *Automatika*, vol. 41, no. 3–4, pp. 159–164, 2000.
- [19] F. D'Agostino, C. Gennarelli, G. Riccio, and C. Savarese, "Data reduction in the NF-FF transformation with bi-polar scanning," *Microwave and Optical Technology Letters*, vol. 36, no. 1, pp. 32–36, 2003.
- [20] F. Ferrara, C. Gennarelli, R. Guerriero, G. Riccio, and C. Savarese, "An efficient near-field to far-field transformation using the planar wide-mesh scanning," *Journal of Electromagnetic Waves and Applications*, vol. 21, no. 3, pp. 341–357, 2007.
- [21] O. M. Bucci, C. Gennarelli, G. Riccio, C. Savarese, and V. Speranza, "Nonredundant representation of the electromagnetic fields over a cylinder with application to the near-field far-field transformation," *Electromagnetics*, vol. 16, no. 3, pp. 273–290, 1996.
- [22] O. M. Bucci, C. Gennarelli, G. Riccio, and C. Savarese, "NF-FF transformation with cylindrical scanning: an effective technique for elongated antennas," *IEE Proceedings—Microwaves, Antennas and Propagation*, vol. 145, no. 5, pp. 369–374, 1998.
- [23] F. D'Agostino, F. Ferrara, C. Gennarelli, G. Riccio, and C. Savarese, "NF-FF transformation with cylindrical scanning from a minimum number of data," *Microwave and Optical Technology Letters*, vol. 35, no. 4, pp. 264–268, 2002.
- [24] O. M. Bucci, F. D'Agostino, C. Gennarelli, G. Riccio, and C. Savarese, "Data reduction in the NF-FF transformation technique with spherical scanning," *Journal of Electromagnetic Waves and Applications*, vol. 15, no. 6, pp. 755–775, 2001.
- [25] F. D'Agostino, F. Ferrara, C. Gennarelli, R. Guerriero, and M. Migliozi, "Effective antenna modellings for NF-FF transformations with spherical scanning using the minimum number of data," *International Journal of Antennas and Propagation*, vol. 2011, Article ID 936781, 11 pages, 2011.
- [26] J. C. Bolomey, B. J. Cown, G. Fine et al., "Rapid near-field antenna testing via arrays of modulated scattering probes," *IEEE Transactions on Antennas and Propagation*, vol. 36, no. 6, pp. 804–814, 1988.
- [27] S. Pivnenko and T. Laitinen, "Spherical near-field antenna measurements with theta-scanning with reduced number of phi-steps," in *Proceedings of the Antenna Measurement Techniques Association (AMTA '09)*, pp. 383–388, Salt Lake City, Utah, USA, November 2009.
- [28] S. Pivnenko and T. Laitinen, "Fast pattern measurement of electrically large antennas by spherical near-field technique," in *Proceedings of the 32nd ESA Workshop on Antennas for Space Applications*, Noordwijk, the Netherlands, October 2010.
- [29] Pivnenko S., "Time-saving scanning schemes for measurement of electrically large antennas by spherical near-field technique," in *Proceedings of the European Conference on Antennas Propagation (EUCAP '11)*, pp. 2009–2013, Rome, Italy, April 2011.

- [30] R. G. Yaccarino, L. I. Williams, and Y. Rahmat-Samii, "Linear spiral sampling for the bipolar planar near-field antenna measurement technique," *IEEE Transactions on Antennas and Propagation*, vol. 44, no. 7, pp. 1049–1051, 1996.
- [31] O. M. Bucci, C. Gennarelli, G. Riccio, and C. Savarese, "Nonredundant NF-FF transformation with helicoidal scanning," *Journal of Electromagnetic Waves and Applications*, vol. 15, no. 11, pp. 1507–1519, 2001.
- [32] O. M. Bucci, F. D'Agostino, C. Gennarelli, G. Riccio, and C. Savarese, "Probe compensated far-field reconstruction by near-field planar spiral scanning," *IEE Proceedings—Microwaves, Antennas and Propagation*, vol. 149, no. 2, pp. 119–123, 2002.
- [33] O. M. Bucci, F. D'Agostino, C. Gennarelli, G. Riccio, and C. Savarese, "Near-field-far-field transformation with spherical spiral scanning," *IEEE Antennas and Wireless Propagation Letters*, vol. 2, pp. 263–266, 2003.
- [34] F. D'Agostino, C. Gennarelli, G. Riccio, and C. Savarese, "Theoretical foundations of near-field-far-field transformations with spiral scanings," *Progress in Electromagnetics Research*, vol. 61, pp. 193–214, 2006.
- [35] F. D'Agostino, F. Ferrara, C. Gennarelli, R. Guerriero, and M. Migliozi, "Near-field-far-field transformation technique with helicoidal scanning for elongated antennas," *Progress in Electromagnetics Research B*, vol. 4, pp. 249–261, 2008.
- [36] F. D'Agostino, F. Ferrara, C. Gennarelli, R. Guerriero, M. Migliozi, and G. Riccio, "NF-FF transformation with helicoidal scanning: an effective source modelling for elongated antennas," *International Journal of Microwave and Optical Technology*, vol. 3, no. 5, pp. 275–282, 2008.
- [37] F. D'Agostino, F. Ferrara, J. A. Fordham et al., "An effective near-field-far-field transformation technique for elongated antennas using a fast helicoidal scan," *IEEE Antennas and Propagation Magazine*, vol. 51, no. 4, pp. 134–141, 2009.
- [38] F. D'Agostino, F. Ferrara, C. Gennarelli, R. Guerriero, and M. Migliozi, "Laboratory tests assessing the effectiveness of the NF-FF transformation with helicoidal scanning for electrically long antennas," *Progress in Electromagnetics Research*, vol. 98, pp. 375–388, 2009.
- [39] F. D'Agostino, F. Ferrara, C. Gennarelli, R. Guerriero, and M. Migliozi, "An effective NF-FF transformation technique with planar spiral scanning tailored for quasi-planar antennas," *IEEE Transactions on Antennas and Propagation*, vol. 56, no. 9, pp. 2981–2987, 2008.
- [40] F. D'Agostino, F. Ferrara, C. Gennarelli, R. Guerriero, M. Migliozi, and G. Riccio, "A nonredundant near-field to far-field transformation with spherical spiral scanning for nonspherical antennas," *The Open Electrical & Electronic Engineering Journal*, vol. 3, pp. 1–8, 2009.
- [41] F. D'Agostino, F. Ferrara, C. Gennarelli, R. Guerriero, and M. Migliozi, "The unified theory of near-field-far-field transformations with spiral scanings for nonspherical antennas," *Progress In Electromagnetics Research B*, no. 14, pp. 449–477, 2009.
- [42] A. Capozzoli, C. Curcio, G. D'Elia, and A. Liseno, "Phaseless antenna characterization by effective aperture field and data representations," *IEEE Transactions on Antennas and Propagation*, vol. 57, no. 1, pp. 215–230, 2009.
- [43] A. Capozzoli, C. Curcio, G. D'Elia, and A. Liseno, "Singular-Value optimization in plane-polar near-field antenna characterization," *IEEE Antennas and Propagation Magazine*, vol. 52, no. 2, pp. 103–112, 2010.
- [44] A. Capozzoli, C. Curcio, G. D'Elia et al., "A SVD-based approach to helicoidal NF-FF transformations," in *Proceedings of the European Conference on Antennas Propagation (EUCAP '10)*, pp. 1–5, Barcelona, Spain, April 2010.
- [45] S. Costanzo, G. Di Massa, and M. D. Migliore, "Integrated microstrip probe for phaseless near-field measurements on plane-polar geometry," *Electronics Letters*, vol. 37, no. 16, pp. 1018–1020, 2001.
- [46] R. G. Yaccarino and Y. Rahmat-Samii, "Phaseless bi-polar planar near-field measurements and diagnostics of array antennas," *IEEE Transactions on Antennas and Propagation*, vol. 47, no. 3, pp. 574–583, 1999.
- [47] S. F. Razavi and Y. Rahmat-Samii, "A new look at phaseless planar near-field measurements: limitations, simulations, measurements, and a hybrid solution," *IEEE Antennas and Propagation Magazine*, vol. 49, no. 2, pp. 170–178, 2007.
- [48] S. Costanzo, G. Di Massa, and M. D. Migliore, "A novel hybrid approach for far-field characterization from near-field amplitude-only measurements on arbitrary scanning surfaces," *IEEE Transactions on Antennas and Propagation*, vol. 53, no. 6, pp. 1866–1874, 2005.

Research Article

Numerical Investigation of the System-Matrix Method for Higher-Order Probe Correction in Spherical Near-Field Antenna Measurements

Thorkild B. Hansen

Seknion Inc., 2000 Commonwealth Ave, Boston, MA 01235, USA

Correspondence should be addressed to Thorkild B. Hansen, thorkild.hansen@att.net

Received 14 October 2011; Accepted 12 December 2011

Academic Editor: Claudio Gennarelli

Copyright © 2012 Thorkild B. Hansen. This is an open access article distributed under the Creative Commons Attribution License, which permits unrestricted use, distribution, and reproduction in any medium, provided the original work is properly cited.

The system-matrix method for higher-order probe correction in spherical near-field scanning is based on a renormalized least-squares approach in which the normal matrix closely resembles the identity matrix when most of the energy of the probe pattern resides in the first-order modes. This method will be “stressed-tested” in the present paper by employing probes for which up to 49% of the pattern energy resides in the higher-order modes. The condition number of the resulting normal matrix will be computed, and its “distance” from the identity matrix displayed. It is also shown how the condition number of the normal matrix can be further reduced.

1. Introduction

The standard theories for spherical near-field scanning of electromagnetic fields [1–5] hold for first-order probes that have $e^{\pm i\phi}$ azimuthal pattern dependence only. For general higher-order two-port probes, which have unequal port patterns that contain modes $e^{i\mu\phi}$ with $\mu \neq \pm 1$, one cannot use these standard theories. (The term “higher-order mode,” refers to all modes with $|\mu| \neq 1$, including the mode $\mu = 0$. Through χ -scanning, the standard method [3] can deal with higher-order probes in special situations. However, this approach does not work in the situation of highest practical importance where the data consists of the output of a two-port higher-order probe.) Therefore, first-order probes have been preferred in spherical near-field scanning over the past 30 years.

Unfortunately, first-order probes are inherently narrow-banded, and thus a large number of different probes (each covering a narrow frequency band) are needed to measure the AUT over a broadband of frequencies. In practice, this means that wide-band characterizations become very time consuming because the spherical scan must be repeated many times. In addition, it takes a considerable amount

of time to calibrate and change probes because precise alignment procedures are required.

Broadband probes that overcome all these problems do indeed exist, but their patterns contain higher-order modes. Typically, most of the probe-pattern energy is still in the first-order modes, but the higher-order modes are nevertheless strong enough to prevent a first-order correction scheme from being accurate. Therefore, the problem of developing probe-corrected theories for spherical near-field scanning that hold for higher-order probes has received considerable attention recently; see [6–8] and references therein.

In the present paper we shall evaluate the system-matrix method presented in [8], which uses a renormalized least-squares approach to obtain a probe-corrected theory for general higher-order two-port probes in spherical scanning. The ports need not have identical patterns, and the theory holds for both a ϕ -scan ($0 \leq \theta \leq \pi$, $0 \leq \phi \leq 2\pi$) or a θ -scan ($0 \leq \theta \leq 2\pi$, $0 \leq \phi \leq \pi$), and the scan points are obtained by rectangular $\theta - \phi$ sampling. The spherical expansion coefficients of the antenna under test (AUT) are determined by solving a linear system of equations involving a square normal matrix. This solution can be achieved in

two alternative ways: (i) an iterative method that employs the conjugate gradient method and (ii) a direct method where the normal matrix is inverted explicitly. Both versions require $O(N^3)$ operations with very little overhead. Here, N is the truncation number in the spherical expansion of the AUT field; see Section 2. Through a validation in [8] with experimental data, it was demonstrated that 29280 spherical expansion coefficients of an AUT can be computed in 8 seconds on a PC running Matlab.

We will “stress-test” the method by using probes for which up to 49% of the pattern energy resides in the higher-order modes. We compute the condition number and other statistics of the resulting normal matrix. Since the AUT spherical expansion coefficients can be obtained more rapidly when the normal matrix is close to the identity matrix, we shall investigate ways to “move” the normal matrix closer to the identity matrix.

The paper is organized as follows. In Section 2 we show how the AUT far-field pattern can be expressed in terms of the transverse spherical vector-wave functions and spherical expansion coefficients. Section 3 describes the renormalized least-squares solution from [8] that will be examined in this paper. In Section 4 we introduce the higher-order test probe that will be used in the numerical examples. Section 5 presents numerical results that include the evaluation of the condition number of the normal matrix for various probes and matrix truncations. In addition, we compute spherical expansion coefficients of a simulated AUT using different truncations of the normal matrix to demonstrate that the higher-order method is exact to machine precision. Moreover, we show that the method is very stable in the presence of noise, as would be expected since the normal matrix is extremely well conditioned. Section 6 presents conclusions. Throughout, we assume time-harmonic fields that have $e^{-i\omega t}$ time dependence with $\omega > 0$.

2. Vector-Wave Expansion of the Electric Field of the AUT

In this section we express the AUT far-field pattern in terms of spherical expansion coefficients and transverse spherical vector-wave functions. The standard spherical coordinates (r, θ, ϕ) with unit vectors given by

$$\begin{aligned}\hat{\mathbf{r}} &= \hat{\mathbf{x}} \cos \phi \sin \theta + \hat{\mathbf{y}} \sin \phi \sin \theta + \hat{\mathbf{z}} \cos \theta, \\ \hat{\boldsymbol{\theta}} &= \hat{\mathbf{x}} \cos \theta \cos \phi + \hat{\mathbf{y}} \cos \theta \sin \phi - \hat{\mathbf{z}} \sin \theta, \\ \hat{\boldsymbol{\phi}} &= -\hat{\mathbf{x}} \sin \phi + \hat{\mathbf{y}} \cos \phi\end{aligned}\quad (1)$$

will be used throughout. Here, the unit vectors for the rectangular coordinates (x, y, z) are $\hat{\mathbf{x}}$, $\hat{\mathbf{y}}$, and $\hat{\mathbf{z}}$. The AUT is shown in Figure 1 inside the scan sphere with radius R . Moreover, the AUT minimum-sphere radius R_{\min} is defined such that the maximum (supremum) value of the coordinate r for all points on the AUT equals R_{\min} .

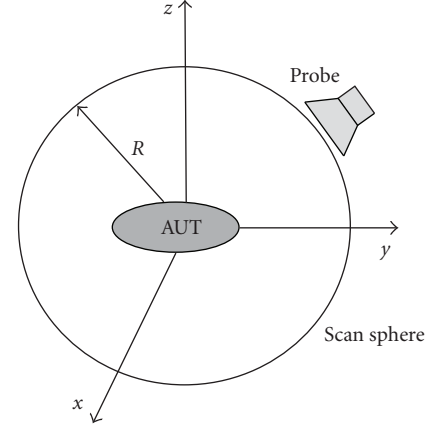


FIGURE 1: A probe with its reference point on the scan sphere of radius R and its normal pointing towards the origin measures the field of the AUT.

The electric and magnetic AUT far fields can be expressed in terms of the far-field pattern $\mathcal{F}(\theta, \phi)$ as [9, page 110]

$$\begin{aligned}\mathbf{E}(\mathbf{r}) &\sim \mathcal{F}(\theta, \phi) \frac{e^{ikr}}{r}, \\ \mathbf{H}(\mathbf{r}) &\sim \sqrt{\frac{\epsilon_0}{\mu_0}} \hat{\mathbf{r}} \times \mathcal{F}(\theta, \phi) \frac{e^{ikr}}{r},\end{aligned}\quad (2)$$

where μ_0 and ϵ_0 are the free-space permeability and permittivity, respectively. Also, $k = \omega \sqrt{\mu_0 \epsilon_0}$ is the wavenumber. The far-field pattern determined from the electric field as

$$\mathcal{F}(\theta, \phi) = \lim_{r \rightarrow \infty} r e^{-ikr} \mathbf{E}(r\hat{\mathbf{r}})\quad (3)$$

can be expressed in terms of the transverse vector-wave functions \mathbf{M}_{nm} and \mathbf{N}_{nm} as

$$\begin{aligned}\mathcal{F}(\theta, \phi) &= \frac{1}{k} \sum_{n=1}^N \sum_{m=-n}^n i^{-n-1} \\ &\times [A_{nm} \mathbf{M}_{nm}(\theta, \phi) + i B_{nm} \mathbf{N}_{nm}(\theta, \phi)],\end{aligned}\quad (4)$$

where A_{nm} and B_{nm} are the spherical expansion coefficients of the AUT, satisfying $A_{nm} = 0$ and $B_{nm} = 0$ when $|m| > n$. The truncation number N is determined from the radius of the minimum sphere as

$$N = kR_{\min} + \gamma(kR_{\min})^{1/3},\quad (5)$$

where the constant γ determines the number of digits of accuracy achieved [10, Section 3.4.2]. The transverse vector-wave functions can be expressed in terms of the spherical harmonic $Y_{nm}(\theta, \phi)$ [11, page 99] as [11, pages 742–746]

$$\mathbf{M}_{nm}(\theta, \phi) = \hat{\boldsymbol{\theta}} \frac{imY_{nm}(\theta, \phi)}{\sqrt{n(n+1)} \sin \theta} - \hat{\boldsymbol{\phi}} \frac{(\partial/\partial \theta)Y_{nm}(\theta, \phi)}{\sqrt{n(n+1)}}\quad (6)$$

and $\mathbf{N}_{nm}(\theta, \phi) = \hat{\mathbf{r}} \times \mathbf{M}_{nm}(\theta, \phi)$. The formula (4) makes it possible to compute the AUT far-field pattern in any direction from the spherical expansion coefficients A_{nm} and B_{nm} . The goal of this paper is to evaluate the method presented in [8] for computing A_{nm} and B_{nm} from the output of a higher-order probe on the scan sphere.

3. Renormalized Least-Squares Formulation for Higher-Order Probes

In this section we briefly outline the method derived in detail in [8]. By applying Fourier series expansions for the d -functions in Jensen's transmission formulas [1–3], one finds that the output of an arbitrary probe on the scan sphere can be expressed as the Fourier series

$$V^{(j)}(\theta, \phi) = \sum_{q=-N}^N \sum_{m=-N}^N \left[\sum_{n=1}^N A_{nm} \mathcal{A}_{mqn}^{(j)} + \sum_{n=1}^N B_{nm} \mathcal{B}_{mqn}^{(j)} \right] \times e^{im\phi} e^{iq\theta} + \epsilon(\theta, \phi), \quad (7)$$

where $\epsilon(\theta, \phi)$ accounts for positioning errors, reflections from chamber walls, inaccuracies in the probe model, and so forth. Here, the index j , which can take the values 1 or 2, represents the two ports of the higher-order probe. Equation (7) holds only when multiple interactions between the probe and AUT are negligible and defines a function that is 2π -periodic with respect to both θ and ϕ .

The probe Fourier coefficient $\mathcal{A}_{mqn}^{(j)}$ is the Fourier coefficient for the output of Port no. j when $A_{n'm'} = \delta_{nn'} \delta_{mm'}$ and $B_{n'm'} = 0$. Similarly, the probe Fourier coefficient $\mathcal{B}_{mqn}^{(j)}$ is the Fourier coefficient for the output of Port no. j when $B_{n'm'} = \delta_{nn'} \delta_{mm'}$ and $A_{n'm'} = 0$. We note that $\mathcal{A}_{mqn}^{(j)} = 0$ and $\mathcal{B}_{mqn}^{(j)} = 0$ when either $|q| > n$ or $|m| > n$. Here, $\delta_{mm'} = 1$ if $m = m'$ and zero otherwise.

It was shown in [8] how the probe Fourier coefficients $\mathcal{A}_{mqn}^{(j)}$ and $\mathcal{B}_{mqn}^{(j)}$ can be computed from the far-field pattern of an arbitrary probe. In the present paper we employ a higher-order probe made from Hertzian dipoles (see Section 4), so the probe output is determined directly from the field on the scan sphere. Hence, we do not need to go through the full formulation developed in [8]. To compute $\mathcal{A}_{mqn}^{(j)}$ and $\mathcal{B}_{mqn}^{(j)}$, we let $V_{A_{nm}}^{(j)}(\theta, \phi)$ denote the higher-order probe output due to a source with $A_{n'm'} = \delta_{nn'} \delta_{mm'}$ and $B_{n'm'} = 0$. Similarly, $V_{B_{nm}}^{(j)}(\theta, \phi)$ is the higher-order probe output due to a source with $A_{n'm'} = 0$ and $B_{n'm'} = \delta_{nn'} \delta_{mm'}$. The Fourier expansion (7) implies that $V_{A_{nm}}^{(j)}(\theta, \phi)$ and $V_{B_{nm}}^{(j)}(\theta, \phi)$ can be computed at $\phi = 0$ through

$$V_{A_{nm}}^{(j)}(\theta, 0) = \sum_{q=-n}^n \mathcal{A}_{mqn}^{(j)} e^{iq\theta}, \quad (8)$$

$$V_{B_{nm}}^{(j)}(\theta, 0) = \sum_{q=-n}^n \mathcal{B}_{mqn}^{(j)} e^{iq\theta}.$$

We extend the θ variable to the entire range $0 \leq \theta \leq 2\pi$ by noting that the spherical unit vector satisfies $\hat{\mathbf{r}}(\theta, \phi) = \hat{\mathbf{r}}(2\pi - \theta, \phi + \pi)$. The standard sampling theorem for bandlimited periodic functions then gives the

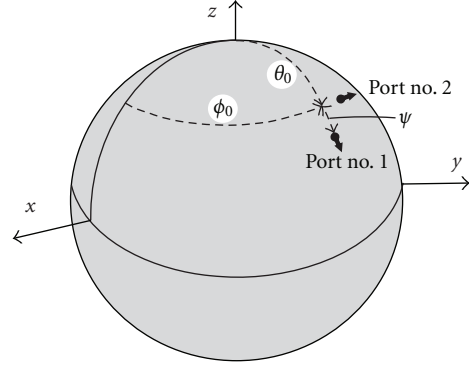


FIGURE 2: The higher-order test probe with its reference point at (θ_0, ϕ_0) on the scan sphere of radius R . The output of Port no. 1 is $V^{(1)}(\theta_0, \phi_0) = E_\theta(R, \theta_0 + \psi, \phi_0)$, and the output of Port no. 2 is $V^{(2)}(\theta_0, \phi_0)$ given by (19).

following exact expressions for the probe Fourier coefficients

$$\mathcal{A}_{mqn}^{(j)} = \frac{1}{2n+2} \sum_{s=0}^{2n+1} V_{A_{nm}}^{(j)}\left(\frac{\pi s}{n+1}, 0\right) e^{-i\pi qs/(n+1)}, \quad (9)$$

$$\mathcal{B}_{mqn}^{(j)} = \frac{1}{2n+2} \sum_{s=0}^{2n+1} V_{B_{nm}}^{(j)}\left(\frac{\pi s}{n+1}, 0\right) e^{-i\pi qs/(n+1)},$$

where $q = -n, \dots, 0, \dots, n$.

Having completed the description of the Fourier formula (7), we next convert it to matrix form. Let the unknown AUT expansion coefficients A_{nm} and B_{nm} be given by the column vector \mathbf{T} with length $O(2N^2)$. Hence, the two-dimensional arrays A_{nm} and B_{nm} are collapsed into one-dimensional arrays and combined in a column vector. Similarly, we let the sampled higher-order probe output $V^{(j)}((t-1)\Delta\theta, (p-1)\Delta\phi)$ be given by the column vector \mathbf{W} of length $O(4N^2)$, where t and p are integers. The sphere is discretized through $\theta_t = (t-1)\Delta\theta$ and $\phi_p = (p-1)\Delta\phi$, where $\Delta\theta$ and $\Delta\phi$ are chosen as usual to be less than or equal to $2\pi/(2N+1)$.

The formula (7) defines the probe matrix $\overline{\mathcal{P}}$, so that the probe output is

$$\mathbf{W} = \overline{\mathcal{P}} \mathbf{T} \quad (10)$$

which is the nonsquare system-matrix equation with more equations than unknowns for determining \mathbf{T} for a given \mathbf{W} . The probe matrix $\overline{\mathcal{P}}$ has the form

$$\overline{\mathcal{P}} = \overline{\mathbf{F}} \overline{\mathbf{Q}}, \quad (11)$$

where matrix multiplications with $\overline{\mathbf{F}}$ can be performed using a 2D FFT algorithm and $\overline{\mathbf{Q}}$ performs the summation over n in the square brackets of (7).

We developed in [8] the renormalized least-squares solution to (10) given by

$$\left(\overline{\mathbf{p}}^{-1}\right)^H \overline{\mathbf{Q}}^H \overline{\mathbf{F}}^H \overline{\boldsymbol{\tau}} \mathbf{W} = \overline{\mathbf{M}} [\overline{\mathbf{p}} \mathbf{T}], \quad (12)$$

where the square matrix $\overline{\mathbf{M}}$ is

$$\overline{\mathbf{M}} = \left(\overline{\mathbf{p}}^{-1}\right)^H \overline{\mathbf{Q}}^H \overline{\mathbf{F}}^H \overline{\boldsymbol{\tau}} \overline{\mathbf{F}} \overline{\mathbf{Q}} \overline{\mathbf{p}}^{-1}. \quad (13)$$

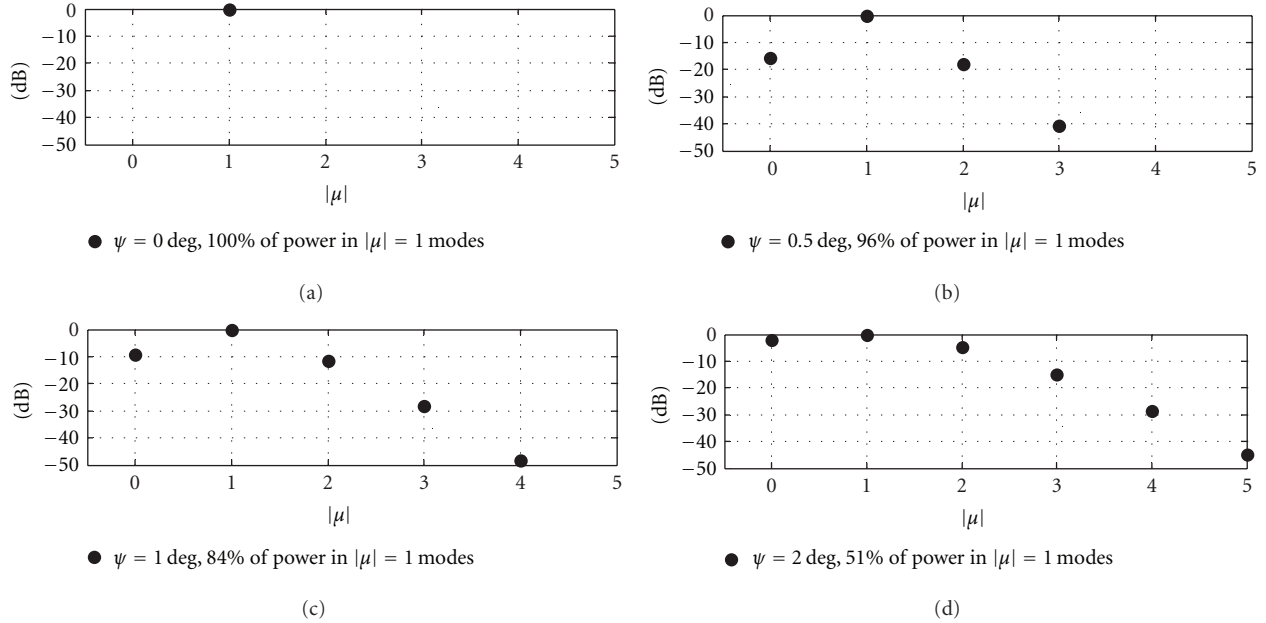


FIGURE 3: The power in the modes of test probes with ψ equal to 0° , 0.5° , 1° , and 2° . The power for each value of $|\mu| = K$ is obtained by summing the power of all modes with $\mu = \pm K$. The plots are normalized so that the power in the $\mu = \pm 1$ modes is 0 dB.

Here $\bar{\tau}$ is a diagonal matrix containing the surface element $\Delta\phi\Delta\theta|\sin[(p-1)\Delta\theta]|$ and \bar{p} is the first-order correction factor, which is a diagonal matrix that represents a first-order correction. The renormalization achieved with \bar{p} results in \bar{M} being almost equal to the identity matrix when most of the probe-pattern energy is in the first-order modes.

In this paper we use the Hertzian-dipole first-order correction factor with elements $\mathcal{U}h_n^{(1)}(kR)$ and $\mathcal{U}g_n^{(1)}(kR)$, where \mathcal{U} is the constant determined from the probe Fourier coefficients as

$$\mathcal{U} = -\sqrt{\frac{8\pi}{3}} \frac{1}{g_1(kR)} \sum_{q=-1}^1 \mathcal{B}_{0q1}^{(1)} e^{iq\pi/2}, \quad (14)$$

where $h_n^{(1)}(z)$ is the spherical Hankel function [11, page 740] and

$$g_n^{(1)}(z) = \frac{1}{z} \frac{\partial}{\partial z} [zh_n^{(1)}(z)]. \quad (15)$$

As discussed in [8], one can compute an optimal first-order correction factor, which may result in more well-conditioned normal matrices than the Hertzian-dipole correction factor used in this paper.

The choice of first-order correction factor \bar{p} does not change the outcome of the computation of the AUT expansion coefficients. It merely affects the matrix \bar{M} and of course the left side of (12). A good correction factor results in \bar{M} being close to the identity matrix. Equation (12) can be solved with respect to $\bar{p}\mathbf{T}$ using a linear iterative solver such as the conjugate gradient method, regardless of how closely \bar{M} resembles the identity matrix. However, when $\bar{M} \approx \bar{I}$, we can obtain a closed-form solution by using the Neumann series. The computation scheme presented here has computational

complexity N^3 [8], and the matrix \bar{M} is never computed explicitly.

4. Higher-Order Test Probe

We shall use an offset Hertzian dipole as the test probe for evaluating the computation scheme. The probe has two ports that each equal the tangential components of the electric field on the scan sphere as shown in Figure 2.

The higher-order test probe is specified by the offset angle ψ . Specifically, when the reference point of the probe is at (θ_0, ϕ_0) , the output of Port no. 1 is the θ component of the electric field at $\mathbf{r}_1(\theta_0, \phi_0) = R\hat{\mathbf{r}}_1 = R\hat{\mathbf{r}}(\theta_0 + \psi, \phi_0)$:

$$V^{(1)}(\theta_0, \phi_0) = \hat{\boldsymbol{\theta}}(\theta_0 + \psi, \phi_0) \cdot \mathbf{E}(\mathbf{r}_1(\theta_0, \phi_0)) = E_\theta(R, \theta_0 + \psi, \phi_0). \quad (16)$$

The output of Port no. 2 is obtained by rotating the Hertzian dipole of Port no. 1 90 degrees with respect to the unit vector $\hat{\mathbf{r}}(\theta_0, \phi_0)$. To determine the location of the dipole for Port no. 2, we introduce two lengths Δ and L so that $(R + \Delta)\hat{\mathbf{r}}_1 = R\hat{\mathbf{r}}_0 + L\hat{\boldsymbol{\theta}}_0$, where $\hat{\mathbf{r}}_0$ and $\hat{\boldsymbol{\theta}}_0$ are the unit vectors corresponding to (θ_0, ϕ_0) . Since $\hat{\mathbf{r}}_1 \cdot \hat{\mathbf{r}}_0 = \cos\psi$, we have $(R + \Delta)\cos\psi = R$ and $(R + \Delta)^2 = R^2 + L^2$, so $L = R\tan\psi$. We can now determine the location \mathbf{r}_2 of the dipole for Port no. 2 by noting that $(R + \Delta)\hat{\mathbf{r}}_2 = R\hat{\mathbf{r}}_0 + L\hat{\boldsymbol{\phi}}_0$ which gives

$$\mathbf{r}_2(\theta_0, \phi_0) = R\hat{\mathbf{r}}_2 = R(\hat{\mathbf{r}}_0 \cos\psi + \hat{\boldsymbol{\phi}}_0 \sin\psi), \quad (17)$$

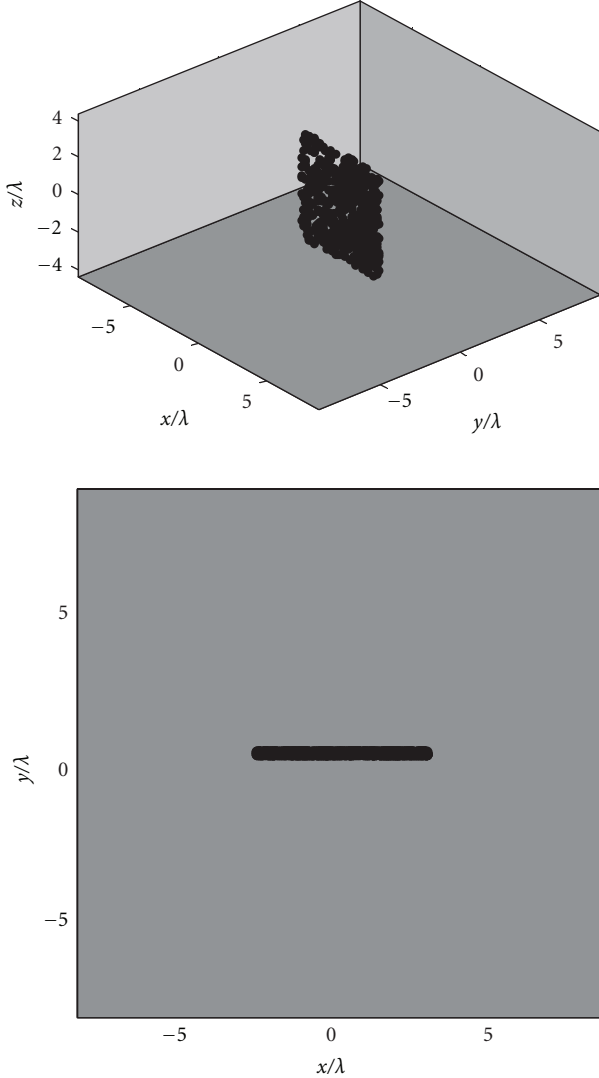


FIGURE 4: The AUT consisting of 500 z -directed Hertzian dipoles randomly distributed in a box with dimensions $-2.8\lambda < x < 2.8\lambda$, $-0.03\lambda < y < 0.03\lambda$, and $-2.8\lambda < z < 2.8\lambda$, so that $R_{\min} = 4\lambda$.

where $\hat{\phi}_0 = \hat{\phi}(\theta_0, \phi_0)$. The direction $\hat{\alpha}_2$ of the dipole for Port no. 2 is tangential to the sphere at \mathbf{r}_2 and lies in the plane containing the origin, $\hat{\mathbf{r}}_2$, and $\hat{\mathbf{r}}_0$:

$$\hat{\alpha}_2(\theta_0, \phi_0) = \frac{1}{\sin \psi} (\hat{\mathbf{r}}_2 \cos \psi - \hat{\mathbf{r}}_0) = \hat{\phi}_0 \cos \psi - \hat{\mathbf{r}}_0 \sin \psi \quad (18)$$

so that the output of Port no. 2 is

$$V_{A_{nm}}^{(2)}(\theta_0, \phi_0) = \hat{\alpha}_2(\theta_0, \phi_0) \cdot \mathbf{E}(\mathbf{r}_2(\theta_0, \phi_0)). \quad (19)$$

When $\psi = 0$, the test probe reduces to a first-order probe with outputs equal to the tangential components of the electric field at (θ_0, ϕ_0) . From [8, equation (1)] it is seen that

$$\begin{aligned} V_{A_{nm}}^{(1)}(\theta, 0) &= \hat{\boldsymbol{\theta}}(\theta + \psi, 0) \cdot \mathbf{M}_{nm}(\theta + \psi, 0) h_n^{(1)}(kR), \\ V_{B_{nm}}^{(1)}(\theta, 0) &= \hat{\boldsymbol{\theta}}(\theta + \psi, 0) \cdot \mathbf{N}_{nm}(\theta + \psi, 0) g_n(kR), \end{aligned}$$

$$\begin{aligned} V_{A_{nm}}^{(2)}(\theta, 0) &= \hat{\alpha}_2(\theta, 0) \cdot \mathbf{M}_{nm}(\hat{\mathbf{r}}_2(\theta, 0)) h_n^{(1)}(kR), \\ V_{B_{nm}}^{(2)}(\theta, 0) &= \hat{\alpha}_2(\theta, 0) \cdot \mathbf{N}_{nm}(\hat{\mathbf{r}}_2(\theta, 0)) g_n(kR) \end{aligned} \quad (20)$$

so that the probe Fourier coefficients $\mathcal{A}_{mqn}^{(j)}$ and $\mathcal{B}_{mqn}^{(j)}$ can be determined from (9).

We shall perform the evaluation of the higher-order computation method using a scan sphere of radius 6λ with a minimum radius of the AUT of $R_{\min} = 4\lambda$ (λ is the wavelength). We employ test probes with ψ equal to 0° , 0.5° , 1° , and 2° . Figure 3 shows the power spectrum of these probes. The value at $|\mu| = K$ is obtained by summing the power of all modes with $\mu = \pm K$. The plots are normalized so that the power in the $\mu = \pm 1$ modes is 0 dB.

Table 1 shows the power content of first-order modes as a function of ψ . The commercially available higher-order probe that was used in the experiential validation in [8] had 97% of its power in the first-order modes. Nevertheless, the remaining 3% of the power residing in the higher-order modes made first-order probe correction completely inadequate. For one of the field components, the AUT far-field pattern error was nearly 10 dB near the main direction; see [8, Figure 5], hence, the need for higher-order methods even when almost all the energy is in the first-order modes.

5. Evaluation of the Normal Matrix

With an $R = 6\lambda$ scan sphere and an AUT minimum radius of $R_{\min} = 4\lambda$, we compute in this section the normal matrix $\bar{\mathbf{M}}$ corresponding to each of the four probes with ψ equal to 0° , 0.5° , 1° , and 2° shown in Figure 3. With $\gamma = 7$, the truncation formula (5) gives $N = 46$, and we sample the sphere with 48 equally spaced samples in θ and 96 equally spaced samples in ϕ . In actual processing of near-field scanning data, one should never compute $\bar{\mathbf{M}}$ explicitly; see the discussion in [8]. Indeed, the computation and storage of $\bar{\mathbf{M}}$ with $N > 75$ is impractical both in terms of computation time and storage requirement on a typical PC. However, we compute $\bar{\mathbf{M}}$ explicitly in this section to evaluate its condition number and to investigate how closely it resembles the identity matrix.

For $N = 46$ the matrix $\bar{\mathbf{M}}$ has size 4416×4416 . We shall also consider “truncated” versions of $\bar{\mathbf{M}}$, where only terms with $n \leq N_{\text{tr}}$ are included. A truncated $\bar{\mathbf{M}}$ corresponds to computing the spherical expansion coefficients A_{nm} and B_{nm} of the AUT only up to $n = N_{\text{tr}} \leq N$ based on data sampled at the original rate. In other words, when working with a truncated $\bar{\mathbf{M}}$, we neglect AUT coefficients with $n > N_{\text{tr}}$ while keeping the sampling rate of the higher-order probe output on the scan sphere unchanged. Table 2 shows the size of the truncated normal matrices that will be considered here.

Table 3 shows the condition numbers for the original $\bar{\mathbf{M}}$ matrix and its truncated versions when $\psi = 0$, $\psi = 0.5^\circ$, $\psi = 1^\circ$, and $\psi = 2^\circ$ probes are employed. Here, the Hertzian-dipole correction factor $\bar{\mathbf{p}}$ is included in the computation of $\bar{\mathbf{M}}$. We see that $\bar{\mathbf{M}}$ is well conditioned in all cases. Moreover, the condition number grows as expected with ψ (the condition number is lowest for the first-order probe). We also see that the condition number decreases with

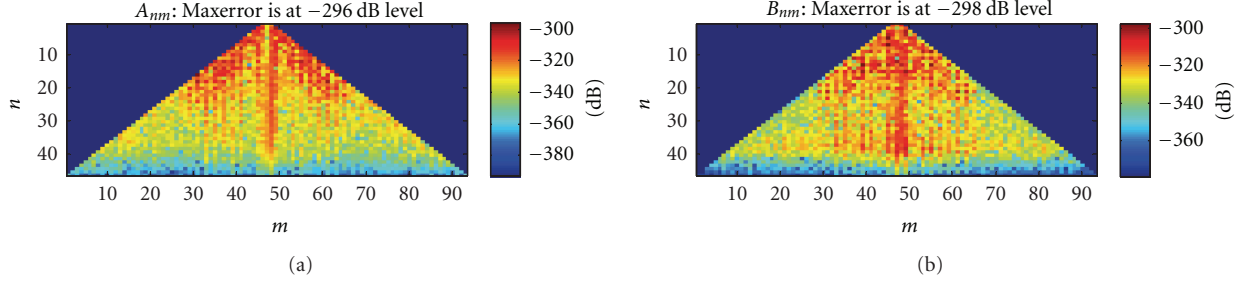


FIGURE 5: Error plots of the spherical expansion coefficients computed from the higher-order probe output with $\psi = 2^\circ$ without truncating the $\bar{\mathbf{M}}$ matrix. (a) is $\mathcal{E}_{A_{nm}}^{(46)}$ and (b) is $\mathcal{E}_{B_{nm}}^{(46)}$.

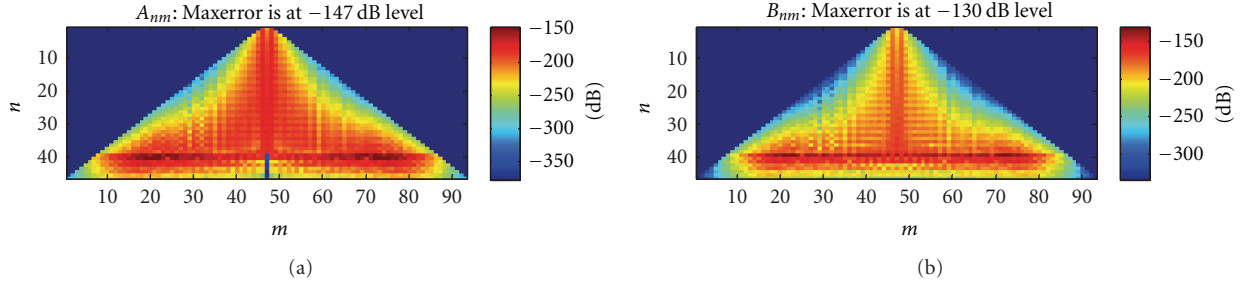


FIGURE 6: Error plots of the spherical expansion coefficients computed from the higher-order probe output with $\psi = 2^\circ$ by truncating the $\bar{\mathbf{M}}$ matrix. (a) is $\mathcal{E}_{A_{nm}}^{(38)}$ and (b) plot is $\mathcal{E}_{B_{nm}}^{(38)}$.

TABLE 1: Probe-mode power spectrum.

	$\psi = 0$	$\psi = 0.5^\circ$	$\psi = 1^\circ$	$\psi = 2^\circ$
Power in modes $ \mu = 1$	100%	96%	84%	51%
Power in modes $ \mu \neq 1$	0%	4%	16%	49%

TABLE 2: Size of truncated $\bar{\mathbf{M}}$ matrices.

N_{tr}	Size ($\bar{\mathbf{M}}$)
46	4416 \times 4416
44	4048 \times 4048
42	3696 \times 3696
40	3360 \times 3360
38	3040 \times 3040

truncation (the matrix truncated at $n = 38$ has a lowest condition number for constant ψ). This also implies that the $\bar{\mathbf{M}}$ matrix of a given size gets more well conditioned as the sampling rate on the scan sphere is increased. The optimal first-order correction factor discussed in [8] may result in even more well-conditioned normal matrices.

Table 4 shows the corresponding condition numbers obtained by setting $\bar{\mathbf{p}} = \bar{\mathbf{I}}$ in the computation of $\bar{\mathbf{M}}$. In other words, no first-order correction factor is applied. In this case the matrix $\bar{\mathbf{M}}$ can be extremely ill conditioned. For example, when $\psi = 2^\circ$ and $N_{tr} = N = 46$ the condition number is $1e5$. Comparing Tables 3 and 4 clearly demonstrates the benefits of using a proper first-order correction factor represented by the diagonal matrix $\bar{\mathbf{p}}$ containing $\mathcal{U}h_n^{(1)}(kR)$ and $\mathcal{U}g_n^{(1)}(kR)$,

TABLE 3: Condition number of $\bar{\mathbf{M}}$ obtained with Hertzian $\bar{\mathbf{p}}$.

N_{tr}	$\psi = 0$	$\psi = 0.5^\circ$	$\psi = 1^\circ$	$\psi = 2^\circ$
46	14.6	26.4	31.3	56.0
44	3.0	4.8	7.4	17.5
42	2.2	3.4	5.3	12.8
40	1.9	2.8	4.3	10.0
38	1.6	2.5	3.7	8.2

TABLE 4: Condition number of $\bar{\mathbf{M}}$ obtained with $\bar{\mathbf{p}} = \bar{\mathbf{I}}$.

N_{tr}	$\psi = 0$	$\psi = 0.5^\circ$	$\psi = 1^\circ$	$\psi = 2^\circ$
46	3e4	6e4	8e4	1e5
44	1e3	2e3	2e3	4e3
42	195	218	255	412
40	46	50	56	85
38	19	20	21	30

where \mathcal{U} is given by (14). Also, since $\bar{\mathbf{p}}$ is a diagonal matrix, its associated computational cost is negligible.

Table 5 shows the largest and smallest diagonal values in $\bar{\mathbf{M}}$ (the diagonal elements are positive) for the different probes and different truncation limits under consideration with $\bar{\mathbf{M}}$ computed using a Hertzian $\bar{\mathbf{p}}$. Also shown are the maximum magnitudes of off-diagonal elements for each matrix. The corresponding values for $\bar{\mathbf{p}} = \bar{\mathbf{I}}$ are shown in Table 6. We see that it is the proper Hertzian correction factor which insures that $\bar{\mathbf{M}}$ is close to the identity matrix. In agreement with the condition numbers in Table 3, the matrix

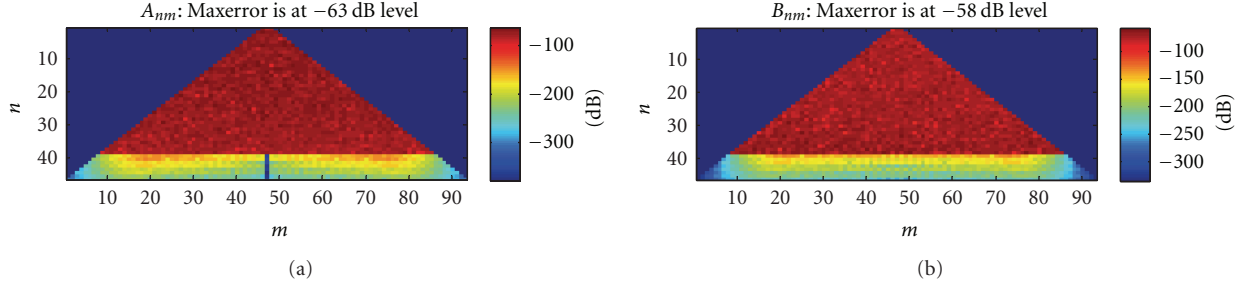


FIGURE 7: Error plots of the spherical expansion coefficients computed from the higher-order probe output with $\psi = 2^\circ$ by truncating the $\bar{\mathbf{M}}$ matrix in the presence of Gaussian probe-output noise at the -60 dB level. (a) is $\mathcal{E}_{A_{nm}}^{(38)}$ and (b) plot is $\mathcal{E}_{B_{nm}}^{(38)}$.

TABLE 5: Properties of $\bar{\mathbf{M}}$ obtained with Hertzian $\bar{\mathbf{p}}$. D is the maximum value occurring in the diagonal (all diagonal elements are positive), d is the minimum value occurring in the diagonal, and O is the maximum magnitude occurring away from the diagonal.

N_{tr}	$\psi = 0$			$\psi = 0.5^\circ$			$\psi = 1^\circ$			$\psi = 2^\circ$		
	D	d	O	D	d	O	D	d	O	D	d	O
46	1.59	0.42	0.18	1.58	0.42	0.18	1.56	0.43	0.17	1.57	0.41	0.17
44	1.10	0.90	0.074	1.09	0.90	0.071	1.07	0.91	0.066	1.09	0.91	0.092
42	1.05	0.94	0.046	1.04	0.95	0.045	1.03	0.95	0.045	1.04	0.96	0.091
40	1.03	0.96	0.034	1.02	0.96	0.03	1.01	0.97	0.045	1.03	0.97	0.090
38	1.02	0.97	0.027	1.02	0.97	0.026	1.01	0.97	0.044	1.02	0.97	0.089

TABLE 6: Properties of $\bar{\mathbf{M}}$ obtained with $\bar{\mathbf{p}} = \bar{\mathbf{I}}$. D is the maximum value occurring in the diagonal (all diagonal elements are positive), d is the minimum value occurring in the diagonal, and O is the maximum magnitude occurring away from the diagonal.

N_{tr}	$\psi = 0$			$\psi = 0.5^\circ$			$\psi = 1^\circ$			$\psi = 2^\circ$		
	D	d	O	D	d	O	D	d	O	D	d	O
46	4.3	$2e-4$	0.15	4.3	$2e-4$	0.15	4.2	$2e-4$	0.14	4.0	$2e-4$	0.11
44	0.28	$2e-4$	$7e-3$	0.28	$2e-4$	$7e-3$	0.28	$2e-4$	$6e-3$	0.27	$2e-4$	$6e-3$
42	$4e-2$	$2e-4$	$8e-4$	$4e-2$	$2e-4$	$8e-4$	$4e-2$	$2e-4$	$7e-4$	$4e-2$	$2e-4$	$7e-4$
40	$9e-3$	$2e-4$	$2e-4$	$9e-3$	$2e-4$	$2e-4$	$9e-3$	$2e-4$	$2e-4$	$9e-3$	$2e-4$	$2e-4$
38	$4e-3$	$2e-4$	$8e-5$	$4e-3$	$2e-4$	$8e-5$	$4e-3$	$2e-4$	$7e-5$	$4e-3$	$2e-4$	$1e-4$

$\bar{\mathbf{M}}$ is closest to the identity matrix for the first-order probe. Also, truncating $\bar{\mathbf{M}}$ moves it closer to $\bar{\mathbf{I}}$.

We finally consider a particular AUT consisting of 500 z -directed Hertzian dipoles randomly distributed in a box with dimensions $-2.8\lambda < x < 2.8\lambda$, $-0.03\lambda < y < 0.03\lambda$, and $-2.8\lambda < z < 2.8\lambda$, as shown in Figure 4. ($\bar{\mathbf{M}}$ is of course independent of the AUT; $\bar{\mathbf{M}}$ depends only on the probe, the sampling rate on the scan sphere, and on the highest value of n for which the AUT spherical expansion coefficients are computed.) We computed the exact spherical expansion coefficients A_{nm}^{exact} and B_{nm}^{exact} of this AUT from its tangential electric field on the scan sphere using a standard first-order method.

We also computed these AUT expansion coefficients from the output of the $\psi = 2^\circ$ higher-order probe using the method described in this paper with $N_{\text{tr}} = 46$ and $N_{\text{tr}} = 38$.

These expansion coefficients are denoted $A_{nm}^{(N_{\text{tr}})}$ and $B_{nm}^{(N_{\text{tr}})}$. Relative dB errors are computed as

$$\begin{aligned} \mathcal{E}_{A_{nm}}^{(N_{\text{tr}})} &= 20 \log_{10} \left(\frac{|A_{nm}^{\text{exact}} - A_{nm}^{(N_{\text{tr}})}|}{\max(|A_{nm}^{\text{exact}}|)} \right), \\ \mathcal{E}_{B_{nm}}^{(N_{\text{tr}})} &= 20 \log_{10} \left(\frac{|B_{nm}^{\text{exact}} - B_{nm}^{(N_{\text{tr}})}|}{\max(|B_{nm}^{\text{exact}}|)} \right). \end{aligned} \quad (21)$$

Figure 5 shows the relative dB errors of the AUT spherical expansion coefficients computed without truncating $\bar{\mathbf{M}}$. The error level is at -300 dB corresponding to machine precision ($1e-15$). Hence, we have numerically validated the higher-order probe-correction scheme. Figure 6 shows the relative dB errors computed with $N_{\text{tr}} = 38$. Here we are neglecting all spherical expansion coefficients with $n > 38$. We see that

the error now is at the -130 dB level, which is still very good by anechoic chamber standards (the error level in a good anechoic chamber is -60 dB).

We next illustrate the benefit of dealing with well-conditioned matrices when the near-field data is noisy. Assume that the truncated $\bar{\mathbf{M}}$ matrix ($N_{\text{tr}} = 38$) is employed in the presence of Gaussian probe-output noise at the -60 dB level. In other words, the exact probe output \mathbf{W} is contaminated by noise as follows:

$$\mathbf{W}^{(\text{noisy})} = \mathbf{W} + A10^{-60/20}[\mathbf{G}_1 + i\mathbf{G}_2]/\sqrt{2}, \quad (22)$$

where \mathbf{G}_1 and \mathbf{G}_2 are independent Gaussian random vectors with mean and standard deviation equal to zero and one, respectively. The amplitude factor A is the square root of the standard deviation of the exact probe-output power. The noisy data $\mathbf{W}^{(\text{noisy})}$ is inserted into (12) truncated at $N_{\text{tr}} = 38$ to get the corresponding set of noisy AUT expansion coefficients. Figure 7 shows that the error level of these AUT expansion coefficients is at -58 dB. Hence, as a consequence of the well-conditioned $\bar{\mathbf{M}}$ matrix, the error of the computed AUT expansion coefficients is roughly at the same level as the noise present in the probe-output data.

6. Conclusions

We evaluated the system-matrix method for higher-order probe correction in spherical scanning using probes with varying higher-order mode pattern energy. The first-order correction factor employed by the method greatly reduces the condition number of the resulting normal matrix, even when half of the probe-pattern energy resides in higher-order modes. Indeed, for the probe with half its energy in the higher-order modes, the first-order correction factor reduced the condition number of a 4416×4416 normal matrix from $1e5$ to 56 .

We also found that even better condition numbers are achieved by truncating the normal matrix; this is equivalent to increasing the sampling rate on the scan sphere for fixed AUT mode truncation number. Increasing the sampling rate by 10% can significantly reduce the condition number and move the normal matrix closer to the identity matrix. This is important for making the Neumann series solution efficient.

For probes (like the one used in the experimental validation in [8]) with a few percent of the pattern energy in higher-order modes, the first-order correction factor resulted in a 3696×3696 normal matrix with a condition number of 3.4. The diagonal elements of this normal matrix were in the range from 0.95 to 1.04, and the maximum magnitude of the off-diagonal elements was 0.045. Without the first-order correction factor, the diagonal elements of this normal matrix were in the range from $2e - 2$ to $4e - 2$, and the maximum magnitude of the off-diagonal elements was $8e - 4$. Due to the well-conditioned normal matrices, the method is well behaved in the presence of noise.

Acknowledgment

The Air Force Office of Scientific Research supported this work.

References

- [1] F. Jensen, *Electromagnetic near-field far-field correlations*, Ph.D. dissertation, Technical University of Denmark, Lyngby, Denmark, 1970.
- [2] P. F. Wacker, "Non-planar near-field measurements: spherical scanning," NBS Internal Report, 1975.
- [3] J. E. Hansen, J. Hald, F. Jensen, and F. H. Larsen, *Spherical Near-Field Antenna Measurements*, Peter Peregrinus, London, UK, 1988.
- [4] A. D. Yaghjian and R. C. Wittmann, "The receiving antenna as a linear differential operator: application to spherical near-field measurements," *IEEE Transactions on Antennas and Propagation*, vol. 33, pp. 1175–1185, 1985.
- [5] T. B. Hansen, "Complex-point dipole formulation of probe-corrected cylindrical and spherical near-field scanning of electromagnetic fields," *IEEE Transactions on Antennas and Propagation*, vol. 57, no. 3, pp. 728–741, 2009.
- [6] C. H. Schmidt and T. F. Eibert, "Multilevel plane wave based near-field far-field transformation for electrically large antennas in free-space or above material halfspace," *IEEE Transactions on Antennas and Propagation*, vol. 57, no. 5, pp. 1382–1390, 2009.
- [7] T. Laitinen, S. Pivnenko, J. M. Nielsen, and O. Breinbjerg, "Theory and practice of the FFT/matrix inversion technique for probe-corrected spherical near-field antenna measurements with high-order probes," *IEEE Transactions on Antennas and Propagation*, vol. 58, no. 8, pp. 2623–2631, 2010.
- [8] T. B. Hansen, "Spherical near-field scanning with higher-order probes," *IEEE Transactions on Antennas and Propagation*, vol. 59, no. 11, pp. 4049–4059, 2011.
- [9] T. B. Hansen and A. D. Yaghjian, *Plane-Wave Theory of Time-Domain Fields*, IEEE Press, New York, NY, USA, 1999.
- [10] W. C. Chew, J. M. Jin, E. Michielssen, and J. Song, *Fast and Efficient Algorithms in Computational Electromagnetics*, Artech House, Boston, Mass, USA, 2006.
- [11] J. D. Jackson, *Classical Electrodynamics*, John Wiley and Sons, New York, NY, USA, 2nd edition, 1975.

Research Article

Reduction of Truncation Errors in Planar, Cylindrical, and Partial Spherical Near-Field Antenna Measurements

Francisco José Cano-Fácila,¹ Sergey Pivnenko,² and Manuel Sierra-Castañer¹

¹ Radiation Group, Signals, Systems and Radiocommunications Department, Technical University of Madrid, Avenue Complutense 30, 28040 Madrid, Spain

² Department of Electrical Engineering, Technical University of Denmark, 2800 Kongens, Lyngby, Denmark

Correspondence should be addressed to Francisco José Cano-Fácila, francisco@gr.ssr.upm.es

Received 12 July 2011; Accepted 8 September 2011

Academic Editor: Claudio Gennarelli

Copyright © 2012 Francisco José Cano-Fácila et al. This is an open access article distributed under the Creative Commons Attribution License, which permits unrestricted use, distribution, and reproduction in any medium, provided the original work is properly cited.

A method to reduce truncation errors in near-field antenna measurements is presented. The method is based on the Gerchberg-Papoulis iterative algorithm used to extrapolate band-limited functions and it is able to extend the valid region of the calculated far-field pattern up to the whole forward hemisphere. The extension of the valid region is achieved by the iterative application of a transformation between two different domains. After each transformation, a filtering process that is based on known information at each domain is applied. The first domain is the spectral domain in which the plane wave spectrum (PWS) is reliable only within a known region. The second domain is the field distribution over the antenna under test (AUT) plane in which the desired field is assumed to be concentrated on the antenna aperture. The method can be applied to any scanning geometry, but in this paper, only the planar, cylindrical, and partial spherical near-field measurements are considered. Several simulation and measurement examples are presented to verify the effectiveness of the method.

1. Introduction

In many cases, antenna parameters, such as gain, directivity, radiation pattern, side-lobe level, and beamwidth, cannot be determined directly from measurements that are obtained in a far-field range because the distance to the far-field region may be too large. However, it is well known that those parameters can be obtained using analytical transformations from near-field measurements [1–4]. Moreover, these types of measurement can be performed in indoor ranges, reducing unwanted contributions from the environment, such as reflections or diffractions, as much as possible.

One important requirement to determine exact far-field patterns from near-field acquisitions is the ability to measure the electric or magnetic field that is tangential to an arbitrary surface that encloses the antenna under test (AUT). If that condition is satisfied, the field can be obtained anywhere outside the measurement surface and specifically in the far-field region by solving an integral over the surface on which

the fields are known [1]. However, the solution of this integral is impractical to determine unless the scan surface supports orthogonal vector wave functions. There are only six coordinate systems that support vector wave functions that satisfy the orthogonality condition, but only three of them (planar, cylindrical, and spherical) are employed because of the simplicity of the required mechanical equipment. These three coordinate systems constitute the classical near-field antenna measurement systems and, although the three near-field techniques are based on the same principle (measurement over a surface in the near-field and transformation to far-field), there are important differences among them. The planar and cylindrical scanning geometries are mechanically simpler than in the case of the spherical near-field (SNF). Moreover, the spherical near-field to far-field transformation is more complex, requiring more calculations to obtain the far-field pattern from the acquired data. However, the most accurate antenna patterns are obtained using this last type of acquisition because it is the only measurement setup where

the AUT is fully enclosed by the acquisition surface. Therefore, there are no truncation errors in the calculated far-field pattern. In the planar near-field (PNF) and cylindrical near-field (CNF) measurements, because of the finite size of the scan surface, the closed surface condition is never fulfilled, and, consequently, the true far-field pattern is never known in the whole sphere, that is, the pattern is only valid within the called reliable region. A second effect, which is caused by the discontinuity of the measured field at the edge of the scan surface, is the presence of a ripple within this region.

Because the truncation error is an unavoidable error in PNF and CNF measurements, and it is not present in SNF measurements, most of the approaches to reduce this kind of error have been specifically proposed for the two first configurations. These approaches can be divided into two groups. The first group attempts to reduce the second effect that was mentioned previously, that is, the ripple within the reliable region by the application of proper window functions to the near-field data. In [5, 6], a directive synthetic array of probes is created by combining near-field data points to reduce the level at the edges of the measurement plane. This approach provides noticeable ripple reduction, especially for the measurement of low-directive antennas. Another ripple reduction approach is proposed in [7, 8] in which raised cosine amplitude and quadratic phase windows are shown to provide high accuracy. Although windowing techniques can greatly reduce erroneous ripples, an extra scan area is needed to obtain the same reliable region. If the scan area is not extended with the use of one of these techniques, the extent of the reliable region is reduced.

The approaches of the second group do not attempt to reduce the ripple within the region in which the far-field pattern is reliable, but they attempt to obtain a good estimation of the true pattern outside of that region. One of these approaches, called the equivalent magnetic current approach [9], presents a method of computing far-fields in the whole forward hemisphere from planar near-field measurements. The idea is to compute the equivalent magnetic currents in the AUT plane by solving the system of integral equations that relate these currents and the measured field. Once these currents are known, it is possible to produce the correct far-fields in front of the AUT. The main drawback of this approach is the great computational complexity that is required to solve the system of integral equations. However, that complexity may be drastically reduced by using a magnetic dipole array approximation instead of the equivalent magnetic current approach, eliminating the numerical integration in the process. Another strategy to reduce truncation errors is to rotate the AUT about one or more axes [10], measuring in different planes and combining them to increase the maximum validity angle. Logically, this technique requires a particular near-field to far-field transformation for each combination of plane acquisitions. In [11], the problem of truncation is addressed using *a priori* information about the AUT. The main idea of this approach is to estimate the near-field data outside of the scanning area by extrapolating the measured data before calculating the far-field pattern. The *a priori* information is employed to obtain a nonredundant and nonuniform representation [12] of the samples that are

taken over the measurement surface. Thanks to this distribution of the samples, a large amount of samples outside of the scan plane can be recovered with good accuracy. This strategy was experimentally validated in [13], obtaining good far-field results for the case of cylindrical scanning. The same idea of nonredundant and nonuniform representation of electromagnetic fields was also used in [14] for extrapolating the data outside of a plane-polar scanning. In this last work, however, optimal sampling interpolation expansions instead of the cardinal series expansions employed in [11, 12] are applied. In [14], it is numerically demonstrated that these new expansions guarantee a better reconstruction of the samples outside the measurement surface for a given number of measurement points. However, these extrapolation methods are not able to remove the truncation error in all the far-field pattern. A new method that is based on the same principle, that is, the use of a nonredundant sampling in the acquisition, was proposed in [15]. In this method, the truncation error is practically eliminated by also addressing points in surfaces external to the actual scanning area. Therefore, this method can be applied whenever the set-up allows the variation of the distance between the AUT and the probe. Another alternative to increase the reliable region by extrapolating the planar near-field data is described in [16]. The extrapolation is achieved by first back-propagating the measured field to the AUT plane. After that, only the samples within the AUT aperture are retained, and they are used to restore the external samples in terms of a diffraction integral along the aperture rim. Finally, the field is transformed back to the measurement plane to obtain new field samples outside of the measurement region. The main drawback of this last approach is, as in [11, 12, 14], the impossibility of recovering samples over an infinite surface with good accuracy, and, therefore, the truncation error is not completely removed for large elevation angles. A recent publication [17] also uses *a priori* information about the AUT in an iterative algorithm to extrapolate the reliable portion of the calculated far-field pattern. This method was proposed for the planar near-field case, and the theoretical basis of the iterative algorithm was presented in [18, 19] by Gerchberg and Papoulis, respectively.

As commented before, truncation errors are always present in PNF and CNF measurements but not in SNF measurements. However, there are special cases, for example, when measuring electrically large antennas, in which the measurement time may be prohibitively long and an acquisition over the whole sphere is not practical. A solution to reduce the data acquisition time is to measure over a partial sphere. Nevertheless, the new acquisition surface does not fully enclose the AUT, and, as in the PNF and CNF cases, a truncation error appears in the far-field pattern. Although this is a typical error in PNF and CNF measurements, there are also some studies that have dealt with this problem in partial SNF measurements. In [20], the truncated spherical near-field data are used to calculate an equivalent currents distribution of a set of dipoles that reproduce the radiation of the AUT. As in [9], once that distribution is known, the far-field pattern is easily computed in the entire sphere. When measuring over a partial sphere, the error that appears in the computed far-field arises from the nonorthogonality of

the classical spherical modal functions in the uncompleted surface. Therefore, the calculated modal coefficients are incorrect. This problem can be solved by employing a new basis function set that is orthogonal over the truncated angular domain. It is subsequently necessary to derive a near-field to far-field transformation for the resulting coefficients. This solution was presented for two-dimensional cylindrical/spherical near-field scanning in [21] and for three-dimensional acoustic spherical near-field scanning in [22]. The alternative expansion considered in these works is based on Slepian functions [23]. In some cases, it is not the measurement time that is the limitation of SNF measurements, but the impossibility to get reliable data over the whole sphere, for example, due to support-structure blockage when measuring electrically small antennas. In [24], a method that is based on a least-squares technique is employed to calculate the spherical wave coefficients using forward hemisphere data only. This method can significantly reduce truncation errors, but it is not efficient for large antennas. This problem is also addressed in [25] where the band-limited property of the spherical wave coefficients is exploited in an iterative algorithm that substitutes the unreliable portion of the measurement sphere with new samples at each iteration.

In the present work, a method to reduce truncation errors when measuring the field overtruncated surfaces is developed. The method is based on the iterative algorithm that was proposed in [18, 19], and it has already been applied to the PNF case in [17]. However, this method can be applied to any scanning geometry by taking certain considerations into account. Therefore, this work can be viewed as a generalization of the method presented in [17]. Moreover, compared to some aforementioned approaches, it is not necessary to take samples in surfaces external to the actual scanning area. Therefore the reduction of truncation errors is achieved without increasing the measurement time. In addition, the computational cost is not large because the method is based on the iterative application of Fourier transforms between the plane wave spectrum (PWS) and the extreme near-field, and those transforms can be made quite rapid by using fast Fourier transform techniques, not as in [9] where the equivalent magnetic currents are obtained by solving a complex system of integral equations.

A bottleneck of the method presented in [17] may be the time required to find the optimum termination point in the iterative procedure. In this work, a faster procedure based on the Gradient Descent algorithm, with which is possible to obtain the iteration number where the error is minimum, is proposed.

The method provides an exact reconstruction when starting from error free data. In practice, the measured data are always affected by errors, and therefore, the method does not converge to the exact solution. However, the method is very insensitive to errors and is able to provide a very good radiation pattern reconstruction using initial data corrupted by noise or other measurement errors.

The main limitation of the method is that the truncation error can only be removed in the forward hemisphere. Moreover, it is within the methods that require *a priori* information about the AUT, like all the methods based on a non-

redundant and nonuniform representation of the samples [11–15]. In our case, it is necessary to know exactly the AUT dimensions. Due to this fact, the best results are obtained when the AUT is an aperture antenna because its dimensions are well defined.

Although our method is a generic approach that can be applied to any scanning geometry, only the most common truncated cases (plane, cylinder, and partial sphere) are considered here.

The paper is organized as follows. Section 2 gives an overview of the concept of the spectral reliable region. The method to reduce truncation errors is described in Section 3 where its convergence is also studied. Section 4 presents a simulated model that is used in Section 5 to analyze the critical aspects of the method. The effectiveness of the method is validated in Section 6 using both the simulated data from Section 4 and measured near-field data. Conclusions are drawn in Section 7.

2. Spectral Reliable Region

The classical way for obtaining the far-field pattern from near-field measurements is to employ the modal expansion method, which is based on the fact that the field over an appropriate surface can be expressed as a linear combination of a set of orthogonal functions. In this method, after the measurement of the tangential components of the electric or magnetic field over a truncated surface, the modal coefficients are obtained by making use of the orthogonalities of the modal functions. However, these functions are orthogonal over the original surface but not over the truncated surface, so these coefficients are calculated erroneously. This error is translated into two different effects in the calculated far-field pattern. On one hand, the results are completely unreliable outside of a certain spectral region. On the other hand, erroneous ripples appear within that region due to the discontinuity of the measured field at the edge of the truncated surface. Therefore, the entire calculated pattern is always affected by errors, and it is not possible to define a region where the error is completely zero. However, the concept of the spectral reliable region is usually applied to refer to the region in which the error is not negligible but is low. A classical definition of this region is given in [3, 26], where geometrical optics is employed to calculate the maximum validity angles that are used to define the reliable region. According to this definition, one particular direction will be within the reliable region when the scan surface includes all of the rays that are parallel to the direction coming from any part of the AUT as shown in Figure 1(a). The opposite situation is depicted in Figure 1(b) in which there are rays that do not lie on the scan surface.

The reliable region defined in this way depends on the AUT size, the distance from the scan surface to the AUT and the shape and size of the acquisition surface. Therefore, even with the use of the same AUT and the same measurement distance, the reliable region will be different for each type of measurement setup and require an independent analysis for each of them. As mentioned before, not only the classical

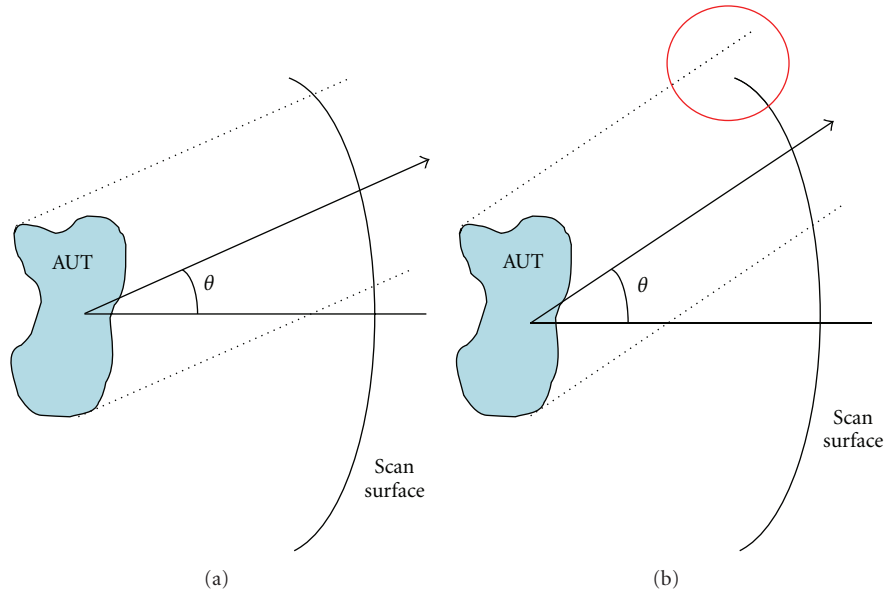


FIGURE 1: Geometrical optics employed to define the spectral reliable region: (a) direction included in the reliable region; (b) direction not included in the reliable region.

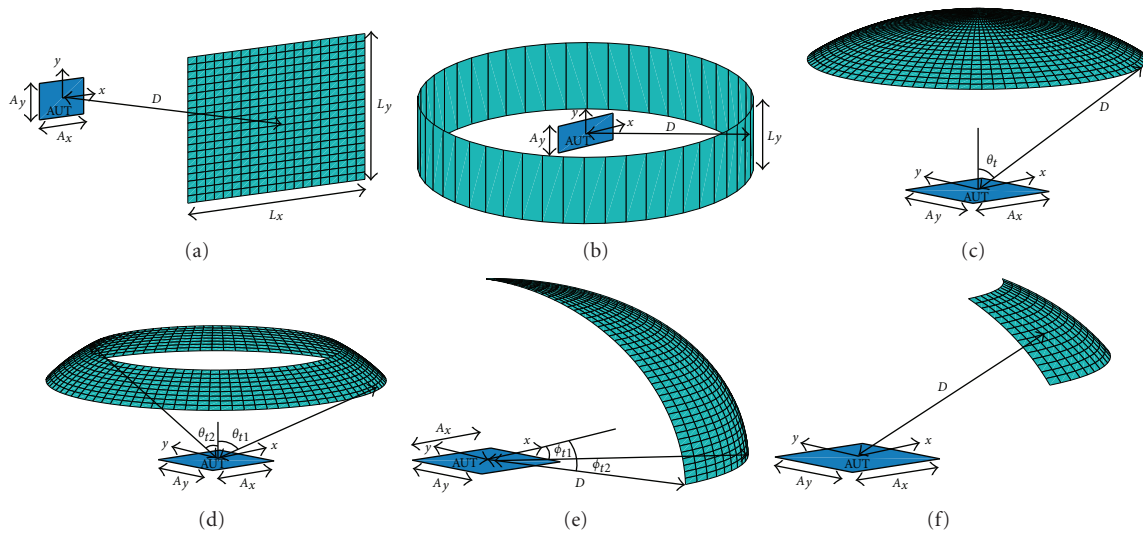


FIGURE 2: Truncation in near-field measurement setups: (a) Planar truncation; (b) Cylindrical truncation; (c) Polar truncation; (d) Spherical ring truncation; (e) Azimuthal truncation; (f) Sectorial truncation.

cases of truncation, that is, the PNF and CNF cases, but also the partial SNF measurements are analyzed here. Logically, because it is possible to sample over different parts of the sphere, there are different types of reliable region, not as in the two first cases, where the shape of the reliable region is always the same. The choice of the sampling region will depend on the expected radiation pattern because if most of the radiated energy is concentrated in that region, the proposed method will provide a better reconstruction. In particular, besides the planar and cylindrical truncation, four different truncations in SNF measurements are studied in this work. The six truncation surfaces for different measurement setups are depicted in Figure 2, and their cor-

responding reliable regions are shown in Figure 3. These reliable regions were determined using geometrical optics, and their mathematical formulations are indicated in Table 1.

3. Extrapolation Method

As shown in the previous section, when measuring over a truncated surface, the calculated far-field pattern can only be considered reliable within a limited known region. Therefore, the truncation problem can be viewed as an extrapolation problem. Various methods have been presented to achieve satisfactory estimates when extrapolating a known portion of a signal. Most of these methods are general

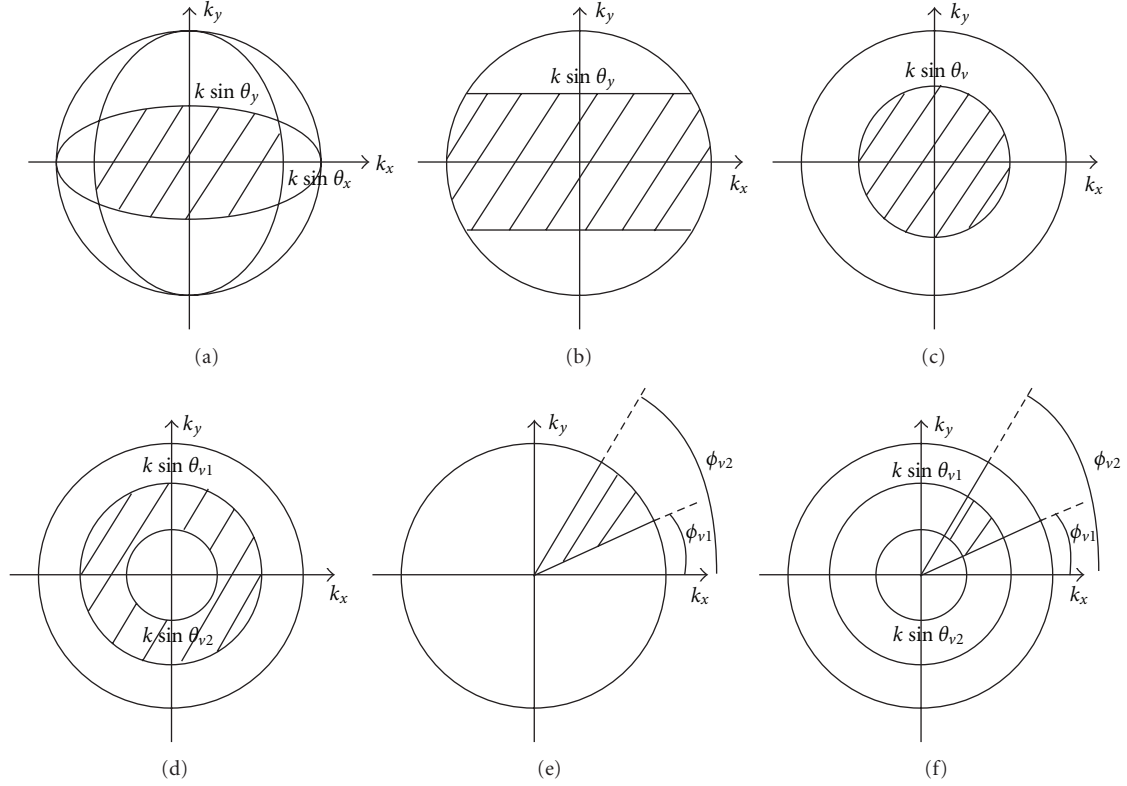


FIGURE 3: Spectral reliable regions: (a) PNF measurement; (b) CNF measurement; (c) SNF measurement with polar truncation; (d) SNF measurement with spherical ring truncation; (e) SNF measurement with azimuthal truncation; (f) SNF measurement with sectorial truncation.

TABLE 1: Determination of the spectral reliable regions based on geometrical optics for each type of measurement setup.

Measurement set-up	Maximum validity angles	Spectral reliable region
PNF measurement	$\theta_x = \arctan((L_x - A_x)/2D)$; $\theta_y = \arctan((L_y - A_y)/2D)$	$\{k_x^2/(k \sin \theta_x)^2 + k_y^2/k^2 < 1\} \cap \{k_x^2/k^2 + k_y^2/(k \sin \theta_y)^2 < 1\}$
CNF measurement	$\theta_y = \arctan((L_y - A_y)/2D)$	$\{ k_y < k \sin \theta_y\}$
SNF measurement with polar truncation	$\theta_v = \theta_t - \arcsin(r_0/D)^*$	$\{k_x^2 + k_y^2 < (k \sin \theta_v)^2\}$
SNF measurement with spherical ring truncation	$\theta_{v1} = \theta_{t1} - \arcsin(r_0/D)$; $\theta_{v2} = \theta_{t2} + \arcsin(r_0/D)^*$	$\{k_x^2 + k_y^2 < (k \sin \theta_{v1})^2\} \cap \{k_x^2 + k_y^2 > (k \sin \theta_{v2})^2\}$
SNF measurement with azimuthal truncation	$\phi_{v1} = \phi_{t1} + \arcsin(r_0/D)$; $\phi_{v2} = \phi_{t2} - \arcsin(r_0/D)^*$	$\{k_y > k_x \cdot \tan \phi_{v1}\} \cap \{k_y < k_x \cdot \tan \phi_{v2}\}$
SNF measurement with sectorial truncation	$\theta_{v1} = \theta_{t1} - \arcsin(r_0/D)$; $\theta_{v2} = \theta_{t2} + \arcsin(r_0/D)^*$ $\phi_{v1} = \phi_{t1} + \arcsin(r_0/D)$; $\phi_{v2} = \phi_{t2} - \arcsin(r_0/D)^*$	$\{k_x^2 + k_y^2 < (k \sin \theta_{v1})^2\} \cap \{k_x^2 + k_y^2 > (k \sin \theta_{v2})^2\}$ $\cap \{k_y > k_x \cdot \tan \phi_{v1}\} \cap \{k_y < k_x \cdot \tan \phi_{v2}\}$

* $r_0 = (1/2)\sqrt{A_x^2 + A_y^2}$.

approaches for the extrapolation of the finite-time segment of a signal, and they are based on deconvolution or predictive filtering. However, there are special solutions that provide better results when the signal satisfies certain properties. This is the case in the alternating orthogonal projection method [17, 18], which consists of the sequential application of two signal operators in two different domains to obtain an approximation sequence with convergence to the desired extrapolation that is guaranteed in theory. This method

is optimally designed for the extrapolation of the time-truncated version of a band-limited signal, that is, its Fourier transform is identically zero outside of some frequency set. Therefore, this last type of method can be employed in our truncation problem because it is necessary to extrapolate a truncated portion of the PWS with a Fourier transform (field distribution on the AUT plane) that is spatially band-limited because the field distribution is theoretically concentrated on the antenna aperture.

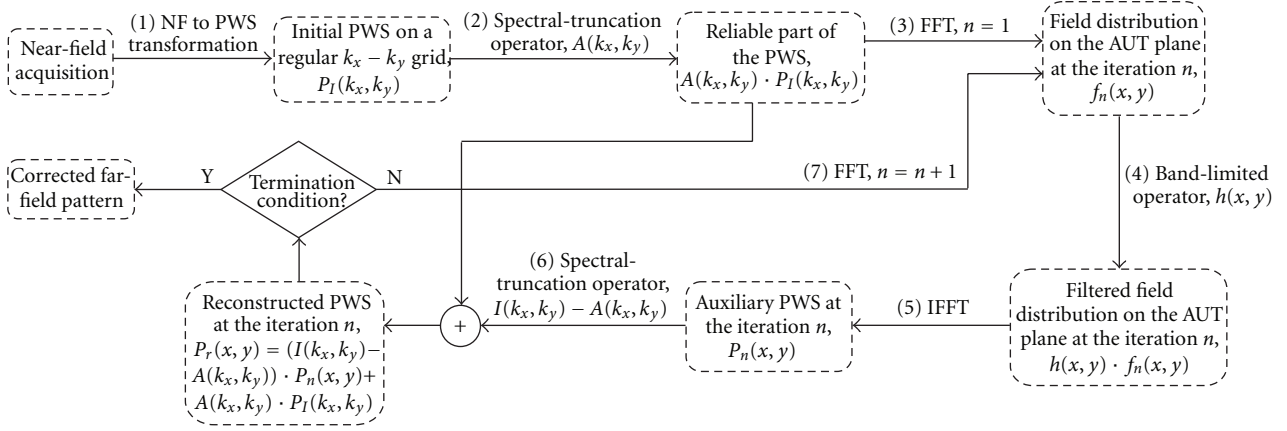


FIGURE 4: Schematic diagram of the method to reduce truncation errors. $*I(k_x, k_y)$ denotes the identity operator in the spectral domain.

Before describing all of the steps of the method, we present the two orthogonal projection operators that play an important role in the method. The first operator is applied in the spectral domain and defines the reliable portion of the PWS. This first operator is given by

$$A(k_x, k_y) = \begin{cases} 1, & \forall (k_x, k_y) \in \Omega_R, \\ 0, & \forall (k_x, k_y) \notin \Omega_R, \end{cases} \quad (1)$$

where A is the spectral-truncation operator and Ω_R is one of the reliable regions that is defined in Table 1. The second operator is called band-limited operator and is applied to the field distribution on the AUT plane:

$$h(x, y) = \begin{cases} 1, & \forall (x, y) \in \omega_{\text{AUT}}, \\ 0, & \forall (x, y) \notin \omega_{\text{AUT}}, \end{cases} \quad (2)$$

where h stands for the band-limited operator and ω_{AUT} is the region where the AUT is located. In the spectral domain, this last operator can be expressed as follows:

$$BP(k_x, k_y) = P(k_x, k_y) * H(k_x, k_y), \quad (3)$$

being B the band-limited operator defined in the spectral domain, $P(k_x, k_y)$ represents the PWS, and H is the inverse Fourier transform of the operator h .

The schematic diagram of the method is shown in Figure 4 and the steps are described as follows.

Step 1. Near-field data are used to calculate the PWS. Because the fast Fourier transform algorithm is employed in the iterative part of the method, the samples of the PWS must be known on a regular k_x - k_y grid.

Step 2. The unreliable portion of the initial PWS is filtered out by the application of the operator that was defined in (1).

Step 3. The field distribution over the AUT plane is obtained by taking the Fourier transform of the filtered PWS.

Step 4. The previous field distribution is spatially filtered using the band-limited operator that was presented in (2).

Step 5. The filtered field distribution is Fourier-transformed back to the spectral domain to obtain an auxiliary PWS.

Step 6. A new reconstructed PWS is calculated by substituting the unreliable portion of the initial PWS for the same portion of the PWS that was obtained in the previous step.

Step 7. If the new PWS fulfills the termination condition, the algorithm stops. If not, a new iteration starting from the Step 4 is performed.

3.1. Convergence. Once the method has been presented, its convergence is analyzed, that is, it is necessary to determine whether the method completely removes the truncation error and provides the exact solution outside of the reliable region. As deduced from Figure 4, if the auxiliary PWS converges to the ideal PWS, we are ensuring the convergence of the method because the information of this PWS is employed to complete the unreliable region. The auxiliary PWS can be written at each iteration as follows

$$P_1 = BAP_I$$

$$P_2 = B[I - A]P_1 + BAP_I = [I - BA]P_1 + BAP_I$$

(4)

⋮

$$P_n = B[I - A]P_{n-1} + BAP_I = [I - BA]P_{n-1} + BAP_I$$

as a consequence, at the n th iteration, the error is given by

$$P_n - P = [I - BA]P_{n-1} + BAP_I - P, \quad (5)$$

where P is the ideal PWS.

If the initial PWS calculated from near-field data does not contain errors within the reliable region, that is, $AP_I = AP$, expression (5) can be rewritten as

$$P_n - P = [I - BA](P_{n-1} - P) \quad (6)$$

because P_{n-1} and P are band-limited functions, that is, $BP_{n-1} = P_{n-1}$ and $BP = P$, (6) may be equivalently expressed as

$$P_n - P = B[I - A](P_{n-1} - P). \quad (7)$$

As observed from (7), the energy in the n th error PWS, as measured by the standard inner product $\varepsilon_n = \langle P_n - P, P_n - P \rangle$, is always less than or equal to the energy in the $(n-1)$ st error PWS. This reduction occurs because the operators $I - A$ and B decrease the energy of the signal upon which they operate. Therefore, at each iteration, the error energy is reduced twice, as demonstrated as follows.

The energy in the $(n-1)$ st error PWS is

$$\varepsilon_{n-1} = \langle P_{n-1} - P, P_{n-1} - P \rangle = \iint_{-\infty}^{\infty} |P_{n-1} - P|^2 dk_x dk_y \quad (8)$$

after applying the operator $I - A$, the new error energy is equal to

$$\begin{aligned} \varepsilon_{n-1/2} &= \langle [I - A](P_{n-1} - P), [I - A](P_{n-1} - P) \rangle \\ &= \iint_{-\infty}^{\infty} |P_{n-1} - P|^2 dk_x dk_y - \iint_{\Omega_R} |P_{n-1} - P|^2 dk_x dk_y \\ &\leq \varepsilon_{n-1}, \end{aligned} \quad (9)$$

using Parseval's identity, one can write

$$\varepsilon_{n-1/2} = \frac{1}{2\pi} \iint_{-\infty}^{\infty} |f|^2 dx dy, \quad (10)$$

where f is the Fourier transform of $[I - A](P_{n-1} - P)$. Finally, the error energy at the n th iteration is given by

$$\varepsilon_n = \langle hf, hf \rangle = \frac{1}{2\pi} \iint_{\omega_{AUT}} |f|^2 dx dy \leq \varepsilon_{n-1/2}. \quad (11)$$

Therefore, we have demonstrated that $\varepsilon_n \leq \varepsilon_{n-1/2} \leq \varepsilon_{n-1}$ for all n , ensuring that when starting from error free data in the reliable region, the method converges monotonically to the correct solution.

In the opposite case, that is, when the reliable portion of the PWS is affected by errors, we cannot write the expression (6) because $AP_I \neq AP$. However, the following relationship can be employed:

$$\delta = AP - AP_I, \quad (12)$$

where δ is the difference between the calculated PWS and the ideal PWS within the reliable region. Therefore, expression (5) takes the form

$$\begin{aligned} P_n - P &= [I - BA](P_{n-1} - P) - B\delta \\ &= B([I - A](P_{n-1} - P) - \delta), \end{aligned} \quad (13)$$

in this case, the band-limited operator, B , also introduces an error reduction. Nevertheless, the error after the application of the first operator is

$$\begin{aligned} \varepsilon_{n-1/2} &= \langle [I - A](P_{n-1} - P) - \delta, [I - A](P_{n-1} - P) - \delta \rangle \\ &= \iint_{-\infty}^{\infty} |P_{n-1} - P|^2 dk_x dk_y - \underbrace{\iint_{\Omega_R} |P_{n-1} - P|^2 dk_x dk_y}_{I_1} \\ &\quad + \underbrace{\iint_{\Omega_R} |\delta|^2 dk_x dk_y}_{I_2}, \end{aligned} \quad (14)$$

now, we can only ensure that $\varepsilon_{n-1/2} \leq \varepsilon_{n-1}$ if $I_1 \leq I_2$, that is, when the difference between the auxiliary PWS in the $(n-1)$ st iteration and the ideal PWS is larger than the difference between the initial PWS and the ideal PWS within the reliable region. As will be shown later, this condition is satisfied in the initial iterations but not for large values of n in which the difference between the auxiliary PWS and the ideal PWS is small and the initial error, δ , is already dominant. Therefore, due to that initial error in the reliable portion of the PWS, the error in the estimated pattern initially decreases with the iteration number, but, after a certain number of iterations, the error starts to increase. The goal is to find the proper termination point in the iterative method.

4. Simulated Models

In the following sections, several results will be presented in order to analyze and validate the proposed method. The input data used to obtain these results are simulated near-field data. The AUT that is employed in the simulations is an aperture with a Gaussian-tapered field distribution, as (15) shows:

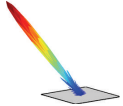
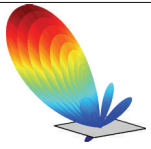
$$\vec{E}_G = E_0 e^{-(x^2/2\sigma_x^2 + y^2/2\sigma_y^2)} \hat{y}, \quad \vec{H}_G = \frac{1}{\eta} \hat{z} \times \vec{E}_G. \quad (15)$$

The frequency is 12 GHz, and the simulations are carried out in the three measurement setups under study. The measurement distance is 100λ for the three cases, and the sampling spacing and the size of the acquisition surfaces are indicated in Table 2 in which the type of phase excitation and the aperture size are also presented. The objective is to generate radiation patterns that steer in different directions with different beamwidths, especially to validate all of the truncation cases that are considered in partial SNF measurements. As observed from Table 2, Models I, II, and III are the same AUT but are measured in different scan surfaces. Models IV and V also have the same radiation pattern, but different acquisitions are employed in each of them. Finally, Model VI is measured using only one acquisition surface.

5. Critical Aspects of the Method

All steps of the proposed method are indicated in Section 3, however, some of these steps need to be described in more

TABLE 2: Parameters of the simulated models.

Model	Measurement setup	Sampling spacing	Measurement interval	Aperture size	Phase excitation	Main beam direction	Radiation pattern
I	PNF measurement	$\Delta x = 0.5\lambda$ $\Delta y = 0.5\lambda$	$x = -0.9 \dots 0.9$ m $y = -0.9 \dots 0.9$ m				
II	CNF measurement	$\Delta z = 0.5\lambda$ $\Delta\phi = 2^\circ$	$z = -1.25 \dots 1.25$ m $\phi = 0^\circ \dots 359^\circ$	$8\lambda \times 8\lambda$	Uniform	$\theta = 0^\circ$	
III	SNF measurement with polar truncation	$\Delta\theta = 2^\circ$ $\Delta\phi = 2^\circ$	$\theta = 0^\circ \dots 30^\circ$ $\phi = 0^\circ \dots 359^\circ$				
IV	SNF measurement with spherical ring truncation	$\Delta\theta = 2^\circ$ $\Delta\phi = 2^\circ$	$\theta = 20^\circ \dots 50^\circ$ $\phi = 0^\circ \dots 359^\circ$	$8\lambda \times 8\lambda$	Progressive	$\theta = 35^\circ$ $\phi = 180^\circ$	
V	SNF measurement with sectorial truncation	$\Delta\theta = 2^\circ$ $\Delta\phi = 2^\circ$	$\theta = 20^\circ \dots 50^\circ$ $\phi = 150^\circ \dots 210^\circ$				
VI	SNF measurement with azimuthal truncation	$\Delta\theta = 2^\circ$ $\Delta\phi = 2^\circ$	$\theta = 0^\circ \dots 90^\circ$ $\phi = 130^\circ \dots 230^\circ$	$4\lambda \times 16\lambda$	Progressive	$\theta = 30^\circ$ $\phi = 180^\circ$	

detail. First, it is necessary to explain how to obtain the PWS on a regular grid in the spectral domain from near-field data that are obtained in the three measurement setups. Second, a modified definition of the spectral reliable region is presented. Finally, an efficient algorithm to find the optimum termination point in the iterative method is proposed.

5.1. PWS on a Regular k_x - k_y Grid. As observed in the description of the method, the fast fourier transform algorithm is used to calculate the field distribution over the AUT plane from the PWS and vice versa. This algorithm is computationally very efficient, but it only works with samples that are distributed on a regular grid in both domains, that is, the samples of the extreme near-field are obtained on a regular x - y grid, and the PWS must be known on a regular k_x - k_y grid.

In the PNF case, the PWS is directly obtained in the required grid because it is calculated as an inverse fast fourier transform of the measured samples taken over a regular x - y grid.

In CNF and SNF cases, additional steps are required because the classical near-field to far-field transformations produce the final results on a regular θ - ϕ grid. Different calculation approaches can be used, but the easiest one is to employ an interpolation algorithm to obtain the samples on the desired grid. This solution introduces an interpolation error, but it does not require a great computational cost.

Two other approaches provide the exact values on the desired grid, but they are more complex. Both of them use the information that is contained in the spherical wave coefficients (SWC), which are known in the SNF case, but

not in the CNF case. However, they can be easily obtained from the far-field pattern [3].

One of these two approaches employs the spherical-wave-expansion-to-plane-wave-expansion (SWE-to-PWE) transformation that is presented in [27] in which it is demonstrated that it is possible to define a rigorous transformation to derive the PWS from the SWC,

$$P(k_x, k_y, z) = \sum_{n=1}^{\infty} \sum_{m=-n}^n Q_{1mn}^{(3)} T_{1mn}(k_x, k_y, z) + Q_{2mn}^{(3)} T_{2mn}(k_x, k_y, z), \quad (16)$$

where $Q_{1mn}^{(3)}$ and $Q_{2mn}^{(3)}$ are the outgoing SWC, and T_{1mn} and T_{2mn} are functions whose details can be found in [27].

The other approach evaluates the far-field pattern functions [3] on the desired directions that are defined by the regular k_x - k_y grid and calculates the far-field pattern as follows:

$$E_{FF}(\theta, \phi) = L \sum_{smn} Q_{smn}^{(3)} K_{smn}(\theta, \phi), \quad (17)$$

where E_{FF} is the far-field pattern, L is a constant, and K are the far-field pattern functions. Logically, when the far-field pattern is known, the PWS can be easily obtained by solving a system of two linear equations.

5.2. Spectral Reliable Region Employed in the Method. As deduced from the convergence analysis of Section 3, when starting from exact data within the spectral reliable region, the proposed method converges to the correct solution. Otherwise, the error decreases with the iteration number,

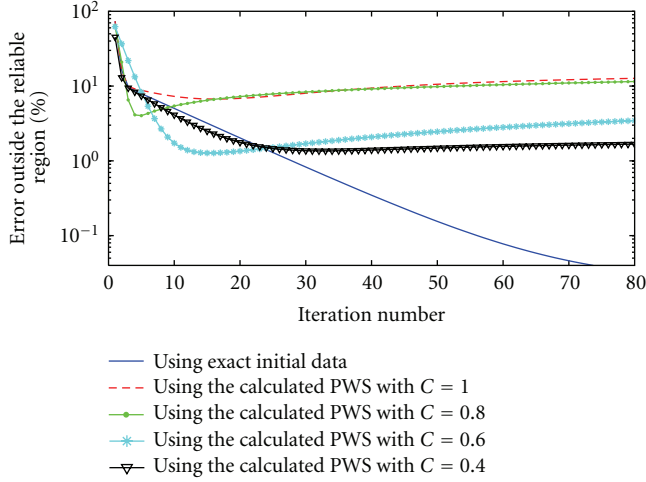


FIGURE 5: Error as a function of the iteration number using different reliable regions.

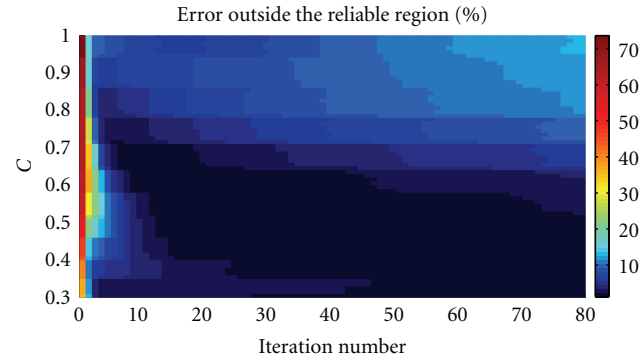


FIGURE 6: Error as a function of the iteration number and the parameter A .

but, after several iterations, it starts to increase. In Section 2, the classical definition of the spectral reliable region based on geometrical optics was presented. However, as noted in Section 1, it is impossible to define a spectral region in which the error in the calculated far-field pattern is completely zero because of the unavoidable presence of ripple errors. Therefore, the error does not decrease monotonically in the iterative method. This effect can be observed in Figure 5, where the error variation with the iteration number is represented for the Model I using different spectral reliable regions. The error in this figure is calculated as

$$\varepsilon_n(\%) = \frac{\sum_{i \notin \Omega_R} |E_n(\theta_i, \phi_i) - E_R(\theta_i, \phi_i)|^2}{\sum_{i \notin \Omega_R} |E_R(\theta_i, \phi_i)|^2} \cdot 100, \quad (18)$$

where $E_n(\theta_i, \phi_i)$ and $E_R(\theta_i, \phi_i)$ are the electric field in the n th iteration and the reference electric field, respectively. As deduced from (18), only samples that are located outside of the reliable region are considered in the determination of the error.

Several conclusions can be extracted from Figure 5. As expected, the error decreases monotonically when using the

TABLE 3: Redefinition of the maximum validity angles.

Measurement setup	New maximum validity angles
PNF measurement	$\theta'_x = C \cdot \theta_x; \theta'_y = C \cdot \theta_y$
CNF measurement	$\theta'_y = C \cdot \theta_y$
SNF measurement with polar truncation	$\theta'_v = C \cdot \theta_v$
SNF measurement with spherical ring truncation	$\theta'_{v1} = \theta_{v1} - (1 - C) \cdot (\theta_{v1} - \theta_{v2})/2$ $\theta'_{v2} = \theta_{v2} + (1 - C) \cdot (\theta_{v1} - \theta_{v2})/2$
SNF measurement with azimuthal truncation	$\phi'_{v1} = \phi_{v1} + (1 - C) \cdot (\phi_{v1} - \phi_{v2})/2$ $\phi'_{v2} = \phi_{v2} - (1 - C) \cdot (\phi_{v1} - \phi_{v2})/2$
SNF measurement with sectorial truncation	$\theta'_{v1} = \theta_{v1} - (1 - C) \cdot (\theta_{v1} - \theta_{v2})/2$ $\theta'_{v2} = \theta_{v2} + (1 - C) \cdot (\theta_{v1} - \theta_{v2})/2$ $\phi'_{v1} = \phi_{v1} + (1 - C) \cdot (\phi_{v1} - \phi_{v2})/2$ $\phi'_{v2} = \phi_{v2} - (1 - C) \cdot (\phi_{v1} - \phi_{v2})/2$

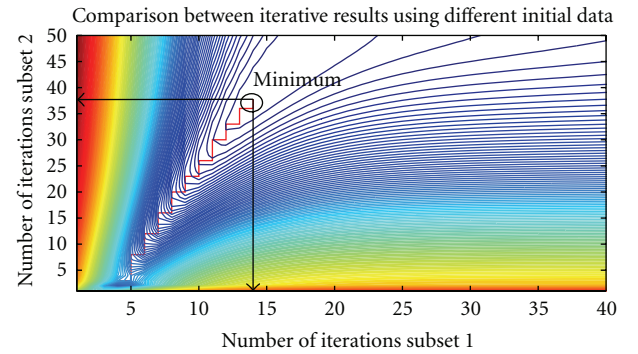


FIGURE 7: Gradient descent algorithm to find the optimum termination point.

exact initial data within the reliable region (see solid blue line). However, it is impossible to obtain those exact values because of the mentioned ripple errors. Then, in order to simulate the real behavior of the error, the PWS obtained from the truncated near-field acquisition is employed. Using this PWS and the spectral reliable region defined by geometrical optics and specified in Table 1, the error curve is as the red dashed line shows. In order to obtain a better convergence, the use of reliable regions smaller than that one defined by geometrical optics is considered. These new regions are determined by redefining the maximum validity angles, as indicated in Table 3 in which a weighting factor ($C < 1$) is introduced. The error variation for $C = 0, 8$, $C = 0, 6$, and $C = 0, 4$ is presented in Figure 5, such that when the value of C is reduced, the minimum error that is achieved with this method is smaller, and the number of iterations that are required to obtain that minimum is larger. However, when that region is smaller than a certain size, the minimum error starts to increase because in addition to removing ripple errors, also useful information is removed. From practical results, we deduce that, in a general case, a value of C between 0.35 and 0.85 will usually give a low minimum error. In Figure 6, the error as a function of the number

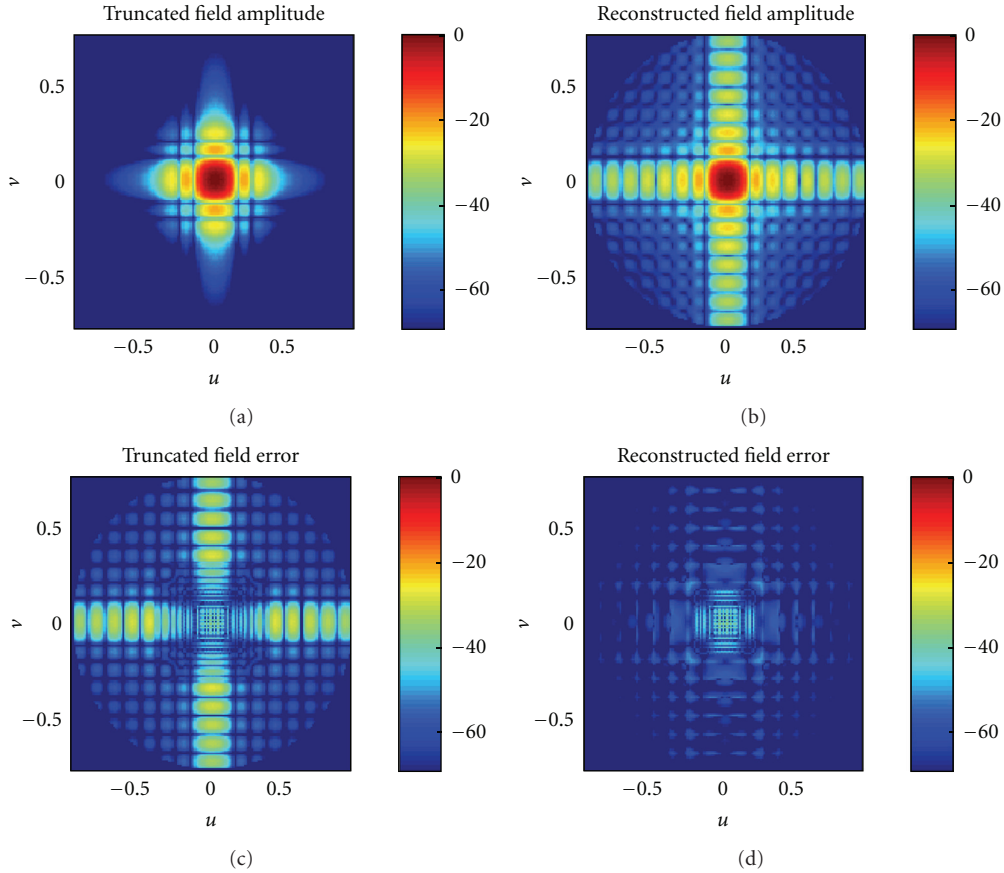


FIGURE 8: Far-field pattern and truncation error in dB before and after applying the iterative method for the Model I.

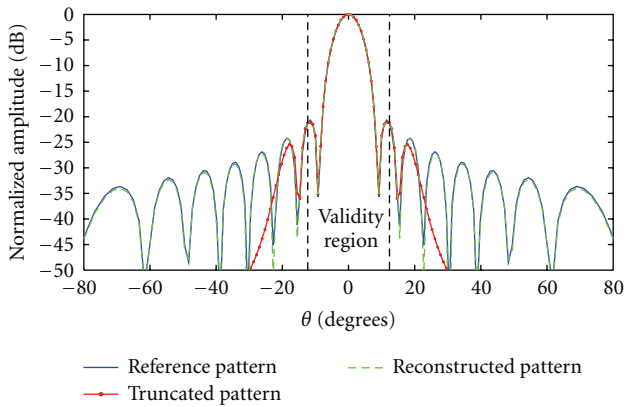


FIGURE 9: Comparison between the truncated, reconstructed and reference far-field patterns for the Model I in the $\phi = 0^\circ$ cut.

of iterations and the parameter C is depicted for the Model I. As observed, very good results are obtained in the mentioned range of C , with an error outside of the reliable region lower than 5%.

5.3. Algorithm to Determine the Proper Termination of the Iterations. Because of the impossibility of determining the



FIGURE 10: Measurement of a rectangular-horn antenna in a planar near-field range.

exact values of the PWS within the reliable region, the error in the iterative method does not decrease monotonically with the iteration number. Nevertheless, as observed in Figure 5, there is always a minimum that can provide an accurate result, and therefore, it can be used as termination point in the iterative part of the method. An algorithm to find that minimum was proposed in [17], and it is based on the following principle: if we use different initial truncated surfaces, the initial error within the reliable region will also be different, and the error in the iterative procedure will vary

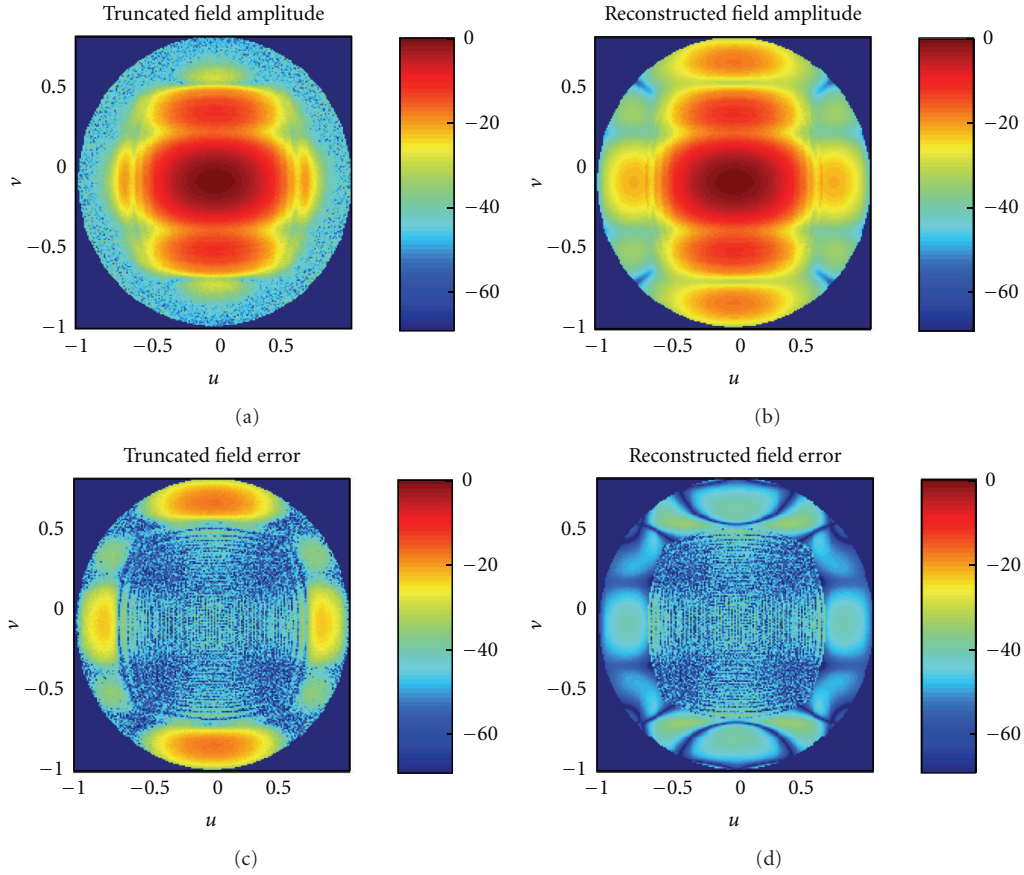


FIGURE 11: Far-field pattern and truncation error in dB before and after applying the iterative method for the rectangular-horn measured in PNE.

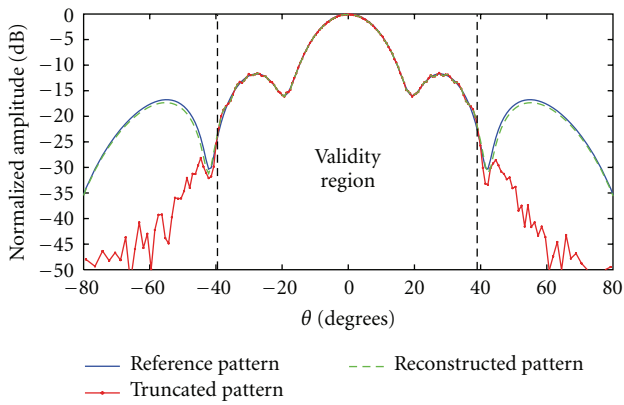


FIGURE 12: Comparison between the truncated, reconstructed and reference far-field patterns for the rectangular horn in the $\phi = 90^\circ$ cut.

in a different way for the same value of C . Therefore, when comparing the iterative results that were obtained in both cases, we will have a minimum when both results have the minimum error. This algorithm does not require additional measurements because two different subsets of the measured near-field data can be used as inputs in the iterative method.

The iterative results obtained in both cases are stored and pairwise-compared to determine the optimum termination point for the two cases when the result of the comparison is minimum. The comparisons are carried out as follows:

$$\mu_{ij} = \sum |E_i^1(\theta, \phi) - E_j^2(\theta, \phi)|^2, \quad (19)$$

where $E_i^1(\theta, \phi)$ and $E_j^2(\theta, \phi)$ are the reconstructed field in the i th iteration using the first data subset and the reconstructed field in the j th iteration using the second data subset, respectively.

The main drawback of this approach is that many iterations and comparisons are required because we do not know where the minimum is *a priori*. To solve this problem, we propose the use of the Gradient Descent algorithm, which is an optimization algorithm to find the minimum. As observed in Figure 7, with this new algorithm, when we move in one direction, we perform a new iteration with one of the two data subsets and obtain a new far-field pattern estimation that is used to perform a new comparison. If the value of this new comparison is larger than the previous one, we change the direction of movement (the iterations are performed using the other data subset). If not, the algorithm performs another iteration using the same data subset. Finally, when the minimum is reached, the algorithm stops. Using

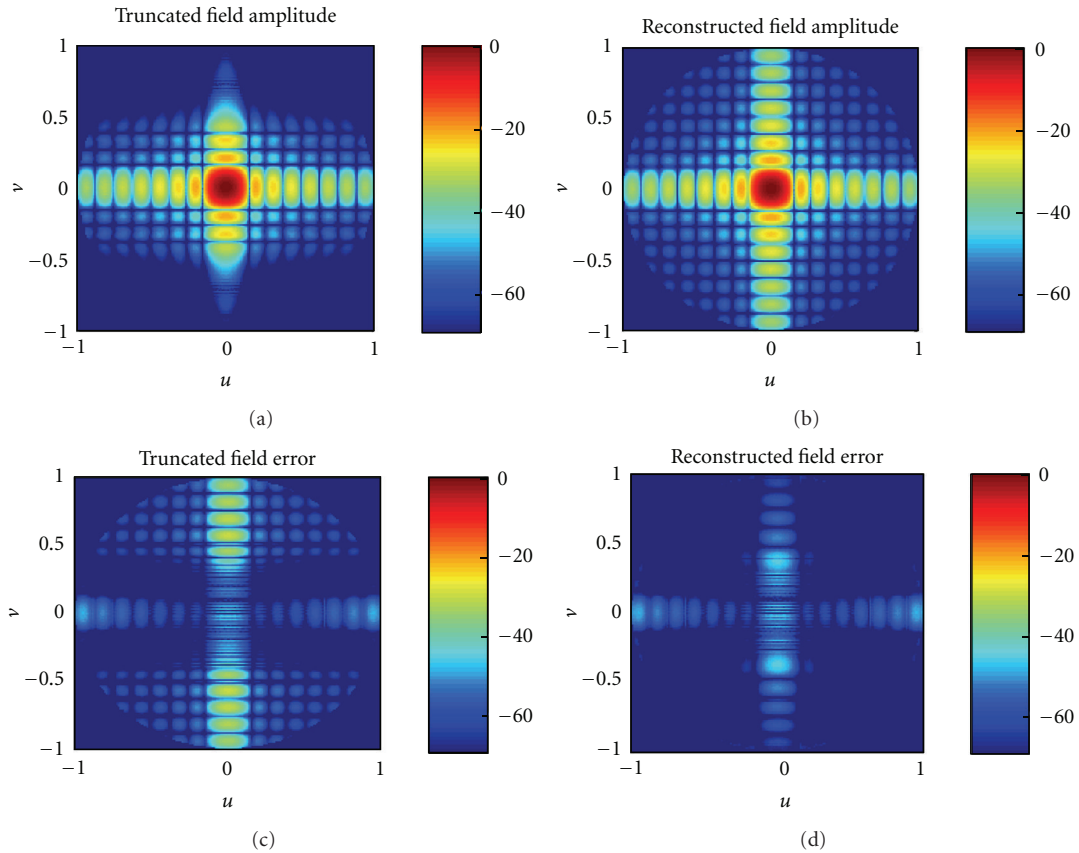


FIGURE 13: Far-field pattern and truncation error in dB before and after applying the iterative method for the Model II.

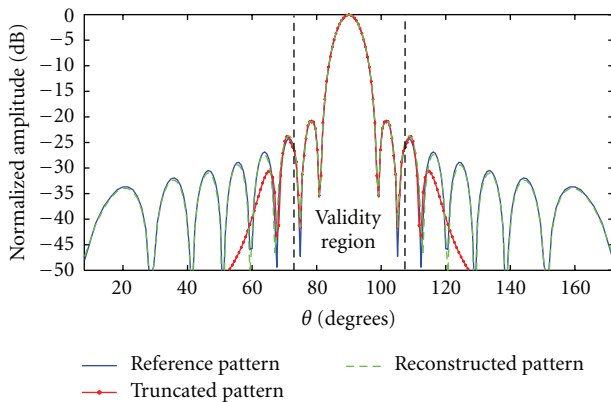


FIGURE 14: Comparison between the truncated, reconstructed and reference far-field pattern for the Model II in the $\phi = 90^\circ$ cut.

this algorithm, both the number of iterations and comparisons may be drastically reduced, thereby requiring less computational time to obtain the minimum.

6. Numerical Results

To verify the accuracy of the proposed method, several examples are analyzed. The objective is to validate the method in all of the cases that are described in Figure 1. This valid-

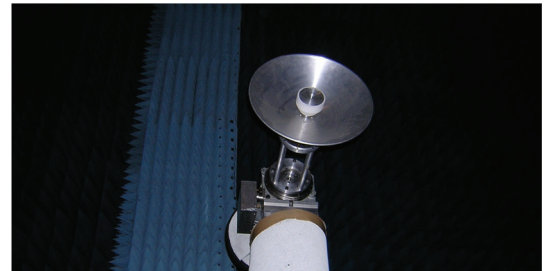


FIGURE 15: Measurement of a Ku-band reflector antenna in a cylindrical near-field range.

ation is carried out independently for each of these cases by employing both the simulated models defined in Section 4 and measured truncated near-field data.

6.1. Planar Near-Field Measurement. The method was already numerically validated for this type of measurement setup in [17]. In this paper, another two examples are presented. The first example uses the information of simulated Model I where the maximum validity angles are $\theta_x = \theta_y = 17.75^\circ$. The iterative method was applied using a value of C equal to 0.7 and the second subset that was employed in the algorithm to find the optimum termination point was obtained from the simulated data by taking only the samples within a square

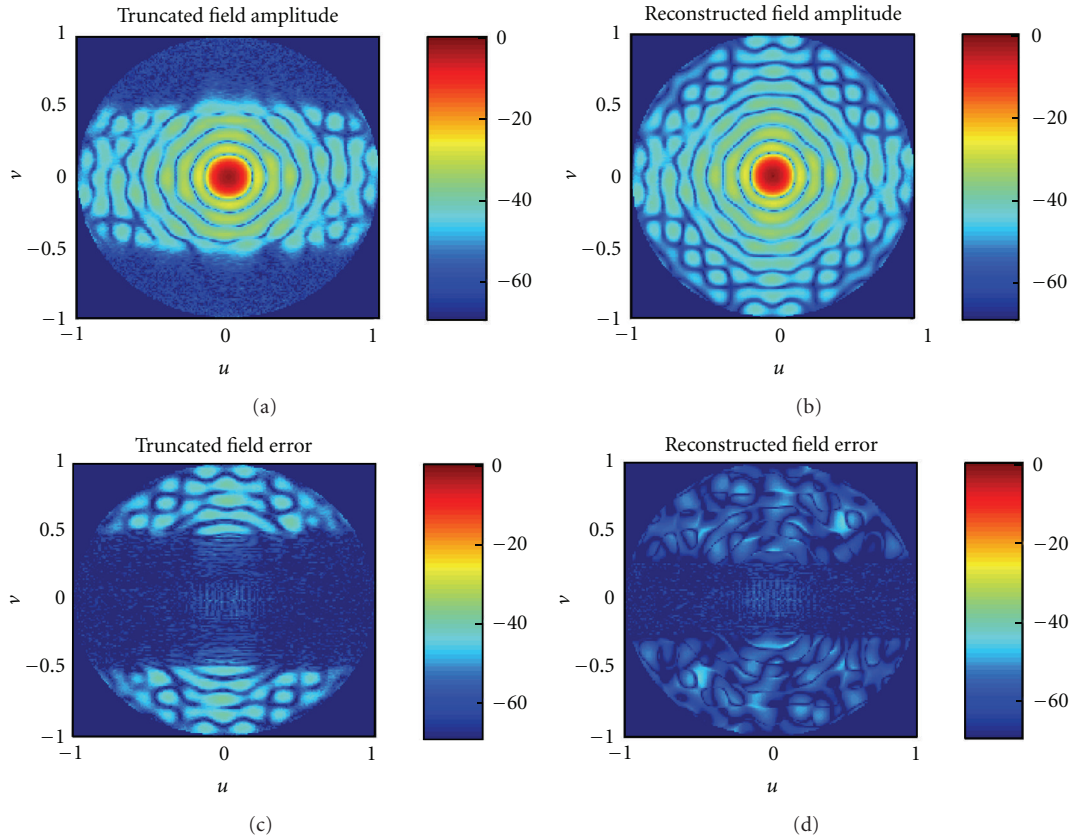


FIGURE 16: Far-field pattern and error in dB before and after applying the iterative method for the reflector measured in CNF.

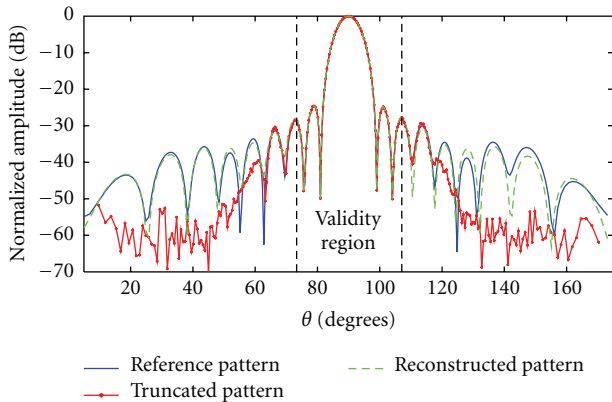


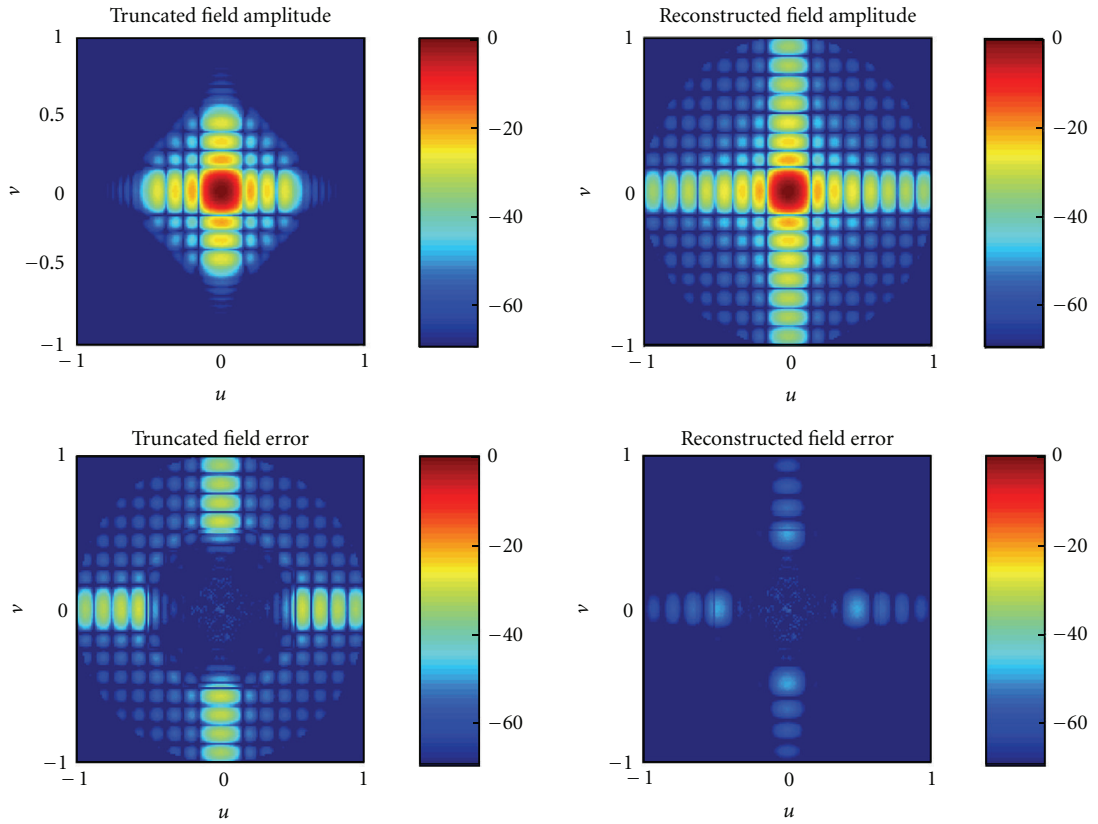
FIGURE 17: Comparison among the truncated, reconstructed, and reference far-field patterns for the reflector in the $\phi = 90^\circ$ cut.

of 1.5 m side. The results of the reconstruction are depicted in Figure 8 in which both the far-field and the truncation error before and after the application of the method are presented. As it is apparent, the proposed procedure provides a great reduction of the truncation error and retrieves the far-field pattern in the forward hemisphere with good accuracy. In this particular case, the error defined in (18) is reduced from 62.3% to 1.2%. The improvement achieved with the method is observed better in Figure 9, where a comparison among the

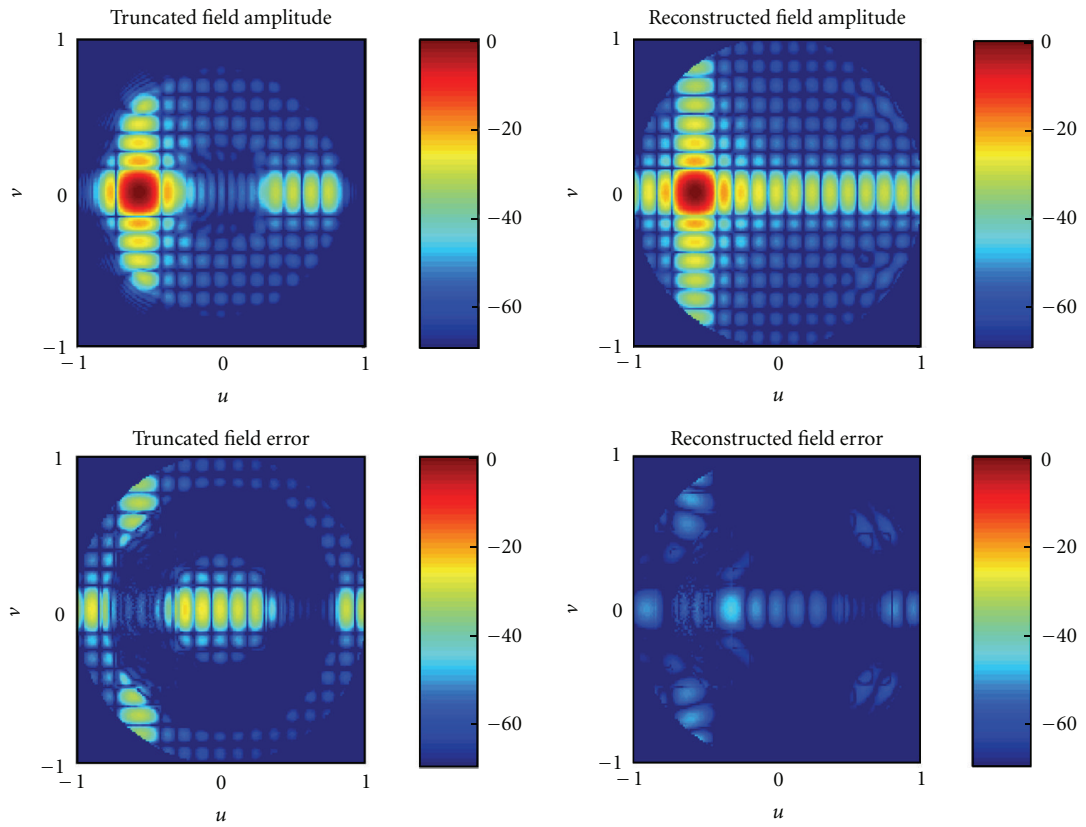
truncated, reconstructed and reference far-field patterns for the $\phi = 0^\circ$ cut is shown.

In the second validation, measured data were employed as input information to the proposed method. The measurement was carried out at 11 GHz using the PNF range in the anechoic chamber at the Technical University of Madrid (UPM). The probe and the AUT were selected to be a corrugated conical-horn antenna and a rectangular-horn antenna, respectively, and they were separated from each other by 1.3 m (see Figure 10). When both antennas were mounted on their respective positioners, a measurement over a $2.7\text{ m} \times 2.7\text{ m}$ acquisition plane was recorded. The same AUT was previously measured in a SNF range in order to obtain a reference pattern for comparison with the results obtained with the presented method. Figure 11 shows a comparison between the truncated and reconstructed far-field patterns and the error before and after applying the method. As in the previous example, a great improvement of the accuracy outside of the reliable region is achieved, which reduces the error from 79.3% to 7.1%. Another comparison is presented in Figure 12.

6.2. *Cylindrical Near-Field Measurement.* As commented before, when measuring an antenna over a cylindrical surface, an unavoidable truncation error appears in the far-field pattern because of the finite size of that surface. Therefore,

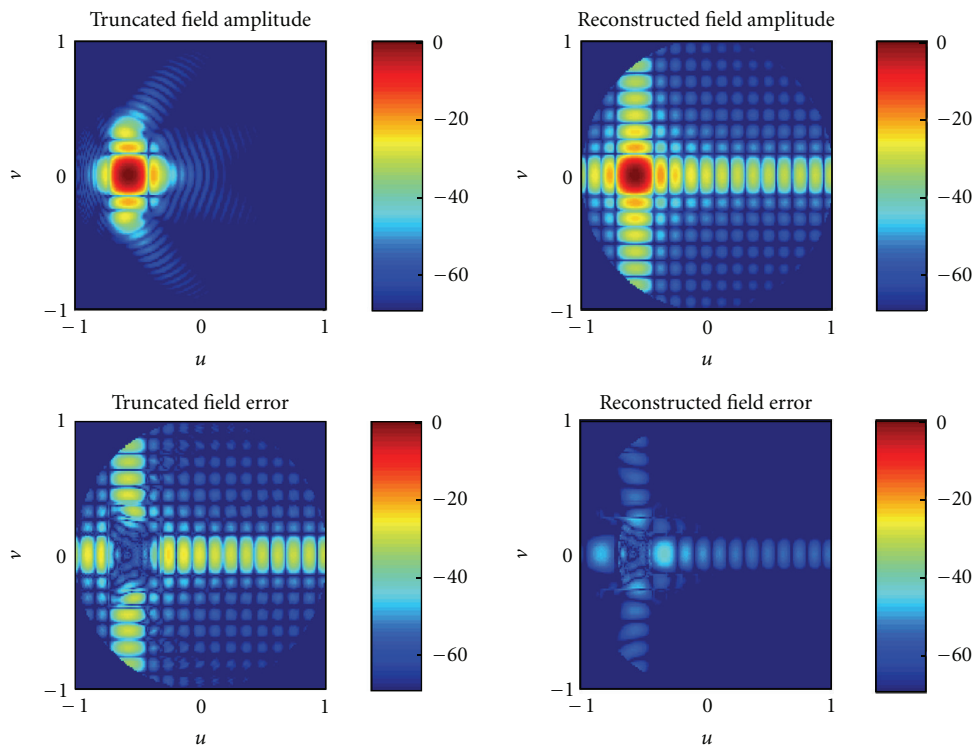


(a)

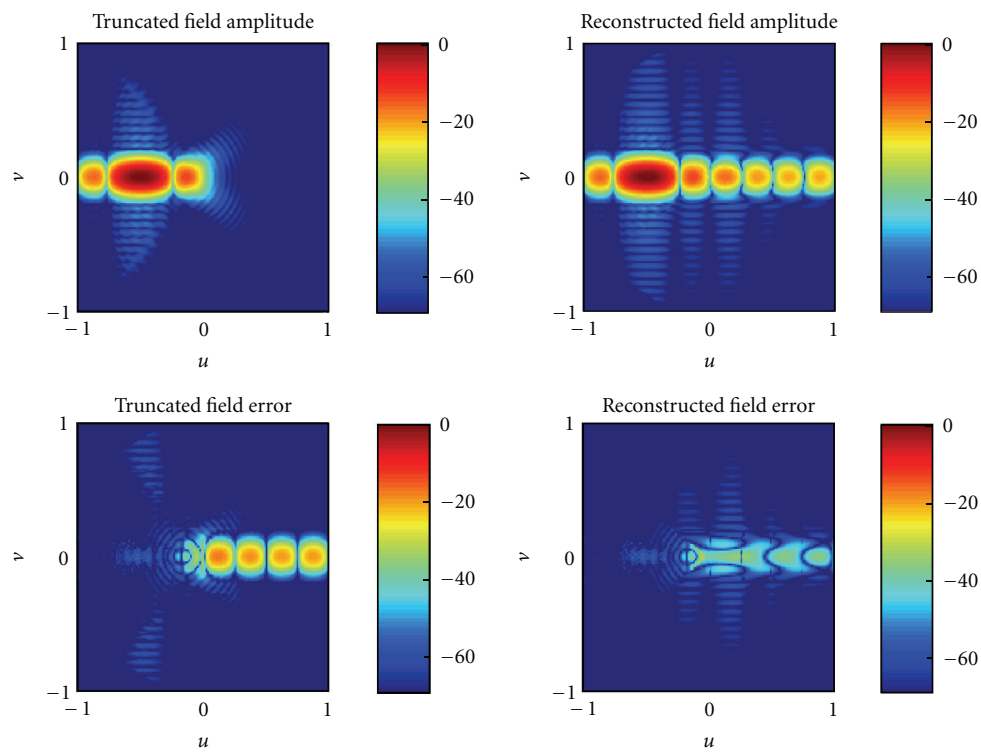


(b)

FIGURE 18: Continued.



(c)



(d)

FIGURE 18: Far-field pattern and error in dB before and after applying the iterative method for the Models III (a), IV (b), V (c), and VI (d).

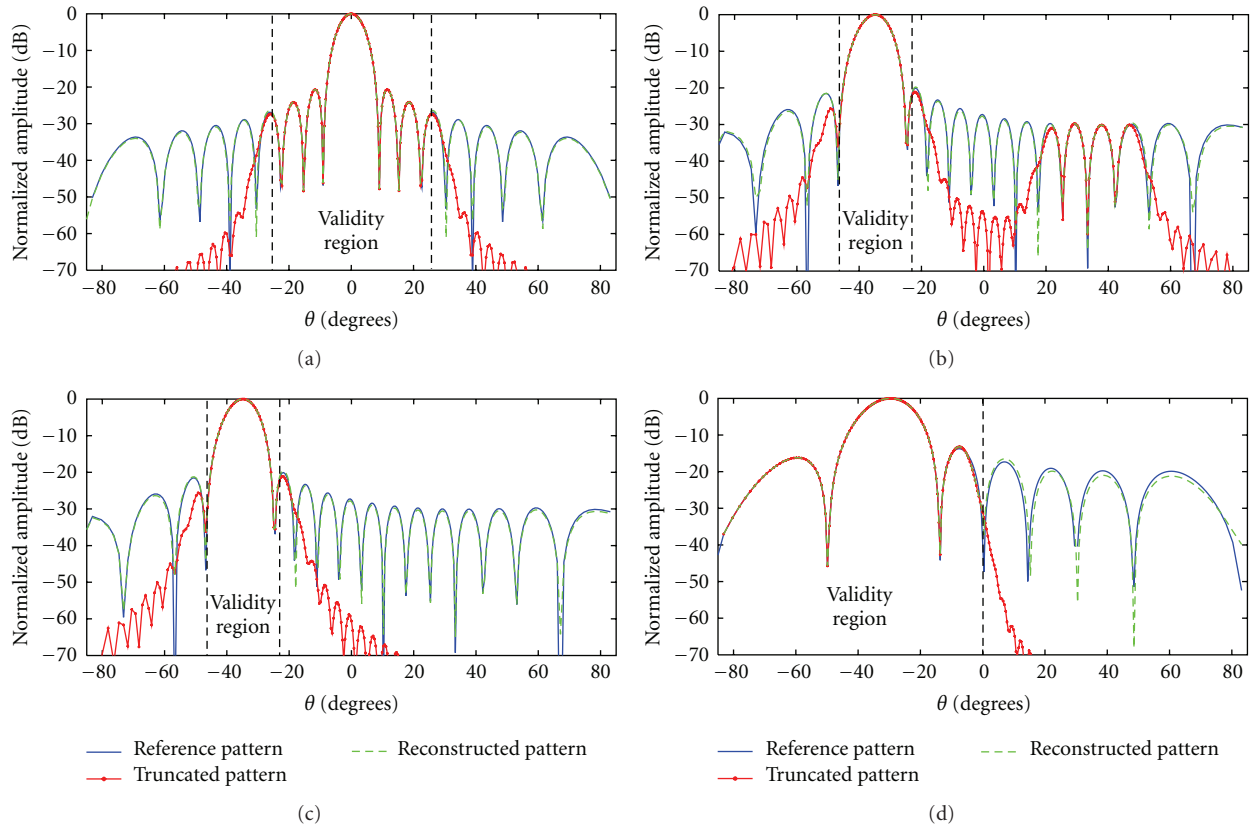


FIGURE 19: Comparison between the truncated, reconstructed and reference far-field patterns for the Models III (a), IV (b), V (c), and VI (d) in the $\phi = 0^\circ$ cut.



FIGURE 20: Measurement of an X-band array antenna in spherical near-field.

in this second part of the numerical results, cylindrical near-field data are employed as input to the iterative method in order to demonstrate its effectiveness in this type of measurement setup.

Logically, because the method uses information about the PWS, only the truncation error in the forward hemisphere may be suppressed. The validation is carried out, as in the previous case, by employing both simulated and measured data. First, the simulated Model II that is described in Table 2 is used. According to the geometrical optics, in this first example, only the far-field pattern in the spectral region defined by $|\nu| < \sin(24.7^\circ)$ can be considered reliable. However, after the application of the method, it is possible

to retrieve the pattern in the whole forward hemisphere with good accuracy, as observed in Figure 13. As in the previous examples, one far-field cut comparison is depicted in Figure 14.

The method was also validated with measured near-field data. The measurement was performed in the CNF range at the UPM. For the experiment, the probe and the AUT consisted of a corrugated conical-horn antenna and a Ku-band reflector with a 40 cm diameter (see Figure 15), respectively. The data were acquired over a cylinder with a height of 2.7 m and a radius of 2.3 m and with a spatial sampling equal to 0.5λ in the vertical direction and 2.5° in the azimuth. As in the PNF case, the AUT was also measured in a whole sphere in order to obtain a reference pattern. From inspection of Figure 16, it is evident that the truncation error is greatly suppressed, reducing the error expressed in (18) from 58.2% to 8.9%. A comparison depicted in Figure 17 shows the reconstructed far-field pattern in the vertical plane versus the truncated and reference far-field pattern.

6.3. Spherical Near-Field Measurement. Finally, the capability of the proposed method to reduce truncation errors in partial SNF measurements is demonstrated. Unlike PNF and CNF measurements, in which the shape of the reliable region is always the same, data can be acquired over different truncated spheres in the spherical case, defining different reliable

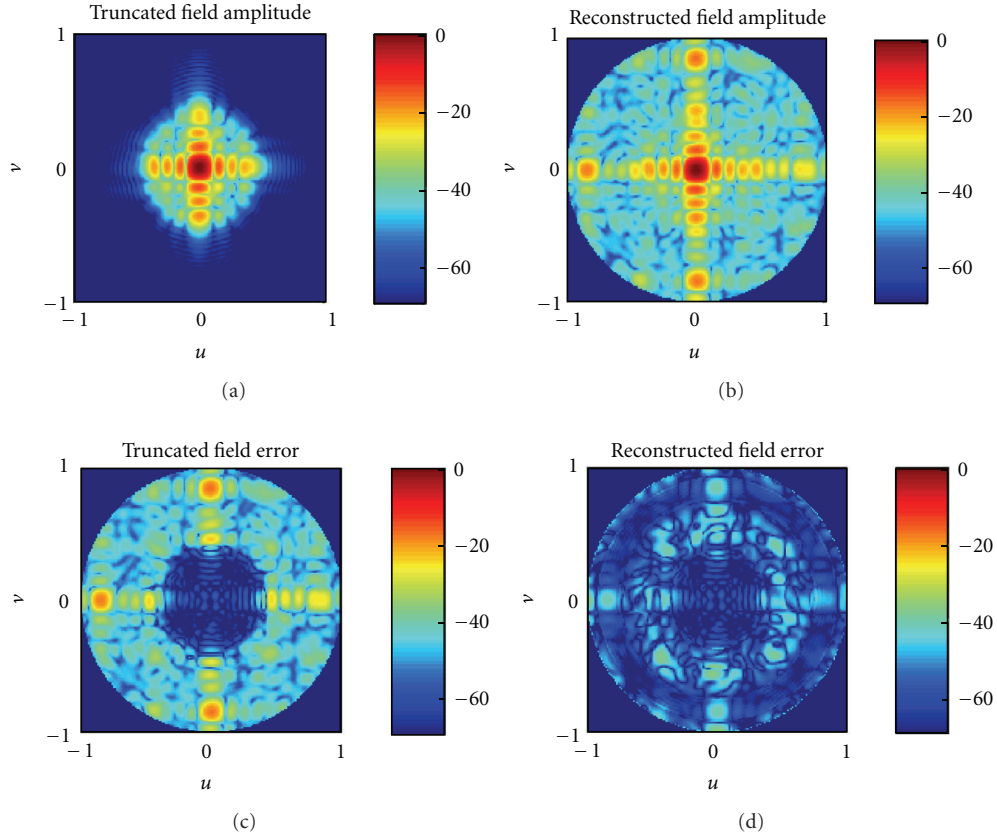


FIGURE 21: Far-field pattern and error in dB before and after applying the iterative method for the array antenna measured in SNF with polar truncation.

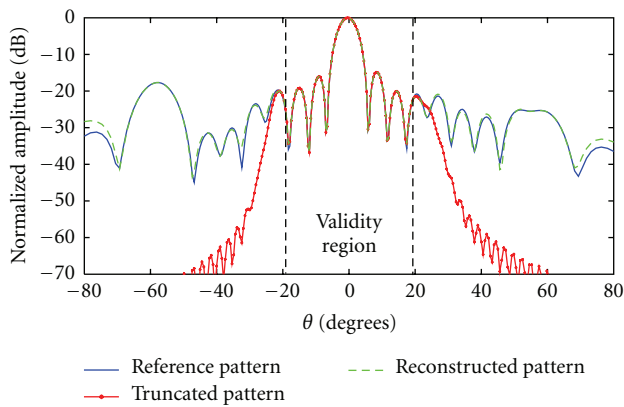


FIGURE 22: Comparison between the truncated, reconstructed and reference far-field pattern for the array in the $\phi = 0^\circ$ cut.

regions. In this work, four types of truncation in the SNF measurements are considered (see Figure 2). The last four simulated models presented in Section 4 are used to analyze the effectiveness of the method in each of these truncations. All of the results are shown in Figures 18 and 19, and they contain the far-field pattern and the error before and after applying the method, as well as a comparison among

the reconstructed, truncated, and reference patterns in one plane, as in the previous examples.

The proposed iterative method was also applied to measured spherical near-field data. The acquisition was performed in the SNF range at the UPM. The AUT was formed by a square array of 256 printed elements covering a large bandwidth in the X-band, and its dimensions were 40 cm \times 40 cm. The array was divided into 16 square subarrays of 4 elements \times 4 elements (see Figure 20). Data were taken in a whole sphere with a spatial sampling equal to 2° both in azimuth and elevation. Because the AUT is steering at broadside, the most appropriate truncation is a polar truncation. Therefore, only measured data from $\theta = 0^\circ$ to $\theta = 20^\circ$ were used as input for the method. After the application of the iterative procedure and comparison with the reference pattern from the whole measurement, the results in Figures 21 and 22 were obtained, in which the truncation error is greatly reduced, as in the previous examples. In this last case, the error of (18), which has been considered to be the quality factor, is reduced from 82.5% to 8.6%.

7. Conclusions

An efficient method to reduce truncation errors when measuring an antenna in planar, cylindrical or partial spherical

near-field setup has been proposed in this paper. The method is based on the Gerchberg-Papoulis iterative algorithm used to extrapolate band-limited functions, and it is a generalization of the approach presented in [17] for the planar case. Therefore, the proposed method can be viewed as a continuation of the work developed in [17], not only extending its applicability, but also introducing new algorithms to reduce the computational time required to remove the truncation errors. The convergence of this method has been mathematically demonstrated. Moreover, a detailed study of the spectral reliable region for each type of measurement setup and an analysis of critical aspects of the method has been performed. Finally, the method has been validated by using both simulated and measured near-field data, showing that it is possible to reduce the truncation errors effectively. It was noted that the proposed method works well for planar aperture antennas because the antenna aperture, in which the fields are assumed to be concentrated, is well defined.

Acknowledgments

This work was developed with the support of the Spanish FPU Grant for Ph.D. students and the financing of the Crocante Project (TEC2008-06736-C03-01/TEC). F. J. Cano-Fácil would also like to thank DTU Electrical Engineering for its support during his stay at the Technical University of Denmark.

References

- [1] A. D. Yaghjian, "An overview of near-field antenna measurements," *IEEE Transactions on Antennas and Propagation*, vol. AP-34, no. 1, pp. 30–44, 1986.
- [2] H. G. Booker and P. C. Clemmow, "The concept of an angular spectrum of plane waves, and its relation to that of polar diagram and aperture distribution," *Proceedings of the IEEE: Radio and Communication Engineering*, vol. 97, no. 45, pp. 11–17, 1950.
- [3] J. E. Hansen, Ed., *Spherical Near-field Antenna Measurements*, Peter Peregrinus, London, UK, 1988.
- [4] W. M. Leach and D. T. Paris, "Probe compensated near-field measurements on a cylinder," *IEEE Transactions on Antennas and Propagation*, vol. AP-21, no. 4, pp. 435–445, 1973.
- [5] P. R. Rousseau, "The planar near-field measurement of a broad beam antenna using a synthetic subarray approach," in *Proceedings of the IEEE Antennas and Propagation Society International Symposium Digest*, pp. 160–163, Montreal, Canada, July 1997.
- [6] T. Al-Mahdawi, "Planar near-field measurement of low directivity embedded antennas using a synthetic array probe technique," in *Proceedings of the IEEE International Antennas and Propagation Symposium Digest*, pp. 1311–1314, June 1998.
- [7] E. B. Joy, "Windows '96 for planar near-field measurements," in *Proceedings of the Antenna Measurement Techniques Association*, pp. 80–85, 1996.
- [8] E. B. Joy, C. A. Rose, A. H. Tinning, and EE6254 Students, "Test-zone field quality in planar near-field measurements," in *Proceedings of the Antenna Measurement Techniques Association*, pp. 206–210, Williamsburg, Va, USA, November 1997.
- [9] P. Petre and T. K. Sarkar, "Planar near-field to far-field transformation using an equivalent magnetic current approach," *IEEE Transactions on Antennas and Propagation*, vol. 40, no. 11, pp. 1348–1356, 1992.
- [10] S. F. Gregson, C. G. Parini, and J. McCormick, "Development of wide-angle antenna pattern measurements using a probe-corrected polyplanar near-field measurement technique," vol. 152, no. 6, pp. 563–572.
- [11] O. M. Bucci, G. D'Elia, and M. D. Migliore, "New strategy to reduce the truncation error in near-field/far-field transformations," *Radio Science*, vol. 35, no. 1, pp. 3–17, 2000.
- [12] O. M. Bucci, C. Gennarelli, and C. Savarese, "Representation of electromagnetic fields over arbitrary surfaces by a finite and nonredundant number of samples," *IEEE Transactions on Antennas and Propagation*, vol. 46, no. 3, pp. 351–359, 1998.
- [13] J. C. Bolomey, O. M. Bucci, L. Casavola, G. D'Elia, M. D. Migliore, and A. Ziyat, "Reduction of truncation error in near-field measurements of antennas of base-station mobile communication systems," *IEEE Transactions on Antennas and Propagation*, vol. 52, no. 2, pp. 593–602, 2004.
- [14] F. D'Agostino, F. Ferrara, C. Gennarelli, R. Guerriero, and G. Riccio, "An effective technique for reducing the truncation error in the near-field-far-field transformation with plane-polar scanning," *Progress in Electromagnetics Research*, vol. 73, pp. 213–238, 2007.
- [15] O. M. Bucci and M. D. Migliore, "A new method for avoiding the truncation error in near-field antennas measurements," *IEEE Transactions on Antennas and Propagation*, vol. 54, no. 10, pp. 2940–2952, 2006.
- [16] L. Infante, E. Martini, A. Peluso, and S. Maci, "The shadow boundary integral for the reduction of the truncation error in near-field to far-field transformations," in *Proceedings of the IEEE Antennas and Propagation Society International Symposium*, pp. 416–419, Washington, DC, USA, July 2005.
- [17] E. Martini, O. Breinbjerg, and S. Maci, "Reduction of truncation errors in planar near-field aperture antenna measurements using the Gerchberg-Papoulis algorithm," *IEEE Transactions on Antennas and Propagation*, vol. 56, no. 11, pp. 3485–3493, 2008.
- [18] R. W. Gerchberg, "Super-resolution through error energy reduction," *Optica Acta*, vol. 21, no. 9, pp. 709–720, 1974.
- [19] A. Papoulis, "A new algorithm in spectral analysis and band-limited extrapolation," *IEEE Transactions on Circuits and Systems*, vol. 22, no. 9, pp. 735–742, 1975.
- [20] M. Serhir, J. M. Geffrin, A. Litman, and P. Besnier, "Aperture antenna modeling by a finite number of elemental dipoles from spherical field measurements," *IEEE Transactions on Antennas and Propagation*, vol. 58, no. 4, Article ID 5398845, pp. 1260–1268, 2010.
- [21] K. T. Kim, "Truncation-error reduction in 2D cylindrical/spherical near-field scanning," *IEEE Transactions on Antennas and Propagation*, vol. 58, no. 6, pp. 2153–2158, 2010.
- [22] K. T. Kim, "Truncation-error reduction in acoustic spherical near-field scanning," in *Proceedings of the Antennas and Propagation Society International Symposium, (APSURSI '10)*, Toronto, Canada, July 2010.
- [23] A. Papoulis, *Signal Analysis*, McGraw-Hill, New York, NY, USA, 1977.
- [24] R. C. Wittmann, C. F. Stubenrauch, and M. H. Francis, "Spherical scanning measurements using truncated data sets," in *Proceedings of the Antenna Measurement Techniques Association*, pp. 279–283, Cleveland, Ohio, USA, November 2002.

- [25] E. Martini, S. Maci, and L. J. Foged, "Spherical near field measurements with truncated scan area," in *Proceedings of the European Conference on Antennas and Propagation*, pp. 3412–3414, Rome, Italy, April 2004.
- [26] A. D. Yaghjian, "Upper bound errors in far-field antenna parameters determined from planar near-field measurements," NBS Technical Report 667, National Bureau of Standards, Boulder, Colo, USA, 1975.
- [27] C. Cappellin, *Antenna diagnostic for spherical near-field antenna measurements*, Ph.D. thesis, Department of Electrical Engineering, Technical University of Denmark, Lyngby, Denmark, 2007.